DEVELOPMENT OF ROBUST AB INITIO METHODS FOR DESCRIPTION OF EXCITED STATES AND AUTOIONIZING RESONANCES

by

Dmitry Zuev

A Dissertation Presented to the
FACULTY OF THE USC GRADUATE SCHOOL
UNIVERSITY OF SOUTHERN CALIFORNIA
In Partial Fulfillment of the
Requirements for the Degree
DOCTOR OF PHILOSOPHY
(CHEMISTRY)

May 2014

Acknowledgements

First of all I would like to express greatest gratitude to my advisor - Professor Anna Krylov. It was a great honor for me to be a part of her bright group all these 5 years. Without her advice, support and motivation throughout all my years in graduate school this work would not be possible. She was always source of inspiration and I knew that her door is always open if I need help or advice. After all these years working with Anna I learnt that she is a great scientist, leader and just a good person.

The group under the strict guidance by Anna has always been full with brilliant and helpful people. I would like to thank Professor Ksenia Bravaya for helping me with making first steps in mastering the field of quantum chemistry. Her diligence and willingness to help were one of the determinant factors in succeeding at my projects. Dr. Zhenya Epifanovsky was the first person who taught me real programming in C++ which allowed me to get a job as a software developer. By looking at his high-class code I always had an example and motivation to be a good programmer. Dr. Thomas Jagau was a fresh blood for our group who helped us to develop new approaches in describing

resonances. His expertise and punctuality allowed us to look at the old problem from the completely different angle.

I would like to thank Dr. Kirill Khistyaev and Nastya Gunina for being good labmates and friends. Besides them I would like to thank other friends outside the lab - Ivan Grishagin, Andrey Rudenko, Anatoly Dryga, Sergey Mukhin. All of them together made my life in Los Angeles interesting and enjoyable. I especially would like to thank my early deceased friend Misha Vinaykin. We were very good friends since Saint Petersburg State University and he was the person who encouraged me to apply to USC for graduate studies. His tragic death was a big loss for scientific community and all his friends.

I would also like to thank other members of Chemistry Department who taught me many important things both in classes and outside it. Professor Curt Wittig taught very interesting class and his lectures were always fun to listen to. Professor Stephen Bradforth and Alexander Benderskii taught a very useful class on Molecular Spectroscopy which helped me to look at the molecules and its properties from a different perspective. I would like to thank Professor Andrey Vilesov who told me and Misha about USC Chemistry Department and explained how to enter graduate school. I would like to thank Michele Dea - the person who is always ready to help with any administrative matters and resolve any problems.

I would like to thank my parents in Russia who were always supportive and made it possible for me to attend and graduate from one of the best Physics Departments in Russia. Without them I would never achieve what I have now.

Graduate school was a time when I was rapidly growing - both intellectually and personally. It was the time when I met many smart people, made very good friends and learnt very important life lessons. I will always remember it as one of the most important and interesting chapters of my life.

Table of contents

List of tables

List of figures

Abbreviations

CAP	complex absorbing potential
CC	coupled-cluster
CCSD	coupled-cluster with single and double substitutions
CD	Cholesky decomposition
CS	complex scaling
EA	electron attachment
EE	excitation energy
ERI	electron repulsion integrals
GFP	green fluorescent protein
GPLMR	generalized preconditioned locally residual method
EOM	equation-of-motion
EOM-CCSD	equation-of-motion coupled-clusters single and double substitutions
HOMO	highest occupied molecular orbital
LUMO	lowest unoccupied molecular orbital
IP	ionization potential

PYP	photoactive yellow protein
pCA	para-coumaric acid
RI	resolution-of-identity

Abstract

High level *ab initio* methods are indispensable tools for theoretical studies of molecular systems. By using quantum-mechanical principles, these methods enable solution of complex chemical problems by using the power of computers. Knowing only the positions and types of the atoms, one can calculate virtually all the properties of the molecules such as charge distributions, dipole moments, reaction and excitation energies. Among *ab initio* techniques coupled cluster (CC) and equation-of-motion EOM family of methods plays a special role. These methods enable accurate and systematic treatment of electron correlation for both the ground and excited states. Accurate recovery of electron correlation is essential for achieving chemical accuracy in calculations (1 kCal/mol).

In Chapter 2 we present high level *ab initio* calculations of the electronic structure of the two isomers of the photoactive yellow protein (PYP) model chromophores. We found that the phenolate and carboxylate isomers of the model chromophore (para-coumaric acid, pCA) have distinctly different pattern of ionization and excitation energies, which contradicts published experimental results. Their excitation energies differ by more than 1 eV and the first excited states in both isomers are autoionizing resonances. The phenolate form of pCA exhibits shape resonance, whereas for carboxylate

we predicted Feshbach-type resonance. Next, in Chapter 3, we investigate how microhydration affects the electronic structure of the PYP and GFP model chromophores. We found that microhydration leads to a larger blue shift in ionization than in excitation energy, thus converting resonances into bound states.

Following our findings of resonance states in gas-phase chromophores we began the development of new methods for proper description of resonance positions and lifetimes. In Chapter 4 we extend EOM methods to atomic resonances by applying complex scaled formalism in which all coordinates are rotated by a complex angle θ. By computing θ-trajectories and finding an optimal angle, θ_{opt}, we are able to find positions and lifetimes of the resonances in He, H^-, and Be. For the description of molecular resonances, we use another approach in which we introduce complex absorbing potential (CAP) into the original Hamiltonian. CAP is devised to absorb the divergent tail of the resonance wave function. By using the CAP-augmented Hamiltonian with EOM methods we study electronically attached shape resonances in various medium-size molecules. We find that an artificial perturbation induced by the CAP can be diminished by introducing a first-order correction to the energy. We also observe that the corrected energies are much less sensitive to the onset of the CAP (e.g., box size) and that accurate results can be obtained using standard basis sets augmented by diffuse functions.

In Chapter 6 improvement of the memory requirements in CC and EOM methods is presented. By performing Cholesky decomposition of the two-electron integrals tensor we significantly reduce its storage requirements from $O(N^4)$ to $O(N^3)$, which extends the applicability of the method to larger systems that may not be accessible by canonical EOM-CCSD. The errors introduced by the decomposition are small and can be controlled by a single threshold specified by the user.

Finally, in Chapter 7 we present a new version of Davidson's algorithm for solving the eigenvalue problems in quantum chemical calculations. These new algorithms facilitate finding the roots either around the user-specified energy shift or by user-defined guess orbitals. These modifications will enable obtaining highly lying states that are not accessible using standard methods that find only the lowest eigenstates. Such enhancements will be useful for many applications, for example, in studies of core ionization processes where the ionization potential can be as high as hundreds of electron-volts. We also present an implementation of a new method for non-Hermitian eigenvalue problems within EOM family of methods, generalized preconditioned locally residual method (GPLMR), which also has the capabilities of finding interior eigenvalues around a specified shift. We present benchmarks for aforecited methods comparing their robustness and computational cost.

Chapter 1: Introduction and overview

1.1 Excited states and resonances in biochromophores

Discovery and development of fluorescent proteins revolutionized bioimaging techniques used in medicine, molecular and cell biology[1–3]. Green fluorescent protein (GFP) naturally found in jellyfish *Aequorea victoria* and its derivatives are widely used as biological markers in living systems, because they can be genetically encoded and because their introduction does not perturb the functions of the host organism[1–6]. The unique properties of GFP allowed researches to observe evolution and processes inside the live cells in real time. The importance of the GFP has been recognized by Nobel Prize in Chemistry in 2008 awarded to Osamu Shimomura, Martin Chalfie, and Roger Y. Tsien "for the discovery and development of the green fluorescent protein, GFP".

The photoactive center of any fluorescent protein is a light absorbing molecule inside the protein called chromophore. The chromophore is responsible for all photochemistry and photophysics of the fluorescent proteins; thus, it is important to understand its function in order to design new mutants with desirable properties. Even though the protein-bound chromophore is affected by interactions with the protein environment, it is important to study its intrinsic properties in a gas phase, such as excitation and ionization energies. These studies allow one to quantify the effect of the protein environment (such as hydrogen bondings) on the spectral properties of the isolated chromophores.

In Chapter 2 we study the gas-phase electronic structure of the two isomers (carboxylate and phenolate) of the model photoactive yellow protein (PYP) chromophore[7–9]. The PYP is naturally found in halophilic bacterium *Halorhodospira halophila*[7,8] and is responsible for negative phototaxis of its host in response to blue light (movement of the bacterium away from the source of the light)[10]. The PYP chromophore is an anionic form of trans p-coumaric acid (pCA^-) that is covalently linked to the protein via a thioester bond[11]. From the point of view of theory, the PYP chromophore is interesting since the first excited state exhibits a resonance character metastable with respect to autoionization.

There were several theoretical[12–16] and experimental[9,16–18] studies of the properties of the PYP chromophore. The previously reported excitation energies in gas phase have large discrepancies among different quantum chemistry methods[16,19] as well as with the experimental absorption[16] maximum. Identical absorption spectra (measured using action spectroscopy) were reported for the carboxylate and phenolate isomers[16]. In Chapter 2, we compute vertical ionization and excitation energies of both forms in gas phase using high level *ab initio* methods. Contrary to the experiment, we find that the two isomers have distinctly different ionization and excitation energies, with a difference in excitation energies more than 1 eV. Our calculations confirm the resonance character of the first excited states in both isomers: the phenolate form exhibits shape resonance, whereas in carboxylate Feshbach resonance is exposed. We also analyze possible dissociation pathways of the two chormophore forms and find that the energetically allowed fragments are CH_3, CH_2O for phenolate, and CH_3, CH_2O, CO_2 for carboxylate. Based on our calculations we conclude that the identical experimental absorption spectrum[16] for the two isomers is caused by the contamination of the carboxylate sample by the phenolate isomer. This conclusion is supported by our findings that there are

no transitions in the carboxylate form near the reported absorption maximum (2.88 eV), the phenolate form is slightly lower in energy in gas phase and its oscillator strength is significantly larger, and there is no additional CO_2 neutral fragments characteristic for caboxylate reported in the experiment.

In Chapter 3 we study the effect of microhydration on the electronic structure of PYP and GFP model chromophores. Water molecules introduce hydrogen bonding similar to that present in a native protein environment[20,21]. The theoretical[12,14,22] and experimental[23–29] studies show that hydrogen bonding, besides electrostatics and covalent interactions inside the protein, can lead to significant spectral shifts. Thus, it is important to understand how these interactions affect ionization and excitation energies of the gas-phase chromophores. We performed high-level *ab initio* calculations of the mono and dihydrated clusters of the model PYP and GFP chromophores. We observe that H-bonding has a higher stabilization effect on the ionization (0.4-0.8 eV) than on excitation (0.1-0.2 eV) energies, transforming the resonances of the bare chromophore into bound states. The previous theoretical[22,30,31] and experimental[16,17,32] studies of the PYP and GFP chromophores show that the protein has very small overall effect on the absorption maximum. Thus, it suggests that hydrogen bonding and other interactions (covalent, electrostatic) have mutually cancelling effects, which leads to small changes in the photochemical properties of the protein-bound chromophores.

1.2 Autoionizing resonance states in atomic and molecular systems

Resonance states appear in different forms in various areas of science. Resonances are defined as nonstationary states with a finite lifetime long enough to be observed and

characterized[33,34]. The energy of the resonance is sufficient to break the system into two or more subsystems. The first description of the resonance states in quantum mechanics was given by Gamow[35] in the context of radioactive α-decay. Since then the resonances have been observed and characterized in such fields as particle[36], atomic[33,37], molecular[33,38,39], and mesoscopic[40,41] physics, as well as chemical dynamics.

The breakdown of the system in the resonance state can take different forms such as radioactive nuclear decay, molecular autodissociation, autoionization, and inelastic scattering of electrons[33]. We are particularly interested in autoionizing resonances, where the system decays by the ejection of a free electron. The examples include excited states of the closed-shell anions (e.g., PYP and GFP chromophores, Chapter 2), electronically attached states of neutral molecules leading to metastable anions (for example $^2\Pi_g$ resonance in N_2^-), as weel as highly excited states of neutral species. These states are common in plasma (electric arcs, supersonic combustion, lighting), interstellar chemistry[42,43], and radiolysis. The resonance states can be characterized as shape or Feshbach types depending on the type of the decay. The shape-type resonance originate from the shape of the potential where the electron can escape the potential barrier by tunneling effect. A Feshbach-type resonance appears as a result of the coupling of a bound state to a continuum. Because of this coupling the state decays in time through an available open channel.

Since the resonance phenomena by its nature is a nonstationary process, a logical approach would be time-dependent formalism that entails solving time-dependent Schrodinger equation by wavepacket propagation[34]. As a simple example, let us consider a wavepacket inside a one dimensional potential[34,44]:

$$V(x) = (1 - \frac{V_0}{cosh^2 \beta x}) e^{-\alpha x^2} \tag{1.1}$$

with parameters $\alpha = 0.05$, $\beta = 1$, $V_0 = 1$. The snapshots of the probability density at different times are given in Figure 1.1[34]. At time 0, the wavepacket is localized and strongly resembles the bound state. As the time goes, the probability density inside the barrier falls due to tunneling of the electron.

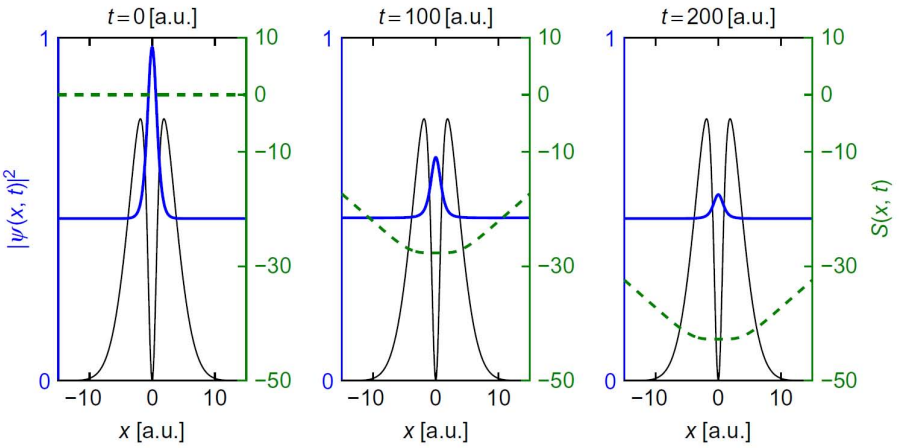

Figure 1.1: Evolution of probability density (solid line) and phase (dashed line) of the wave packet

If we consider the particle inside the interaction region, the wave function can be written as:

$$\psi_R(x,t) = e^{-i(E_R - \frac{i}{2}\Gamma)t}\psi_0(x) \tag{1.2}$$

This means that the wavepacket inside the interaction region can be considered as a bound stationary state with a complex energy:

$$E = E_R - \frac{i}{2}\Gamma \tag{1.3}$$

Here E_R is the position of the resonance and $\Gamma = \frac{1}{\tau}$ is inversely proportional to the lifetime. Outside the potential, the wave function has an oscillatory behavior resembling the escaping free particle.

As we saw, the behavior of the resonance state can be described in time-dependent framework by wavepacket propagation. However, in practice such calculations are difficult due to steep scaling of full-dimensional calculations. Furthermore, there are many robust quantum chemical time-independent methods developed for the description of bound states and, as we saw previously, in the interaction region the resonance state resembles the bound state, but with a complex energy. It would be beneficial if one could adapt a powerful tool-set of quantum chemistry for calculations of resonance states, so the same information as from wave packet propagation could be obtained from time-independent calculations.

Now let us consider the particle inside the potential (equation 1.1) by solving time-independent Schrodinger equation:

$$[-\frac{1}{2}\frac{\partial^2}{\partial x^2} + V(x)]\phi(x) = E\phi(x) \tag{1.4}$$

with outgoing flux conditions (Siegert boundary conditions)[45] $\phi(|x| \geq L) = e^{ik|x|}$. These boundary conditions make the Hamiltonian non-Hermitian resulting in complex eigenvalues (energies) which is the case for resonance states. Wavevector for resonance state is $k = k_r - ik_i$, where k_r and k_i are positive numbers; energy and wave function for resonance state are defined by equation 1.3 and 1.2, respectively. The time dependent part of the wave function decays exponentially with time ($e^{-\Gamma t}$ factor), however the spatial part of the wave function has a divergent behavior at infinity:

$$\phi(x \to \pm\infty) = A_{\pm} e^{\pm k_r x} e^{k_i |x|} \tag{1.5}$$

Thus, the spatial part of the wave function is not square-integrable (does not belong to L^2) and is not normalizable. Since most of the standard methods employ square-integrable wave functions, resonance states cannot be straightforwardly described by them.

One technique for transforming Siegert solutions into square-integrable wave functions is through complex scaling method introduced by Balslev, Combes[46], and Simon[47]. The idea of the method is to rotate all the coordinates into the complex plane by performing the dilation transformation, $r \rightarrow re^{i\theta}$. In the limit of complete basis set the complex-scaled Hamiltonian has the same bound-state spectrum, the continuum states rotate by angle 2θ down to the complex energy plane, and resonance states become square-integrable wave functions with complex energies[33]. Complex scaling transformation allows one to describe a resonance state as a single discrete bound-like state with a complex energy, for which standard time-independent methods of quantum chemistry can be applied.

Another method for transforming the diverging Siegert wave function is a complex absorbing potential (CAP) method which was first introduced in the context of the wavepacket propagation in 1986[48]. The goal of the CAP in time-dependent picture is to absorb the escaping wave packet avoiding the artificial reflection at the edge of the numeric grid. The spectral properties of the time-independent Hamiltonians perturbed by artificial complex potential $-i\eta W$ (where W can be a simple parabolic function $(r-r_0)^2$) were first studied by Meyer[49]. It was shown that in the complete basis set, the exact position of the resonance and the respective square-integrable wave function can be obtained in the limit of $\eta \rightarrow 0$. In practice, one works with incomplete basis sets, thus some optimal value of the CAP strength (η_{opt}) has to be reached to stabilize the resonance[49,50]. The CAP method can be viewed as an alternative to the complex scaling

approach and can be also combined with standard time-independent quantum chemical methods for bound states. We also note that reflection-free CAPs[50] are equivalent to exterior complex scaling approach[51,52] where the coordinates are complex-scaled only at the outer region of the molecule.

Here we present an extension of EOM-CCSD methods to study the resonance states in time-independent formalism. EOM methods have been proven to provide accurate description of excitation (EE), attachment (EA), and ionization (IP) energies for bound target states[53–57]. EOM-CC methods are size-extensive and provide balanced and accurate recovery of both ground and excited state correlation energies, which is essential for achieving high accuracy. Reliability and robustness of the EOM methods make it a natural choice for extending the formalism towards the description of resonance states. First, in Chapter 4 we present an implementation of complex-scaled EOM-EE-CCSD method and benchmark calculations of Feshbach resonances in small atomic systems (He, H^-, Be). We observe extreme sensitivity of the results to the choice of the one electron basis set and conclude that the basis should be flexible enough to describe the wave function for all rotation angles θ, as well as accurately recover correlation energy. We conclude that even though complex scaling method has rigorous theoretical foundations, its practical applications to chemically interesting molecular systems are problematic due to basis set issues and breakdown of the Born-Oppenheimer approximation[58] under complex scaling transformation. For calculation of molecular resonances we present an implementation of complex absorbing potential within EOM-EA and EOM-EE methods (CAP-EOM-EA and CAP-EOM-EE) in Chapter 5. We realize that the distortion of energies due to inclusion of the artificial CAP to the Hamiltonian can be mitigated by a first-order correction to the energy. We calculate shape resonances for a variety of medium-size anions ($N_2^-, C_2H_4^-, CO^-$ etc.) using CAP-EOM-EA and observe that

first-order corrected energies are much less sensitive to the CAP onset (e.g. box size) and give reliable position and lifetimes.

1.3 Improvement of efficiency and robustness of excited state methods

Wave function based *ab initio* methods provide the most reliable way for recovery of electron correlation, which is essential for the accurate determination of molecular properties. Among *ab initio* methods, coupled-cluster (CC) and equation-of-motion (EOM) methods represent the most successful approach to accurate many-electron wave functions of ground and excited states[53]. These methods have become the most successful and widely used tools of quantum chemistry.

However, high computational and memory cost of CC and EOM methods restricts their applications to the molecules of moderate sizes. For example, coupled-cluster with single and double substitutions (CCSD) scales as $O(N^4)$ in memory and $O(N^6)$ in computational cost (where N is the number of the basis functions) meaning that if one doubles the system size, the amount of memory and computations increases roughly 16 times and 64 times, respectively. Reducing the scaling of these methods and improving their efficiency would expand their applicability to larger systems, such as those in biology, solid-state, and polymer chemistry.

The problem of the high memory and computational cost arises from the fact that the two-electron part of the Hamiltonian and wave function parameters are represented as high-order tensors for which the cost grows exponentially with the number of dimensions. For example, consider coupled cluster methods in which the wave function is written in the following form[53,59–62]:

$$\Psi = exp(T_1 + T_2 + ... + T_N)\Phi_0 \tag{1.6}$$

where Φ_0 is a single Slater determinant (usually a Hartree-Fock determinant) and T_k represents k-fold excitations. In second quantization form they can be written as:

$$T_1 = \sum_{ia} t_i^a a^+ i \tag{1.7}$$

$$T_2 = \frac{1}{4} \sum_{ijab} t_{ij}^{ab} a^+ b^+ ij \tag{1.8}$$

$$... \tag{1.9}$$

where a^+ and i represent creation and annihilation operators, and $t_i^a, t_{ij}^{ab}, ...$ are coupled-cluster amplitudes. In CCSD only single and double excitation operators are included. The tensor of double excitation amplitudes (t_{ij}^{ab}) is a fourth-order tensor, thus the amount of memory required for its storage scales as $O(N^4)$. If we also include triple excitations (t_{ijk}^{abc}) then the resulting tensor is the tensor of order 6 and the memory will scale as $O(N^6)$. As we can see, the inclusion of higher order excitations increases the memory requirements dramatically.

Solving for the CC wave function entails finding the CC amplitudes ($t_i^a, t_{ij}^{ab}, ...$), this is done by projecting on the reference and all excited determinants giving rise to the following set of equations[60]:

$$\langle \Phi_0 | e^{-T} (H - E_{CCSD}) e^T | \Phi_0 \rangle = 0 \tag{1.10}$$

$$\langle \Phi_i^a | e^{-T} (H - E_{CCSD}) e^T | \Phi_0 \rangle = 0 \tag{1.11}$$

$$\langle \Phi_{ij}^{ab} | e^{-T} (H - E_{CCSD}) e^T | \Phi_0 \rangle = 0 \tag{1.12}$$

$$... \tag{1.13}$$

When this set of equations is appropriately factorized, all terms involve the contraction of the cluster operator T with either two- or four-index quantities from the Hamiltonian[63]. The contractions of the amplitudes with the two-electron part (which is the tensor of order 4) is the most expensive step in the calculations of CC wave functions; it costs $O(N^6)$ for CCSD and $O(N^8)$ for CCSDT.

In EOM-EE the wave function of an excited state is written as:

$$\Psi_{EOM} = \hat{R} exp(\hat{T}) |\Phi_0> \tag{1.14}$$

where $\hat{R}$ is a general excitation operator.

$$R^{\hat{E}E} = \sum_{ia} r_i^a a^\dagger i + \frac{1}{4} \sum_{ijab} r_{ij}^{ab} a^\dagger b^\dagger ji + ... \tag{1.15}$$

Similar to CCSD, the memory scaling for storing R amplitudes is increasing with the inclusion of higher n-tuple excitations. The problem of finding $r_i^a, r_{ij}^{ab}, ...$ amplitudes is formulated as a non-Hermitian eigenvalue problem:

$$(\bar{H} - E_{CC} I) R = R\Omega \tag{1.16}$$

$$\bar{H} = e^{-T} H e^T \tag{1.17}$$

which is traditionally solved by using Davidson's method[64], where the construction of the full Hamitonian matrix is avoided. The most expensive step in solving EOM-EE-CCSD problem using Davidson's procedure is the calculation of the projection of the Hamiltonian on the space of double excitations:

$$\sigma_{ij}^{ab} = ((\bar{H}_{DD} - E_{CC} I) R_2)_{ij}^{ab} \tag{1.18}$$

Similar to CCSD, it involves contractions of R amplitudes with T amplitudes and electron-repulsion integrals (ERI) which leads to computational scaling of $O(N^6)$.

As we saw in the case of CC and EOM, high memory and computational cost arises due to the storage and contraction of high-order tensors such ERI tensor and CC/EOM amplitudes. Let us now turn our attention to the electronic Hamiltonian of a system with N_e electrons and M nuclei:

$$H_{elec} = -\sum_{i=1}^{N_e} \frac{1}{2}\nabla_i^2 - \sum_{i=1}^{N_e}\sum_{A=1}^{M} \frac{Z_A}{r_{iA}} + \sum_{i=1}^{N_e}\sum_{j>i}^{N_e} \frac{1}{r_{ij}} \tag{1.19}$$

The first term of the Hamiltonian is electronic kinetic energy, second term is nucleus-electron attraction (Z_A is the charge of the nuclei), and the last term describes electron-electron Coulomb repulsion (two-electron part of the Hamiltonian). In the Gaussian basis set two-electron part of the Hamiltonian in atomic orbital basis is represented as a 4th-order ERI tensor:

$$(\mu\nu|\lambda\sigma) = \int \chi_\mu(\vec{r}_1)\chi_\nu(\vec{r}_1)\frac{1}{|\vec{r}_1 - \vec{r}_2|}\chi_\lambda(\vec{r}_2)\chi_\sigma(\vec{r}_2)d\vec{r}_1 d\vec{r}_2$$

the memory requirements for this tensor scale as $O(N^4)$ with the number of basis functions $\chi_\lambda(\vec{r})$. The most computationally expensive operations in CC and EOM methods involve the contractions of various tensors (e.g. R and T amplitudes) with the ERI tensor, which results in the computational cost of $O(N^6)$.

In Chapter 6 we present an implementation of Cholesky decomposition of the ERI tensor within CC and EOM methods. Most of the "product densities" $\chi_\mu(\vec{r})\chi_\nu(\vec{r})$ in ERI tensor are linearly dependent and this fact can be exploited performing Cholesky decomposition:

$$(\mu\nu|\lambda\sigma) \approx \sum_{P=1}^{M} B_{\mu\nu}^{P} B_{\lambda\sigma}^{P}, \tag{1.20}$$

The Cholesky decomposition allows one to remove redundant linear-dependent product densities from the original tensor achieving more efficient representation. Thus, the original ERI tensor of order 4 can be presented as a tensor of order 3 with linearly growing rank M. The rank depends on the accuracy of decomposition which can be controlled by the user and is linear with a small prefactor depending on the target accuracy. Thus, by performing Cholesky decomposition of ERI tensor we reduce the memory requirements for storing ERI and its intermediates from $O(N^4)$ to $O(N^3)$. Cholesky decomposition is a general approach which does not require any specific information about system or basis set, but relies on numerical procedure with controllable decomposition precision.

All equations for CCSD and EOM-CCSD families of methods have been rewritten to utilize Cholesky decomposed integrals. The savings in memory are evident for large systems (around 1000 basis functions) where the memory and disk requirements are reduced by more than an order of magnitude. It makes CC and EOM methods applicable to the chemical systems of much larger sizes, that are beyond the reach of the canonical implementations. The ERI presented in Cholesky-decomposed form do not allow one to rewrite the equations to reduce the computational scaling due to the presence of the exchange. However, because of a significantly reduced memory and disk savings, we observed much better parallel performance due to smaller I/O overheads and more efficient CPU utilization leading to significantly reduced calculation time. The benchmarks for various systems show that the errors introduced by Cholesky decomposition are small and controllable for both ground and excited states.

In Chapter 7 we address another issue of EOM methods - problem of effective search of few desired excited states. The problem of finding EOM wave function is a non-Hermitian eigenvalue problem (equation 1.16) with matrix of huge sizes that cannot be explicitly constructed and diagonalized. The most popular method for solution of this kind of problems in quantum chemistry is Davidson's method - it allows one to find a few (1-10) smallest eigenvalues in an iterative manner. However, many applications (such as core ionization processes[65–67]) require calculation of the roots that are high in energy (often, they are dominated by transitions from a paticular low lying orbital). Conventional Davidson's method cannot handle such tasks, since the calculation of all lower eigenvalues required to find a desired one. In Chapter 7 we present two new versions of Davidson's algorithm within EOM family of methods. The first version allows one to solve for the states around the energy shift chosen by the user (e.g. 2 roots around 300 eV), which should be useful if approximate experimental or theoretical energy value of the transition is available. Second modification of the Davidson's algorithm enables to solve for the eigenpair specified by the user-defined guess (e.g. ionization from HOMO-3 orbital) that will be helpful if the state dominated by particular transition (e.g. ionization from 1s Carbon orbital) is required. We also present an implementation of a new numerical method for non-Hermitian eigenvalue problems - Generalized Preconditioned Locally Minimal Residual (GPLMR) method[68] within EOM. This method also allows finding the roots around chosen energy shift and its convergence speed and memory requirements can be controlled by the user. We present benchmarks of these methods comparing their convergence properties, computational and memory costs.

1.4 Chapter 1 references

[1] R.Y. Tsien. The green fluorescent protein. *Annu. Rev. Biochem.*, 67:509–544, 1998.

[2] M. Chalfie, Y. Tu, G. Euskirchen, W.W. Ward, and D.C. Prasher. Green fluorescent protein as a marker for gene expression. *Science*, 263:802–805, 1994.

[3] M. Zimmer. Green fluorescent protein (GFP): Applications, structure, and related photophysical behavior. *Chem. Rev.*, 102:759–781, 2002.

[4] M. Kneen, J. Farinas, Y. Li, and A.S. Verkman. Green fluorescent protein as a noninvasive intracellular pH indicator. *Biophys. J.*, 74:1591–1599, 1998.

[5] Y. Wang, J.Y.-J. Shyy, and S. Chien. Fluorescence proteins, live-cell imaging, and mechanobiology: Seeing is believing. *Ann. Rev. Biomed. Eng.*, 10:1–38, 2008.

[6] R. N. Day and M. W. Davidson. The fluorescent protein pallete: Tools for cellular imaging. *Chem. Soc. Rev.*, 38:2887–2921, 2009.

[7] T.E. Meyer. Isolation and characterization of soluble cytochromes, ferredoxins and other chromophoric proteins from the halophilic phototrophic bacterium ectothiorhodospira halophila. *Biochem. and Biophys. J.*, 806:175–183, 1985.

[8] T.E. Meyer, E. Yakali, M.A. Cusanovich, and G. Tollint. Properties of a water-soluble, yellow protein isolated from a halophilic phototrophic bacterium that has photochemical activity analogous to sensory rhodopsin. *Biochem. J.*, 26:418–423, 1987.

[9] K.J. Hellingwerf, J. Hendriks, and Thomas Gensch. Photoactive yellow protein, a new type of photoreceptor protein: Will this "yellow lab" bring us where we want to go? *J. Phys. Chem.*, 107:1082–1094, 2003.

[10] W.W. Sprenger, W.D. Hoff, J.P. Armitage, and K.J. Hellingwer. The eubacterium ectothiorhodospira halophila is negatively phototactic, with a wavelength dependence that fits the absorption spectrum of the photoactive yellow protein. *J. of Bacteriology*, 175:3096–3104, 1993.

[11] M. Baca, G.E.O. Borgstahl, M. Boissinot, P.M. Burke, D.R. Williams, K.A. Slater, and E.D. Getzoff. Complete chemical structure of photoactive yellow protein: Novel thioester-linked 4-hydroxycinnamyl chromophore and photocycle chemistry. *Biochemistry*, 33:14369–14377, 1994.

[12] E. Gromov, I. Burghardt, J. Hynes, H. Köppel, and L. Cederbaum. Electronic structure of the photoactive yellow protein chromophore: Ab initio study of the low-lying excited singlet states. *Photochem. and Photobiol.*, 190:241–257, 2007.

[13] E. V. Gromov, I. Burghardt, H. Köppel, and L. S. Cederbaum. Impact of sulfur vs oxygen on the low-lying excited state of trans-p-coumaric acid and trans-p-coumaric thio acid. *J. Phys. Chem. A*, 109:4623–4631, 2005.

[14] E. V. Gromov, I. Burghardt, H. Köppel, and L. S. Cederbaum. Electronic structure of the PYP chromophore in its native protein environment. *J. Am. Chem. Soc.*, 129:6798–6806, 2007.

[15] A. Sergi, M. Grüning, M.Ferrario, and F. Buda. Density functional study of the photoactive yellow protein's chromophore. *J. Phys. Chem. B*, 105:4386, 2001.

[16] T. Rocha-Rinza, O. Christiansen, J. Rajput, A. Gopalan, D.B. Rahbek, L.H. Andersen, A.V. Bochenkova, A.A.Granovsky, K.B. Bravaya, A.V. Nemukhin, K.L. Christiansen, and M.B. Nielsen. Gas phase absorption studies of photoactive yellow protein chromophore derivatives. *J. Phys. Chem. A*, 113:9442–9449, 2009.

[17] I.B. Nielsen, S. Boye-Peronne, M.O.A. El Ghazaly, M.B. Kristensen, S.B. Nielsen, and L.H. Andersen. Absorption spectra of photoactive yellow protein chromophores in vacuum. *Biophys. J.*, 89:2597–2604, 2005.

[18] L. Lammich, J. Rajput, and L.H. Andersen. Photodissociation pathways of gas-phase photoactive yellow protein chromophores. *Phys. Rev. E*, 78:051916, 2008.

[19] E.M. Gonzalez, L. Guidonib, and C. Molteni. Chemical and protein shifts in the spectrum of the photoactive yellow protein: a time-dependent density functional theory/molecular mechanics study. *Phys. Chem. Chem. Phys.*, 11:4556–4563, 2009.

[20] U.K. Genick, S.M. Soltis, P. Kuhn, I.L. Canestrelli, and E.D. Getzoff. Structure at 0.85 Å resolution of an early protein photocycle intermediate. *Nature*, 392:206–209, 1998.

[21] R. Moukhametzianov, J.P. Klare, R. Efremov, C. Baeken, A. Göppner, J. Labahn, M. Engelhard, G. Büldt, and V.I. Gordeliy. Development of the signal in sensory rhodopsin and its transfer to the cognate transducer. *Nature*, 440:115–119, 2006.

[22] A. Sinicropi, T. Anduniow, N. Ferre, R. Basosi, and M. Olivucci. Properties of the emitting state of the green fluorescent protein resolved at the CASPT2//CASSCF/CHARMM level. *J. Am. Chem. Soc.*, 127:11534–11535, 2005.

[23] P. Changenet-Barret, P. Plaza, M.M. Matrin, H.Chosrowjan, S. Taniguchi, N. Mataga, Y. Imamoto, and M. Kataoka. Structural effects on the ultrafast photoisomerization of photoactive yellow protein. Transient absorption spectroscopy of two point mutants. *J. Phys. Chem. C*, 113:11605–11613, 2009.

[24] K. Mihara, O. Hisatomi, Y. Imamoto, M. Kataoka, and F. Tokunaga. Functional expression and site-directed mutagenesis of photoactive yellow protein. *Biochem. J.*, 121:876–880, 1997.

[25] A. Philip, K. Eisenman, G. Papadantonakis, and W. Hoff. Functional tuning of photoactive yellow protein by active site residue. *Biochemistry*, 47:13800–13810, 2008.

[26] J. Sniegowski, M. Phail, and R. Wachter. Maturation efficiency, trypsin sensitivity, and optical properties of Arg96, Glu222, and Gly67 variants of green fluorescent protein. *Biochem. Biophys. Res. Commun*, 332:657–663, 2005.

[27] M.A. van der Horst, J.C. Arents, R. Kort, and K.J. Hellingwerf. Binding, tuning and mechanical function of the 4-hydroxy-cinnamic acid chromophore in photoactive yellow protein. *Photochem. and Photobiol. Sci.*, 6:571–579, 2007.

[28] G. Jung, J. Wiehler, and A.Zumbusch. The photophysics of green fluorescent protein: Influence of the key amino acids at positions 65, 203, and 222. *Biophys. J.*, 88:1932–1947, 2005.

[29] J. Rajput, D.B. Rahbek, G. Aravind, and L.H. Andersen. Spectral tuning of the photoactive yellow protein chromophore by h-bonding. *Biophys. J.*, 98:488–492, 2010.

[30] K. Bravaya, M.G. Khrenova, B.L. Grigorenko, A.V. Nemukhin, and A.I. Krylov. The effect of protein environment on electronically excited and ionized states of the green fluorescent protein chromophore. *J. Phys. Chem. B*, 8:8296–8303, 2011.

[31] T. Rocha-Rinza, K. Sneskov, O. Christiansen, U. Ryde, and J.I. Kongsted. Unraveling the similarity of the photoabsorption of deprotonated p-coumaric acid in the gas phase and within the photoactive yellow protein. *Phys. Chem. Chem. Phys.*, 13:1585–1589, 2011.

[32] L.H. Andersen, A. Lappierre, S.B. Nielsen, I.B. Nielsen, S.U. Pedersen, U.V. Pedersen, and S. Tomita. Chromophores of the green fluorescent protein studied in the gas phase. *Eur. Phys. J. D*, 20:597–600, 2002.

[33] W. P. Reinhardt. Complex coordinates in the theory of atomic and molecular structure and dynamics. *Annu. Rev. Phys. Chem.*, 33:223–255, 1982.

[34] S. Klaiman and I. Gilary. On resonance: a first glance into the behavior of unstable states. In C.A. Nicolaides, J.R. Sabin, and E.J. Brändas, editors, *Adv. Quantum Chem.*, volume 63, chapter 1, pages 1–31. Elsevier Inc., 2012.

[35] G. Gamow. The quantum theory of the atom nucleus. *Z. Phys.*, 51:204, 1928.

[36] E. Eichten. γ family of resonances above threshold. *Phys. Rev. D*, 22:1819, 1980.

[37] N. Moiseyev, P.R. Certain, and F. Weinhold. Complex-coordinate studies of helium autoionizing resonances. *Int. J. Quant. Chem.*, 14:727–736, 1978.

[38] T. Sommerfeld, U. V. Riss, H.-D. Meyer, L. S. Cederbaum, B. Engels, and H. U. Suter. Temporary anions - calculation of energy and lifetime by absorbing potentials: the N_2^- $^2\Pi_g$ resonance. *J. Phys. B*, 31(18):4107, 1998.

[39] N. Moiseyev and C. Corcoran. Autoionizing states of H_2 and H_2^- using the complex-scaling method. *Phys. Rev. A*, 20:814–817, 1979.

[40] M. Heiblum, M.V. Fischetti, W.P. Dumke, D.J. Frank, I.M. Anderson, C.M. Knoedler, and L. Osterling. Electron interference effects in quantum wells: Observation of bound and resonant states. *Phys. Rev. Lett.*, 58:816, 1987.

[41] G. Garcia-Calderon. Tunneling in semiconductor resonant structures. *Phys. Low-Dimens. Semicond. Struct.*, 6:1993, 267.

[42] D.O. Kashinski, D. Talbi, and A.P. Hickman. Ab initio calculations of autoionizing states using block diagonalization: collinear diabatic states for dissociative recombination of electrons with N_2H^+. *Chem. Phys. Lett.*, 529:10–15, 2012.

[43] R.D. Thomas. When electrons meet molecular ions and what happens next: dissociative recombination from interstellar molecular clouds to internal combustion engines. *Mass Spec. Rev.*, 27:485–530, 2008.

[44] N. Rosen and P.M. Morse. On the vibrations of polyatomic molecules. *Phys. Rev.*, 42:210, 1932.

[45] A. J. F. Siegert. On the derivation of dispersion formula for nuclear reactions. *Phys. Rev.*, 56:750, 1939.

[46] E. Balslev and J. M. Combes. Spectral properties of many-body Schrödinger operators with dilatation-analytic interactions. *Commun. Math. Phys.*, 22:280–294, 1971.

[47] B. Simon. Quadratic form techniques and the Balslev-Combes theorem. *Commun. Math. Phys.*, 27:1–9, 1972.

[48] R. Kosloff and D. Kosloff. Absorbing boundaries for wave propagation problems. *J. Comput. Phys.*, 63(2):363–376, 1986.

[49] U. V. Riss and H.-D. Meyer. Calculation of resonance energies and widths using the complex absorbing potential method. *J. Phys. B*, 26:4503–4536, 1993.

[50] U.V. Riss and H.-D. Meyer. Reflection-free complex absorbing potentials. *J. Phys. B*, 28:1475–1493, 1995.

[51] N. Lipkin, N. Moiseyev, and E. Brändas. Resonances by the exterior-scaling method within the framework of the finite-basis-set approximation. *Phys. Rev. A*, 40:549–553, 1989.

[52] C.W. McCurdy, T.N. Rescigno, and D. Byrum. Making complex scaling work for long-range potentials. *Phys. Rev. A*, 56:1958–1969, 1997.

[53] T. Helgaker, P. Jørgensen, and J. Olsen. *Molecular electronic structure theory*. Wiley & Sons, 2000.

[54] H. Sekino and R.J. Bartlett. A linear response, coupled-cluster theory for excitation energy. *Int. J. Quant. Chem. Symp.*, 26:255–265, 1984.

[55] J.F. Stanton and R.J. Bartlett. The equation of motion coupled-cluster method. A systematic biorthogonal approach to molecular excitation energies, transition probabilities, and excited state properties. *J. Chem. Phys.*, 98:7029–7039, 1993.

[56] M. Head-Gordon and T.J. Lee. Single reference coupled cluster and perturbation theories of electronic excitation energies. In R.J. Bartlett, editor, *Modern Ideas in Coupled Cluster Theory*. World Scientific, Singapore, 1997.

[57] A.I. Krylov. Equation-of-motion coupled-cluster methods for open-shell and electronically excited species: The hitchhiker's guide to Fock space. *Annu. Rev. Phys. Chem.*, 59:433–462, 2008.

[58] N. Moiseyev. *Non-Hermitian quantum mechanics*. Cambridge University Press, 2011.

[59] J. Cizek. On the correlation problem in atomic and molecular systems. Calculation of wavefunction components in Ursell-type expansion using quantum-field theoretical methods. *J. Chem. Phys.*, 45:4256–4266, 1966.

[60] G.D. Purvis and R.J. Bartlett. A full coupled-cluster singles and doubles model: The inclusion of disconnected triples. *J. Chem. Phys.*, 76:1910–1918, 1982.

[61] R.J. Bartlett. Coupled-cluster theory and its equation-of-motion extensions. *Wiley Interdisciplinary Reviews: Computational Molecular Science*, 2(1):126–138, 2012.

[62] A. Szabo and N.S. Ostlund. *Modern Quantum Chemistry: Introduction to Advanced Electronic Structure Theory*. McGraw-Hill, New York, 1989.

[63] J.F. Stanton, J. Gauss, J.D. Watts, and R.J. Bartlett. A direct product decomposition approach for symmetry exploitation in many-body methods. I. energy calculations. *J. Chem. Phys.*, 94:4334–4345, 1990.

[64] E.R. Davidson. The iterative calculation of a few of the lowest eigenvalues and corresponding eigenvectors of large real-symmetric matrices. *J. Comput. Phys.*, 17:87–94, 1975.

[65] R. Franchy and D. Menzel. Adsorbate core ionization as primary process in electron-and photon-stimulated desorption from metal surfaces. *Phys. Rev. Lett.*, 43:865–867, 1979.

[66] J. F. Morar, F. J. Himpsel, G. Hollinger, J. L. Jordan, G. Hughes, and F. R. McFeely. C 1s excitation studies of diamond (111). i. surface core levels. *Phys. Rev. B*, 33:1340, 1986.

[67] P.-F. Loos and X. Assfeld. Core-ionized and core-excited states of macromolecules. *Int. J. Quant. Chem.*, 107:2243–2252, 2007.

[68] E. Vecharynski, F. Xue, and C. Yang. Generalized preconditioned locally minimal residual (GPLMR) method. private communication, 2013.

Chapter 2: Electronic structure of the two isomers of the anionic form of p-coumaric acid chromophore

2.1 Introduction

Photoactive yellow protein (PYP) is a small bacterial photoreceptor found in Halorhodospira halophila[1,2], which is responsible for the negative phototaxis of its host bacteria in response to blue light[3]. The PYP chromophore is a prosthetic group of para-coumaric acid (pCA) linked to the protein by the thio-ester covalent bond[4,5]. Inside the protein, the chromophore exists in the anionic (deprotonated) form[4,5]. Absorption of blue light (λ_{max}=446 nm or 2.78 eV[3]) triggers the chromophore's trans-cis photoisomerization, which, in turn, initiates the cascade of processes leading to signal transduction[6,7].

To understand the complex photochemistry of photoactive proteins, it is desirable to distinguish between the intrinsic properties of the chromophore and effects due to chromophore-protein interactions, which may affect both the optical properties and the response to light absorption, e.g. dynamics on excited-state potential energy surfaces. Therefore, the properties of excited states of the unperturbed isolated chromophores are of particular interest. Several synthetic analogues of the PYP chromophore have been

studied experimentally in gas phase[8–11]. Dynamics of the gas-phase photoisomerization of the 4-(3-oxobut-1-enyl)-phenolate anion (P^-) was studied using femtosecond mass-selection/electron detachment techniques[11]. This study demonstrated that the protein environment plays a twofold role, i.e., (i) impeding electron detachment from the chromophore and (ii) directing the photoreaction towards the cis photoproduct[11]. Based on these experiments, the vertical detachment energy for the P^- chromophore was estimated to be 2.9 eV[11].

The gas-phase absorption spectra of different model PYP chromophores including pCA^-, methylated pCA^- analogues and *trans*-thiophenyl-p-coumarate (pCT^-) have been measured using action spectroscopy coupled with ion-storage ring and electrospray techniques[8–10]. An interesting feature of these anionic systems is that the photoabsorption initiates two competing processes, i.e., photodetachment and fragmentation. Consequently, the photoabsorption bands obtained by action spectroscopy include signal from detachment, from excitation followed by fragmentation, and from autoionization.

Determination of the relative cross sections of these processes is a challenging task and is still an open problem. Therefore, the interpretation of the action spectroscopy photoabsorption spectra requires caution. An attempt to distinguish between the detachment and excitation channels for the anionic chromophore of the green fluorescent protein (GFP) has been reported by Frobes and Jockusch[12]. Although a fulfilling completely different physiological function, the GFP chromophore features remarkably similar electronic structure patterns, e.g., the lowest excited state of its anionic form is also an autoionizing resonance state[13,14].

The pCA anion serves as a minimal model of the PYP chromophore. Two pCA^- isomers that have been studied experimentally[10] are the phenolate and carboxylate forms

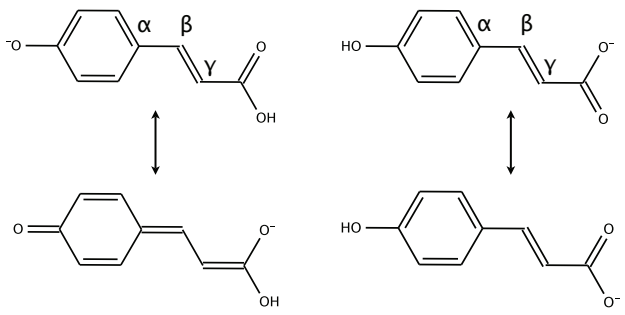

Figure 2.1: The resonance structures of the model PYP chromophore, pCA^-, in the phenolate (left) and carboxylate (right) forms.

shown in Fig. 2.1. The carboxylate is believed to be the more stable isomer in polar solvents[10], whereas in the gas phase, the phenolate isomer is 13 kcal/mol lower in energy[10]. Their relative stability can be explained by different charge distribution patterns of the two isomers discussed in Section 2.3.1 — the more localized charge on carboxylate can be solvated more efficiently, whereas in the gas phase the isomer with more delocalized excess charge becomes more stable.

In solution, isomerization between these two tautomers may occur. Since it is not clear whether gas-phase equilibrium conditions are reached in electrospray, methyl-substituted ethers of the pCA^- isomers have been used in the experiment[10]. Although the absorption spectra of the two isomers in solution are considerably different (4.40 eV and 3.49 eV for carboxylate and phenolate, respectively[10]), their gas-phase absorption maxima were reported to be identical (2.88 eV).

The absorption spectra of pCA^- has attracted considerable attention from theory for the following reasons: (i) it was found that the excited state of the phenolate form of the anion is a resonance state lying above the detachment continuum[15,16]; and (ii) there are large discrepancies in excitation energies computed by different quantum chemistry methods[10,17] as well as between theoretical and experimental absorption maxima[10].

Thus, pCA^- features a complex electronic structure characteristic of closed-shell anions and presents an interesting benchmark system for *ab initio* methods.

There are numerous theoretical studies on the absorption of the isolated PYP chromophores[10,15–18]. Gromov *at el.* have studied absorption of the gas-phase PYP chromophore in neutral[15] and anionic states[18]. However, when considering the anionic chromophore, the authors mainly focused on the phenolate, the biologically relevant form. In line with early evidence of the resonance character of the first excited state of the PYP chromophore based on the phenolate anion model[16], Gromov *et al.* have demonstrated that the lowest excitation energy of a realistic chromophore (3.17-3.18 eV, EOM-CCSD) is indeed above the detachment continuum (2.51-2.90 eV, OVGF)[18,19]. The conclusion was further supported by other theoretical results for pCA^- [10]. Ma *et al.*[17] used many-body Green's function theory (MBGFT) to study excited states of the the carboxylate and phenolate forms of pCA^-. They reported excitation energies of 2.95 and 4.37 eV for phenolate and carboxylate, respectively[17]. As a possible explanation of the experimental results, the authors suggested that the only form present in the gas phase is phenolate[17]. Since the methylated species were used in the experiment[10], this conclusion seems questionable. Bochenkova and co-workers have reported excitation energies for the carboxylate and phenolate forms of pCA^- that are within 0.1 eV of the experimental peaks obtained with the augmented multiconfigurational quasidegenerate perturbation theory technique (aug-MCQDPT2)[10]. At the same time, excitation energies computed using the approximate coupled-cluster doubles scheme (CC2, 4.79 and 3.10 eV for carboxylate and phenolate pCA^-, respectively)[10] are in agreement with the MBGFT results. Thus, either the absorption spectra of the deprotonated pCA present a very challenging problem for modern quantum chemical methods or the experimental results require re-interpretation.

This study presents electronic structure calculations of the two pCA^- isomers. We characterized the lowest excited and ionized states of the chromophore using high-level *ab initio* methods including EOM-CCSD[20–24], state-specific and multistate multireference perturbation theory (SS-CASPT2 and MS-CASPT2)[25], and a coupled-cluster method with an approximate account of triple excitations, CC3[26]. We rationalize the observed difference in the absorption spectra of the two molecules on the basis of the Hückel model. We also analyze the photodissociation pathways and suggest the formation of the CO_2 photofragment as an experimental probe for the carboxylate isomer of pCA^-.

2.2 Computational details

The equilibrium geometries of both isomers were optimized using MP2 with the aug-cc-pVDZ[27] basis set. The resolution-of-the-identity (RI) technique[28–31] was employed. C_s symmetry was imposed during the geometry optimization. The following convergence thresholds were used in the optimization procedure: 1×10^{-6} hartree for the energy, 3×10^{-4} hartree/Å for the energy gradient, and 1.2×10^{-3} Å for displacements.

Geometry optimizations of neutral radicals were performed with the long-range corrected ωB97X functional[32] using the aug-cc-pVDZ basis and with the IP-CISD (configuration interaction with single and double substitutions for ionized states)[33] method with the 6-31+G(d,p) basis set. IP-CISD is an approximation to EOM-IP-CCSD (EOM-CCSD for ionized states)[20,34–38], which scales as N^5 and employs an uncorrelated Hartree-Fock determinant as a reference instead of the CCSD wave function. For comparison purposes and zero-point energy (ZPE) calculations, the structures of the closed-shell anions have been also reoptimized with ωB97X/6-31+G(d,p). The absence of imaginary frequencies obtained by ωB97X/6-31+G(d,p) verify that the stationary points

are indeed true minima, except the planar C_s structure for carboxylate, which was found to be a transition state with a single imaginary frequency corresponding to the rotation along the single bond at the bridge. This is probably caused by steric repulsion between the hydrogen atoms at the bridge C_β atom and the phenol ring. The structure reoptimized without the C_s symmetry constraint is non-planar with a C-C_α-C_β-C_γ torsional angle of 14.5°. The energy difference between the two structures is minor [0.04 kcal/mol, ωB97X/6-31+G(d,p)]. We do not anticipate significant effects of slight non-planarity on excitation energies and employ the planar geometry in all calculations. A higher torsional rigidity of the phenolate isomer can be explained by the two resonance structures (Fig. 2.1) resulting in the allylic character of the bridge moiety, and, consequently, partial double-bond character of C_α-C_β.

Dissociation energies (D_e) for different fragmentation channels were computed with ωB97X/6-311++G(2df,2pd) as the difference between ground-state energies of the initial molecule and the dissociation products. Zero-point energy (ZPE) corrections were calculated with ωB97X/6-31+G(d,p) at the geometries reoptimized at the same level of theory. To analyze conformational flexibility of the chromophore, we also performed *ab initio* molecular dynamics (AIMD) simulations using the B3LYP functional and the 6-31+G(d,p) basis set. The trajectories were propagated for 5 ps with the time-step of 0.5 fs. The grid used for all DFT calculations contained 75 points in the Lebedev[39] radial grid and 302 points in the Euler-Maclaurin[40] angular grid.

Vertical excitation energies were computed using EOM-EE-CCSD (EOM-CCSD for excitation energies)[20–22,24], CC3[26], and CASPT2[25]. Vertical detachment energies were computed by using Koopmans' theorem (i.e., negatives of orbital energies) and by EOM-IP-CCSD[34,35,37] with the 6-311+G(df,pd) basis.

The EOM-CCSD error bars are 0.1–0.3 eV for electronic states dominated by single excitations. Including triples reduces the errors to 0.01–0.02 eV[41]. In a recent benchmark study, Schreiber *et al.*[42] reported EOM-CCSD mean absolute and maximum errors of 0.12 and 0.23 eV, respectively. A recent study of uracil[43] demonstrated that even for well-behaved molecules inclusion of triple excitations and extending the basis set beyond augmented double-zeta can affect vertical excitations by as much as 0.3 eV. The CC3 method[26], which is an iterative CC method with an approximate inclusion of triple excitations, has been shown to reduce the EOM-CCSD error bars down to 0.016 eV (maximum error) for singly excited state[42].

The multireference calculations were performed with the complete active space SCF (CASSCF) method[44] to account for near-degeneracies of different electronic configurations followed by multireference second-order perturbation theory (CASPT2)[45] to include dynamical correlation. These calculations were performed with the 6-31G(d,p)[46], ANO-RCC-VDZP and ANO-RCC-VTZP[47,48] basis sets. The ANO-RCC bases were used together with the Douglas-Kroll Hamiltonian[49] relativistic correction. For the first two rows of the periodic table, the ANO-RCC basis sets perform similarly to the ANO-L non-relativistic bases.

The active space was designed to include all p-orbitals perpendicular to the molecular plane for accurate description of the lowest $\pi \rightarrow \pi^*$ excitations. The resulting active space included 14 electrons in 12 orbitals. The state-averaged CASSCF approach was used with equal weight on the six lowest states. In subsequent CASPT2 and MS-CASPT2[25] calculations, the standard IPEA shift of 0.25[50] was employed and the 1s core orbitals of the second row elements were frozen in the calculations of the dynamical correlation correction. Oscillator strengths were computed using the complete active space state interaction (CASSI) algorithm[51]. The calculations employed the

recently developed Cholesky decomposition (CD) methods to handle the two-electron integrals[52,53]. The calculations used the so-called atomic compact CD (acCD) auxiliary basis set[54,55] (generated with a CD threshold of 10^{-4}) along with the CD-CASSCF[56] and CD-CASPT2[57] implementations. In the CD-CASSCF implementation the Local Exchange approximation[58] was employed. The errors in excitation energies introduced by these approximations are less than 0.001 eV, as demonstrated in the recent benchmark study[59].

The Cartesian geometries, relevant energies, and harmonic frequencies are provided in Supporting Materials for Ref. 60. The wave function analysis was performed using Natural Bond Orbitals (NBO) procedure[61,62]. The EOM-CC and DFT calculations were performed with Q-Chem[63]. The CC3 and CASPT2 calculations were performed using PSI III[64] and MOLCAS[65], respectively.

2.3 Results and discussion

2.3.1 Structures and charge distributions of pCA^-

We considered several rotamers of the pCA^- anion derived by rotation along the phenolic C-O (carboxylate), C_γ-C(OOH) and C-O(H) (phenolate) bonds. All excitation and ionization energies for the phenolate are reported for the lowest energy structure with the C_γ-C(OOH) and C-O(H) bonds in *anti* and *syn* configurations, respectively. For the carboxylate, all results are obtained for the lowest energy syn-OH rotamer, except CASPT2 and CC3 excitation energies. CASPT2 and CC3 calculations were performed for the anti-OH rotamer, which is slightly higher in energy (by 0.06 and 0.55 kcal/mol at the RI-MP2/aug-cc-pVDZ and CCSD/6-31+G(d,p) levels, respectively; see Supporting Materials for Ref. 60).

The difference in the bond length alternation (BLA) patterns in the carboxylate and phenolate structures can be qualitatively explained by the analysis of leading resonance structures[10]. The two dominant resonance forms of the phenolate isomer are: (i) enol with the negative charge hosted by the –COOH fragment; and (ii) phenol with the charge localized on the phenolate oxygen. BLA at the bridging C-C bonds (C_α-C_β-C_γ) for the phenol-like resonance structure corresponds to the single C_α-C_β and double C_β-C_γ bonds (Fig. 2.1), whereas the enol-like resonance structure has an opposite pattern. The two dominant resonance structures of carboxylate only affect the carboxylate moiety and do not disturb BLA in the bridge region. Thus, C_α-C_β is a single bond, and C_β-C_γ is a double bond.

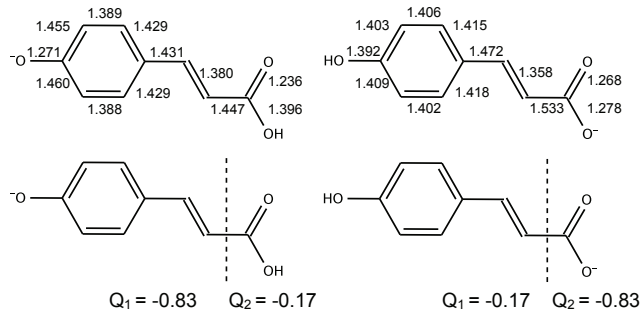

Figure 2.2: Relevant geometric parameters (RI-MP2/aug-cc-pVDZ) and NBO charge distributions for the ground electronic state of the phenolate (left) and carboxylate (right) forms of pCA^-.

The optimized geometries and the NBO charge distributions of both isomers are shown in Fig. 2.2. To quantify the charge distribution, we divide the molecule into two parts, as shown in Fig. 2.2. In the carboxylate, the excess charge is hosted by the CO_2 group, whereas in the phenolate the charge is located mainly on the phenol ring and the bridge and is more delocalized. This explains preferential deprotonation of the carboxylate in polar solutions, as solvation of the more compact carboxylate anion is more efficient. Although the charge distribution in phenolate does not reveal significant

contribution of the enol resonance form, its signature can be found in the optimized geometrical parameters. The resonance analysis above predicts that the difference between the C_α-C_β and C_β-C_γ bond lengths should be larger in the carboxylate isomer, and this is indeed the case — the difference in the bond lengths is almost twice larger in carboxylate (0.114 Å) than in phenolate (0.051 Å) revealing notable contribution of the enol resonance structure. The latter effect is even more important for the anionic form of the GFP chromophore[14,66,67] where the two chromophore moieties (phenolic and imidazolone rings) are more similar.

2.3.2 Ab initio calculations of the electronically excited and ionized states of pCA^-

As a closed-shell system, the pCA^- anion is stable in the gas phase and has a relatively large VDE. Detachment energies calculated by EOM-IP-CCSD are summarized in Table 2.1. The computed VDE for the phenolate isomer agrees well with the experimental value of 2.9 eV reported for a similar model PYP chromophore[11]. Interestingly, Koopmans' theorem fails to predict the correct ordering of the ionized states in the carboxylate. According to Koopmans' theorem, the lowest ionization corresponds to electron removal from the HOMO (Fig. 2.3), which is a π-like orbital delocalized over the phenol ring and the bridge, whereas the negative charge is mainly located on the carboxylate group and one could expect ionization from the latter moiety. Electron correlation changes the ordering of the ionized states and the lowest ionized state at the EOM-IP-CCSD level indeed corresponds to electron detachment from the carboxylate orbital (HOMO-3) formed by oxygen lone pairs (see Fig. 2.3). The differences between Koopmans and EOM-IP-CCSD VDEs range from 0.3 - 2.2 eV. Thus, correlation is required for both quantitative accuracy and for determining the correct state ordering.

All ionized states have predominantly single-configurational Koopmans character (the leading R_1 amplitude is greater than 0.95).

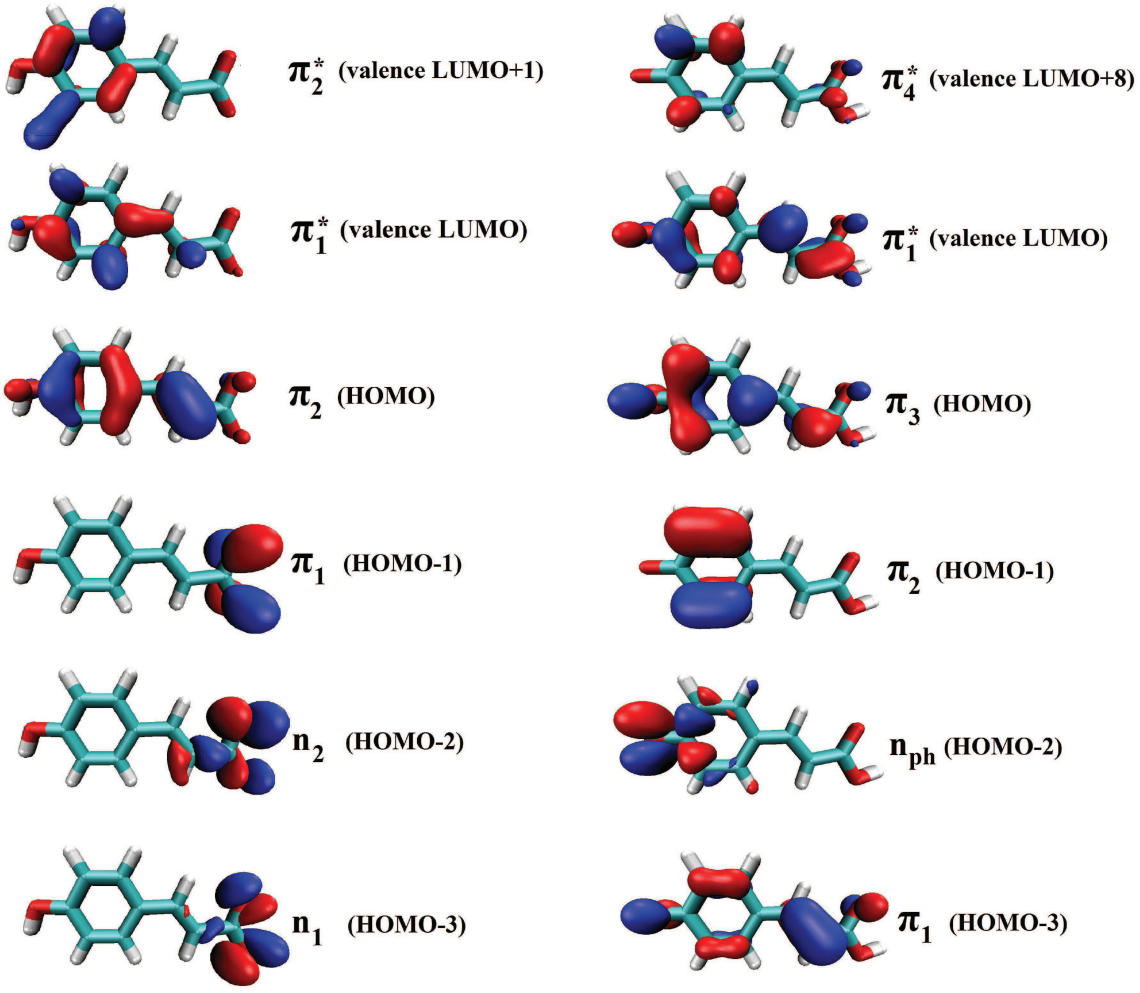

Figure 2.3: Relevant MOs in the 6-31+G(d,p) basis. The π_3^* orbital for carboxylate and π_2^*, π_3^* orbitals for phenolate (not shown) are of diffuse character.

The basis set effects on computed VDEs were analyzed by using several bases in the EOM-IP-CCSD calculations of the carboxylate isomer. VDEs for the first ionized state computed with 6-311+G(d,p), 6-311(2+,+)G(d,p) and 6-311+G(df,pd) are 3.80,

3.80 and 3.91 eV, respectively. Thus, the addition of diffuse functions has only minor effect on VDEs, whereas the effect of polarization is more pronounced.

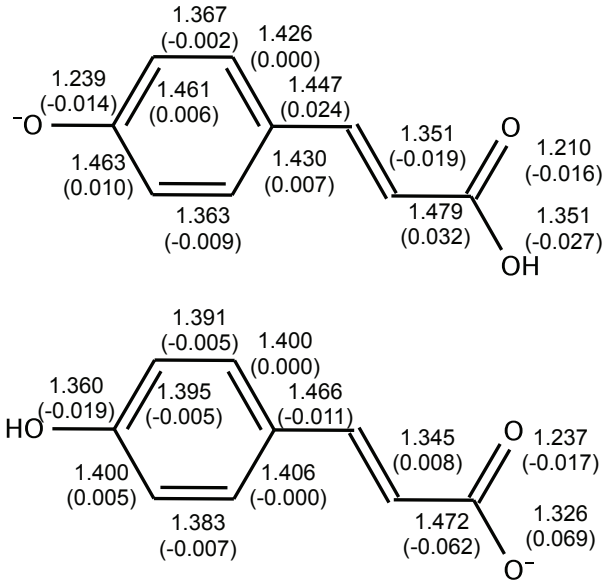

Figure 2.4: Equilibrium structures of the ionized pCA^- optimized by ωB97X/aug-cc-pVDZ. Ionization-induced changes in the bond lengths, i.e. difference in the bond lengths between the neutral and anionic state optimized geometries (computed at the same level of theory), are given in parentheses.

The relaxation energies (VDE-AIE) are 0.4 eV and 0.2 eV for the first ionized state of carboxylate and phenolate, respectively. The comparison of the anionic and neutral states' geometries is presented in Fig. 2.4. The observed trends can be explained by the analysis of the corresponding MOs. The lowest ionized state of phenolate corresponds to electron removal from the conjugated π-system. The HOMO is bonding with respect to the three phenol carbon atoms, the C_α-C_β bridge and C_γ–C(OOH) bonds (Fig. 2.3). Thus, detachment from the HOMO leads to the increase in these bond lengths. In contrast, the HOMO has anti-bonding character with respect to phenolic O–C and C–O in the carboxyl group, and ionization results in bond length contraction (Fig. 2.4).

Table 2.1: Vertical detachment energies (VDE, eV) for the two pCA^- isomers estimated by Koopmans theorem (KT, eV) and computed with EOM-IP-CCSD/6-311+G(df,pd)//RI-MP2/aug-cc-pVDZ.
EOM-IP-CCSD/6-311+G(df,pd) adiabatic detachment energies (ADE, eV) computed using ωB97X/aug-cc-pVDZ optimized geometries of the neutrals for the first ionized state and IP-CISD/6-31+G(d,p) for the subsequent ones are also given.

Carboxylate

Target state	Orbital	KT	VDE	ADE
1^2A'	n_1	6.08	3.91	3.54
2^2A'	n_2	6.01	4.07	–
1^2A"	π_1	5.54	4.18	3.99
2^2A"	π_2	4.72	4.75	4.57

Phenolate

Target state	Orbital	KT	VDE	ADE
1^2A"	π_3	3.26	2.92	2.72
$1\ ^2$A'	n_{ph}	6.68	4.54	–
$2\ ^2$A"	π_2	5.84	5.6	–

Table 2.2: Vertical excitation energies (E_{ex}, eV) and oscillator strengths (f_l, in parenthesis) of the carboxylate pCA^- isomer. The RI-MP2/aug-cc-pVDZ optimized geometries were used for the excitation energy calculations.

Carboxylate

Method	Transition character			
	$n\pi^*$	$n\pi^*$	$\pi\pi^*$	$\pi\pi^*$
CAM-B3LYP/aug-cc-pVTZ [a]	–	–	4.70	–
CC2/aug-cc-pVTZ [a]	–	–	4.79	–
MRMP2/(p-type) d-aug-cc-pVDZ [a]	–	–	5.17	–
MCQDPT2/(p-type) d-aug-cc-pVDZ [a]	–	–	3.05	–
aug-MCQDPT2/(p-type) d-aug-cc-pVDZ [a]	–	–	2.85	–
MBGFT [b]	–	–	4.37	–
SS-CASPT2/ANO-RCC-VDZP	–	–	4.25	4.31
SS-CASPT2/ANO-RCC-VTZP	–	–	4.09	4.17
MS-CASPT2/6-31G(d,p)	–	–	4.21 (0.021)	4.36 (0.064)
MS-CASPT2/ANO-RCC-VDZP	–	–	4.19 (0.102)	4.28 (0.033)
MS-CASPT2/ANO-RCC-VTZP	–	–	3.88 (0.252)	4.11 (0.042)
EOM-EE-CCSD/6-31G(d,p)	–	–	4.70 (0.027)	4.89 (0.018)
EOM-EE-CCSD/6-31+G(d,p)	4.17($< 10^{-3}$)	4.24($< 10^{-3}$)	4.5(0.030)	–
CC3/6-31+G(d,p)	–	–	4.21	–

[a] Ref. 10;

[b] non-standard Gaussian basis set (total 690 functions), Ref. 17

Lowest ionized state of the carboxylate corresponds to detachment from the HOMO-3, which is a σ-like orbital (Fig. 2.3). Electron detachment from the negatively charged COO group in the carboxylate reduces electron repulsion between the phenolic and carboxyl moieties thus reducing the C_γ–C(OO) bond length. Ionization also detunes the resonance in the carboxyl group; the BLA patterns in the carboxyl group of the ionized carboxylate and phenolate isomers are very similar (Fig. 2.4).

Despite relatively high detachment energy, both phenolate and carboxylate isomers do not support bound electronically-excited singlet states, and the lowest valence excitation is embedded in the detachment continuum (Tables 2.1 – 2.2). Such resonance states are common in molecular anions[13,68] and play an important role in dissociative electron attachment processes[69,70]. A complete description of the resonance excited states requires taking into account their interactions with the continuum. Several techniques can be used to tackle this problem, such as stabilization[71] and complex Hamiltonian methods including complex absorption potential[72,73] and complex-scaling methods[74–77]. In traditional electronic structure calculations, increasing the basis set results in low-lying excited states corresponding to excitation to diffuse orbitals approximating the continuum. These continuum-like states can mix with the metastable valence excited state (see, for example, Ref. 13) presenting an obstacle for obtaining converged (with respect to the one-electron basis set) results. By using bases with moderate diffuse character we enforce the localization of the excited state preventing its mixing with the diffuse continuum-like states, which can be thought of as approximate diabatization.

Table 2.3: Vertical excitation energies (E_{ex}, eV) and oscillator strengths (f_l, in parenthesis) of the phenolate pCA^- isomer. The RI-MP2/aug-cc-pVDZ optimized geometries were used for the excitation energy calculations.

Phenolate

Method	Leading configurations			
	$\pi\pi^*$	$n\pi^*$	$\pi\pi^*$	$\pi\pi^*$
TDDFT/TZP [a]	3.24	–	–	–
CAM-B3LYP/aug-cc-pVTZ [b]	3.40	–	–	–
CC2/6-31G* [c],*	2.89 (0.995)	—	4.04 (0.056)	–
CC2 /cc-pVDZ [d]	3.10 (1.234)	3.37 ($< 10^{-3}$)	4.33 (0.081)	–
CC2/aug-cc-pVTZ [b]	3.10	–	–	–
MRMP2/(p-type) d-aug-cc-pVDZ [b]	2.79	–	–	–
MCQDPT2 /(p-type) d-aug-cc-pVDZ [b]	2.81	–	–	–
aug-MCQDPT2 / (p-type) d-aug-cc-pVDZ [b]	2.82 (0.99)	–	–	–
EOM-CCSD/6-31G* [c],[f]	3.18 (1.016)	–	4.34 (0.042)	–
EOM-CCSD/cc-pVDZ [d],[f]	3.17 (1.237)	3.98 ($< 10^{-3}$)	4.49 (0.055)	–
MBGFT[e]	2.95	–	–	–
SS-CASPT2/ANO-RCC-VDZP	3.08	–	4.14	4.80
SS-CASPT2/ANO-RCC-VTZP	2.98	–	3.94	4.59
MS-CASPT2/6-31G(d,p)	3.17 (1.124)	–	4.23 (0.105)	4.90 (0.025)
MS-CASPT2/ANO-RCC-VDZP	3.07 (1.076)	–	4.12 (0.115)	4.82 (0.013)
MS-CASPT2/ANO-RCC-VTZP	2.96 (1.005)	–	3.93 (0.123)	4.64 (0.003)
EOM-EE-CCSD/6-31G(d,p)	3.35 (1.072)	–	4.53 (0.071)	–
EOM-EE-CCSD/6-31+G(d,p)	3.19(1.06)	4.20($< 10^{-3}$)	4.23(0.1)	4.87(0.01)
CC3/6-31+G(d,p)	2.98	–	–	–

[a] Ref. 78;[b] Ref. 10; [c] Ref. 19;[d] Ref. 18; [e] non-standard Gaussian basis set (total 690 functions), Ref. 17; [f] $pCTM^-$ anion.

In both isomers, the lowest bright state is a $\pi \rightarrow \pi^*$ transition. According to the EOM-EE-CCSD results, this state has mixed character in carboxylate, i.e., HOMO $\rightarrow$ valence LUMO (R_1=0.40) and HOMO $\rightarrow$ valence LUMO+1 (R_1=0.39). Tables 2.3 and 2.2 compare performance of different methods for excitation energies of the pCA^- chromophores. The phenolate isomer is relatively well-behaved. The excited-state wave function is dominated by a single one-electron excitation ($\pi_3\pi_1^*$). Both single- (CC2, EOM-CCSD) and multi-reference approaches (MRMP2, MCQDPT2, CASPT2) as well as MBGFT yield similar S_0-S_1 excitation energies (Table 2.3). The difference between MS-CASPT2 and SS-CASPT2 excitation energies is 0.02 eV. EOM-EE-CCSD provides a slightly higher excitation energy than MS-CASPT2 (0.2 eV). This trend agrees with the benchmark studies by Schreiber *et al.*[42]. The difference is due to the absence of triple excitations in EOM-EE-CCSD, as the inclusion of triples at the CC3 level results in the decrease of excitation energy of the same magnitude (0.2 eV). Good agreement between MS-CASPT2/TZVP and CC3/TZVP for one-electron excitation dominated transition was also pointed out in Ref. 42. The excitation energy is sensitive to addition of diffuse basis functions to the basis set (0.16 eV). The extension of the basis from double- to triple-zeta quality results in the decrease of the MS-CASPT2 excitation energies by 0.11 eV (Table 2.3). Our best estimate of the S_0-S_1 excitation energy of phenolate is 3.0 eV.

Carboxylate presents a more complex case. Previous quantum chemistry calculations yielded excitation energies (of the bright state) varying in the range of 2.85-4.79 eV. The discrepancies can be explained by the complex electronic structure of the molecule manifesting itself in a complete breakdown of the Koopmans picture, e.g.,

Hartree-Fock yields an incorrect order of the occupied MOs, as discussed above. Moreover, the two lowest valence virtual MOs are nearly generate (5.06 and 5.09 eV). While Koopmans theorem is rarely accurate, its failure in this system shows that correlation is essential for determining relative energies of the states with very different charge distributions (localized on the carboxylate moiety in the σ-system or delocalized in the π-system). Although CC and EOM-CC methods are invariant with respect to unitary transformations with active occupied and/or virtual orbital spaces (and are not very sensitive to small variations in occupied-virtual separation), breakdown of the Koopmans picture suggests that correlation is very important and one may need to go beyond double excitations.

According to the EOM-CCSD/6-31G(d,p) calculations, the vertical excitation energy for the bright state is 4.7 eV, and the wave function of the lowest excited state has multiconfigurational character dominated by two $\pi \rightarrow \pi^*$ transitions. As in the case of the phenolate, the addition of diffuse basis functions decreases the EOM-EE-CCSD excitation energy by 0.2 eV. The inclusion of triple excitations results in a decrease of 0.29 eV. We also note excellent agreement between CC3 and CASPT2. The difference between the SS- and MS-CASPT2 values is slightly larger than in the phenolate (0.2 eV). As discussed below, we consider the SS-CASPT2 value to be more reliable in this case. Thus, our best estimate of the excitation energy of the bright state in the carboxylate is 4.2 eV.

The (MS-)CASPT2/ANO-RCC-VTZP calculations of pCA^- are, in most aspects, routine, and one can expect an accuracy of 0.1-0.2 eV[42]. However, in the analysis of the results, some care has to be taken owing to potential problems due to the resonance character of the excited states. In particular, the response to one-particle basis set

expansions, the reference weight in the perturbational treatment of the dynamical correlation, i.e., the weight of the reference CASSCF wave function in the CASPT2 first order solution, and the difference between SS- and MS-CASPT2 should be carefully monitored. First, let us establish that the active orbitals of the two species are correct and that no spurious diffuse orbitals contaminate the CASSCF expansion, which is a tell-tale sign of either the presence of Rydberg states or the electron detachment continuum. The active orbitals of both pCA^- isomers were inspected visually and found to be of a valence π-like character. To further quantify the orbital character, we monitored the $\langle r^2 \rangle$ expectation value of the six SA-CASSCF states (for each isomer) and found that none of the CASSCF states developed diffuse character. Next, we inspected the reference weights in the state-specific CASPT2/ANO-RCC-VTZP calculations. For the carboxylate form we found that the fifth root in SS-CASPT2 has a substantially lower reference weight as compared to the rest. In phenolate we found two states with somewhat lower reference weights: the fourth and the sixth roots. Inspection on the weights in the SS-CASPT2 calculation with the ANO-RCC-VDZP basis reveals no roots with low reference weights (in both isomers). In the carboxylate, the observed basis set dependence of the reference weight is further aggravated by the fact that the perturbational correction introduces significant diffuseness and significant mixing in the MS-CASPT2 procedure. The observed problematic behavior in the MS-CASPT2 calculations is likely due to low detachment energies of these species and, consequently, the resonance character of the excited states. As pointed out by Serrano-Andrés *et al.*[79], the MS-CASPT2 procedure could be overestimating the mixing between reference states and in this case the SS-CASPT2 results could be more reliable. We also note that the basis set effects are smaller at the SS-CASPT2 level, e.g., as we go from the ANO-RCC-VDZP to the ANO-RCC-VTZP basis, the excitation energy of carboxylate decreases by

0.30 and 0.14 eV at the MS-CASPT2 and SS-CASPT2 levels, respectively. Hence, we consider the SS-CASPT2/ANO-RCC-VTZP results as our best estimate. Despite the observed problematic behavior, the differences between the SS- and MS-CASPT2 values are only 0.02 and 0.2 eV for phenolate and carboxylate, respectively. In the latter case, the deviation is due to mixing of the nearly degenerate first and second $\pi \rightarrow \pi^*$ transitions at the MS-CASPT2 level, which increases the energy splitting between the two states (Table 2.2). However, the resulting perturbation-modified CAS solution for the lowest $\pi \rightarrow \pi^*$ transition has also significant admixtures of higher CASSCF states. Moreover, as mentioned above, the perturbative treatment increases the diffuse character of the state. Therefore, it is not clear whether the large non-diagonal elements of the MS-CASPT2 effective Hamiltonian matrix are caused by the interaction of the closely lying first and second $\pi \rightarrow \pi^*$ states or artificial interaction with the continuum. Therefore, we consider SS-CASPT2 results to be more reliable in the case of carboxylate.

Closely related to the CASPT2 and MS-CASPT2 multireference methods are MRMP2 and MCQDPT2, respectively. For phenolate, excitation energies computed with MRMP2 and CASPT2 differ by 0.3 eV. Multistate multireference MCQDPT2 and MS-CASPT2 methods also yield results within 0.3 eV, the MS-CASPT2 excitation energy being higher. The difference is likely due to the IPEA correction used in the CASPT2 and MS-CASPT2 calculations.

For carboxylate, in contrast, the excitation energies computed with the two sets of methods are rather different (see Table 2.2). Note that 5.17 eV MRMP2 excitation energy corresponds to the sixth CASSCF root and the resulting MRMP2 state[10]. The CASPT2 excitation energy for the sixth excited state (5.32 eV, ANO-RCC-VDZP) is only slightly higher than the reported MRMP2 value. However, there is striking difference between the MS-CASPT2 and MCQDPT2 excitation energies[10]. The two methods

differ by: (i) slightly different choices of the zero-order Hamiltonian; and (ii) using internally contracted versus non-contracted basis for the secondary space in MS-CASPT2[25] and MCQDPT2[80], respectively. Overall, one can expect similar performance of the two approaches. In addition to the above differences, more diffuse basis set was used in Ref. 10. The non-diagonal elements of the MS-CASPT2/ANO-RCC-VDZP effective Hamiltonian result in strong mixing between the states, however, the perturbation-modified CAS solution of the lowest excited state is dominated by the lowest CASSCF excited root (the effective Hamiltonian matrix and eigenvectors are given in Supporting Materials for Ref. 60). The mixing between the high-lying fifth and sixth (forth and sixth with CASSCF/ANO-RCC-VDZP) CASSCF states increases upon the increase of the basis set to ANO-RCC-VTZP and the lowest perturbation-modified CAS solution is represented by nearly equal contributions from the second, fifth, and sixth CASSCF roots. Therefore, the non-diagonal effective Hamiltonian matrix elements that couple the fifth and the sixth CASSCF/ANO-RCC-VTZP (fourth and sixth with ANO-RCC-VDZP) states are very sensitive to the basis set. The difference between the MS-CASPT2 and MCQDPT2 excitation energies could be due to even stronger mixing between these CASSCF states in a more diffuse basis set. Indeed, the MCQDPT2 perturbation-modified CAS solution for the lowest excited state is dominated by the sixth CASSCF state, and the corresponding excitation energy is 3.05 eV[10].

The SS-CASPT2/ANO-RCC-VTZP values of the lowest excitation energies are 4.16 and 2.98 eV, for the carboxylate and phenolate forms, respectively. The CC3/6-31G+(d,p) values are 4.21 and 2.98 eV, the corresponding EOM-CCSD values are 4.17 and 3.19 eV.

Our best estimates of vertical excitation energies of the bright $\pi \rightarrow \pi^*$ state are 3.0 and 4.2 eV for the phenolate and carboxylate forms of pCA^-, respectively. The higher

excitation energy of the carboxylate can be explained by qualitative analysis of the electronic structure: in the carboxylate, one can expect excitation energy close to that of neutral phenol (4.5 eV[81]), whereas in the phenolate, the phenol-like electronic structure is strongly perturbed by the residing negative charge resulting in the red-shifted absorption. A similar mechanism of the tuning of optical properties of biochromophores was found to be important in chemically initiated electron-exchange luminescence of luciferins[82]. The Hückel model provides an alternative explanation of the observed trend in excitation energies (see Sec. 2.3.3).

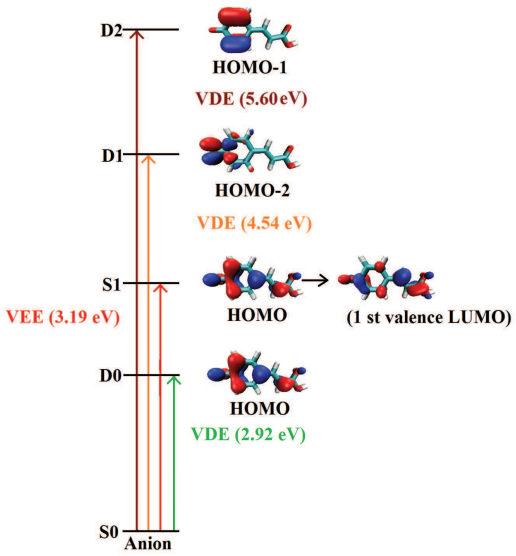

Figure 2.5: Energy level diagram of the ionized and electronically excited states of the phenolate form. VEE: EOM-EE-CCSD/6-31+G(d,p); VDE: EOM-IP-CCSD/6-311+G(df,pd).

As mentioned above, an interesting feature of the both isomers is the resonance or near-resonance character of the lowest bright excited state. However, the two isomers show qualitatively different types of the resonance. As follows from Fig. 2.5, the S_1 state of phenolate is a shape resonance that lies above its own continuum (detachment

from the HOMO). The energy diagram is different for carboxylate (Fig. 2.6), i.e., the S_1 state is above three ionized states corresponding to electron detachment from HOMO-1, HOMO-2 and HOMO-3 and 0.25 eV below its own continuum (detachment from HOMO). This is an example of a Feshbach resonance. One would expect longer life-times for this type of metastable state.

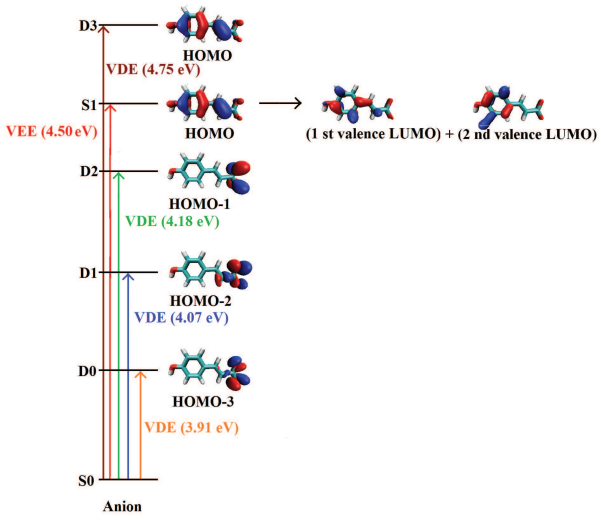

Figure 2.6: Energy level diagram of the ionized and electronically excited states of the carboxylate form. VEE: EOM-EE-CCSD/6-31+G(d,p); VDE: EOM-IP-CCSD/6-311+G(df,pd).

It should be noted that the converged energies of the resonance states may differ from the excitation energies reported here due to basis set effects and interactions with the continuum. Thus, more elaborate calculations are required to evaluate the positions of the resonances and the lifetimes of the metastable excited states in these complex systems.

2.3.3 Molecular orbital framework

As in the case of GFP[14], the trends in electronic properties of the isomers can be explained by a simple Hückel-like model. Although the resulting excitation and ionization energies cannot be considered as quantitative, this analysis provides a qualitative explanation of the observed differences between the two isomers.

As the electronic density redistribution mainly involves the bridge region for both isomers (see Fig. 2.3), the analysis is based on a model system consisting of the three bridge carbons. Assuming almost perfect resonance for the phenolate, which makes the three atoms (C_α, C_β and C_γ) equivalent, the Hückel Hamiltonian is written as follows:

$$H = \begin{pmatrix} \varepsilon & \alpha & 0 \\ \alpha & \varepsilon & \alpha \\ 0 & \alpha & \varepsilon \end{pmatrix}, \tag{2.1}$$

where ε is an atomic *p*-orbital energy and α is a coupling matrix element between the two neighboring centers. This model is exactly equivalent to the Huckel's solution for the allyl radical. The diagonalization of this matrix yields the following eigenvalues:

$$E_1^{Ph} = \varepsilon + \sqrt{2}\alpha \tag{2.2}$$

$$E_2^{Ph} = \varepsilon \tag{2.3}$$

$$E_3^{Ph} = \varepsilon - \sqrt{2}\alpha \tag{2.4}$$

The corresponding eigenfunctions $\{\phi_i\}_{i=1,3}$ are depicted in Fig. 2.7. The validity of Hückel's description is supported by the analysis of the MOs: the shapes of the HOMO-5, HOMO and LUMO in the bridge C_α – C_γ region are indeed similar to the

$\{\phi_i\}_{i=1,3}$ Hückel solutions. The corresponding detachment and excitation energies are $-(\varepsilon)$ and $-\sqrt{2}\alpha$, respectively.

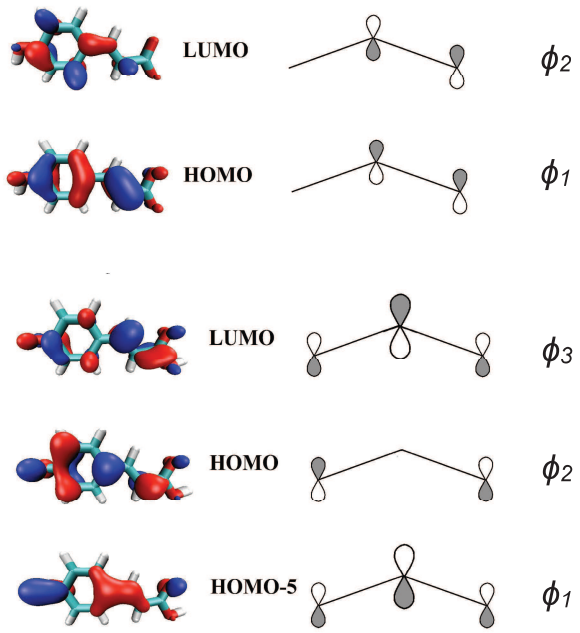

Figure 2.7: Schematic representation of the Hückel model eigenfunctions (see text) and the corresponding MOs for the carboxylate (top) and the phenolate (bottom) pCA$^-$.

For the carboxylate isomer, BLA in the bridge region is larger suggesting that the three carbons are no longer equivalent. Assuming $\varepsilon_\alpha << \varepsilon_\beta = \varepsilon_\gamma = \varepsilon$ and neglecting the coupling between C_α and C_β, we arrive to the following Hamiltonian:

$$h = \begin{pmatrix} \varepsilon' & 0 & 0 \\ 0 & \varepsilon & \alpha \\ 0 & \alpha & \varepsilon \end{pmatrix} \tag{2.5}$$

which gives rise to the eigenvalues:

$$E_1^{Carb} = \varepsilon + \alpha \tag{2.6}$$

$$E_2^{Carb} = \varepsilon - \alpha \tag{2.7}$$

The resulting detachment and excitation energies for the carboxylate are $(-\varepsilon - \alpha)$ and -2α. Therefore, Hückel's model predicts higher excitation and detachment energies for the carboxylate isomer.

The model yields the following estimates of the transition dipole moments matrix elements for carboxylate and the phenolate: $\langle \pi | \mu | \pi^* \rangle = \frac{x_0}{2}$ and $\langle \pi | \mu | \pi^* \rangle = \frac{x_0}{\sqrt{2}}$, respectively, where x_0 is the average C-C bond length between the bridge atoms (see Appendix for Ref. 60). This suggests that the oscillator strength for the phenolate form is higher than that of carboxylate, which is indeed confirmed by *ab initio* calculations (see Tables 2.3 and 2.2). Additional details of the Hückel analysis are given in the Appendix for Ref. 60.

2.3.4 Theory versus experiment

As mentioned above, recent gas-phase action spectroscopy measurements reported identical absorption maxima for the carboxylate and phenolate isomers of pCA^-. As a source of gas-phase anions, the electrospray technique was used[8–10] and the ions were extracted from water-methanol solution. It has been demonstrated that for tyrosine, which also exists in the carboxylate and phenolate forms, the electrospray extraction from methanol-water solution results in the gas-phase mixture with relative abundances of the two isomers corresponding to the gas-phase equilibrium distribution[83]. In aqueous solution, deprotonation of carboxylate is preferable[83]. It was also shown that the relative

populations are very sensitive to the presence of methanol in the solution. Thus, it is not clear which of the pCA^- isomers is present in gas phase when the electrospray technique is used[17,83]. To achieve isomer specificity, the methylated analogues of pCA were used in the experiment[10]. The comparison of the results obtained for non-methylated species with the absorption spectra of the methylated compounds is justified because only a minor effect of methylation on excitation energies was reported for pCA^- at the CC2 level of theory[10] and there is good agreement between EOM-CCSD and CC2 for this system. (see Tables 2.2 and 2.3).

The comparison of our calculations with the experimental spectra [10,] is presented in Fig. 2.8. This experiment[10] did not distinguish between the detachment and excitation channels. Thus, both detachment and excitation can contribute to the experimental band. The computed SS-CASPT2/ANO-RCC-VTZP excitation and EOM-IP-CCSD/6-311+G(df,pd) detachment energies for the phenolate chromophore are 2.98 eV and 2.92 eV, and, therefore, both can be responsible for the band maximum. For carboxylate, the respective values are 4.17 and 3.91 eV. These values do not agree with the experimental peak, and the discrepancies are much larger than the anticipated error bars of these methods.

According to our calculations (and in agreement with previous studies), there are no transitions below 3.9 in the carboxylate (see Table 2.2). We considered dipole-bound states[84] and isomerization in the gas phase as possible explanations of these discrepancies. The dipole bound states can exist in pCA^- (dipole moment 4.82 D for carboxylate and 3.01 for phenolate neutral radicals), however, they cannot account for the 1 eV difference.

One of the possible explanations of the experimental results is a contamination of the carboxylate sample by the phenolate form. If this was the case, the experiment

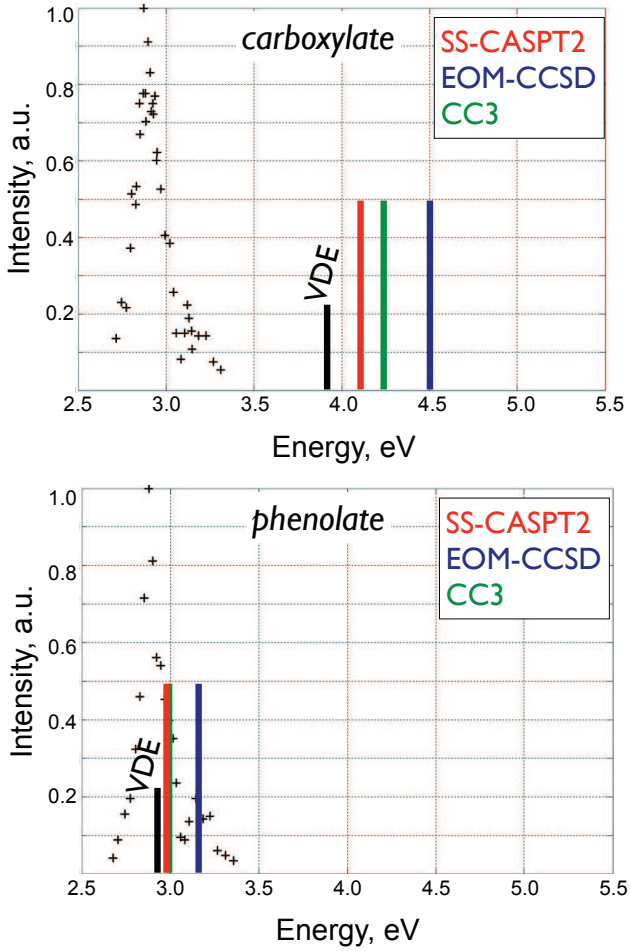

Figure 2.8: The experimental spectra and calculated VDE and VEE of the carboxylate (top) and phenolate (bottom) forms of pCA$^-$. The experimental maximum is 2.88 eV (430 nm). The heights of the bars representing vertical excitation and ionization energies are arbitrary.

signal could be dominated by the phenolate owing to its much larger oscillator strength. The reported identical spectra for the two isomers[10] support this assumption. Since the higher-energy region was not probed, the signal due to carboxylate was not observed.

The photo-induced fragmentation channels have been experimentally determined by registering the masses of the resulting charged fragments[10]. The 146 amu signal for the anionic photoproduct was reported for both carboxylate and phenolate (methylated

pCA$^-$). This channel was ascribed to the detachment of the neutral OCH_3 fragment. Note that the experimental mass resolution was $\pm$ 2 amu[10]. The high yield of the neutral fragments other than ionized chromophore shows that the excitation to the S_1 state is an efficient channel, in addition to possible direct detachment for both forms of the chromophore. Thus, the experimental absorption bands for phenolate and carboxylate represent, at least partially, transition to the resonance electronically-excited states.

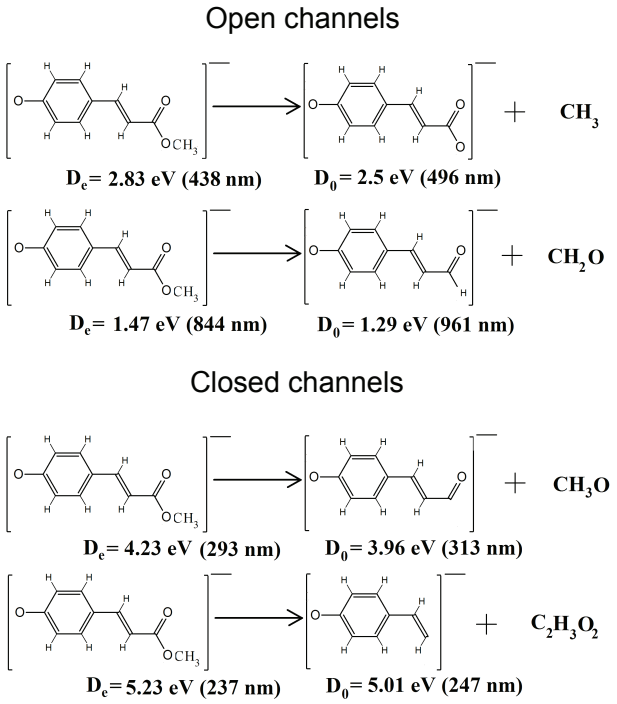

Figure 2.9: Energetically allowed (top) and forbidden (bottom) fragmentation channels and the corresponding dissociation energies for the phenolate form of pCA$^-$. D_0 and D_e denote dissociation energies computed with and without ZPE correction, respectively.

To analyze the fragmentation pathways, we computed dissociation energies for methylated pCA$^-$ in the phenolate and carboxylate forms (Figs 2.9 and 2.10). The results for non-methylated pCA$^-$ are given in the Supporting Materials for Ref. 60. Our

calculations show that the only energetically allowed channels for the phenolate correspond to the abstraction of CH_3 and CH_2O, as shown in Fig. 2.9. Within the experimental mass resolution, formaldehyde (CH_2O) is indistinguishable from the OCH_3 radical. Moreover, the mass of the anionic fragment resulting from the CH_3 detachment from pCA^- is 151 amu, which is $\sim 91\%$ from the mass of the parent ion, whereas only the daughter ions with masses in the range of 20-80% of the parent ion mass are captured in this experimental setup[9]. Therefore, the predicted photo-fragmentation products for phenolate agree with the experimental data. For carboxylate, in addition to the detachment of the neutral CH_3 and CH_2O fragments, there is a low-energy fragmentation channel leading to CO_2 formation. This additional channel is specific for the carboxylate and can be used as an experimental probe to distinguish between the isomers. No evidence for CO_2 formation was reported in Ref. 10 raising a question about the nature of the absorbing species. Note that the production of CO_2 was reported as an efficient fragmentation channel in non-methylated pCA^-[10].

Besides dissociation, photodetachment has been experimentally registered for the phenolate form[10], which is consistent with computed detachment energies (Table 2.1). Indeed, the experimental absorption maximum value (2.88 eV) is close to the calculated VDE (2.92 eV) suggesting an alternative decay route for the excited phenolate form.

Another factor that may affect the spectra is the presence of different rotamers and low-barrier hindered rotation along single bonds of the chromophore. To quantify the effect of the phenolic OH group rotation on the absorption spectra of carboxylate, we computed excitation energies of the anti- and syn- rotamers using EOM-EE-CCSD/6-31+G(d,p). We found that isomerization has only minor effect on vertical excitation energy (changes about 0.08 eV). We analyzed conformational flexibility using AIMD simulations. The average values of C-C_α-C_β-C_γ and C_β-C_γ-C(O)-O dihedral angles

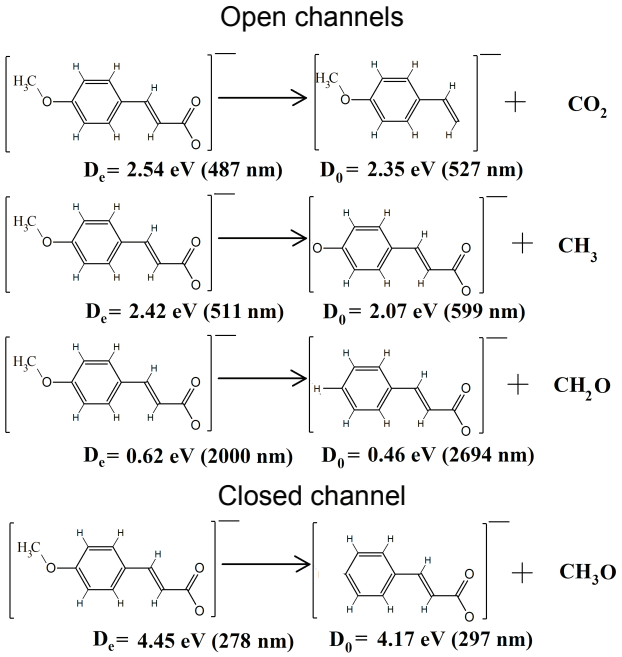

Figure 2.10: Energetically allowed (top) and forbidden (bottom) fragmentation channels and the corresponding dissociation energies for the carboxylate form of pCA$^-$. D_0 and D_e denote dissociation energies computed with and without ZPE correction, respectively.

along 2 ps trajectories for the methylated carboxylate are 7.18° and 4.7° (methylated phenolate - 9.03° and 5.95°), respectively (T = 298 K). Thus, the chromophore is rather inflexible and we anticipate no significant distortion of the conjugated π-system due to rotation along single bonds, and, consequently, no significant variations in excitation energy.

We suggest that the action spectra measured for the two methylated pCA$^-$ isomers in Ref. 10 are due to the phenolate isomer (which probably contaminated the carboxylate sample) based on the following considerations: (i) there are no one-photon transitions (either excitation or ionization) below 3.8 eV in the carboxylate; (ii) the oscillator

strength for the lowest bright state of the phenolate is three orders of magnitude higher than in the carboxylate. Thus, a small admixture of the phenolate may result in a relatively large signal; (iii) in the carboxylate there is an additional fragmentation channel leading to CO_2 production, which is not accessible in the phenolate; however, this product was not observed in the experiment[10]; (iv) in the gas phase, phenolate is lower in energy than carboxylate[10]. An alternative explanation might be due to two-photon absorption, however, it does not explain the striking similarity of the two spectra.

2.4 Conclusions

We report an electronic structure study of the excited and ionized states of pCA^-, a model PYP chromophore. We compare the optical properties (vertical excitation and detachment energies) of the two isomers, phenolate and carboxylate. In addition to the high-level calculations of the vertical excitation and detachment energies, we present a qualitative explanation of the observed differences. Our best estimates of vertical excitation energies of the two isomers are 3.0 eV and 4.2 eV (SS-CASPT2/ANO-RCC-VTZP) for phenolate and carboxylate, respectively. We note excellent agreement between SS-CASPT2 and CC3 (although the latter was employed with a modest basis set). The EOM-CCSD values are within 0.2 eV of CC3.

Our results do not support the experimental conclusion that the two isomers have identical absorption spectra[10]. As a possible explanation, we suggest contamination of the carboxylate sample by the phenolate isomer. Due to the large difference in oscillator strength of the two isomers (three orders of magnitude), a small admixture of phenolate may result in relatively large absorption. The absence of CO_2 fragments (which can be produced in by the carboxylate) in the experiment supports our suggestion that the recordered spectrum is due to phenolate. Our work suggests that the experiment should

be revisited probing higher energies for the spectroscopic signature of the carboxylate isomer. The production of CO_2 at higher energies would confirm the presence of the carboxylate form.

2.5 Chapter 2 references

[1] T.E. Meyer. Isolation and characterization of soluble cytochromes, ferredoxins and other chromophoric proteins from the halophilic phototrophic bacterium ectothiorhodospira halophila. *Biochem. and Biophys. J.*, 806:175–183, 1985.

[2] T.E. Meyer, E. Yakali, M.A. Cusanovich, and G. Tollint. Properties of a water-soluble, yellow protein isolated from a halophilic phototrophic bacterium that has photochemical activity analogous to sensory rhodopsin. *Biochem. J.*, 26:418–423, 1987.

[3] W.W. Sprenger, W.D. Hoff, J.P. Armitage, and K.J. Hellingwer. The eubacterium ectothiorhodospira halophila is negatively phototactic, with a wavelength dependence that fits the absorption spectrum of the photoactive yellow protein. *J. of Bacteriology*, 175:3096–3104, 1993.

[4] W. D. Hoff, P. Düx, K. Hård, B. Devreese, I. M. Nugteren-Roodzant, W. Crielaard, R. Boelens, R. Kaptein, J. van Beeuman, and K. J. Hellingwerf. Thiol ester-linked p-coumaric acid as a new photoactive prosthetic group in a protein with rhodopsin-like photochemistry. *Biochemistry*, 33:13959–13962, 1994.

[5] M. Baca, G.E.O. Borgstahl, M. Boissinot, P.M. Burke, D.R. Williams, K.A. Slater, and E.D. Getzoff. Complete chemical structure of photoactive yellow protein: Novel thioester-linked 4-hydroxycinnamyl chromophore and photocycle chemistry. *Biochemistry*, 33:14369–14377, 1994.

[6] R. Kort, H. Vonk, X. Xu, W.D. Hoff, W. Crielaard, and K. J. Hellingwerf. Evidence for trans-cis isomerization of the p-coumaric acid chromophore as the photochemical basis of the photocycle of photoactive yellow protein. *FEBS Lett.*, 382:73 – 78, 1996.

[7] L. J. G. W. van Wilderen, M. A. van der Horst, I. H. M. van Stokkum, K. J. Hellingwerf, R. van Grondelle, and M. L. Groot. Ultrafast infrared spectroscopy reveals a key step for successful entry into the photocycle for photoactive yellow protein. *Proc. Nat. Acad. Sci.*, 103(41):15050–15055, 2006.

[8] I.B. Nielsen, S. Boye-Peronne, M.O.A. El Ghazaly, M.B. Kristensen, S.B. Nielsen, and L.H. Andersen. Absorption spectra of photoactive yellow protein chromophores in vacuum. *Biophys. J.*, 89:2597–2604, 2005.

[9] L. Lammich, J. Rajput, and L.H. Andersen. Photodissociation pathways of gas-phase photoactive yellow protein chromophores. *Phys. Rev. E*, 78:051916, 2008.

[10] T. Rocha-Rinza, O. Christiansen, J. Rajput, A. Gopalan, D.B. Rahbek, L.H. Andersen, A.V. Bochenkova, A.A.Granovsky, K.B. Bravaya, A.V. Nemukhin, K.L. Christiansen, and M.B. Nielsen. Gas phase absorption studies of photoactive yellow protein chromophore derivatives. *J. Phys. Chem. A*, 113:9442–9449, 2009.

[11] I-R. Lee, W. Lee, and A H. Zewail. Primary steps of the photoactive yellow protein: Isolated chromophore dynamics and protein directed function. *Proc. Nat. Acad. Sci.*, 103:258–262, 2006.

[12] M.W. Forbes and R.A. Jockusch. Deactivation pathways of an isolated green fluorescent protein model chromophore studied by electronic action spectroscopy. *J. Am. Chem. Soc.*, 131:17038–17039, 2009.

[13] E. Epifanovsky, I. Polyakov, B.L. Grigorenko, A.V. Nemukhin, and A.I. Krylov. Quantum chemical benchmark studies of the electronic properties of the green fluorescent protein chromophore: I. Electronically excited and ionized states of the anionic chromophore in the gas phase. *J. Chem. Theory Comput.*, 5:1895–1906, 2009.

[14] E. Epifanovsky, I. Polyakov, B.L. Grigorenko, A.V. Nemukhin, and A.I. Krylov. The effect of oxidation on the electronic structure of the green fluorescent protein chromophore. *J. Chem. Phys.*, 132:115104, 2010.

[15] E. V. Gromov, I. Burghardt, H. Köppel, and L. S. Cederbaum. Impact of sulfur vs oxygen on the low-lying excited state of trans-p-coumaric acid and trans-p-coumaric thio acid. *J. Phys. Chem. A*, 109:4623–4631, 2005.

[16] Z. He, C. H. Martin, R. Birge, and K.F. Freed. Theoretical studies on excited states of a phenolate anion in the environment of the photoactive yellow protein. *J. Phys. Chem. A*, 104:2939–2952, 2000.

[17] Y. Ma, M. Rohlfing, and C. Molteni. Modeling the excited states of biological chromophores with many-body Green's function theory. *J. Chem. Theory Comput.*, 6:257–265, 2010.

[18] E. Gromov, I. Burghardt, J. Hynes, H. Köppel, and L. Cederbaum. Electronic structure of the photoactive yellow protein chromophore: Ab initio study of the low-lying excited singlet states. *Photochem. and Photobiol.*, 190:241–257, 2007.

[19] E. V. Gromov, I. Burghardt, H. Köppel, and L. S. Cederbaum. Electronic structure of the PYP chromophore in its native protein environment. *J. Am. Chem. Soc.*, 129:6798–6806, 2007.

[20] D. Sinha, D. Mukhopadhyay, and D. Mukherjee. A note on the direct calculation of excitation-energies by quasi-degenerate MBPT and coupled-cluster theory. *Chem. Phys. Lett.*, 129:369–374, 1986.

[21] J.F. Stanton and R.J. Bartlett. The equation of motion coupled-cluster method. A systematic biorthogonal approach to molecular excitation energies, transition probabilities, and excited state properties. *J. Chem. Phys.*, 98:7029–7039, 1993.

[22] S.V. Levchenko and A.I. Krylov. Equation-of-motion spin-flip coupled-cluster model with single and double substitutions: Theory and application to cyclobutadiene. *J. Chem. Phys.*, 120(1):175–185, 2004.

[23] J. Simons. *Encyclopedia of computational chemistry*, chapter Equation of motion (EOM) methods for computing electron affinities. J. Wiley & Son, New York, 1998.

[24] A.I. Krylov. Equation-of-motion coupled-cluster methods for open-shell and electronically excited species: The hitchhiker's guide to Fock space. *Annu. Rev. Phys. Chem.*, 59:433–462, 2008.

[25] J. Finley, P.-Å. Malmqvist, B.O. Roos, and L. Serrano-Andrés. The multi-state caspt2 method. *Chem. Phys. Lett.*, 288:299–306, 1998.

[26] H. Koch, O. Christiansen, P. Jørgensen, A.M.S. de Meras, and T. Helgaker. The CC3 model: An iterative coupled cluster approach including connected triples. *J. Chem. Phys.*, 106:1808–1818, 1997.

[27] T.H. Dunning. Gaussian basis sets for use in correlated molecular calculations. I. The atoms boron through neon and hydrogen. *J. Chem. Phys.*, 90:1007–1023, 1989.

[28] M.W. Feyereisen, G. Fitzgerald, and A. Komornicki. *Chem. Phys. Lett.*, 208:359, 1993.

[29] O. Vahtras, J. Almlöf, and M.W. Feyereisen. *Chem. Phys. Lett.*, 213:514, 1993.

[30] A. Komornicki and G. Fitzgerald. *J. Chem. Phys.*, 98:1398, 1993.

[31] D.E. Bernhold and R.J. Harrison. *Chem. Phys. Lett.*, 250:477, 1996.

[32] J.-D. Chai and M. Head-Gordon. Systematic optimization of long-range corrected hybrid density functionals. *J. Chem. Phys.*, 128:084106, 2008.

[33] A.A. Golubeva, P.A. Pieniazek, and A.I. Krylov. A new electronic structure method for doublet states: Configuration interaction in the space of ionized 1h and 2h1p determinants. *J. Chem. Phys.*, 130(12):124113, 2009.

[34] S. Pal, M. Rittby, R.J. Bartlett, D. Sinha, and D. Mukherjee. Multireference coupled-cluster methods using an incomplete model space — application to ionization-potentials and excitation-energies of formaldehyde. *Chem. Phys. Lett.*, 137:273–278, 1987.

[35] J.F. Stanton and J. Gauss. Analytic energy derivatives for ionized states described by the equation-of-motion coupled cluster method. *J. Chem. Phys.*, 101(10):8938–8944, 1994.

[36] M. Kamiya and S. Hirata. Higher-order equation-of-motion coupled-cluster methods for ionization processes. *J. Chem. Phys.*, 125:074111–074125, 2006.

[37] P.A. Pieniazek, S.A. Arnstein, S.E. Bradforth, A.I. Krylov, and C.D. Sherrill. Benchmark full configuration interaction and EOM-IP-CCSD results for prototypical charge transfer systems: Noncovalent ionized dimers. *J. Chem. Phys.*, 127:164110, 2007.

[38] P.A. Pieniazek, S.E. Bradforth, and A.I. Krylov. Charge localization and Jahn-Teller distortions in the benzene dimer cation. *J. Chem. Phys.*, 129:074104, 2008.

[39] V.I. Lebedev. Values of the nodes and weights of ninth to seventeenth order Gauss-Markov quadrature formulae invariant under the octahedron group with inversion. *Zh. Vychisl. Mat. Mat. Fiz.*, 15:48–54, 1975.

[40] W.C. Murray, N.C. Handy, and G.J. Laming. Quadrature schemes for integrals of density functional theory. *Mol. Phys.*, 78:997–1014, 1993.

[41] H. Larsen, K. Hald, J. Olsen, and P. Jørgensen. Triplet excitation energies in full configuration interaction and coupled-cluster theory. *J. Chem. Phys.*, 115:3015–3020, 2001.

[42] M. Schreiber, M.R. Silva-Junior, S.P.A. Sauer, and W. Thiel. Benchmarks for electronically excited states: CASPT2, CC2, CCSD, and CC3. *J. Chem. Phys.*, 128:134110, 2008.

[43] E. Epifanovsky, K. Kowalski, P.-D. Fan, M. Valiev, S. Matsika, and A.I. Krylov. On the electronically excited states of uracil. *J. Phys. Chem. A*, 112:9983–9992, 2008.

[44] B.O. Roos, P.R. Taylor, and P.E.M. Siegbahn. A complete active space SCF method (CASSCF) using a density matrix formulated super-CI approach. *Chem. Phys.*, 48:157–173, 1980.

[45] K. Andersson, P.-Å. Malmqvist, B.O. Roos, A.J. Sadlej, and K. Wolinski. 2nd order perturbation theory with a CASSCF reference function. *J. Phys. Chem.*, 94:5483–5488, 1990.

[46] P.C. Hariharan and J.A. Pople. *Theor. Chim. Acta*, 28:213, 1973.

[47] P.O. Widmark, P.Å. Malmqvist, and B. Roos. *Theor. Chim. Acta*, 77:291, 1990.

[48] B.O. Roos, R. Lindh, P.Å. Malmqvist, V. Veryazov, and P.O. Widmark. Main group atoms and dimers studied with a new relativistic ano basis set. *J. Phys. Chem.*, 108:2851–2858, 2004.

[49] M. Douglas and N.M. Kroll. Quantum electrodynamical corrections to the fine structure of helium. *Ann. Phys. (NY)*, 82:89–155, 1974.

[50] G. Ghigo, B.O. Roos, and P.-Å. Malmqvist. *Chem. Phys. Lett.*, 396:142, 2004.

[51] P.-Å. Malmqvist and B.O. Roos. The CASSCF state interaction method. *Chem. Phys. Lett.*, 155:189–194, 1989.

[52] N.H.F. Beebe and J. Linderberg. Simplifications in the generation and transformation of two-electron integrals in molecular calculations. *Int. J. Quant. Chem.*, 12:683–705, 1977.

[53] F. Aquilante, T. B. Pedersen, and R. Lindh. Density fitting with auxiliary basis sets from Cholesky decompositions. *Theor. Chem. Acc.*, 124:1–10, 2009.

[54] F. Aquilante, L. Gagliardi, T. B. Pedersen, and R. Lindh. Atomic Cholesky decompositions: A route to unbiased auxiliary basis sets for density fitting approximation with tunable accuracy and efficiency. *J. Chem. Phys.*, 130:154107, 2009.

[55] F. Aquilante, R. Lindh, and T. B. Pedersen. Unbiased auxiliary basis sets for accurate two-electron integral approximations. *J. Chem. Phys.*, 127:114107, 2007.

[56] F. Aquilante, T. B. Pedersen, R. Lindh, B. O. Roos, A. S. de Merás, and H. Koch. Accurate ab initio density fitting for multiconfigurational self-consistent field methods. *J. Chem. Phys.*, 129:024113, 2008.

[57] F. Aquilante, P.Å. Malmqvist, T. B. Pedersen, A. Ghosh, and B.O. Roos. Cholesky decomposition-based multiconfiguration second-order perturbation theory (cd-caspt2): Application to the spin-state energetics of co-iii(diiminato)(nph). *J. Theor. Comput. Chem.*, 4:694–702, 2008.

[58] F. Aquilante, T. B. Pedersen, and R. Lindh. Low-cost evaluation of the exchange fock matrix from cholesky and density fitting representations of the electron repulsion integrals. *J. Chem. Phys.*, 126:194106, 2007.

[59] J. Boström, M. G. Delcey, F. Aquilante, L. Serrano-Andrés, T. B. Pedersen, and R. Lindh. Calibration of cholesky auxiliary basis sets for multiconfigurational perturbation theory calculations of excitation energies. *J. Theor. Comput. Chem.*, 6:747–754, 2010.

[60] D. Zuev, K.B. Bravaya, T.D. Crawford, R. Lindh, and A.I. Krylov. Electronic structure of the two isomers of the anionic form of p-coumaric acid chromophore. *J. Chem. Phys.*, 134:034310, 2011.

[61] F. Weinhold and C. R. Landis. Natural bond orbitals and extensions of localized bonding concepts. *Chem. Ed.: Res. & Pract. Eur.*, 2:91–104, 2001.

[62] E.D. Glendening, J.K. Badenhoop, A.E. Reed, J.E. Carpenter, J.A. Bohmann, C.M. Morales, and F. Weinhold. NBO 5.0. Theoretical Chemistry Institute, University of Wisconsin, Madison, WI, 2001.

[63] Y. Shao, L. Fusti-Molnar, Y. Jung, J. Kussmann, C. Ochsenfeld, S. Brown, A.T.B. Gilbert, L.V. Slipchenko, S.V. Levchenko, D.P. O'Neill, R.A. Distasio Jr, R.C. Lochan, T. Wang, G.J.O. Beran, N.A. Besley, J.M. Herbert, C.Y. Lin, T. Van Voorhis, S.H. Chien, A. Sodt, R.P. Steele, V.A. Rassolov, P. Maslen, P.P. Korambath, R.D. Adamson, B. Austin, J. Baker, E.F.C. Byrd, H. Daschel, R.J. Doerksen, A. Dreuw, B.D. Dunietz, A.D. Dutoi, T.R. Furlani, S.R. Gwaltney, A. Heyden, S. Hirata, C.-P. Hsu, G.S. Kedziora, R.Z. Khalliulin, P. Klunziger, A.M. Lee, W.Z. Liang, I. Lotan, N. Nair, B. Peters, E.I. Proynov, P.A. Pieniazek, Y.M. Rhee, J. Ritchie, E. Rosta, C.D. Sherrill, A.C. Simmonett, J.E. Subotnik, H.L. Woodcock III, W. Zhang, A.T. Bell, A.K. Chakraborty, D.M. Chipman, F.J. Keil, A. Warshel, W.J. Hehre, H.F. Schaefer III, J. Kong, A.I. Krylov, P.M.W. Gill, M. Head-Gordon. Advances in methods and algorithms in a modern quantum chemistry program package. *Phys. Chem. Chem. Phys.*, 8:3172–3191, 2006.

[64] T.D. Crawford, C.D. Sherrill, E.F. Valeev, J.T. Fermann, R.A. King, M.L. Leininger, S.T. Brown, C.L. Janssen, E.T. Seidl, J.P. Kenny, and W.D. Allen. PSI3: An open-source ab initio electronic structure package. *J. Comput. Chem.*, 28:1610–1616, 2007.

[65] F. Aquilante, L. de Vico, N. Ferré, G. Ghigo, P-Å Malmqvist, P. Neogrády, T. B. Pedersen, M. Pitonăk, M. Reiher, B. Roos, L. Serrano-Andrés, M. Urban, V. Veryazov, and R. Lindh. Molcas 7: The next generation. *J. Comput. Chem.*, 31:224–247, 2010.

[66] S. Olsen and S.C. Smith. Bond selection in the photoisomerization reaction of anionic green fluorescent protein and kindling fluorescent protein chromophore models. *J. Am. Chem. Soc.*, 130:8677–8689, 2008.

[67] I. Polyakov, E. Epifanovsky, B.L. Grigorenko, A.I. Krylov, and A.V. Nemukhin. Quantum chemical benchmark studies of the electronic properties of the green fluorescent protein chromophore: II. Cis-trans isomerization in water. *J. Chem. Theory Comput.*, 5:1907–1914, 2009.

[68] J. Simons. Molecular anions. *J. Phys. Chem. A*, 112:6401–6511, 2008.

[69] J. Simons. How do low-energy (0.1-2 eV) electrons cause DNA-strand breaks? *Acc. Chem. Res.*, 39:772–779, 2006.

[70] M. Sobczyk and J. Simons. The role of excited Rydberg states in electron transfer dissociation. *J. Phys. Chem. B*, 110:7519, 2006.

[71] A.U. Hazi and H.S. Taylor. Stabilization method of calculating resonance energies: Model problem. *Phys. Rev. A*, 1:1109, 1970.

[72] U. V. Riss and H.-D. Meyer. Calculation of resonance energies and widths using the complex absorbing potential method. *J. Phys. B*, 26:4503–4536, 1993.

[73] G. Jolicard and E. J. Austin. Optical potential stabilisation method for predicting resonance levels. *Chem. Phys. Lett.*, 121:106–110, 1985.

[74] J. Aguilar and J. M. Combes. A class of analytic perturbations for one-body Schrödinger Hamiltonians. *Commun. Math. Phys.*, 22:269–279, 1971.

[75] E. Balslev and J. M. Combes. Spectral properties of many-body Schrödinger operators with dilatation-analytic interactions. *Commun. Math. Phys.*, 22:280–294, 1971.

[76] B. Simon. Quadratic form techniques and the Balslev-Combes theorem. *Commun. Math. Phys.*, 27:1–9, 1972.

[77] W. P. Reinhardt. Complex coordinates in the theory of atomic and molecular structure and dynamics. *Annu. Rev. Phys. Chem.*, 33:223–255, 1982.

[78] A. Sergi, M. Grüning, M.Ferrario, and F. Buda. Density functional study of the photoactive yellow protein's chromophore. *J. Phys. Chem. B*, 105:4386, 2001.

[79] L. Serrano-Andrés, M. Merchán, and R. Lindh. Computation of conical intersections by using perturbation techniques. *J. Chem. Phys.*, 122:104107, 2005.

[80] H. Nakano. Quasi-degenerate perturbation-theory with multiconfigurational self-consistent-field reference functions. *J. Chem. Phys.*, 99:7983–7992, 1993.

[81] S. J. Martinez III and J. C. Alfano annd D. H. Levy. Rotationally resolved fluorescence excitation spectra of phenol and 4-ethylphenol in a supersonic jet. *J. Molec. Spect.*, 152:80–88, 1992.

[82] Y.-J. Liu, L. De Vico, and R. Lindh. Ab initio investigation on the chemical origin of the firefly bioluminescence. *J. Photochem. Photobiol. A*, 194:261–267, 2008.

[83] Z. Tian and S. R. Kass. Does electrospray ionization produce gas-phase or liquid-phase structure. 130:10842 – 10843, 2008.

[84] K.D. Jordan and F. Wang. Theory of dipole-bound anions. *Annu. Rev. Phys. Chem.*, 54:367–396, 2003.

Chapter 3: Effect of microhydration on the electronic structure of the chromophores of the photoactive yellow and green fluorescent proteins

3.1 Introduction

Microsolvation is often used to study the effect of individual solvent-solute interactions. For example, the protein environment and bulk water feature multiple hydrogen-bonding interactions, in addition to covalent linkage and electrostatics. These effects can be quantified by considering well-defined model systems, such as microhydrated chromophores[1,2]. Hydrogen-bonding interactions in photoactive proteins can modulate optical properties of the chromophore, as has been demonstrated by theoretical[3,4] and experimental studies[5–10].

This paper focuses on the chromophores of two important photoactive biomolecules, photoactive yellow (PYP) and green fluorescent (GFP) proteins. PYP, which was found in the *Halorhodospira halophila* bacterium[11,12], serves as a blue light receptor of its host and is responsible for negative phototaxis[13]. The PYP chromophore is one of the

simplest model systems for studying spectral tuning by protein (or solvent) environment, which is relevant, for example, for understanding properties of fluorescent biomarkers[14] and the mechanics of color vision[15]. GFP, which was isolated from jellyfish *Aequorea victoria*[16], has a natural function of converting blue to green light. Proteins from the GFP family are widely used as genetically encoded biomarkers for *in vivo* imaging[17–20].

The isolated PYP and GFP chromophores have attracted attention both from experimentalists and theoreticians. The most commonly used model system representing the GFP chromophore is 4-hydroxybenzylidene-2,3-dimethylimidazolinone (HBDI), whereas for PYP it is para-coumaric acid (pCA). In spite of entirely different biological functions and origins, their electronic structure has several similar features[21]. Anionic forms (deprotonated at the phenol end) play a crucial role in photophysics of both chromophores and feature a phenolate moiety connected by a methine bridge to either imidazolinone (HBDI) or carboxylate (pCA). The pCA anion exists in two tautomeric forms (carboxylate and phenolate) that have different electronic structure and optical properties[22,23]. Both anionic GFP and PYP (phenolate) chromophores can be represented by the two interacting resonance structures leading the bond-order scrambling and allylic-like molecular orbitals (MOs) spanning the bridge region[21]. The character of the bright state in both chromophores (phenolate PYP isomer) is remarkably similar and can be described as a $\pi \rightarrow \pi^*$ transition between the (allylic-like) HOMO and LUMO[21]. The gas-phase calculations of the model PYP (phenolate and carboxylate isomers)[4,22,24] and GFP[25,26] chromophores have revealed the resonance (i.e., metastable with respect to electron-detachment and dissociation) character of the first bright excited state. In both chromophores, the lowest bright state is above electron detachment continuum; however, the type of resonance is different. In the case of $HBDI^-$[25] and the phenolate

isomer of pCA^- [22], the $\pi \rightarrow \pi^*$ state is above the state of the neutral derived by removing the electron from the π orbital (HOMO of the anion) — this type of resonance is called a shape resonance. In the carboxylate isomer of pCA^-[22], the excited state is a Feshbach resonance, as it is located above the continuum corresponding to the ionization from a lone-pair orbital and is, therefore, uncoupled (in the Koopmans picture) from the continuum (see[22] for details).

The gas-phase experiments investigated the properties of isolated model PYP[27–30] and GFP[31–34] chromophores. The properties of the chromophores in solutions have also been characterized[35–45]. Rocha-Rinza *et al.* have studied photo-absorption of the methylated pCA^- phenolate and carboxylate isomers using gas-phase action spectroscopy. They reported almost identical spectra for both isomers, in contradiction to the theoretical results[22,23,29] that predict higher excitation and detachment energies for the carboxylate species.

In general, protein environment can significantly alter both geometry and electronic structure of the chromophore group. In the case of GFP and PYP, however, the protein appears to have a very small net effect on the absorption maximum, as demonstrated the action spectroscopy studies[27,29,33] and high-level calculations[46–48]. Experimentally, it has been shown[7] (for PYP) that the presence of Glu46 H-bonded to the chromophore blue-shifts the absorption maximum by about 0.3 eV. The thioester covalent linkage between the protein and the chromophore, on the other hand, red-shifts the absorption maximum, as was demonstrated by mutation studies[9]. The electronic structure calculations tell the same story — the overall small effect on the absorption is due cancellation of (somewhat larger) shifts induced by individual interactions[48]. Thus, it is interesting to investigate how hydrogen-bonding affects the absorption spectrum of the bare chromophore.

The effects of H-bonding on electronic structure of the chromophores were studied by both theory[49] and experiment[50]. Rajput *et al.* have analyzed the influence of H-bonding in microhydrated pCA^- clusters on the spectral tuning of the PYP chromophore[50] employing same action spectroscopy coupled with ion-storage ring and electrospray setup as in their studies of the isolated species[27–29]. They observed that the carboxylate isomer prefers to cluster with one water molecule, whereas the phenolate attaches two water molecules[50]. The photoabsorption maximum of the dihydrated phenolate chromophore showed an unusually large blue shift of 0.71 eV with respect to the bare chromophore. Upon excitation, the system was reported to decay via detachment of the water molecules, in contrast to the relaxation of the bare chromophore via electron detachment or dissociation[29].

Several theoretical studies investigated the effect of the environment on the chromophores' properties. Gromov *et al.* have thoroughly studied the effects of the protein[4] and hydrogen-bonding interactions[49]. Owing to the anionic nature of the chromophore and partial charge-transfer character of the $\pi \rightarrow \pi^*$ transition, the influence of environment is expected to be pronounced. The key results obtained by Gromov *et al.* are electrostatic stabilization by Arg52 against autodetachment and spectral shifts due to the H-bonding with Tyr42 and Glu46[4]. In contrast to the isolated anion, the first excited state was found to be stable with respect to autoionization. The same result in the hybrid QM/MM calculations of the protein-bound chromophore[51]. Thus, the protein environment converts the exited states into the bound electronic states[4,51]. The stabilizing effect of the protein environment has been also reported for the GFP chromophore whose detachment energy increases in the protein by approximately 2.2 eV [47].

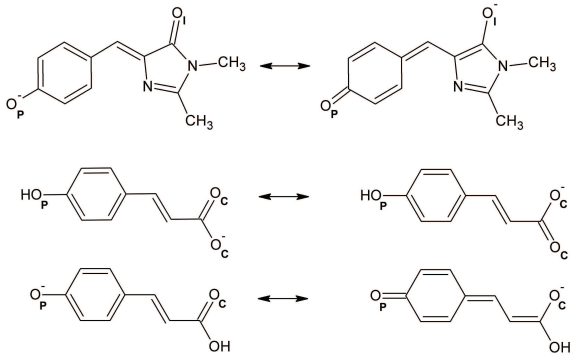

Figure 3.1: Model chromophores and hydration sites. From top to bottom: HBDI$^-$, pCA$^-$ carboxylate (PYPa), pCA$^-$ phenolate (PYPb). Microhydrated structures are labeled according to the hydration centers (P or I for HBDI$^-$, and P or C for pCA$^-$)

In this work, we investigate the effect of microhydration on the relative energy of the excited and ionized states of the pCA$^-$ and HBDI$^-$ chromophores, in order to understand how the solvation and the hydrogen bonds formed in the protein environment affect the spectral properties of the chromophore. The structures of the model chromophores are shown in Fig. 3.1. We employ high-level electronic structure methods to quantify the effect of adding of one and two water molecules to these model systems and analyze the structural and spectral changes induced by microhydration.

3.2 Computational details

The model systems used to represent the PYP and GFP chromophores with two sites of hydration are shown in Fig. 3.1. The geometry of HBDI$^-$ was optimized with density functional theory (DFT) using the ωB97X-D long-range and dispersion-corrected hybrid density functional[52] that includes long-range Hartree–Fock exchange mitigating the notorious self-interaction error. The 6-31+G(d,p) basis set has been used for these calculations. For HBDI$^-$, the average deviation of the computed bond lengths

from the structure[26] optimized using a larger basis set (cc-pVTZ) is around 0.005 Å. Both isomers of pCA^- were optimized with resolution of identity Møller-Plesset perturbation theory (RIMP2)[53–56] with the aug-cc-pVDZ basis set[57]. The cyclic pCA^- isomers (Fig. 3.2) were optimized with ωB97X-D/aug-cc-pVDZ. The following convergence thresholds were used in the optimization procedure: 1×10^{-6} hartree for the energy, 1×10^{-4} hartree/Å for the energy gradient, and 1.2×10^{-3} Å for displacements. All microhydrated pCA^- structures have C_s symmetry except PYPa-W_C, PYPa-W_CW_P and the cyclic isomers. All $HBDI^-$ structures are non-planar and have C_1 symmetry.

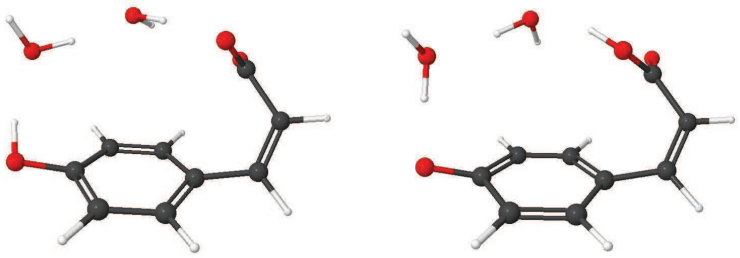

Figure 3.2: Structures of the microhydrated pCA^- cyclic isomers. Left: Cyclic isomer of PYPa (D_e = 1.38 eV). Right: Cyclic isomer of PYPb (D_e = 0.68 eV).

Binding energies (D_e) of different microsolvated isomers were computed with ωB97X-D/6-311++G(2df,2pd)[58] and with RIMP2/aug-cc-pVDZ for the GFP and PYP chromophores respectively, as the differences between the ground-state energies of the microsolvated molecule and the dissociation products. The grid used in all DFT calculations contained 75 points in the Lebedev[59] radial grid and 302 points in the Euler-Maclaurin[60] angular grid.

Vertical excitation energies for pCA^- were computed using equation-of-motion coupled-cluster method with singles and doubles (EOM-CCSD) for excitation energies (EOM-EE-CCSD)[61–64] with the 6-31+G(d,p) basis set; for the lower-symmetry cyclic isomers we used 6-31+G(d). Previous benchmark calculations[22] for the bare

chromophore have shown relatively minor basis set dependence of excitation energies, e.g., increasing the basis beyond a polarized double zeta basis affects the transition energies of the lowest excited states by 0.1-0.2 eV. Moreover, these errors are systematic, and are expected to cancel out when solvent-induced shifts are computed[65].

Vertical detachment energies were computed by EOM-CCSD for ionization potentials (EOM-IP-CCSD)[66–68] with the 6-311+G(df,pd) basis; for the cyclic isomers we used 6-31+G(d,p). Calculations of the ionization energies of uracil[69] by EOM-IP-CCSD with various bases show that typical error bars in IEs computed with these basis sets are about 0.2 eV.

EOM-CC methods[64] provide accurate and balanced treatment of dynamical and static correlation energy, accurately reproducing excited and ionized states properties. In these calculations, we employ well-behaved closed-shell reference states, thus, the target excited and ionized states are not affected by spin-contamination. The anticipated error bars for these methods are 0.1–0.3 eV[22,69–71].

Excitation energies for all microsolvated $HBDI^-$ have been calculated with SOS-CIS(D)[72], scaled opposite spin configuration interaction singles with the second-order perturbative doubles correction, and the cc-pVTZ basis set. This method has been shown to give accurate results for the excitation energies of the isolated and protein-bound anionic GFP chromophore[25,47]. Detachment energies were calculated with ωB97X-D/6-311++G(2df,2pd). These detachment energies were corrected by using energy additivity scheme based on the EOM-IP-CCSD/6-311(2+,+)G(2df,2pd) extrapolated value for the bare chromophore from Ref. 25:

$$DE_{hydrated,corrected} = DE_{bare,corrected} + DE_{hydrated,DFT} - DE_{bare,DFT},$$

where $DE_{bare,corrected}$ is the best estimate of the detachment energy of bare $HBDI^-$ calculated by ωB97X-D/6-311++G(2df,2pd) and corrected by the DFT/EOM-IP-CCSD difference computed in a smaller basis set[25].

We also performed benchmark calculations (for $HBDI^-$) to quantify the dependence of excitation energies on the general and auxiliary basis used in the SOS-CIS(D)[72] calculations. The results are given in Supporting Materials for Ref. 73. All calculations were performed with Q-Chem[74].

3.3 Results and discussion

3.3.1 Optimized structures and binding energies of the mono- and dihydrated chromophores

The equilibrium structures of the bare [22,25] and monohydrated chromophores are shown in Fig. 3.3. The effect of microsolvation on the structure is relatively small, e.g. the magnitude of the changes in bond lengths is about 0.01 Å. The effect is larger for $HBDI^-$. This is because it is more symmetric and the two resonance configurations[26] contribute almost equally to the chromophore structure leading to more allylic character of the bridge relative to pCA^-[22] (Fig. 3.1). The water molecules stabilize one resonance structure more than another, which changes the bond lengths patterns and reduces the allylic character. Likewise, the phenolate form of pCA^- has more allylic character[22] than the carboxylate, which results in a more pronounced geometry changes due to microhydration.

The microhydrated clusters and corresponding binding energies are shown in Figs. 3.7–3.2. The lowest-energy monohydrate of PYPa is PYPa-W_C in which water forms two hydrogen bonds with the carboxy oxygens making this structure more stable.

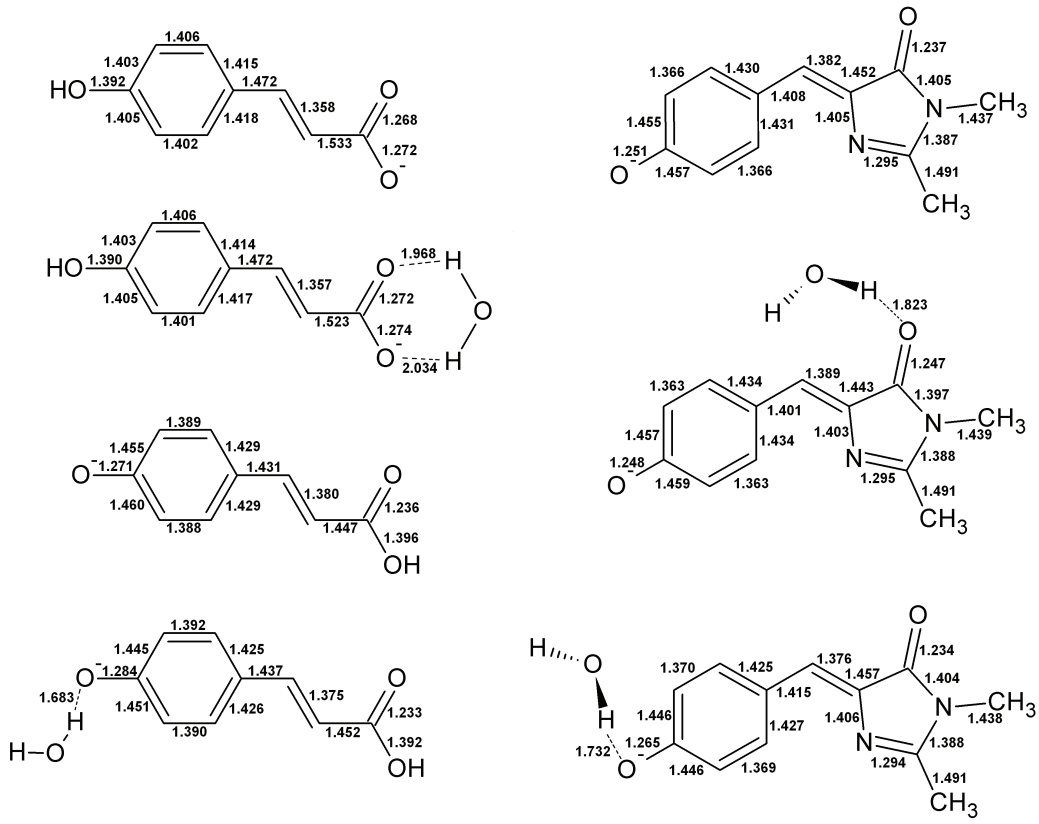

Figure 3.3: Equilibrium structures of pCA$^-$ (left column), HBDI$^-$ (right column) and their monohydrates.

The phenolate isomer, PYPb-W$_P$, has two energetically equivalent structures that have slightly higher binding energy than PYPa-W$_C$. We found that PYPb-W$_P$W$_{P2}$ (Fig. 3.8) isomer is slightly lower in energy (by 0.03 eV) than PYPb-W$_P$W$_{P1}$ suggested to be the most stable structure in Ref. 50. In the former case, the two water molecules form a weak hydrogen bond with each other, which results in additional stabilization. We also found several cyclic dihydrated isomers (Fig. 3.2). PYPa-cyclic is slightly higher in energy than the lowest PYPa dihydrate, PYPa-W_CW_C (by 0.03-0.04 eV), whereas PYPb-cyclic is significantly less stable than PYPb-W$_P$W$_{P2}$ (by about 0.5 eV). The cyclic isomers might play an important role in the pCA$^-$ isomerization by proton transfer via water

chain. Since PYPa is more stable in solution whereas PYPb is more stable in the gas phase, such a pathway may be responsible for the isomerization upon introducing pCA^- into gas phase by electrospray.

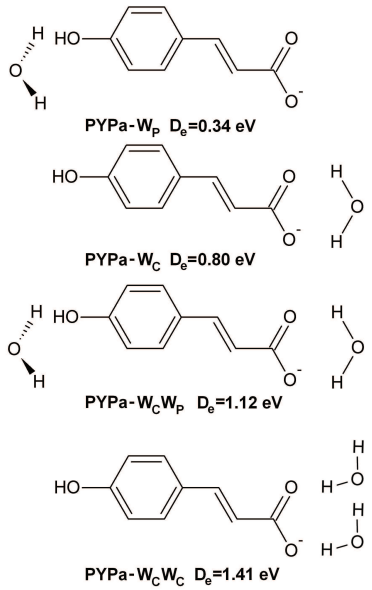

Figure 3.4: Structures and binding energies (D_e, eV) of microsolvated model systems of the pCA^- (PYPa, carboxylate) chromophore.

We observe that binding energies are nearly additive for all microhydrated systems, except cyclic isomers. The energy required to detach all water molecules is approximately equal to the sum of the energies required to detach each water molecule (the deviations are very small), as illustrated in Fig. 3.5. This suggests that the interaction energy between water molecules is negligible in comparison to the interaction energy between the chromophore and water. However, we expect higher non-additive contributions to interaction energy in larger systems, in which the polarization effects giving rise to three-body interactions are more pronounced (see, for example, Ref. 65).

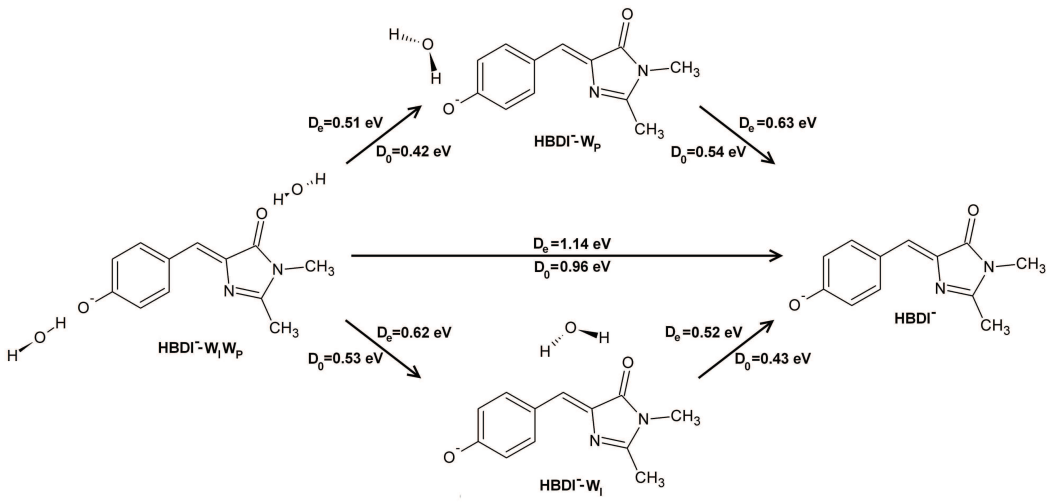

Figure 3.5: Binding energies (D_e, eV) of the $HBDI^-$-water complexes.

3.3.2 Electronically excited and ionized states of microhydrated pCA^-

Previous excitation and detachment energy calculations for the bare PYP and GFP chromophores[4,22,24–26,75] show that the excited states are above the detachment continuum. Such resonance states are common in molecular anions[26,76]. In the protein environment, the excited state is stable with respect to autoionization, thus the environment plays an important role in stabilizing the anionic species[47,75].

Table 3.1: Vertical excitation energies (eV), oscillator strengths (f_l, in parenthesis) and detachment energies (eV) of the microhydrated pCA^-. Excitation energies and transition dipole moments were computed by EOM-EE-CCSD/6-31+G(d,p) and EOM-EE-CCSD/6-31+G(d), respectively, ionization energies — by EOM-IP-CCSD/6-311+G(df,pd).

System	Excitation energy		Detachment energy
	$\pi \rightarrow \pi_1^*$	$\pi \rightarrow \pi_2^*$	
PYPa [22]	4.50 (0.03)	4.89 (0.019)	3.91
PYPa-W_C	4.47 (0.03)	5.13 (0.26)	4.72
PYPa-$W_C W_C$	4.49 (0.03)	5.21 (0.58)	5.10
PYPa-cyclic[a]	4.79	5.58	4.29
PYPb [22]	3.19 (1.06)	4.23(0.10)	2.92
PYPb-W_C	3.12 (1.11)	4.27 (0.09)	3.06
PYPb-W_{P1}	3.25 (1.01)	4.32 (0.08)	3.29
PYPb-$W_C W_P$	3.20 (1.07)	4.34 (0.07)	3.37
PYPb-$W_P W_{P1}$	3.38 (0.98)	4.41 (0.06)	3.63
PYPb-$W_P W_{P2}$	3.37 (1.01)	4.34 (0.07)	3.72
PYPb-cyclic[a]	3.78 (0.26)	3.99 (0.13)	2.97

[a] excitation and detachment energies for the cyclic isomers were calculated by EOM-EE-CCSD/6-31+G(d) and EOM-IP-CCSD/6-31+G(d,p).

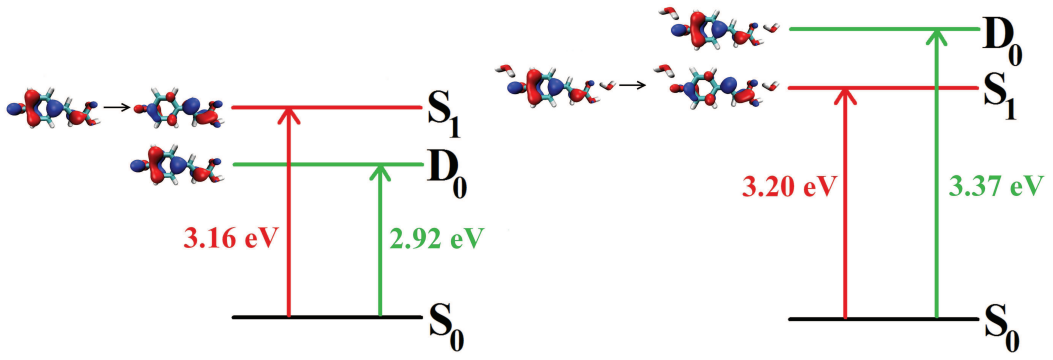

Figure 3.6: Electronically excited and ionized states in PYPb and PYPb-$W_C W_P$.

Vertical excitation and detachment energy calculations for microhydrated pCA^- are given in Table 3.1. The calculations show that in most cases microhydration has a minor effect on the excitation energies (about 0.1-0.3 eV), whereas the detachment energies change dramatically (up to 1.2 eV). The water molecules stabilize both ground and excited states of the anionic chromophore by a similar value, which results in the mutual cancellation and an overall small change in the excitation energy. Interestingly, the cyclic forms of pCA^- show more pronounced effect of microhydration on the excitation energies (≈0.3-0.6 eV), whereas detachment energy changes less. Large shifts of excitation energy in this case are due to distortion of the planar π-conjugated system of the chromophore. For almost all the structures (except PYPb-W_C and all cyclic forms of pCA^-, Table 3.1), the microhydration converts the first excited state to a bound state (see Fig. 3.6). The same effect was reported for the deprotonated para-coumaric methyl thioester ($pCTMe^-$) — upon hydration of this species by two water molecules, detachment energy increases by 0.7 eV, which is sufficient to stabilize the resonance[75]. Gromov *et al.* emphasizes[4] that in the case of the native PYP chromophore hydrogen bonding plays a similar role, however, the dominant stabilization effects are due to the positively charged Arg52 residue that acts as a counter-ion leading the detachment

energy increase by several eV[4]. Similar conclusions have been derived from a recent computational study of GFP[47]. The effects of hydrogen bonding in PYP were reported[4] to be most prominent for the states that are less affected by the Arg52 residue. Our results for excitation energies show blue shifts of 0.1-0.2 eV, which is consistent with the results of Gromov *et al.*[4], but is in contradiction with the experimentally reported shifts of 0.71 eV for a dihydrated pCA^-. Interestingly, PYPb-cyclic shows the shift in excitation energy of 0.6 eV, which is close to the experimental observation.

Table 3.2: Vertical excitation and detachment energies (eV) of the microhydrated deprotonated HBDI. Excitation energies were computed by SOS-CIS(D)/cc-pVTZ, detachment energies — by ωB97X-D/6-311++G(2df,2pd).

System	Excitation energy		Detachment energy	
	$\pi \rightarrow \pi_1^*$	$\pi \rightarrow \pi_2^*$	DFT	corrected
$HBDI^-$	2.61	4.38	2.66	2.45
$HBDI^-$-W_I	2.59	4.50	3.07	2.86
$HBDI^-$-W_P	2.64	4.34	3.13	2.92
$HBDI^-$-W_IW_P	2.59	4.40	3.34	3.13
$HBDI^-$-W_IW_I	2.62	4.59	3.26	3.05
$HBDI^-$-W_PW_P	2.71	4.31	3.45	3.24

The $HBDI^-$ excitation and detachment energies are collected in Table 3.2. Similarly to pCA^-, bare $HBDI^-$ features the resonance excited state[25]. The addition of water molecules raises the detachment energy more than excitation energy, thus converting the resonance into a bound state.

In sum, our results show a moderate change in excitation energies for both the GFP and PYP chromophores (around 0.1 eV). However, microsolvation does not represent the solution environment; several solvation shells are required to correctly simulate bulk

environment[65]. Interestingly, in most cases, the microhydration does not affect the transition dipole moments, which change by less than 10 %. However, the second bright transition in PYPa shows larger sensitivity — monohydration changes it by more than an order of magnitude (see Table 3.1). This can be explained by the hydration-induced changes in the wave function. The second transition in PYPa has a mixed character dominated by excitations from HOMO-1 (which is localized on the carboxylate moiety) and the HOMO (delocalized over the entire π-conjugated system). Addition of a water molecule on the carboxylate side stabilizes HOMO-1 more than the HOMO thus increasing the HOMO contribution to the second bright transition. Since the HOMO has a larger overlap with the target virtual orbital, this leads to the increase of the oscillator strength (see Supporting Materials for Ref. 73 for more details).

3.3.3 Theory versus experiment: microhydrated clusters of the PYP chromophore

Recent experimental work of Rajput *et al.*[50] on photoabsorption of microhydrated pCA^- reported interesting results on the energetics of H-bonding and spectral tuning. It was observed that the phenolate primarily binds two water molecules, whereas the carboxylate only appears as monohydrate. However, the apparent mass distribution was affected by the experimental conditions[77]. Our theoretical results lend no support to preferential binding, i.e., the analysis of binding energies does not reveal any "magic numbers". Binding energies of single water molecule by the carboxylate (PYPa-W_C, Fig. 3.7) and the phenolate (PYPb-W_{P1} and PYPb-W_{P2}, Fig. 3.8) are comparable (difference is about 0.18 eV), therefore, the formation of a stable hydrogen bond is anticipated in both cases. The binding energy of the dihydrated carboxylate (PYPa-W_CW_C) is even higher than for the phenolate (PYPb-W_PW_{P2}), therefore, one would except to

observe the formation of monohydrates and dihydrates in both phenolate and carboxylate species. A possible explanation might be due to the potential role of cyclic dihydrates in the carboxylate-phenolate isomerization. In the cyclic isomers the carboxylate and phenolate moieties are connected via a chain of H-bonds forming a perfect path for a low-barrier proton migration, and, therefore, the carboxylate-to-phenolate isomerization upon ion extraction from solution (carboxylate is the lowest energy isomer in solution, whereas in the gas phase, phenolate is more stable) may proceed through the formation of these isomers, leading to preferential formation of phenolate dihydrates. However, one can expect similar structures being formed with three and more water molecules. Thus, the origin for selectivity of binding of one (carboxylate) and two (phenolate) water molecules is likely to be due to the effects of the trap conditions on the resulting mass distribution rather than intrinsic energetics of microsolvated chromophores.

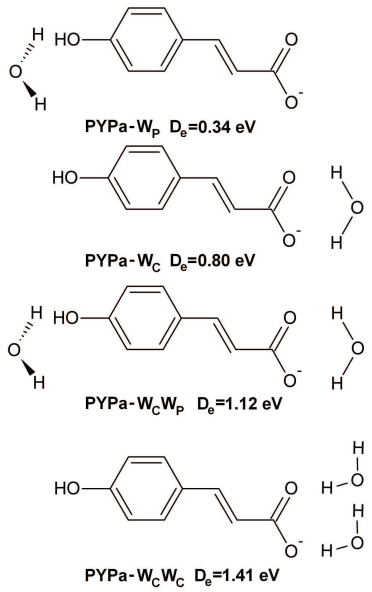

Figure 3.7: Structures and binding energies (D_e, eV) of microsolvated model systems of the pCA^- (PYPa, carboxylate) chromophore.

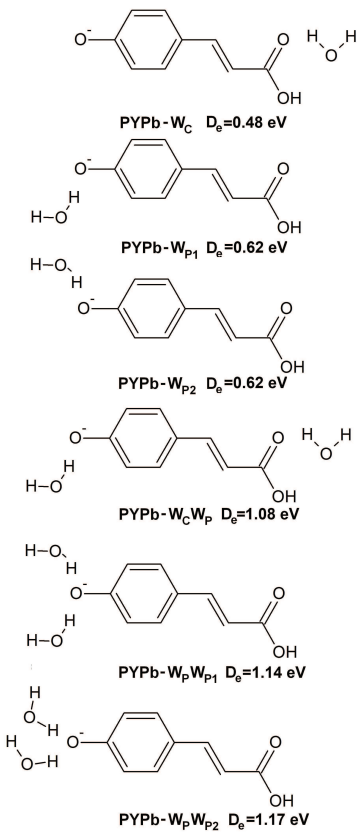

Figure 3.8: Structures and binding energies (D_e, eV) of microsolvated model systems of the pCA^- (PYPb, phenolate) chromophore.

The reported[50] photoabsorption maximum of the dihydrated chromophore had an unusually large blue shift of 0.71 eV with respect to the bare chromophore. Our results show much smaller shift (0.1-0.2 eV) for the proposed PYPb-W$_P$W$_{P1}$ isomer, in agreement with Gromov *et al.*[4]. The PYPb-cyclic isomer shows large blue shift (0.6 eV), which is close to the experimental one. The absolute values of calculated excitation energies are systematically higher (by about 0.3 eV[22]); however, we expect much better accuracy for the excitation energy shifts due to error cancellation. Therefore, the experimental absorption maximum could be explained by assuming a strongly non-Boltzmann population of different isomers in the electrospray-generated sample. However, even

under non-equilibrium conditions it is not clear why the signal from the lowest-energy PYPb-$W_P W_{P1}$ isomer that should appear 0.2 eV blue-shifted with respect to the bare chromophore is missing in the action spectrum.

Upon excitation, the dihydrate was reported[50] to decay via the detachment of the water molecules, in contrast to the bare chromophore, which undergoes electron detachment or dissociation[29]. Our calculations confirm that, as expected, the energy of water binding is smaller than the energy for breaking covalent bonds in the molecule or electron detachment, and that this energy provides sufficient relaxation for the energetic chromophore to drop below the fragmentation/detachment onset. This holds for all isomers (see Figs. 3.7 - 3.2 for water binding energies, and Ref. 22 for the dissociation and detachment energies of pCA^-). The possible explanation for missing electron-detachment channel in microhydrated pCA^- is stabilization of the resonance excited state with respect to the continuum that shuts down autoionization and relatively low cross-sections from direct detachment relative to electron-excitation transitions.

Despite the detailed characterization of electronic structure of excited and electron-detached state of the microhydrated PYP chromophores, the experimental data by Rajput *et al.*[50] cannot be fully understood on the basis of the present theoretical results. More theoretical and isomer-specific experimental studies are necessary to explain the observed mass distribution of microhydrates and the origin of the 0.7 eV shift in the observed absorption maximum of dihydrated PYPb, as well as the absence of the direct detachment channel, which is energetically allowed for most of the pCA^- phenolate microhydrated clusters.

3.4 Conclusions

We performed comprehensive calculations of mono- and dihydrated clusters of the model GFP and PYP chromophores in their anionic states (deprotonated HBDI and pCA). We do not observe significant three-body effects in the binding energies of the dihydrated species. The lowest energy isomers of the microhydrated species feature nearly unperturbed chromophores hydrated at the obvious CO sites that host excess negative charge (phenolate, imidazolinone, carboxylate). In these isomers, the microhydration has small effect on the excitation energies (blue shifts of 0.1-0.2 eV), however, it increases VDE by 0.2-1.2 eV, which reverses the relative order of the excited and ionized states. Thus, these isomers cannot explain experimentally observed large blue shifts in excitation energies.

We have identified several unusual isomers of dihydrated pCA^- in which the chromophore is highly distorted and water molecules form a bridge between the carboxylate and phenolate moiety. We expect that these isomers may play a role in the carboxylate-phenolate isomerization of pCA^-. These isomers feature small changes in the electron detachment energies, but a large (0.6 eV) blue shifts in the excitation energies, which is close to the experimentally observed shift of 0.7 eV[50].

3.5 Chapter 3 references

[1] U.K. Genick, S.M. Soltis, P. Kuhn, I.L. Canestrelli, and E.D. Getzoff. Structure at 0.85 Å resolution of an early protein photocycle intermediate. *Nature*, 392:206–209, 1998.

[2] R. Moukhametzianov, J.P. Klare, R. Efremov, C. Baeken, A. Göppner, J. Labahn, M. Engelhard, G. Büldt, and V.I. Gordeliy. Development of the signal in sensory rhodopsin and its transfer to the cognate transducer. *Nature*, 440:115–119, 2006.

[3] E. V. Gromov, I. Burghardt, H. Köppel, and L. S. Cederbaum. Impact of sulfur vs oxygen on the low-lying excited state of trans-p-coumaric acid and trans-p-coumaric thio acid. *J. Phys. Chem. A*, 109:4623–4631, 2005.

[4] E. V. Gromov, I. Burghardt, H. Köppel, and L. S. Cederbaum. Electronic structure of the PYP chromophore in its native protein environment. *J. Am. Chem. Soc.*, 129:6798–6806, 2007.

[5] P. Changenet-Barret, P. Plaza, M.M. Matrin, H.Chosrowjan, S. Taniguchi, N. Mataga, Y. Imamoto, and M. Kataoka. Structural effects on the ultrafast photoisomerization of photoactive yellow protein. Transient absorption spectroscopy of two point mutants. *J. Phys. Chem. C*, 113:11605–11613, 2009.

[6] K. Mihara, O. Hisatomi, Y. Imamoto, M. Kataoka, and F. Tokunaga. Functional expression and site-directed mutagenesis of photoactive yellow protein. *Biochem. J.*, 121:876–880, 1997.

[7] A. Philip, K. Eisenman, G. Papadantonakis, and W. Hoff. Functional tuning of photoactive yellow protein by active site residue. *Biochemistry*, 47:13800–13810, 2008.

[8] J. Sniegowski, M. Phail, and R. Wachter. Maturation efficiency, trypsin sensitivity, and optical properties of Arg96, Glu222, and Gly67 variants of green fluorescent protein. *Biochem. Biophys. Res. Commun*, 332:657–663, 2005.

[9] M.A. van der Horst, J.C. Arents, R. Kort, and K.J. Hellingwerf. Binding, tuning and mechanical function of the 4-hydroxy-cinnamic acid chromophore in photoactive yellow protein. *Photochem. and Photobiol. Sci.*, 6:571–579, 2007.

[10] G. Jung, J. Wiehler, and A.Zumbusch. The photophysics of green fluorescent protein: Influence of the key amino acids at positions 65, 203, and 222. *Biophys. J.*, 88:1932–1947, 2005.

[11] T.E. Meyer. Isolation and characterization of soluble cytochromes, ferredoxins and other chromophoric proteins from the halophilic phototrophic bacterium ectothiorhodospira halophila. *Biochem. and Biophys. J.*, 806:175–183, 1985.

[12] T.E. Meyer, E. Yakali, M.A. Cusanovich, and G. Tollint. Properties of a water-soluble, yellow protein isolated from a halophilic phototrophic bacterium that has photochemical activity analogous to sensory rhodopsin. *Biochem. J.*, 26:418–423, 1987.

[13] W.W. Sprenger, W.D. Hoff, J.P. Armitage, and K.J. Hellingwer. The eubacterium ectothiorhodospira halophila is negatively phototactic, with a wavelength dependence that fits the absorption spectrum of the photoactive yellow protein. *J. of Bacteriology*, 175:3096–3104, 1993.

[14] A.A. Pakhomov and V.I. Martynov. GFP: structural insights into spectral tuning. *Chem. Biol.*, 15:755–764, 2008.

[15] M. Hoffmann, M. Wanko, P.Strodel, P.H. König, T. Frauenhrim, K.Schulten, W. Thiel, E. Tajkorshid, and M. Elstner. Color tuning in rhodopsins: The mechanism for the spectral shift between bacteriorhodopsin and sensory rhodopsin II. *J. Am. Chem. Soc.*, 128:10808–10818, 2006.

[16] O. Shimomura, F. Johnson, and Y. Saiga. Extraction, purification and properties of aequorin, a bioluminescent protein from the luminous hydromedusan, aequorea. *J. Cell. Comp. Physiol.*, 59:223–239, 1962.

[17] R. Heim, D.C. Prasher, and R.Y. Tsien. The green fluorescent protein. *Proc. Nat. Acad. Sci.*, 91:12501, 1994.

[18] M. Zimmer. Green fluorescent protein (GFP): Applications, structure, and related photophysical behavior. *Chem. Rev.*, 102:759–781, 2002.

[19] Y. Wang, J.Y.-J. Shyy, and S. Chien. Fluorescence proteins, live-cell imaging, and mechanobiology: Seeing is believing. *Ann. Rev. Biomed. Eng.*, 10:1–38, 2008.

[20] O.V. Stepanenko, V.V. Verkhusha, I.M. Kuznetsova, V.N. Uversky, and K.K. Turoverov. *Curr. Protein Pept. Sci.*, 9:338, 2008.

[21] K. Bravaya, B.L. Grigorenko, A.V. Nemukhin, and A.I. Krylov. Quantum chemistry behind bioimaging: Insights from ab initio studies of fluorescent proteins and their chromophores. *Acc. Chem. Res.*, 45:265–275, 2012.

[22] D. Zuev, K.B. Bravaya, T.D. Crawford, R. Lindh, and A.I. Krylov. Electronic structure of the two isomers of the anionic form of p-coumaric acid chromophore. *J. Chem. Phys.*, 134:034310, 2011.

[23] Y. Ma, M. Rohlfing, and C. Molteni. Modeling the excited states of biological chromophores with many-body Green's function theory. *J. Chem. Theory Comput.*, 6:257–265, 2010.

[24] Z. He, C. H. Martin, R. Birge, and K.F. Freed. Theoretical studies on excited states of a phenolate anion in the environment of the photoactive yellow protein. *J. Phys. Chem. A*, 104:2939–2952, 2000.

[25] E. Epifanovsky, I. Polyakov, B.L. Grigorenko, A.V. Nemukhin, and A.I. Krylov. Quantum chemical benchmark studies of the electronic properties of the green fluorescent protein chromophore: I. Electronically excited and ionized states of the anionic chromophore in the gas phase. *J. Chem. Theory Comput.*, 5:1895–1906, 2009.

[26] E. Epifanovsky, I. Polyakov, B.L. Grigorenko, A.V. Nemukhin, and A.I. Krylov. The effect of oxidation on the electronic structure of the green fluorescent protein chromophore. *J. Chem. Phys.*, 132:115104, 2010.

[27] I.B. Nielsen, S. Boye-Peronne, M.O.A. El Ghazaly, M.B. Kristensen, S.B. Nielsen, and L.H. Andersen. Absorption spectra of photoactive yellow protein chromophores in vacuum. *Biophys. J.*, 89:2597–2604, 2005.

[28] L. Lammich, J. Rajput, and L.H. Andersen. Photodissociation pathways of gas-phase photoactive yellow protein chromophores. *Phys. Rev. E*, 78:051916, 2008.

[29] T. Rocha-Rinza, O. Christiansen, J. Rajput, A. Gopalan, D.B. Rahbek, L.H. Andersen, A.V. Bochenkova, A.A.Granovsky, K.B. Bravaya, A.V. Nemukhin, K.L. Christiansen, and M.B. Nielsen. Gas phase absorption studies of photoactive yellow protein chromophore derivatives. *J. Phys. Chem. A*, 113:9442–9449, 2009.

[30] I-R. Lee, W. Lee, and A H. Zewail. Primary steps of the photoactive yellow protein: Isolated chromophore dynamics and protein directed function. *Proc. Nat. Acad. Sci.*, 103:258–262, 2006.

[31] M.W. Forbes and R.A. Jockusch. Deactivation pathways of an isolated green fluorescent protein model chromophore studied by electronic action spectroscopy. *J. Am. Chem. Soc.*, 131:17038–17039, 2009.

[32] S.B. Nielsen, A. Lapierre, J.U. Andersen, U.V. Pedersen, S. Tomita, and L.H. Andersen. Absorption spectrum of the green fluorescent protein chromophore anion *in vacuo*. *Phys. Rev. Lett.*, 87:228102, 2001.

[33] L.H. Andersen, A. Lappierre, S.B. Nielsen, I.B. Nielsen, S.U. Pedersen, U.V. Pedersen, and S. Tomita. Chromophores of the green fluorescent protein studied in the gas phase. *Eur. Phys. J. D*, 20:597–600, 2002.

[34] K. Chingin, R.M. Balabin, V. Frankevich, K. Barylyuk, R. Nieckarz, P. Sagulenko, and R. Zenobi. Absorption of the green fluorescent protein chromophore anion in the gas phase studied by a combination of FTICR mass spectrometry withlaser-induced photodissociation spectroscopy. *Int. J. Mass Spectrom.*, 306:241–245, 2011.

[35] K.M. Solntsev, O. Poizat, J. Dong, J. Rehault, Y. Lou, C. Burda, and L.M. Tolbert. Meta and para effects in the ultrafast excited-state dynamics of the green fluorescent protein chromophores. *J. Phys. Chem. B*, 112:2700–2711, 2008.

[36] J. Dong, F. Abulwerdi, A. Baldridge, J. Kowalik, K.M. Solntsev, and L.M. Tolbert. Isomerization in fluorescent protein chromophores involves addition/elimination. *J. Am. Chem. Soc.*, 130:14096–14098, 2008.

[37] J.-S. Yang, G.-J. Huang, Yi-H. Liu, and S.-M. Peng. Photoisomerization of the green fluorescence protein chromophore and the meta- and para-amino analogues. *Chem. Commun.*, pages 1344–1346, 2008.

[38] M. Vengris, I.H.M. van Stokkum, X. He, A.F. Bell, P. Tonge, R. van Grondelle, and D.S. Larsen. Ultrafast excited and ground-state dynamics of the green fluorescent protein chromophore in solution. *J. Phys. Chem. A*, 108:4587–4598, 2004.

[39] L.M. Tolbert, A. Baldridge, J. Kowalik, and K.M. Solntsev. Collapse and recovery of green fluorescent protein chromophore emission through topological effects. *Acc. Chem. Res.*, 45:171–181, 2012.

[40] K.M. Solntsev, D. Ghosh, A. Amador, M. Josowicz, and A.I. Krylov. What drives the redox properties of model green fluorescence protein chromophores? *J. Phys. Chem. Lett.*, 2:2593–2597, 2011.

[41] P. Changenet-Barret, P. Plaza, and M.M. Martin. Primary events in the photoactive yellow protein chromophore in solution. *Chem. Phys. Lett.*, 336:439–444, 2001.

[42] D.S. Larsen, M. Vengris, I.H.M. van Stokkum, M.A. van der Horst, R.A. Cordfunke, K.J. Hellingwerf, and R. van Grondelle. Initial photo-induced dynamics of the photoactive yellow protein chromophore in solution. *Chem. Phys. Lett.*, 369:563–569, 2003.

[43] D.S. Larsen, M. Vengris, I.H.M. van Stokkum, M.A. van der Horst, F.L. de Weerd, K.J. Hellingwerf, and R. van Grondelle. Photoisomerization and photoionization of the photoactive yellow protein chromophore in solution. *Biophys. J.*, 86:2538–2550, 2004.

[44] A. Espagne, P. Changenet-Barret, P. Plaza, and M.M. Martin. Solvent effect on the excited-state dynamics of analogues of the photoactive yellow protein chromophore. *J. Phys. Chem. A*, 110:3393–3404, 2006.

[45] A. Espagne, P. Changenet-Barret, J.-B. Baudina, P. Plaza, and M.M. Martin. Photoinduced charge shift as the driving force for the excited-state relaxation of analogues of the photoactive yellow protein chromophore in solution. *J. Photochem. Photobiol. A*, 185:245–252, 2007.

[46] A. Sinicropi, T. Anduniow, N. Ferre, R. Basosi, and M. Olivucci. Properties of the emitting state of the green fluorescent protein resolved at the CASPT2//CASSCF/CHARMM level. *J. Am. Chem. Soc.*, 127:11534–11535, 2005.

[47] K. Bravaya, M.G. Khrenova, B.L. Grigorenko, A.V. Nemukhin, and A.I. Krylov. The effect of protein environment on electronically excited and ionized states of the green fluorescent protein chromophore. *J. Phys. Chem. B*, 8:8296–8303, 2011.

[48] T. Rocha-Rinza, K. Sneskov, O. Christiansen, U. Ryde, and J.I. Kongsted. Unraveling the similarity of the photoabsorption of deprotonated p-coumaric acid in the gas phase and within the photoactive yellow protein. *Phys. Chem. Chem. Phys.*, 13:1585–1589, 2011.

[49] M. de Groot, E.V. Gromov, H. Köppel, and W.J. Buma. High-resolution spectroscopy of methyl 4-hydroxycinnamate and its hydrogen-bonded water complex. *J. Phys. Chem. B*, 112:4427–4434, 2008.

[50] J. Rajput, D.B. Rahbek, G. Aravind, and L.H. Andersen. Spectral tuning of the photoactive yellow protein chromophore by h-bonding. *Biophys. J.*, 98:488–492, 2010.

[51] E.M. Gonzalez, L. Guidonib, and C. Molteni. Chemical and protein shifts in the spectrum of the photoactive yellow protein: a time-dependent density functional theory/molecular mechanics study. *Phys. Chem. Chem. Phys.*, 11:4556–4563, 2009.

[52] J.-D. Chai and M. Head-Gordon. Long-range corrected hybrid density functionals with damped atom-atom dispersion interactions. *Phys. Chem. Chem. Phys.*, 10:6615–6620, 2008.

[53] M.W. Feyereisen, G. Fitzgerald, and A. Komornicki. *Chem. Phys. Lett.*, 208:359, 1993.

[54] O. Vahtras, J. Almlöf, and M.W. Feyereisen. *Chem. Phys. Lett.*, 213:514, 1993.

[55] A. Komornicki and G. Fitzgerald. *J. Chem. Phys.*, 98:1398, 1993.

[56] D.E. Bernhold and R.J. Harrison. *Chem. Phys. Lett.*, 250:477, 1996.

[57] T.H. Dunning. Gaussian basis sets for use in correlated molecular calculations. I. The atoms boron through neon and hydrogen. *J. Chem. Phys.*, 90:1007–1023, 1989.

[58] M.J. Frisch, J.A. Pople, and J.S. Binkley. Self-consistent molecular orbital methods 25. Supplementary functions for Gaussian basis sets. *J. Chem. Phys.*, 80:3265–3269, 1984.

[59] V.I. Lebedev. Values of the nodes and weights of ninth to seventeenth order Gauss-Markov quadrature formulae invariant under the octahedron group with inversion. *Zh. Vychisl. Mat. Mat. Fiz.*, 15:48–54, 1975.

[60] W.C. Murray, N.C. Handy, and G.J. Laming. Quadrature schemes for integrals of density functional theory. *Mol. Phys.*, 78:997–1014, 1993.

[61] D. Sinha, D. Mukhopadhyay, and D. Mukherjee. A note on the direct calculation of excitation-energies by quasi-degenerate MBPT and coupled-cluster theory. *Chem. Phys. Lett.*, 129:369–374, 1986.

[62] J.F. Stanton and R.J. Bartlett. The equation of motion coupled-cluster method. A systematic biorthogonal approach to molecular excitation energies, transition probabilities, and excited state properties. *J. Chem. Phys.*, 98:7029–7039, 1993.

[63] S.V. Levchenko and A.I. Krylov. Equation-of-motion spin-flip coupled-cluster model with single and double substitutions: Theory and application to cyclobutadiene. *J. Chem. Phys.*, 120(1):175–185, 2004.

[64] A.I. Krylov. Equation-of-motion coupled-cluster methods for open-shell and electronically excited species: The hitchhiker's guide to Fock space. *Annu. Rev. Phys. Chem.*, 59:433–462, 2008.

[65] D. Ghosh, O. Isayev, L.V. Slipchenko, and A.I. Krylov. The effect of solvation on vertical ionization energy of thymine: From microhydration to bulk. *J. Phys. Chem. A*, 115:6028–6038, 2011.

[66] S. Pal, M. Rittby, R.J. Bartlett, D. Sinha, and D. Mukherjee. Multireference coupled-cluster methods using an incomplete model space — application to ionization-potentials and excitation-energies of formaldehyde. *Chem. Phys. Lett.*, 137:273–278, 1987.

[67] J.F. Stanton and J. Gauss. Analytic energy derivatives for ionized states described by the equation-of-motion coupled cluster method. *J. Chem. Phys.*, 101(10):8938–8944, 1994.

[68] P.A. Pieniazek, S.A. Arnstein, S.E. Bradforth, A.I. Krylov, and C.D. Sherrill. Benchmark full configuration interaction and EOM-IP-CCSD results for prototypical charge transfer systems: Noncovalent ionized dimers. *J. Chem. Phys.*, 127:164110, 2007.

[69] A.A. Golubeva and A.I. Krylov. The effect of π-stacking and H-bonding on ionization energies of a nucleobase: Uracil dimer cation. *Phys. Chem. Chem. Phys.*, 11:1303–1311, 2009.

[70] M. Schreiber, M.R. Silva-Junior, S.P.A. Sauer, and W. Thiel. Benchmarks for electronically excited states: CASPT2, CC2, CCSD, and CC3. *J. Chem. Phys.*, 128:134110, 2008.

[71] E. Epifanovsky, K. Kowalski, P.-D. Fan, M. Valiev, S. Matsika, and A.I. Krylov. On the electronically excited states of uracil. *J. Phys. Chem. A*, 112:9983–9992, 2008.

[72] Y.M. Rhee and M. Head-Gordon. Scaled second order perturbation corrections to configuration interaction singles: efficient and reliable excitation energy methods. *J. Phys. Chem. A*, 111:5314–5326, 2007.

[73] D. Zuev, K. Bravaya, M. Makarova, and A.I. Krylov. Effect of microhydration on the electronic structure of the chromophores of the photoactive yellow and green fluorescent proteins. *J. Chem. Phys.*, 135:194304, 2011.

[74] Y. Shao, L. Fusti-Molnar, Y. Jung, J. Kussmann, C. Ochsenfeld, S. Brown, A.T.B. Gilbert, L.V. Slipchenko, S.V. Levchenko, D.P. O'Neill, R.A. Distasio Jr, R.C. Lochan, T. Wang, G.J.O. Beran, N.A. Besley, J.M. Herbert, C.Y. Lin, T. Van Voorhis, S.H. Chien, A. Sodt, R.P. Steele, V.A. Rassolov, P. Maslen, P.P. Korambath, R.D. Adamson, B. Austin, J. Baker, E.F.C. Byrd, H. Daschel, R.J. Doerksen, A. Dreuw, B.D. Dunietz, A.D. Dutoi, T.R. Furlani, S.R. Gwaltney, A. Heyden, S. Hirata, C.-P. Hsu, G.S. Kedziora, R.Z. Khalliulin, P. Klunziger, A.M. Lee, W.Z. Liang, I. Lotan, N. Nair, B. Peters, E.I. Proynov, P.A. Pieniazek, Y.M. Rhee, J. Ritchie, E. Rosta, C.D. Sherrill, A.C. Simmonett, J.E. Subotnik, H.L. Woodcock III, W. Zhang, A.T. Bell, A.K. Chakraborty, D.M. Chipman, F.J. Keil, A. Warshel, W.J. Hehre, H.F. Schaefer III, J. Kong, A.I. Krylov, P.M.W. Gill, M. Head-Gordon. Advances in methods and algorithms in a modern quantum chemistry program package. *Phys. Chem. Chem. Phys.*, 8:3172–3191, 2006.

[75] E. Gromov, I. Burghardt, J. Hynes, H. Köppel, and L. Cederbaum. Electronic structure of the photoactive yellow protein chromophore: Ab initio study of the low-lying excited singlet states. *Photochem. and Photobiol.*, 190:241–257, 2007.

[76] J. Simons. Molecular anions. *J. Phys. Chem. A*, 112:6401–6511, 2008.

[77] D. Rahbek. private communication, 2011.

Chapter 4: Complex-scaled equation-of-motion coupled-cluster method with single and double substitutions for autoionizing excited states

4.1 Introduction

Autoionizing (or electron-detaching) states are ubiquitous in physics, chemistry, biology, and technology. They are common in energetic environments such as plasmas (electric arcs, supersonic combustion, plasma displays, extremely hot flames, lightning, polar aurorae, etc), as well as processes in condensed media initiated by electron attachment to neutral closed-shell species, as in radiolysis and DNA damage by slow electrons[1,2]. Dissociative recombination via autoionizing states is important in interstellar chemistry[3,4]. A new wave of interest to autoionizing states has been stimulated by advances in new light sources and, in particular, attosecond and X-ray spectroscopies[5–9].

Electronically excited states of closed-shell anionic species are often resonances, which is relevant to the gas-phase studies of several of biochromophores, such as model chromophores of green fluorescent[10–13] and photoactive yellow[14–16] proteins.

Resonance phenomena are not limited to electron ejection processes. Generally, resonances are associated with non-stationary states of a system that has: (i) enough energy to break up into two or more subsystems; and (ii) a lifetime long enough to be characterized experimentally[17–19]. This implies that the decay process of such energetic system is long enough compared to the time scale of an observation. Other examples of resonances include radioactive nuclear decay, molecular predissociation, predesorption from surfaces, and inelastic scattering phenomena[17,19].

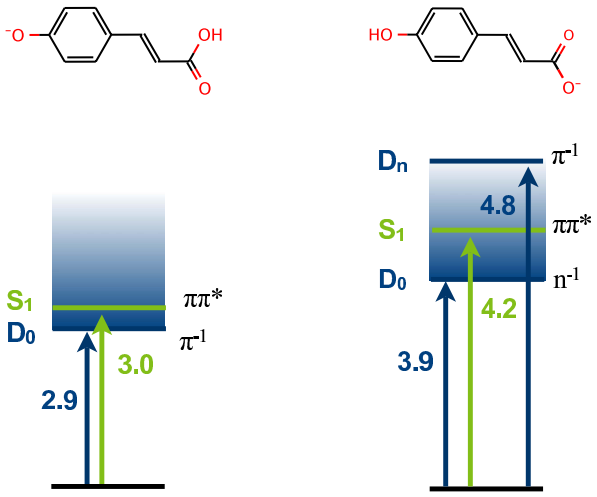

Figure 4.1: Lowest vertical excitation (S_1) and detachment energies (D_0, D_n) for model Photoactive Yellow Protein (PYP) chromophores in the phenolate (left) and carboxylate (right) isomeric forms, the energies are in eV. The character of the resonance state is different in the two isomers. In the phenolate, where electron detachment from S_1 to the lowest detachment continuum is a Koopmans-allowed one-electron transition, the excited state is a shape resonance. Carboxylate, in which the electron detachment from S_1 to D_0 is a Koopmans-forbidden two-electron process, is an example of a Feshbach resonance.

Depending on their decay mechanism, metastable states are described as shape or Feshbach resonances[a,18,19]. In the context of autoionizing (or autodetaching) electronic states, shape resonances are excited states that are above their own electron-detached states, such as the $\pi \rightarrow \pi^*$ state of the phenolate form of the PYP chromophore, which lies above electron detachment from the π orbital (Fig. 4.1, left). In this case, electron detachment is a Koopmans-allowed one-electron process. A Feshbach resonance is an excited state that is below its own continuum, but above another ionization threshold, e.g., such as the $\pi \rightarrow \pi^*$ state of the carboxylate isomer of the PYP chromophore that lies above the lowest IE (corresponding to the electron removal from a lone pair orbital), but below the detachment from the π orbital (Fig. 4.1, right). In this case, electron ejection is a Koopmans-forbidden two-electron transition and the excited-state decay is governed by electron correlation. In the present paper, we consider atomic Feshbach resonances, $(2s)^2$ states in He and H^- and $1s^22p3s$ state in Be, which are formally doubly excited states. In both cases, the decay of the resonance involves the removal of one electron and a simultaneous transition of the second electron to a lower s-orbital.

Resonances belong to the continuum spectrum and can be described either as non-stationary solutions of the time-dependent Schrödinger equation or as stationary exponentially diverging solutions of the time-independent Schrödinger equation[19,20]. Resonance wave functions obtained in the latter formalism are not L^2-integrable and cannot be represented by expansions over Gaussian basis sets. Moreover, the continuum part of the spectrum cannot be described by methods such as Davidson diagonalization formulated for discrete eigen-problems. Owing to these features, standard excited-state

[a] A shape resonance (often called an open-channel resonance) is associated with the shape of potential curve that has a barrier along the decay coordinate, such as, for example, a particle that can tunnel through a centrifugal barrier. In this case the shape of the barrier controls the lifetime of the system. Shape resonances are purely quantum-mechanical phenomena; they become bound states in the semi-classical limit as $\hbar \rightarrow 0$. Feshbach-type resonances arise due to the coupling of a bound state with the continuum via other degrees of freedom. Such resonances can be described classically.

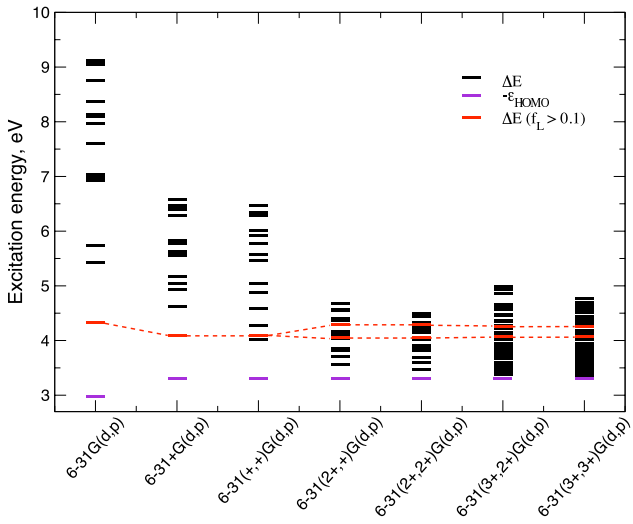

Figure 4.2: CIS calculations of the excited states of the phenolate form of the PYP chromophore. In a small basis set, which is not capable of representing continuum states, the $\pi\pi^*$ transition (shown in red) appears as an isolated eigen-state and its energy approximates the position of the resonance. As the basis set is increased, numerous pseudo-continuum states appear below the resonance, making it more and more difficult to compute sufficiently large number of states such that the resonance is also included. Moreover, the target state of interest begins to mix with pseudo-continuum states loosing its oscillator strength. In sum, standard excited-state methods are not capable of yielding converged (with respect to the basis set) positions of the auto-ionizing resonances and their lifetimes. The symmetry-decoupled Feshbach resonances, such as $\pi\pi^*$ state in the carboxylate form of PYP, are uncoupled from the continuum at the CIS level and their positions can be computed by standard approaches.

methods cannot tackle resonances, as illustrated in Fig. 4.2 which demonstrates the behavior of a shape resonance in an excited-state calculation[b]. However, energies of

[b]It can be easily shown that in a CIS calculation the onset of the ionization continuum is exactly at Koopmans ionization energy (see, for example, Ref. 13). Likewise, in time-dependent density functional calculations (when using Tamm-Dancof approximation), the continuum states converge to the Kohn-Sham orbital energies (which may differ considerably from the ΔE values of ionization energies computed using the same functional). In EOM-CC calculations of excitation energies, the continuum begins at the respective EOM-IP-CC value (EOM-CC for ionization potentials). Thus, it is straightforward to determine whether an excited state is a resonance or not at a particular level of theory when employing these methods. No similar statement can be made for multi-reference methods.

resonances can be computed by standard methods if they are decoupled from the continuum by symmetry. These symmetry-decoupled resonances are of Feshbach type and can only be coupled to the continuum by two-electron excitations. For example, an A' excited state that lies above A'' continuum (such as $\pi\pi^*$ state in the carboxylate form of PYP), is completely decoupled from the continuum at the CIS (configuration interaction singles) level. However, at the higher levels of theory, such as equation-of-motion coupled-cluster with single and double substitutions (EOM-CCSD), a weak coupling is present in the calculation.

There are three different computational strategies for resonances[18,19]. The first one is grounded in Hermitian quantum mechanics and entails using time-dependent framework[21–23], stabilization techniques[24–26], Stieltjes-Tchebycheff approach[27], or computing resonance energies as poles of scattering matrix[28]. The second approach is to impose pure outgoing boundary conditions for the standard molecular Hamiltonian[18,19]. The third strategy is based on analytic continuation of the Hamiltonian to the complex plane, e.g., via complex scaling[17,18,29–31] or complex absorbing potential (CAP)[32,33] approaches.

Following second approach, the so-called Siegert formalism, one arrives to an exponentially decaying in time eigenstate and a complex eigenvalue associated with it:

$$\psi_{res}(r,t) = \phi(r) exp(-iE_{res}t), \tag{4.1}$$

$$E_{res} = E_R - i\Gamma/2, \tag{4.2}$$

where E_R is a resonance position and Γ is a resonance width ($\Gamma = \frac{1}{\tau}$, where τ is a lifetime)[17,19,20,34]. $\phi(r)$ resembles a bound-state wave function inside interaction region (usually, some sort of a potential well), but is exponentially diverging outside. Alternatively, an identical energy expression can be derived by using a diabatic representation[35]

in which resonances are described as bound states coupled with the continuum and by applying a partitioning technique leading to a non-Hermitian effective Hamiltonian[36].

Complex scaling and CAP approaches provide a link between quantum chemistry methods developed for bound states and resonances such that the resonance wave function is obtained as a square-integrable eigen-function of a modified non-Hermitian Hamiltonian (complex-scaled or augmented by CAP). The CAP methods, in which complex potential $-i\eta\hat{W}$ devised to absorb the diverging tail of the resonance wave function is added to the Hamiltonian, were originally developed for shape resonances, and a special care should be taken when the approach is used for Feshbach resonance states[37]. Moreover, CAPs give rise to reflections, and, consequently, the eigenvalues of the modified Hamiltonian coincide with the resonance poles only in the limit of the zero CAP strength (even in the complete one-electron basis set)[38]. Several approaches for construction of reflection-free CAPs have been suggested[37–39].

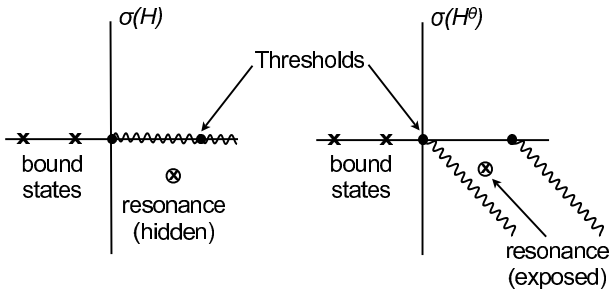

Figure 4.3: The transformation of the spectrum of the Hamiltonian upon complex-scaling of all coordinates as described by the Balslev-Combes theorem.

Complex scaling formalism[17,18,29–31] is an elegant and mathematically rigorous way to deal with the excited states embedded in the continuum (it can also be used for nuclear scattering problem). By scaling all electronic (and, in principle, nuclear) coordinates by

a complex number $e^{i\theta}$ (dilation transformation), one arrives to a non-Hermitian Hamiltonian operator that has the same discrete spectrum as the unscaled operator and whose continuum states are rotated into the complex plane by 2θ exposing the resonances, as illustrated in Fig. 4.3. Under this transformation the resonance wave function becomes L^2-integrable, provided that angle θ exceeds a critical value θ_c[19]:

$$\theta_c = atan\frac{\Gamma}{2(E_R - E_t)} \tag{4.3}$$

where E_t is the threshold, i.e., ionization or detachment energy. E_R and $-i\Gamma/2$ are real and imaginary parts of the resonance eigenvalue, according to the Siegert representation from Eq. (4.2).

Formally, complex scaling can be applied in the same manner to both atomic and molecular systems; however, in the latter case additional steps are necessary in order to extract physically meaningful potential energy surfaces from complex-scaled Born-Oppenheimer calculations[19,40].

Complex scaling and CAP techniques have been applied to several *ab initio* methods. Complex-scaled and CAP Hartree-Fock (HF)[41,42] and density functional theory (DFT)[43] methods have been introduced; these approaches are only applicable for metastable ground electronic states. Complex-scaled configuration-interaction (CI)[41] and multiconfigurational self-consistent field (MCSCF)[42] were successfully used to study resonances in atoms and small molecules, e.g., He, H_2, Be^-[40–42,44]. Complex-scaled multiconfigurational time-dependent HF method has been applied to describe doubly-excited resonance states in Be[45]. Fock-space multireference coupled-cluster methods combined with CAPs have been developed by Pal and co-workers[46,47]. Recently, a CAP version of EOM-CCSD for electron attachment (EOM-EA-CCSD) has

been reported by Ghosh et al.[48] and applied to study electron-attached states of neutral molecules.

Here, we present an implementation of the complex-scaled EOM-EE-CCSD method designed to study electronically excited resonance states in systems with bound ground electronic states. In EOM-EE-CC the excited-state wave function is described by excitation operators R acting on the reference-state CC wave function:

$$|\Psi\rangle = \hat{R}e^{\hat{T}}|0\rangle \tag{4.4}$$

where $|0\rangle$ is the reference Slater determinant (usually satisfying HF equations) and $\hat{T}$ is a coupled-cluster operator. EOM-EE-CC ansatz enables simultaneous treatment of non-dynamical and dynamical electron correlation, yields spin-pure wave functions, and provides a balanced description of states of different character. Thus, EOM-CC is a natural choice for extending excited-state methodology to resonances via complex scaling and CAP approaches.

The excitation level in operators T and R can be truncated giving rise to the hierarchy of approximate EOM-CC models converging to the exact solution. In this paper, we consider EOM-CC with single and double substitutions, EOM-CCSD. We present the complex-scaled EOM-EE-CCSD method (cs-EOM-EE-CCSD) and provide the details of the implementation. We then consider Feshbach $2s^2$ resonances in He, H^-, and Be. Since Feshbach resonances decay is a two-electron process, it is governed by electron correlation. Consequently, complex-scaled HF or CIS cannot predict lifetimes of Feshbach resonances[49].

For two electron systems such as He and H^-, EOM-EE-CCSD is equivalent to full configuration interaction (FCI) and is, therefore, exact in terms of many-electron expansion. Thus, we can focus on one-electron basis set dependence of the results. One

of the well-known drawbacks of complex scaling approach is its extreme sensitivity to one-electron basis set size, which is commonly attributed to a more diffuse character of resonances and their coupling with the continuum. We analyzed the physical origins of this dependence and found that for the Feshbach resonances the dependence is due to electron correlation. In particular, a balanced description of angular and radial electron correlation is important for obtaining converged results. These findings allow us to develop guidelines for choosing basis sets which are optimal for resonances.

The structure of the paper is as follows. The theory of cs-EOM-EE-CCSD and implementation details are given in Sec. 4.2. The results of benchmark calculations are discussed in Section 4.3. The basis set effects are discussed in Sec. 4.3.1. The application of cs-EOM-EE-CCSD to many-electron systems and the importance of the reference-state choice are discussed in Sec. 4.3.2. Our concluding remarks are given in Sec. 4.4.

4.2 Complex-scaling formalism: General theory and EOM-EE-CCSD implementation

Upon complex-scaling (or dilation) transformation the original molecular Hamiltonian is transformed in such a way that resonance wave function can be obtained as a square-integrable eigenfunction of the complex-scaled Hamiltonian [given that the complex-scaling parameter, θ, is greater than the critical value, see Eq. (4.3)][17,18,29–31,50]. Both the electronic and nuclear coordinates are scaled by the factor $e^{i\theta}$ ($r \rightarrow re^{i\theta}$, $R \rightarrow Re^{i\theta}$). The resulting Hamiltonian is non-Hermitian and, therefore, can have complex eigenvalues. The scaled molecular Hamiltonian assumes the following form:

$$H^{\theta} = e^{-2i\theta}T_N + e^{-2i\theta}T_e + e^{-i\theta}V_{NN} + e^{-i\theta}V_{Ne} + e^{-i\theta}V_{ee} \tag{4.5}$$

The theoretical justification of complex scaling is given by the Balslev-Combes theorem[29–31]. As illustrated in Fig. 4.3, (i) the eigenvalues corresponding to the bound states of the original Hamiltonian and the threshold energies (ionization or electron-detachment energies) are unaffected by the complex scaling transformation; (ii) the segments of the continuum starting at the thresholds are rotated by 2θ down to the complex plane; (iii) new complex, discrete eigenvalues of H^{θ} may appear in the lower half of the complex energy plane; they are associated with the resonance states. The real (E_R) and imaginary (-Γ/2) parts of the eigenvalue correspond to the resonance position and width (Γ), respectively, and the lifetime is $1/\Gamma$, as in Eq. (4.2). As a result, L^2-integrable complex eigenfunction of the H^{θ} associated with the resonance state can be computed in a way similar to conventional quantum chemistry calculations.

Mathematically, this transformation can be described as a similarity transformation (see, for example, Ref. 18):

$$H(\theta) = \hat{S}H\hat{S}^{-1}$$
$$\hat{S} = e^{i\theta r\frac{\partial}{\partial r}}$$

As such, it does not alter the discrete spectrum of the Hamiltonian; yet, it converts resonance wave functions into "bound"-like wave functions that can be considered as a part of the "generalized" Hilbert space[19].

The observation that complex scaling is a similarity transformation highlights interesting parallels between complex scaling and EOM-CC techniques. In the latter, the similarity transformation permits obtaining accurate correlated many-electron energies

using compact expansions of the wave function, i.e., one can perform a similarity transformation that results in $\bar{H} = e^{-T} H e^{T}$ (where T is coupled-cluster substitution operator) whose lowest eigen-state is just a single Slater determinant, Φ_0, and the respective eigen-energy is exact. Such transformation would require the operator T to include up to N-electron excitations; however, an approximate T including only singles and doubles still yields rather compact wave functions and accurate energies. In complex-scaling formalism, one obtains energies of continuum states from a spatially compact (i.e., L^2-integrable) wave function. In the case of exact solution (that requires using a complete one-electron basis set) the energies are independent of θ and the bound states are unaffected by the transformation, but in a finite representation, the approximate solutions deviate from the exact result (energies of bound states may change, and energies of resonances are θ-dependent). An important difference between the two cases, however, is that similarity transformation in complex scaling formalism affects boundary conditions, whereas in EOM it does not.

To implement a complex-scaled *ab initio* method, one can either employ complex basis functions, or work with real one-electron basis and to scale the Hamiltonian matrix elements:

$$H_{ij} = T_{ij} + V_{ij} \rightarrow H_{ij}(\theta) = e^{-2i\theta} T_{ij} + e^{-i\theta} V_{ij}. \tag{4.6}$$

In the latter case (the so-called direct approach), a complex wave function is represented by an expansion in the basis of Slater determinants built from real orbitals, but with complex expansion coefficients (amplitudes). Such approach allows one to employ standard quantum chemistry codes for one- and two-electron integrals computed using Gaussian

basis functions[c]. Our implementation of the cs-EOM-EE-CCSD method is based on the direct approach.

There are several subtleties related to the complex scaling approach that deserve special attention. In particular, the Balslev-Combes theorem is only strictly valid for the exact solution, whereas truncated one- and many- electron basis sets introduce dependency of eigenvalues on the complex-scaling parameter, θ. Complex-scaling makes the Hamiltonian non-Hermitian, which requires reformulation of variational principle such that it can be used in the framework of variational methods such as HF or CI (to emphasize the difference, the name "complex stationary principle" is often used). These implications of the complex-scaling of the electronic Hamiltonian for practical quantum-chemistry calculations are discussed below.

In addition, Born-Oppenheimer approximation applied to complex-scaled molecular Hamiltonian results in electronic Hamiltonian with nuclear coordinates shifted to the complex plane (see discussion in supplementary material for Ref. 51). However, this is not a concern for atomic resonances that are the focus of this paper.

4.2.1 C-product versus scalar product

A non-Hermitian form of the complex-scaled Hamiltonian implies modifications of standard quantum chemistry approaches developed for bound states of the original molecular Hamiltonian. One can use a generalized variational principle based of bi-orthogonal formulation, similarly to non-Hermitian EOM-CC theory[52,53]. In this

[c]Here, the non-complex-scaled HF reference is assumed. If the complex-scaled HF is employed molecular orbitals are no longer real. In this case an integral transformation routine has to be modified accounting for the transformation from integrals computed in the real AO basis to the basis of complex MO.

approach, one considers left and right eigenstates, $< \Psi_L|$ and $|\Psi_R >$, of the Hamiltonian and formulates stationary principle by using the following expectation value: $\frac{<\Psi_L|H|\Psi_R>}{<\Psi_L|\Psi_R>}$.

In the case when the initial Hamiltonian is Hermitian complex-scaling transformation renders it into the complex-symmetric form and bi-orthogonal variational principle turns into a complex analogue of variational principle employing so-called c-product[18,54,55], $\langle\psi_i|\psi_j\rangle_C = \int \psi_i\psi_j dr$, instead of the standard scalar product, $\langle\psi_i|\psi_j\rangle = \int \psi_i^*\psi_j dr$. Sommerfeld and Tarantelli[56] compared the performance of c-product and regular scalar product for iterative diagonalization of complex-symmetric matrices in the context of CAP/CI. Although both formulations are legitimate for the case when real orbitals are involved, they found that the c-product version is less numerically stable[56].

Since EOM-CCSD similarity-transformed $\bar{H}$ is non-Hermitian by itself, the EOM-EE-CCSD equations can be formulated exploiting stationary principle for the biorthogonal space of left and right eigen-vectors (see [53] and refs. therein), the validity of which is not affected by complex-scaling transformation.For the implementation of cs-EOM-EE-CCSD that involves non-complex-scaled HF and non-complex-scaled CCSD, the difference between c-product and scalar product only appears at the cs-EOM-EE-CCSD stage of calculation.All calculations reported here for the He and H^- $2s^2$ resonances were performed using full diagonalization of the Hamiltonian matrix. As the guess vectors employed in these calculations have no imaginary component, c-product and regular scalar product formulations are equivalent in this case. In the cs-EOM-EE-CCSD implementation based on complex-scaled HF and CCSD, we employed c-product in all three steps (HF, CCSD, and EOM).

4.2.2 One- and many electron basis sets

Balslev-Combes theorem is formulated for operators H and H^{θ}. Thus, when their basis set representations are used, the theorem is valid only in the limit of the exact representation of the Hamiltonian. That is, only when H and H^{θ} operators are represented in the complete one- and many- electron bases, the theorem holds true. Obviously, this is not the case for a finite one-electron basis set and truncated wave function expansion[41,54].

When using incomplete one-electron bases, the eigen-values become θ-dependent and θ-trajectories, E(θ), need to be computed. If eigenvalues become nearly stationary with respect to θ at some value (θ_{opt}), one can reason that in the vicinity of such θ_{opt} the Balslev-Combes theorem holds approximately and the respective E(θ) exhibits the behavior as in the exact limit. Thus, the "best" value of E(θ) is E(θ_{opt}). Moreover, stationary E(θ) ensures that the virial theorem is satisfied for the resulting resonance solution[19,54]. Moiseyev and co-authors proved that optimal θ ($dE/d\theta = 0$, $\theta = \theta_{opt}$) corresponds to a cusp in the θ-trajectory plot when only real (imaginary) part of θ is varied and imaginary (real) part is kept fixed[57,58]. From the practical point of view, the stationary point corresponding to the minimal value of the $|\frac{dE}{d\theta}|$ provides an estimate of resonance's position and lifetime. The value $|\frac{dE}{d\theta}|_{\theta=\theta_{opt}}$ quantifies to which degree the stationary condition is satisfied (or, rather, unsatisfied) at θ_{opt}.

As illustrated below, despite the L^2-integrable character of the target wave function the complex-scaled calculations are much more sensitive to the completeness of one-electron basis set than standard *ab initio* methods. The reasons for this sensitivity are the following. First, the interaction of the resonance state with continuum needs to be accurately described. Thus, one needs to employ relatively diffuse basis sets. Second, although complex-scaling does not change the eigenvalues of bound states (in the complete one- and many- electron limit), it does change the corresponding wave functions

introducing oscillatory behavior, which is most prominent for core electrons in many-electron systems[d,59,60]. To accurately describe these changes of the wave function along θ-trajectories, sufficiently flexible bases are necessary. Finally, as demonstrated below, for Feshbach resonances (whose lifetimes are determined by electron correlation), basis sets need to be capable of describing both radial and angular correlation accurately and in a balanced way. Below we quantify these effects and explore strategies for developing more compact basis sets, which is necessary for applications of complex-scaling methods to realistic systems.

A number of approaches have been developed to tackle the core electrons problem[59], the simplest of which is a subtracted-core technique; it can be easily applied in complex-scaled EOM-EE-CCSD by freezing core electrons in post-cs-HF calculations.

4.2.3 Complex-scaled EOM-EE-CCSD

Detailed discussion of the EOM-EE-CCSD method is available in numerous original and review papers (see, for example, Refs. 52, 53, 61–64). Here, only the main aspects relevant for the comparison between the regular and complex-scaled EOM-EE-CCSD approaches are summarized.

---

[d] At small r, a one-electron function for an electron in a many-electron atom can be approximately described as $\phi(r) \approx R_{nl}(r)\exp(-Zr/na_0)Y_{lm}(\theta,\phi)$, where R_{nl} are hydrogenic radial functions and Z is the nuclear charge[59]. In addition to scaling the radial part, complex scaling ($r \rightarrow re^{i\theta}$) introduces an oscillatory behavior to the one-electron function: $R_{nl}(re^{i\theta})\exp(-Zrcos(\theta)/na_0)\exp(-iZrsin(\theta)/na_0))Y_{lm}(\theta,\phi)$. One can clearly see that oscillations are larger for higher values of the nuclear charge.

We begin with the excited-state wave function ansatz given by Eq. (5.2) with $\hat{R}$ including single and double excitations:

$$\hat{R} = \hat{R}_0 + \hat{R}_1 + \hat{R}_2 \tag{4.7}$$

$$\hat{R}_0 = r_0 \tag{4.8}$$

$$\hat{R}_1 = \sum_{ia} r_i^a a^\dagger i \tag{4.9}$$

$$\hat{R}_2 = \frac{1}{4} \sum_{ijab} r_{ij}^{ab} a^\dagger b^\dagger ji \tag{4.10}$$

The amplitudes $\hat{T}$ are computed by solving the CCSD equations for the reference state. Since $\hat{T}$ and $\hat{R}$ commute, $R|0\rangle$ is an eigen-function of the similarity-transformed Hamiltonian, $\bar{H} = e^{-T} H e^{T}$. Thus, amplitudes $\hat{R}$ are found by diagonalization of the normal-ordered similarity-transformed Hamiltonian ($\bar{H}_N = \bar{H} - E_{CC}$, $E_{CC} = \langle 0|\bar{H}|0\rangle$) in the basis of the reference, $|0\rangle$, singly, Φ_i^a, and doubly, Φ_{ij}^{ab} excited determinants:

$$\begin{pmatrix} 0 & \bar{H}_{OS} & \bar{H}_{OD} \\ 0 & \bar{H}_{SS} - E_{CC} & \bar{H}_{SD} \\ 0 & \bar{H}_{DS} & \bar{H}_{DD} - E_{CC} \end{pmatrix} \begin{pmatrix} R_0 \\ R_1 \\ R_2 \end{pmatrix} = \omega \begin{pmatrix} R_0 \\ R_1 \\ R_2 \end{pmatrix} \tag{4.11}$$

As amplitudes $\hat{T}$ satisfy the CCSD equations, H_{OS} and H_{OD} equal to 0, and, therefore, excited states are not coupled to the reference. Therefore, the diagonalization is performed in the singles and doubles block of the $\bar{H}_N$ matrix. To compute several lowest eigenvalues of the $\bar{H}_N$ matrix, the generalized Davidson iterative diagonalization

method is employed[65–67]. The σ-vectors corresponding to the product of $\bar{H}$ and trial vectors required for Davidson diagonalization have the following form:

$$\sigma_i^a = [(\bar{H}_{SS} - E_{CC})R_1]_i^a + [\bar{H}_{SD}R_2]_i^a \tag{4.12}$$

$$\sigma_{ij}^{ab} = [\bar{H}_{DS}R_1]_{ij}^{ab} + [(\bar{H}_{DD} - E_{CC})R_2]_{ij}^{ab}. \tag{4.13}$$

These equations provide the starting point for the derivation of the so-called programmable expressions.

Complex-scaled EOM-EE-CCSD can be formulated using three different approaches that can be arranged in the following hierarchical order: (i) cs-EOM-EE-CCSD/CCSD/HF in which complex-scaling is introduced only in EOM; (ii) cs-EOM-EE-CCSD/cs-CCSD/HF with both EOM and CC steps performed employing complex-scaled Hamiltonian; (iii) fully complex-scaled approach, cs-EOM-EE-CCSD/cs-CCSD/cs-HF. We have implemented all three models. Since similarity-transformed $\bar{H}$ has the same spectrum as original H, the first approach should yield the exact spectrum in the limit of complete one and many- electron bases. Since the present implementation is aimed to autoionizing excited states for systems with closed-shell bound ground states, the main focus of this paper is on cs-EOM-EE-CCSD/CCSD/HF. For Be $1s^2 2p3s$ resonance, we report the results computed with all three methods. The detailed comparison of the three schemes is the subject of the future work.

Žd'ánská and Moiseyev recently showed that complex-scaled HF orbitals used in complex-scaled active-space CI calculations of He atom doubly-excited resonance state are superior to real non-complex-scaled orbitals[41]. One can expect similar behavior for cs-EOM-EE-CCSD, i.e. the reference state will affect the final solution in particular

for large values of complex-scaling parameter θ when conventional HF reference is no longer a good approximation to a mean-filed stationary solution for H^{θ}.

Practically, scaling of the $\bar{H}^{\theta}$ matrix elements is achieved by scaling all terms including two-electron integrals, $\langle pq||rs\rangle$, by the factor $e^{-i\theta}$ and by splitting all terms containing the Fock matrix into two parts, i.e., the kinetic energy part which is scaled by the factor $e^{-2i\theta}$, and the rest of one-electron part and mean-field two-electron contribution scaled by $e^{-i\theta}$. Therefore, complex-scaling transforms the EOM-EE-CCSD matrix equations, Eq. (4.11), to the following form:

$$\begin{pmatrix} 0 & \bar{H}^{\theta}_{OS} & \bar{H}^{\theta}_{OD} \\ \bar{H}^{\theta}_{SO} & \bar{H}^{\theta}_{SS} - E^{\theta}_{CC} & \bar{H}^{\theta}_{SD} \\ \bar{H}^{\theta}_{DO} & \bar{H}^{\theta}_{DS} & \bar{H}^{\theta}_{DD} - E^{\theta}_{CC} \end{pmatrix} \begin{pmatrix} R_0 \\ R_1 \\ R_2 \end{pmatrix} = \omega \begin{pmatrix} R_0 \\ R_1 \\ R_2 \end{pmatrix} \tag{4.14}$$

where $E^{\theta}_{CC} = \langle 0|\bar{H}^{\theta}|0\rangle$.

Note that E^{θ}_{CC}, ω, and amplitudes in R_0, R_1, R_2 operators are now complex. Using non-complex-scaled CCSD reference, which does not satisfy complex-scaled CCSD equations, introduces coupling between the reference and excited states, i.e., $\bar{H}^{\theta}_{SO}$ and $\bar{H}^{\theta}_{DO}$ are no longer zeroes. Furthermore, additional disconnected terms appear in the $\bar{H}^{\theta}_{DS}$ block (see supplementary materials for Ref. 51). Therefore, in contrast to EOM-EE-CCSD, ground and excited states interact and iterative Davidson diagonalization of $\bar{H}^{\theta}$ in the basis of $|0\rangle$, Φ^{a}_{i} and Φ^{ab}_{ij} has to be performed, similar to EOM-EE-CCSD(2,3)[68]. The cs-EOM-CCSD/cs-CCSD equations, in which the reference is decoupled from the target states, do not have such additional terms; these equations are solved in the singles and doubles block as in regular EOM-EE-CCSD.

The corresponding Davidson σ-vectors are:

$$\sigma_0 = \bar{H}^{\theta}_{OS} R_1 + \bar{H}^{\theta}_{OD} R_2 \tag{4.15}$$

$$\sigma^a_i = (\bar{H}^{\theta}_{SO} R_0)^a_i + ((\bar{H}^{\theta}_{SS} - E^{\theta}_{CC}) R_1)^a_i + (\bar{H}^{\theta}_{SD} R_2)^a_i \tag{4.16}$$

$$\sigma^{ab}_{ij} = (\bar{H}^{\theta}_{DO} R_0)^{ab}_{ij} + (\bar{H}^{\theta}_{DS} R_1)^{ab}_{ij} + ((\bar{H}^{\theta}_{DD} - E^{\theta}_{CC}) R_2)^{ab}_{ij} \tag{4.17}$$

The programmable equations are given in supplementary material in Ref. 51. The resulting equations are implemented using our new general tensor library[69,70].

4.3 Results and discussion

A very unfavorable feature of complex-scaling formalism is that the incompleteness of one- and many- electron bases leads to the θ-dependence of the eigen-values of the scaled Hamiltonian, for both the ground and target resonance states. We address the effects of the one-electron basis set by considering two-electron systems, He and H^-, for which cs-EOM-EE-CCSD provides exact (in a given one-electron basis) solution and which have been extensively studied.

4.3.1 Two-electron systems: $2s^2$ resonances in He and H^-

Although the resonances in complex scaling formalism become L^2-integrable, the choice of the optimal basis set for description of the resonance states is not trivial. The optimal basis should be diffuse enough to be suitable for pseudo-continuum states, which can be mixed with the resonance, and flexible enough to describe the wave function transformation upon complex scaling. Moreover, the basis should be sufficiently

flexible to accurately describe electron correlation, which is essential for Feshbach resonances.

To gain insight into these effects, we performed the following sets of calculations:

- We demonstrate the convergence of the resonance energy and lifetime for the He $2s^2$ state using a large even-tempered spd basis. This calculation also validates our implementation.

- We investigate the utility of standard basis sets in complex-scaling calculations by considering various polarized triple-zeta and higher-quality basis sets.

- The effect of adding diffuse basis functions to standard basis sets was analyzed by considering the same valence set augmented by an increasing number of the diffuse basis functions.

- The effect of higher angular momentum functions was analyzed by comparing basis sets of approximately same size but having different number of s, p, and d-functions.

- The effect of uncontracting of the valence basis functions in the standard bases was analyzed.

Table 4.1: Gaussian basis set exponents (α) of the first basis function and scaling factors (k, $\alpha_{i+1} = \alpha_i/k$) used in the even-tempered series.

He			
	α [k], s	α [k], p	α [k], d
6-311(+,+)G(d,p)+[NsNpNd]	1.23×10^{-1} [2.000]	2.34×10^{-1} [2.000]	9.37×10^{-1}[2.000]
aug-cc-pVTZ+[NsNpNd]	2.44×10^{-2} [2.000]	8.13×10^{-2} [2.000]	2.34×10^{-1} [2.000]
aug-cc-pVQZ+[NsNpNd]	2.44×10^{-2} [2.000]	8.13×10^{-2}[2.000]	2.34×10^{-1}[2.000]
30s15p10d	100 [2.043]	30 [2.295]	30 [3.201]
30s15p	100 [2.043]	30 [2.295]	–
20s10p10d (a)	100 [2.043]	30 [2.295]	30 [3.201]
20s10p10d (b)	100 [2.976]	30 [3.642]	30 [3.642]
H^-			
6-311(+,+)G(d,p)+[NsNp]	1.80×10^{-2} [2.000]	3.75×10^{-1} [2.000]	–
aug-cc-pVTZ+[NsNpNd]	1.26×10^{-2} [2.000]	5.10×10^{-2} [2.000]	1.24×10^{-1} [2.000]
aug-cc-pVQZ+[NsNpNd]	1.18×10^{-2} [2.000]	4.24×10^{-2} [2.000]	9.50×10^{-2} [2.000]

Table 4.2: Complex energies of the $2s^2$ resonance in helium calculated by cs-EOM-EE-CCSD in different bases.

Basis set	Number of basis functions	Re(E_{res}), hartree	Im(E_{res}), hartree	Γ, eV	θ_{opt}, rad	$\lvert\frac{\partial E}{\partial \theta}\rvert$, hartree/rad
aug-cc-pvtz + [3s3p]	35	-0.7751	-0.00170	0.0925	0.200	0.00192
aug-cc-pvtz + [3s3p3d]	50	-0.7753	-0.00154	0.0838	0.175	0.00167
6-311(+,+)G(d,p) + [3s3p]	18	-0.7768	-0.00122	0.0664	0.375	0.00224
aug-cc-pvqz + [3s3p]	58	-0.7768	-0.00200	0.1088	0.225	0.00450
6-311(+,+)G(d,p) + [10s5p5d]	56	-0.7771	-0.00166	0.0903	0.300	0.00351
aug-cc-pvtz + [10s5p5d]	73	-0.7754	-0.00168	0.0914	0.200	0.00126
aug-cc-pvqz + [10s5p5d]	96	-0.7769	-0.00196	0.1067	0.225	0.00402
6-311(+,+)G(d,p) + [3s3p3d] + dodecahedron	54	-0.7770	-0.00180	0.0980	0.200	0.00197
30s15p10d	125	-0.7778	-0.00223	0.1214	0.325	5.24×10^{-5}
30s15p	75	-0.7773	-0.00226	0.1227	0.325	1.64×10^{-4}
20s10p5d (a)[a]	75	-0.7778	-0.00225	0.1223	0.300	4.88×10^{-5}
20s10p5d (b)[b]	75	-0.7769	-0.00245	0.1332	0.175	0.01169
Ho [71]		-0.7779	-0.00227	0.1235	–	–

[a] 20s10p5d (a) is formed from 30s15p10d by exclusion of the 10 s-, 5 p-, and 5 d-type most diffuse basis functions. [b] 20s10p5d (b) even-tempered basis covers the same range of the gaussians' exponents, but with a greater scaling factor (see Table 4.1.)

Table 4.3: Energies of the $2s^2$ resonance in H^- calculated by cs-EOM-EE-CCSD in different bases. ΔE is given relative to the 1s ground state of neutral hydrogen computed for corresponding basis set.

Basis set	Number of basis functions	Re(E_{res}), hartree	ΔE, eV	Im(E_{res}), hartree	Γ, eV	θ_{opt}, rad	$\lvert\frac{\partial E}{\partial \theta}\rvert$, hartree/rad
aug-cc-pvtz + [3s]	26	-0.1262	10.1667	-0.00070	0.0381	0.200	0.00295
aug-cc-pvtz + [3s3p]	35	-0.1484	9.5626	-0.00091	0.0495	0.225	0.00292
aug-cc-pvtz + [3s3p3d]	50	-0.1488	9.5517	-0.00089	0.0484	0.200	0.00321
6-311(+,+)G(d,p) + [3s3p]	18	-0.1251	10.1967	-0.00229	0.1247	0.325	0.00814
aug-cc-pvqz + [3s3p]	58	-0.1485	9.5633	-0.00083	0.0454	0.225	0.00048
aug-cc-pvtz + [10s5p5d]	73	-0.1487	9.5544	-0.00063	0.0342	0.250	0.00108
aug-cc-pvqz + [10s5p5d]	96	-0.1488	9.5551	-0.00069	0.0375	0.250	0.00018
Ho *et al.*[72]		–	9.5574	–	0.0472	–	–
Bardsley and Junker [73]		–	9.5572	–	0.0474	–	–
Bhatia [74]		–	9.5570	–	0.0458	–	–

Each diffuse series (s, p, and d) used to augment standard basis sets consisted of even-tempered basis functions. The first exponents in the series, which are basis-set specific, and the scaling factors are summarized in Table 4.1. The full diagonalization procedure of the similarity-transformed Hamiltonian has been employed. The values of the resonance energies and lifetimes for different bases are summarized in Tables 4.2 and 4.3.

Resonance energies and lifetimes convergence to the exact limit: An even-tempered 30s15p10d basis

To demonstrate the convergence of the He $(2s)^2$ resonance energy and lifetime with respect to the one-electron basis set we employed an extensive and flexible basis, namely, an even-tempered 30s15p10d basis from Ref. 41. The real and imaginary parts of the resonance eigenvalue at the stationary point of the resulting θ-trajectory (Fig. 4.4) are -0.77776 and -0.00223 a.u., respectively. The values are in agreement with the solution obtained employing Hylleraas basis: -0.77787 and -0.00227 a.u.[71]. Even though the resonance energy and lifetime are very close to the numerically exact values, the ground-state energy still has a noticeable imaginary part (7.46×10^{-4} a.u., θ=0.450). We also obtained satisfactory results by truncating the 30s15p10d basis by removing the most diffuse 10s, 5p, and 5d basis functions (the size of the resulting basis is thus 75): -0.77778 and -0.00224 a.u., for the real and imaginary parts, respectively. In contrast, increasing the scaling factor used to form even-tempered basis or removing d-type basis functions from the basis have pronounced effects on the shape of the θ-trajectory and the resulting eigenvalue at the stationary point (Fig. 4.4, Table 4.2). The origins of these effects are discussed in details below.

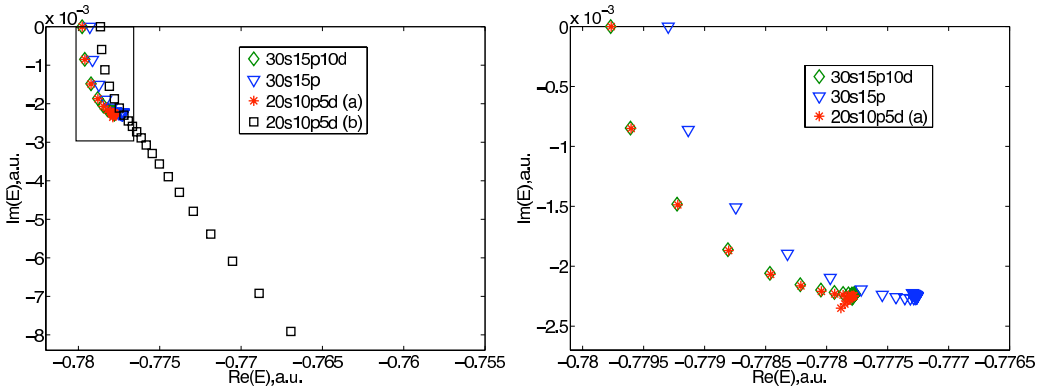

Figure 4.4: θ-trajectories for the $2s^2$ Feshbach resonance in He shown on different scale. Angle θ varies from 0 to 0.500 radian (step 0.025 rad). 30s15p10d basis corresponds to even-tempered basis, the gaussians' exponents values, α, vary within the range: $10^{-7} \leq \alpha \leq 100$, $2.66 \times 10^{-4} \leq \alpha \leq 30$, and $2.66 \times 10^{-4} \leq \alpha \leq 30$ for s, p, and d functions respectively. 30s15p is the same basis without d-type basis functions. 20s10p5d (a) is formed from 30s15p10d by exclusion of the 10 s-, 5 p-, and 5 d-type most diffuse basis functions. 20s10p5d (b) even-tempered basis covers the same range of the gaussians' exponents, but with a greater scaling factor.

These calculations illustrate the sensitivity of the results to the basis set and provide validation of our implementation. Our next step is to investigate whether highly-optimized standard basis sets, such as series of Dunning bases that are known to provide accurate and balanced description of electron correlation in the ground and excited states, may be efficiently employed in calculations of resonances. Our aim was to reduce basis set size by combining these standard basis set with additional even-tempered functions.

Standard basis sets and the effect of diffuse basis functions

One may expect that accurate description of resonances requires large number of diffuse basis functions. Even in the complex-scaling case, when the wave function becomes

square-integrable, the exponent can be quite small featuring a tail that (slowly) goes to zero at infinity.

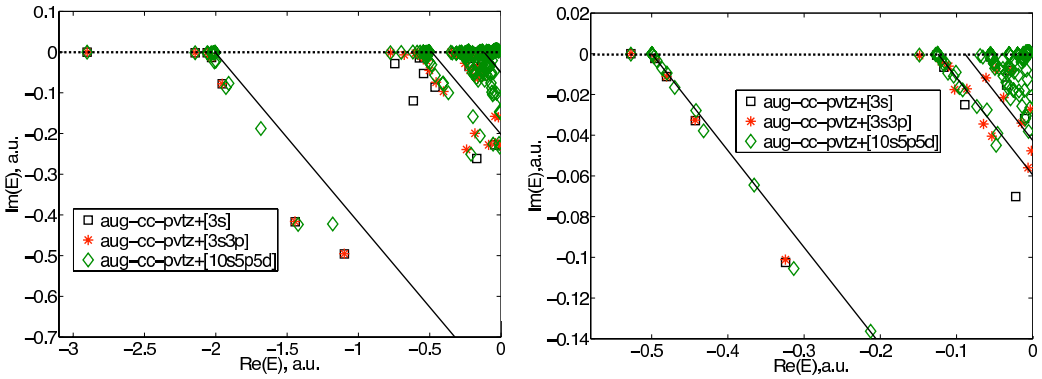

Figure 4.5: cs-EOM-EE-CCSD total energies for the ground and ^1S excited states of He (left panel) and H^- (right panel). θ values corresponding to θ_{opt} for the aug-cc-pVTZ+[10s5p5d] basis are 0.200 and 0.225 for He and H^-, respectively. Three rays with the origin at the three lowest IEs of He and H^- and rotated by the angle 2θ to the lower complex plain are shown in black. In the limit of the complete basis set the rays should coincide with the corresponding continuum branches.

To analyze the convergence of the results with respect to adding diffuse basis functions, we augmented the aug-cc-pVTZ basis by the diffuse basis functions: 3s, 3s3p, 3s3p3d, and 10s5p5d (i.e., 3s3p set consists of three additional s-functions and 9 p-functions). Fig. 4.5 shows cs-EOM-EE-CCSD (equivalent to FCI) total energies of the ground and ^{1}S excited states of He and H^- atoms for $\theta = 0.200$ and 0.225 rad, respectively. Unless mentioned otherwise, θ is real, which means that the cusp conditions for θ-trajectories are not necessarily satisfied, as the optimal θ may be complex.

Extension of the 3s diffuse set to 3s3p and 3s3p3d does not change the qualitative behavior of the spectrum upon complex scaling but, as will be shown below, is crucial for the quantitative description of the resonance energy and lifetime. We observe 3 branches formed by discretized continuum eigen-states corresponding to excitation

to very diffuse molecular orbitals. Those branches exhibit behavior dictated by the Balslev-Combes theorem and are rotated by the angle close -2θ to the lower complex plane with respect to the corresponding ionization energy. The ground state energy lies very close to the real axis and its energy is close to that of the unscaled $\bar{H}$. The absolute values of the energy deviation are 1.67x10^{-3}/1.64x10^{-3}/1.64x10^{-3} and 3.08x10^{-4}/1.69x10^{-4}/1.69x10^{-4} hartree for aug-cc-pVTZ basis with 3s/3s3p/3s3p3d diffuse sets for He and H^-, respectively. These energy deviations are mainly due to the drift in the real part of the eigenvalue as θ changes from 0 to θ_{opt}, for example, for aug-cc-pVTZ+[3s] the shifts in real and imaginary part for He and H^- are –1.65x10^{-3}/–2.4x10^{-4} (Re/Im) and –3.62x10^{-4}/5.5x10^{-5}, respectively. The 2s^2 resonances for both systems lie close to the real axis.

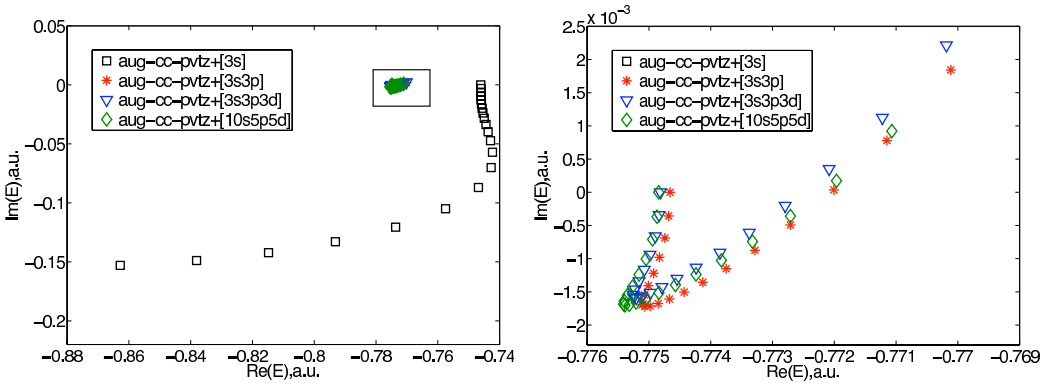

Figure 4.6: θ-trajectories for the 2s^2 Feshbach resonance in He shown on different scale. Angle θ varies from 0 to 0.500 radian (step 0.025 rad). See text for the diffuse subsets (3s, 3s3p, 3s3p3d, 10s5p5d) exponents definition.

θ-trajectories for the He 2s^2 resonance computed with the aug-cc-pVTZ basis augmented with different diffuse subsets are shown in Fig. 4.6. As discussed in Sec. 4.2, the resonance eigenvalues are identified as a point with the lowest absolute value of energy derivative with respect to the complex scaling parameter, $|\frac{dE}{d\theta}|$. Further extension of the 3s diffuse subset to 6s basis functions results in only minor changes in the resonance

trajectories (not shown, see supplementary materials in Ref. 51, Fig. S1). Thus, the aug-cc-pVTZ+3s basis recovers the bulk of the radial electronic correlation. In contrast, additional diffuse p-orbitals (3s3p) are crucial for accounting for angular electronic correlation in the resonance state. As one can see, the shape of the resonance trajectory changes dramatically upon switching from the 3s to the 3s3p subsets. Further addition of higher angular momentum basis functions (3s3p3d) does not have notable effect on either shape of the trajectory or the resulting resonance energy and lifetime. Therefore, the aug-cc-pVTZ+3s3p basis is sufficient to account for the most of the radial and angular electronic correlation contributions. Indeed, the real and imaginary parts of the resonance energy for aug-cc-pVTZ+3s3p (-0.7751 and -0.0017 hartree) are close to the exact solution for He $2s^2$ resonance (-0.7779 and -0.0023 hartree[71]) The best agreement with the exact solution is achieved for the aug-cc-pVQZ basis with the 3s3p diffuse subsets ($E_{Res} = -0.7768 - i0.0020$ hartree). Note that the values change only slightly upon further extension of the diffuse set to 10s5p5d ($E_{Res} = -0.7769 - i0.00196$ hartree). We observe the same trends for the H^- $2s^2$ resonance state. Addition of the 3p diffuse functions results in dramatic change in the trajectories shape (Fig. S2). The resulting resonance positions and widths are given in Table 4.3.

Despite being convenient for *ab initio* calculations, L^2-integrable Gaussian basis functions are not optimal for the description of the continuum states. However, Gaussians can be used to approximate the continuum states[75–77]. In attempt to reduce the number of required diffuse basis functions and to achieve more uniform approximation of the continuum states, we considered the 6-311(+,+)G(d,p)+[3s3p3d] basis augmented by diffuse functions distributed in the vertices on the dodecahedron grid (one s-type basis function per vertex located 1 Å from He, with the exponent of 0.02772). The $\theta-$trajectories for 6-311(+,+)G(d,p)+[3s3p3d] with grid-distributed basis

functions (54 basis functions), and atom-centered basis of the comparable size 6-311(+,+)G(d,p)+10s5p5d (56 basis functions) are shown in Fig. S3 in supplementary material for Ref. 51. Using the grid refines the solution, making the trajectory more compact and the singularity point more pronounced. However, there is no significant change in the resulting resonance position and width. In addition, the employed basis functions are relatively compact, and the improvement in the resonance states description is likely to be not because of better approximation of the continuum, but because of the better description of the angular electronic correlation. The trajectories computed for the more sparse grid, or more diffuse Gaussian exponent do not lead to any improvement in comparison to the atom-centered basis set (see supplementary material for Ref. 51, Fig. S3). In short, the addition of grid-distributed functions does not lead to a significant improvement in the description of the resonance states relative to the atom-centered ones, which is consistent with a rather compact wave function of the resonance state, as discussed below.

The effect of the valence basis set

Whereas it is not surprising that the description of resonance states is sensitive to the diffuseness of the basis, the variations in the valence basis set also have a profound effect on the shape of θ-trajectories. This is illustrated in Fig. 4.7 that compares θ trajectories computed with three different valence basis sets [6-311(+,+)G(d,p), aug-cc-pVTZ, and aug-cc-pVQZ] augmented with similar diffuse subsets. Despite notable change in the shapes of θ-trajectories for He $2s^2$ resonance (Fig. 4.7), the shift in the resonance position and width is rather small, e.g., transition from the 6-311(+,+)G(d,p) to aug-cc-pVQZ basis results in the shift of $< 1\text{x}10^{-4}$ (E_R) and -0.0008 ($\Gamma/2$) hartree. Interestingly, for the largest aug-cc-pVQZ+[3s3p] basis, there is no well-defined stationary

point: the minimal value of the $\frac{dE}{d\theta}$ along the trajectory is 4.5x10^{-3} hartree/rad and is more than twice greater that for other bases. The effect of the valence basis set is even more pronounced in the case of doubly excited resonance state in H^- (Fig. S4, supplementary materials for Ref. 51). Dunning's aug-cc-pVTZ and aug-cc-pVQZ augmented with 3s3p diffuse functions result in similar trajectories, which differ strongly from the 6-311(+,+)G(d,p)+[3s3p] one. Therefore, more flexible diffuse aug-cc-pVNZ bases perform better than the corresponding Pople's ones. Note, however, that the trajectories are plotted for α=1 ($\alpha = e^{-\theta_{Im}}$), which is not necessarily an optimal value, and therefore the cusp conditions do not hold in this case. Trajectories with pronounced cusp features can be obtained by varying α, which is illustrated by the θ-trajectories for the $2s^2$ resonance of He shown in Fig. S5 in supplementary material for Ref. 51.

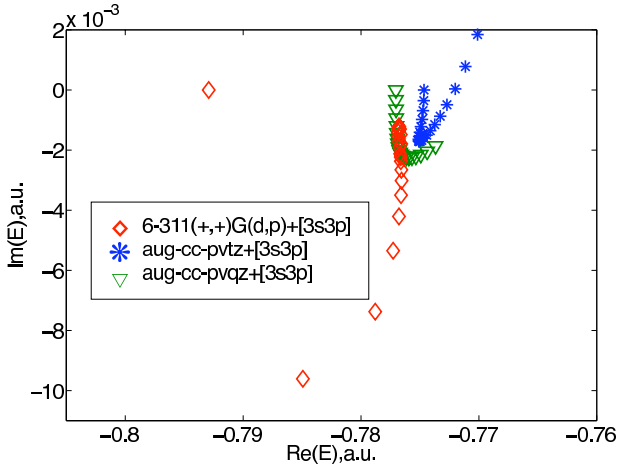

Figure 4.7: θ-trajectories for the $2s^2$ Feshbach resonance in He. Angle θ varies from 0 to 0.500 radian (step 0.025 rad).

As mentioned above, the complex-scaling transformation of the $\bar{H}$ matrix changes bound-states wave functions. To analyze the ability of basis sets to describe this wave function transformation, we considered aug-cc-pVTZ+[10s5p5d] and its fully uncontracted counterpart. The resulting trajectories for the ground state and $2s^2$ resonance

of He are shown in Fig. S6 (supplementary material for Ref. 51). As expected, uncontracting the basis makes the ground state trajectory more compact, i.e., the ground state approaches stationary condition, and the basis set approaches convergence. As uncontracted s-type basis functions are compact and do not contribute significantly to the description of the diffuse $2s^2$ state, uncontraction of the basis has only a minor effect on the resonance state.

The character of the resonance wave function

To rationalize the effects of basis sets, we focus on the changes in the wave function character upon complex-scaling. Below we characterize the ground and $2s^2$ states of He by analyzing the electronic densities, $< R^2 >$ expectation values and wave function expansion in terms of valence or diffuse excitation for the case of unscaled ($\theta = 0$) and scaled ($\theta = 0.200$) $\bar{H}$. The electronic densities for the He ground and $2s^2$ resonance states are shown in Fig. 4.8. The densities are computed from the unrelaxed EOM-EE-CCSD one particle density matrix:

$$\gamma_{pq} =< 0|e^{-T}L|p^{+}q|Re^{T}|0 > \tag{4.18}$$

For $\theta = 0$, the electronic densities are real (Fig. 4.8). The ground-state density almost coincides with the square of the He 1s orbital. The resonance state density has proper nodal structure consistent with the squared 2s orbital. Complex scaling transforms electronic density into a complex-valued function[e] of coordinates (Fig. 4.8). As one can

[e]The discussion of the physical interpretation of the complex electronic density for resonances can be found in Refs. 19,78,79. Barkay and Moiseyev[78] showed that the phase of the complex density probability is related to the resonant tunneling probability[78].

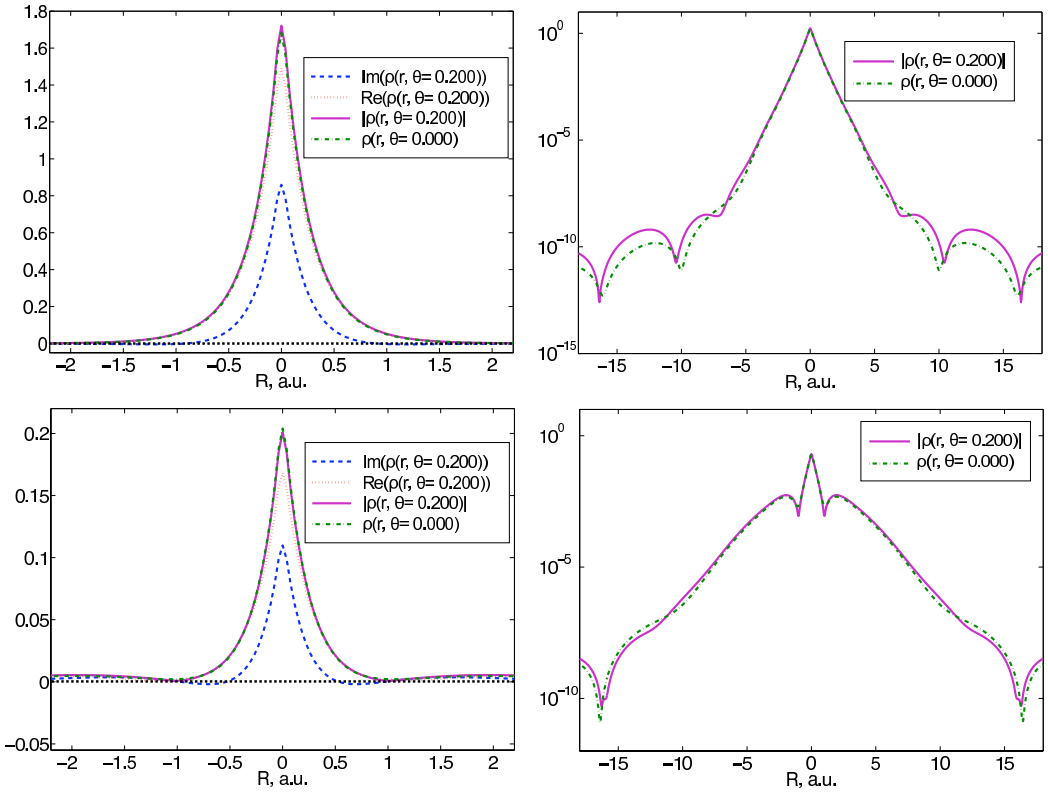

Figure 4.8: cs-EOM-EE-CCSD/aug-cc-pVTZ+[3s3p] electronic densities for the ground state (top) and $2s^2$ resonance (bottom) of He atom plotted in regular (left) and logarithmic (right) scale. Densities for θ=0 and θ=0.200 (real and imaginary parts, and the absolute value) are shown.

see, the real part of the ground state density resembles that for $\theta = 0$, whereas the imaginary part has more pronounced oscillatory behavior consistent with the wave function transformation discussed above. We observe similar patterns for the electronic density of the resonance state. The real part resembles that of the resonance state for θ=0 , and the imaginary part has more oscillating character. Overall, the changes in the electron density are small and are similar in magnitude to changes in hydrogenic 1s functions in the same range of θ (see supplementary material for Ref. 51, Fig. S7).

As complex-scaling make resonance to appear as a single L^2-integrable eigen-state of the complex-scaled Hamiltonian, one may expect that the wave function becomes more compact upon complex-scaling transformation. This is confirmed by the analysis of R^2 expectation values. $< R^2 >$ for the ground and $2s^2$ states of He for θ=0 is 2.40 and 25.96 Å^2, whereas for θ=0.200 the corresponding values are 2.40 and 25.92 Å^2. Therefore, the resonance wave function becomes slightly more compact, although the R^2 changes are not dramatic due to the dominant contribution of valence excitations to the wave function, which is discussed below.

To quantify contributions of excitations to the pseudo-continuum orbitals to the resonance wave function we divided all doubly-excited configurations into three groups: excitations to the orbitals with $\langle R^2 \rangle < 100$ Å^2 (valence), $\langle R^2 \rangle \geq 100$ Å^2 (diffuse), and mixed excitations. The decomposition of the wave functions into the contributions from each of these groups for θ=0.200 is shown in Fig. 4.9A for the three different basis sets: aug-cc-pVTZ augmented by 3s, 3s3p, and 3s3p3d diffuse sets. The 3s3p and 3s3p3d sets result in qualitatively the same character of the wave functions, which differ significantly from that for the 3s basis. Note that the purely diffuse contributions decrease upon transition from 3s to 3s3p and 3s3p3d. In addition, the contribution of mixed excitations is reduced thus increasing the valence character of the resonance state. This can be rationalized as follows. In the absence of higher angular momentum basis functions electron repulsion can only be mitigated by electrons avoiding each other in a radial dimension ("one in, one out", radial electron correlation) which results in an increased diffuseness of the wave function. Adding higher angular momentum functions allows electrons to avoid each other via correlated angular motions (angular electron correlation) leading to a more compact resonance state[f]. In agreement with

[f]When electrons cannot avoid each other angularly, they try to do it radially which results in a more diffuse wave function.

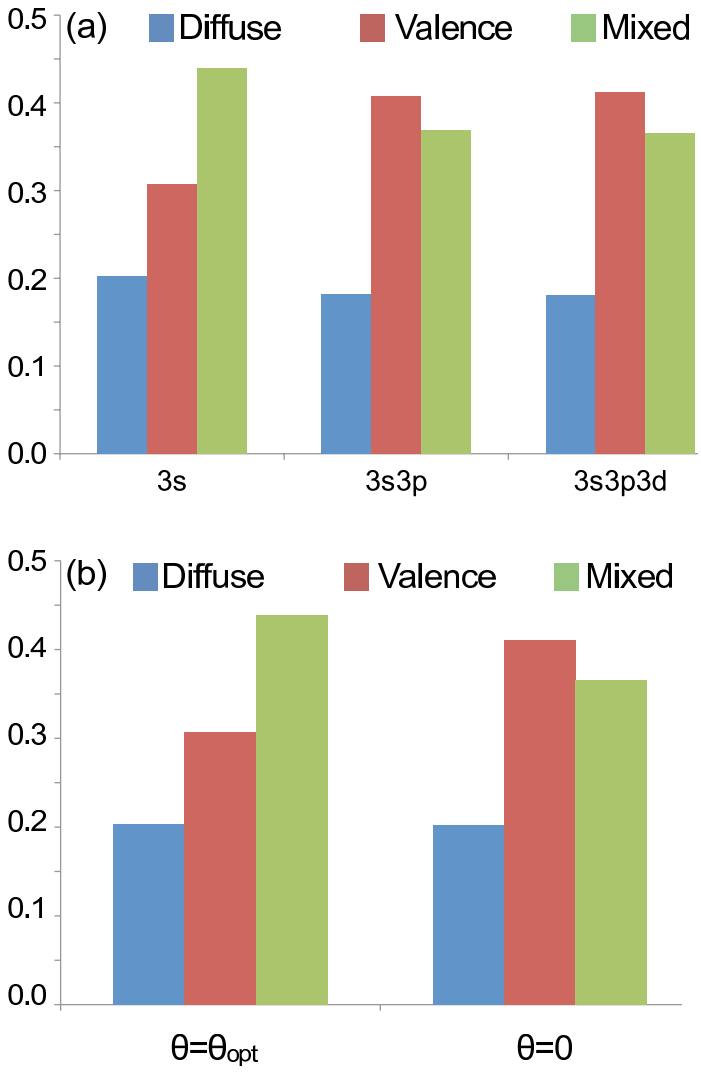

Figure 4.9: Decomposition of the He $2s^2$ resonance wave function into the excitations to diffuse orbitals ($< R^2 >> 100$ Å^2, shown in blue), valence orbitals ($< R^2 ><$ 100 Å^2, shown in red), and mixed double excitations (green) for (A) aug-cc-pVTZ basis augmented with 3s, 3s3p and 3s3p3d diffuse subsets; θ=0.250; and for (B) $\theta = \theta_{opt} = 0.200$ and $\theta = 0$; aug-cc-pVTZ/3s3p3d basis set is used. Absolute values of amplitudes are used for the analysis.

a slightly decreased $< R^2 >$ for the resonance wave function for the complex-scaled

Hamiltonian (θ=0.200) relative to the wave function of the original unscaled Hamiltonian, the contribution of the excitations to the diffuse orbitals also decreases (Fig. 4.9B).

As one can see from Fig. 4.8 and Fig. S7 of supplementary material in Ref. 51, there is no visually pronounced effect of the complex scaling on the one-particle electronic density for moderate values of the complex-scaling parameter, θ. However, the energies of both the ground and resonance states do depend on θ-dependence giving rise to θ-trajectories. To better understand the connection of energy θ-dependence to the changes of the wave function, and consequently electronic density, we performed the following energy decomposition analysis. The energy of a state can be decomposed into the contributions from one-electron and two-electron operators in the following form:

$$E = Tr[\gamma h] + Tr[\Gamma II] \tag{4.19}$$

where γ and Γ are one- and two-particle density matrices, respectively, and h and II are the one-electron Hamiltonian matrix and two-electron integral tensor. Upon complex-scaling transformation the θ-dependent energy assumes the following form:

$$E^{\theta} = e^{-2i\theta} Tr[\gamma^{\theta} T] + e^{-i\theta} Tr[\gamma^{\theta} V_{Ne}] + e^{-i\theta} Tr[\Gamma^{\theta} I] \tag{4.20}$$

where γ^{θ} and Γ^{θ} are one- and two-particle density matrices corresponding to the complex-scaled wave function. The results of the analysis performed for the aug-cc-pVTZ+[3s3p3d] basis for the He ground and resonance ($2s^2$) states are shown in Fig. 4.10.

As the Feshbach resonance state decay is a two-electron process, one may expect that the stationary point on the θ-trajectory which defines resonance lifetime is due to two-electron part of the energy decomposition [Eq. (4.20)]. In contrast, the θ-dependence of the ground state energy can be both due to correlation effects via two-electron part and one-electron part as complex-scaling affects the wave function. This is indeed confirmed by Fig. 4.10.

As illustrated by Fig. 4.10 (top), both the kinetic energy ($Tr[\gamma^{\theta}T]$) and electron-nucleus attraction ($Tr[\gamma^{\theta}V_{Ne}]$) contributions to the total energy of the ground state depend strongly on θ, the changes in the real and imaginary part of energy are as large as ∼0.5-1.5 a.u. Importantly, the θ-dependence of these terms is solely due to the θ-dependence of the density matrix, γ^{θ}. Therefore, energy decomposition allows one to trace the origin of the trajectory θ-dependence to the density matrix changes upon variations of θ. Proper scaling of kinetic energy and electron-nucleus attraction terms by $e^{-2i\theta}$ and by $e^{-i\theta}$, respectively, decreases the θ-dependence by an order of magnitude. Moreover, summing up the two contribution results in partial cancellation of θ-dependence, and the total one-electron part of the energy only varies within ~ 0.01 a.u. for the real and imaginary parts. Interestingly, the shape of the resulting trajectory is similar to that of the total energy. Thus, the main cause of the total energy θ-dependence of the ground state is due to the θ-dependence of the one-electron density matrix.

The situation is quite different for the resonance state. Similar to the ground state, the kinetic energy and electron-nucleus attraction contributions notably depend on θ. Scaling T and V_{Ne} parts by $e^{-2i\theta}$ and by $e^{-i\theta}$, respectively, results in more stable (i.e., constant) energies with respect to the θ variations. The changes in $e^{-2i\theta}Tr[\gamma^{\theta}T]$ and $e^{-i\theta}Tr[\gamma^{\theta}V_{Ne}]$ are of the opposite sign and partially cancel out upon summation of the two terms. Note that, in contrast to the ground state, the trajectory for the one-electron

energy differs considerably from the total energy trajectory. This is because the resonance state decay resulting in non-zero imaginary part of the total energy (in a complete basis set limit) is a two-electron process.

4.3.2 Many-electrons systems: Be atom

As an example of many-electron system, we consider doubly-excited 2p3s resonance in Be. We employ spd uncontracted basis sets derived from the basis optimized for electron-attached resonance states in Be[80] and used in calculations of the 2p3s resonance of Be[45]. The exponents of basis functions are given in supplementary material for Ref. 51.

We begin by considering cs-EOM-EE-CCSD based on the non-complex-scaled HF and CCSD. In this case, EOM-EE-CCSD results for many-electron atoms will depend on the specific choice of the reference orbitals and amplitudes T.

Note that the cs-EOM-EE-CCSD θ-trajectories are plotted for the total energy of the excited state, $E_i = \omega_i + \langle 0|\bar{H}^{\theta}|0\rangle$, where ω_i is an eigen-value of the complex-scaled $\bar{H}^{\theta}_N$ and $\langle 0|\bar{H}^{\theta}|0\rangle$ is an expectation value of $\bar{H}^{\theta}$ for the non-complex-scaled HF reference, $|0\rangle$. If the θ-trajectories are plotted for the excitation energies instead, the cusp feature may be masked by the evolution of the ground state energy and no stationary point may be observed. This was also mentioned in the context of cs-MCTDHF (multi-configurational time-dependent HF) theory where no cusps were found on excitation energies θ-trajectories and well-defined cusps were only observed for the total energy trajectories[45].

The θ-trajectories for the 15 lowest ^{1}P states are shown in Fig. S9A in supplementary material for Ref. 51. One can immediately see that the computed trajectories do not follow the Balslev-Combes theorem; they are shifted by 1.5 hartree to the upper complex

plane as θ changes from 0 to 0.475. The origin of this behavior can be traced to the non-complex-scaled HF reference. The latter is not a variational mean-field solution for $\bar{H}^{\theta}$. The changes of $\langle 0|\bar{H}^{\theta}|0\rangle$ and $\langle 0|H^{\theta}|0\rangle$ along the θ-trajectory (θ varies from 0 to 0.475) are illustrated in Fig. S9B. One can see that upon the θ increase the imaginary part of $\langle 0|\bar{H}^{\theta}|0\rangle$ rises steeply by up to 1.5 hartree. Comparison of the trajectories reveals that all 15 eigenvalues are dominated by the $\langle 0|\bar{H}^{\theta}|0\rangle$ expectation value beginning from relatively low values of the complex-scaling parameter. This is due to the fact that the conventional HF solution is no longer a good reference for the cs-EOM-EE-CCSD $\bar{H}^{\theta}$ solutions[g].

This numeric result illustrates that complex-scaled HF and/or complex-scaled CCSD that can account for orbital relaxation via T_1 operator, should be used for proper description of resonance states in many-electron systems. Indeed, when fully complex-scaled calculation is performed, the solutions of cs-EOM-EE-CCSD behaves in accordance to the Balslev-Combes theorem, as illustrated in Figs. 4.11 and S10-S16. We note that as long as complex-scaling is engaged at the CCSD level, the shape of the trajectories is not very sensitive to the underlying HF reference, as one can see from Fig. 4.11. This is because coupled-cluster ansatz is rather orbital insensitive owing to the ability of $exp(T_1)$ to describe orbital relaxation.

[g]The EOM-EE-CCSD energies are invariant with respect to the occupied-occupied and virtual-virtual orbital rotations. Moreover, their dependence on occupied-virtual rotations is relatively weak, because orbital relaxation is approximately accounted for by T_1. In the implementation of cs-EOM-EE-CCSD in which both HF and CCSD calculations are performed for the unscaled Hamiltonian and scaling is introduced only at the EOM stage, the T_1 operator does not account for proper orbital relaxation and the results become sensitive to the reference choice.

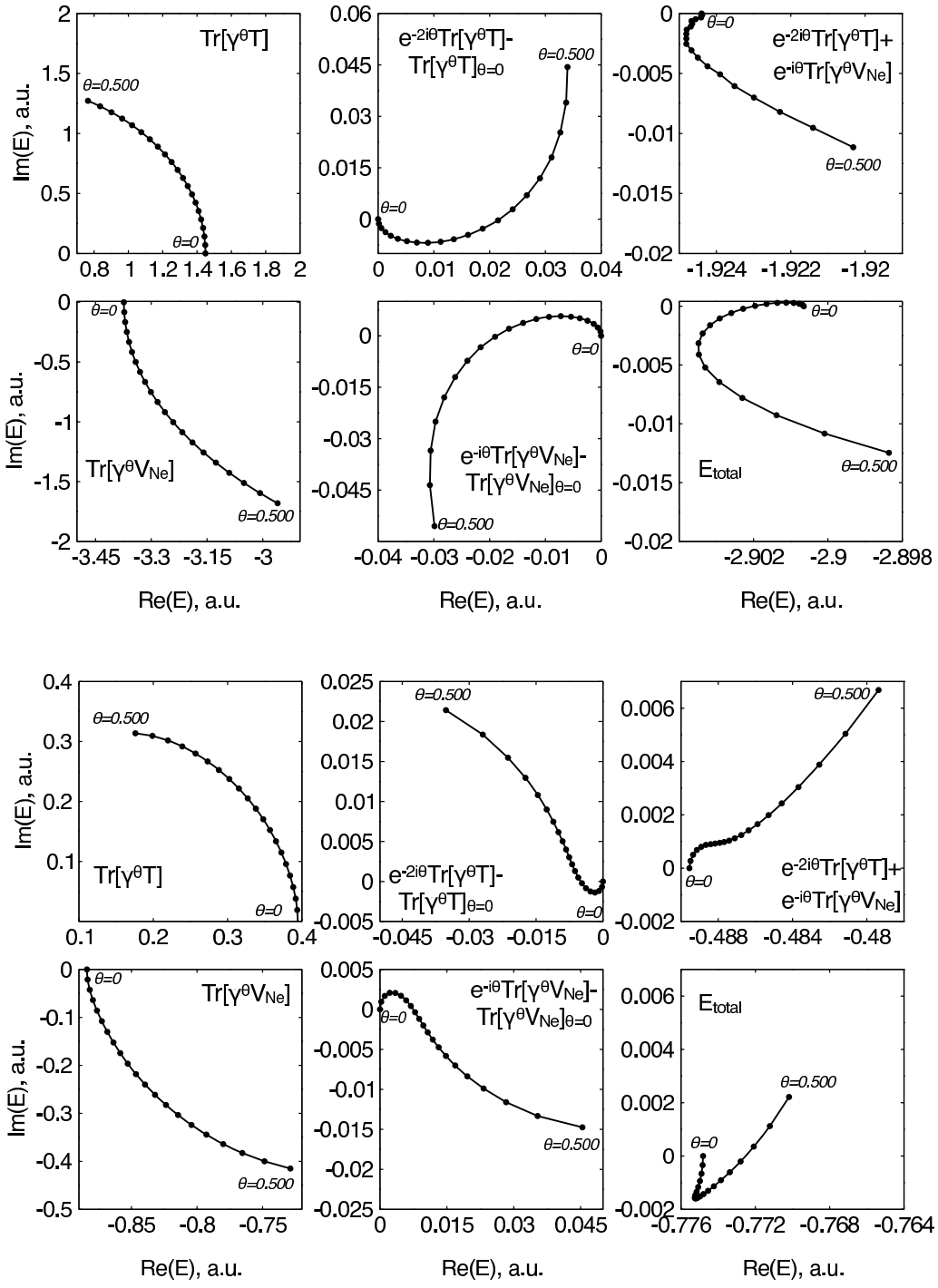

Figure 4.10: Energy decomposition analysis for the ground state (top) and $2s^2$ resonance (bottom) of He. CS-EOM-EE-CCSD/aug-cc-pVTZ+[3s3p3d].

Table 4.4: Energies of the $1s^2 2p3s$ resonance in Be calculated in different bases.

	Number of basis functions	Re(E_{Res}), hartree	Im(E_{Res}), hartree	ΔE, eV	Γ, eV	θ, rad	$\left\|\frac{\partial E}{\partial \theta}\right\|$ hartree/rad
cs-EOM-EE-CCSD/cs-CCSD/cs-HF							
14s11p	47	-14.2479	-0.00993	11.22	0.5404	0.300	0.01222
14s14p	56	-14.2482	-0.00990	11.21	0.5388	0.250	0.00868
14s11p, FC	47	-14.2090	-0.0110	11.13	0.5986	0.300	0.01186
14s11p2d	57	-14.2549	-0.01140	11.07	0.6204	0.250	0.00746
14s11p5d	72	-14.2575	-0.00715	11.01	0.3891	0.225	0.01020
14s14p5d, FC	81	-14.2171	-0.00855	10.92	0.4653	0.275	0.00411
cs-EOM-EE-CCSD/cs-CCSD/HF							
14s11p	47	-14.2425	-0.01022	11.36	0.5562	0.325	0.03212
CMCTDHF/14s14p5d[45]	81	–	–	11.01	0.434	–	–
Experiment[81]	–	–	–	10.89	0.531	–	–

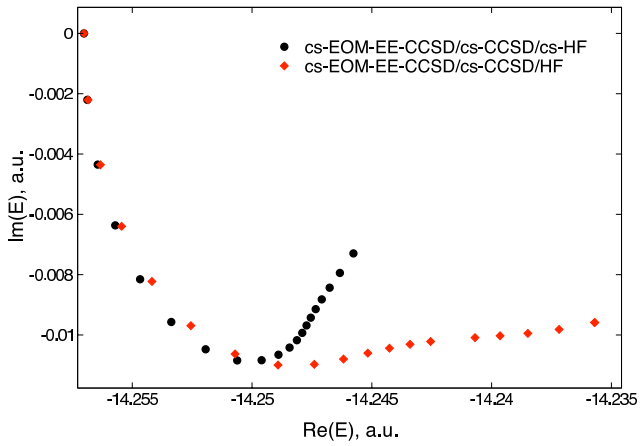

Figure 4.11: θ-trajectories for the $1s^2 2p3s$ resonance in Be computed with cs-EOM-EE-CCSD/cs-CCSD/cs-HF and cs-EOM-EE-CCSD/cs-CCSD/HF using the 14s11p basis set.

Table 4.4 summarizes the computed values of the position and width of the 2p3s resonance. The cs-EOM-EE-CCSD/cs-CCSD/cs-HF calculation with the 14s14p5d basis and using frozen core yields 10.92 and 0.465 eV for the resonance position and width, respectively. The values are in good agreement with the experimental values (ΔE=10.89 eV and Γ=0.531 eV). Full cs-EOM-EE-CCSD results (with all electrons active) are close to the frozen core approximation, as validated for 14s11p basis for which the values of resonance position and width computed with and without frozen core approximation differ by less than 0.1 eV. Detailed study of the basis set effects in the framework of cs-EOM-EE-CCSD calculations of many-electron atomic resonances is the subject of future work.

4.4 Conclusions

We present the implementation of the complex-scaled EOM-EE-CCSD approach, a method capable of describing both shape and Feshbach resonances from the first principles. As benchmark systems, we considered Feshbach $2s^2$ resonances in He, H^-, and Be. We investigated the basis set effects on the computed resonance energy and lifetime and analyzed its origin. We found that even moderately diffuse basis sets, e.g., aug-cc-pVTZ+[3s3p3d], are sufficient to reproduce the resonance lifetimes with a reasonable accuracy. This result is supported by the analysis of the radial electronic densities, which exhibit no significant continuum tail even in the case of non-complex-scaled calculations. As Feshbach resonance decay is a two-electron process, proper treatment of electron correlation is crucial. We show that one has to use flexible enough bases which enable proper account for both radial and angular electronic correlation. For the $(2s)^2$ resonances, inclusion of at least p-type functions is required. Furthermore, the basis should be sufficiently flexible to describe changes in the wave function along θ-trajectory. That is why simple even-tempered bases show better performance than highly-optimized (for $\theta = 0$) standard basis sets augmented by additional diffuse sets.

Benchmark calculations on many-electron systems (Be) point to the importance of using complex-scaled HF reference and cs-CCSD for reliable description of ground and resonance states within the complex-scaled post-HF methods. cs-EOM-EE-CCSD/CCSD/HF yields qualitatively incorrect shapes of the θ-trajectories. Engaging cs-CCSD partially recovers orbital relaxation via T_1 coupled-cluster operator resulting in an accurate description of the resonance position and width. The most complete

cs-EOM-EE-CCSD/cs-CCSD/cs-HF method is a preferred approach; it provides quantitatively correct description of resonance position and width for Be 2p3s resonance, the model system of resonances in many-electron atoms.

4.5 Chapter 4 references

[1] B. Boudaïffa, P. Cloutier, D. Hunting, M. A. Huels, and L. Sanche. Resonant formation of DNA strand breaks by low-energy (3 to 20 eV) electrons. *Science*, 287:1658–1660, 2000.

[2] J. Simons. How do low-energy (0.1-2 eV) electrons cause DNA-strand breaks? *Acc. Chem. Res.*, 39:772–779, 2006.

[3] D.O. Kashinski, D. Talbi, and A.P. Hickman. Ab initio calculations of autoionizing states using block diagonalization: collinear diabatic states for dissociative recombination of electrons with N_2H^+. *Chem. Phys. Lett.*, 529:10–15, 2012.

[4] R.D. Thomas. When electrons meet molecular ions and what happens next: dissociative recombination from interstellar molecular clouds to internal combustion engines. *Mass Spec. Rev.*, 27:485–530, 2008.

[5] P.B. Corkum and F. Krausz. Attosecond science. *Nat. Phys.*, 3:381–387, 2007.

[6] V. Strelkov. Role of autoionizing state in resonant high-order harmonic generation and attosecond pulse production. *Phys. Rev. Lett.*, 104:123901, 2010.

[7] C. Bressler and M. Chergui. Ultrafast X-ray absorption spectroscopy. *Chem. Rev.*, 104:1781–1812, 2004.

[8] J. Ullrich, A. Rudenko, and R. Moshammer. Free-electron lasers: new avenues in molecular physics and photochemistry. *Annu. Rev. Phys. Chem.*, 63, 2012. 635-660.

[9] R. Santra. Concepts in x-ray physics. *J. Phys. B.*, 42:023001, 2009.

[10] L.H. Andersen, H. Bluhme, S. Boyé, T.J.D. Jørgensen, H. Krogh, I.B. Nielsen, S.B. Nielsen, and A. Svendsen. Experimental studies of the photophysics of gas-phase fluorescent protein chromophores. *Phys. Chem. Chem. Phys.*, 6:2617–2627, 2004.

[11] S.B. Nielsen, A. Lapierre, J.U. Andersen, U.V. Pedersen, S. Tomita, and L.H. Andersen. Absorption spectrum of the green fluorescent protein chromophore anion *in vacuo*. *Phys. Rev. Lett.*, 87:228102, 2001.

[12] M.W. Forbes and R.A. Jockusch. Deactivation pathways of an isolated green fluorescent protein model chromophore studied by electronic action spectroscopy. *J. Am. Chem. Soc.*, 131:17038–17039, 2009.

[13] E. Epifanovsky, I. Polyakov, B.L. Grigorenko, A.V. Nemukhin, and A.I. Krylov. Quantum chemical benchmark studies of the electronic properties of the green fluorescent protein chromophore: I. Electronically excited and ionized states of the anionic chromophore in the gas phase. *J. Chem. Theory Comput.*, 5:1895–1906, 2009.

[14] E. V. Gromov, I. Burghardt, H. Köppel, and L. S. Cederbaum. Impact of sulfur vs oxygen on the low-lying excited state of trans-p-coumaric acid and trans-p-coumaric thio acid. *J. Phys. Chem. A*, 109:4623–4631, 2005.

[15] Z. He, C. H. Martin, R. Birge, and K.F. Freed. Theoretical studies on excited states of a phenolate anion in the environment of the photoactive yellow protein. *J. Phys. Chem. A*, 104:2939–2952, 2000.

[16] D. Zuev, K.B. Bravaya, T.D. Crawford, R. Lindh, and A.I. Krylov. Electronic structure of the two isomers of the anionic form of p-coumaric acid chromophore. *J. Chem. Phys.*, 134:034310, 2011.

[17] W. P. Reinhardt. Complex coordinates in the theory of atomic and molecular structure and dynamics. *Annu. Rev. Phys. Chem.*, 33:223–255, 1982.

[18] N. Moiseyev. Quantum theory of resonances: calculating energies, widths and cross-sections by complex scaling. *Phys. Rep.*, 302:212–293, 1998.

[19] N. Moiseyev. *Non-Hermitian quantum mechanics*. Cambridge University Press, 2011.

[20] S. Klaiman and I. Gilary. On resonance: a first glance into the behavior of unstable states. In C.A. Nicolaides, J.R. Sabin, and E.J. Brändas, editors, *Adv. Quantum Chem.*, volume 63, chapter 1, pages 1–31. Elsevier Inc., 2012.

[21] D. Neuhauser. Time-dependent reactive scattering in the presence of narrow resonances: Avoiding long propogation times. *J. Chem. Phys.*, 95:4927–4932, 1991.

[22] E.J. Heller. The semiclassical way to molecular spectroscopy. *Acc. Chem. Res.*, 14:368–375, 1981.

[23] F. Grossmann. Time-dependent semiclassical calculation of resonance lifetimes. *Chem. Phys. Lett.*, 262:470–476, 1996.

[24] A.U. Hazi and H.S. Taylor. Stabilization method of calculating resonance energies: Model problem. *Phys. Rev. A*, 1:1109, 1970.

[25] V.A. Mandelshtam, T.R. Ravuri, and H.S. Taylor. The stabilization theory of scattering. *J. Chem. Phys.*, 101:8792–8799, 1994.

[26] V.A. Mandelshtam and H.S. Taylor. Spectral projection approach to the quantum scattering calculations. *J. Chem. Phys.*, 102:7390–7399, 1995.

[27] P.W. Langhoff. Stieltjes-Tchebycheff moment-theory approach to molecular photoionization studies. In V. McKoy T. Rescigno and B. Schneider, editors, *Electron Molecule and Photon Molecule Collisions*, pages 183–224. Plenum, New York, 1979.

[28] I. Shimamura. Quasi-bound states of electronic and positronic few-body systems: Analysis of multichannel scattering information. In *Advances in Quantum Chemistry*, volume 63, pages 165–245. Elsevier Inc., 2012.

[29] J. Aguilar and J. M. Combes. A class of analytic perturbations for one-body Schrödinger Hamiltonians. *Commun. Math. Phys.*, 22:269–279, 1971.

[30] E. Balslev and J. M. Combes. Spectral properties of many-body Schrödinger operators with dilatation-analytic interactions. *Commun. Math. Phys.*, 22:280–294, 1971.

[31] B. Simon. Quadratic form techniques and the Balslev-Combes theorem. *Commun. Math. Phys.*, 27:1–9, 1972.

[32] G. Jolicard and E. J. Austin. Optical potential stabilisation method for predicting resonance levels. *Chem. Phys. Lett.*, 121:106–110, 1985.

[33] U. V. Riss and H.-D. Meyer. Calculation of resonance energies and widths using the complex absorbing potential method. *J. Phys. B*, 26:4503–4536, 1993.

[34] N. Moiseyev and J.O. Hirschfelder. Representation of several complex coordinate methods by similarity transformation operators. *J. Chem. Phys.*, 88:1063, 1988.

[35] W. Domcke. Theory of resonance and threshold effects in electron-molecule collisions: The projection-operator approach. *Phys. Reports*, 208:97–188, 1991.

[36] H. Feshbach. A unified theory of nuclear reactions .2. *Ann. Phys. (N.Y.)*, 19:287–313, 1962.

[37] Y. Sajeev and N. Moiseyev. Reflection-free complex absorbing potential for electronic structure calculations: Feshbach-type autoionization resonances of molecules. *J. Chem. Phys.*, 127:034105, 2007.

[38] U.V. Riss and H.-D. Meyer. Reflection-free complex absorbing potentials. *J. Phys. B*, 28:1475–1493, 1995.

[39] Y. Sajeev, M. Sindelka, and N. Moiseyev. Reflection-free complex absorbing potential for electronic structure calculations: Feshbach type autoionization of helium. *Chem. Phys.*, 329:307–312, 2006.

[40] P. Balanarayan, Y. Sajeev Y., and N. Moiseyev. Ab initio complex molecular potential energy surfaces by back-rotation transformation method. *Chem. Phys. Lett.*, 524:84–89, 2012.

[41] P.R. Zdanska and N. Moiseyev. Hartree-Fock orbitals for complex-scaled configuration interaction calculation of highly excited Feshbach resonances. *J. Chem. Phys.*, 123:194105, 2005.

[42] D.L. Yeager and M.K. Mishra. Algebraic modifications to second quantization for non-Hermitian complex scaled Hamiltonians with application to a quadratically convergent multiconfigurational self-consistent field method. *Int. J. Quant. Chem.*, 104:871–879, 2005.

[43] Y. Zhou and M. Ernzerhof. Calculating the lifetimes of metastable states with complex density functional theory. *J. Phys. Chem. Lett.*, 3:1916–1920, 2012.

[44] K. Samanta and D.L. Yeager. Investigation of ^{2}P Be^- shape resonances using a quadratically convergent complex multicongurational self-consistent field method. *J. Phys. Chem. B*, 112:16214–16219, 2008.

[45] S. B. Zhang and D. L. Yeager. A complex scaled multiconfigurational time-dependent HartreeFock method for studying resonant states. *Mol. Phys.*, 110:663–667, 2012.

[46] Y. Sajeev, R. Santra, and S. Pal. Analytically continued Fock-space multireference coupled-cluster theory: Application to the $^2\Pi_g$ shape resonance in e-N_2 scattering. *J. Chem. Phys.*, 122:234320, 2005.

[47] S. Pal, Y. Sajeev, and N. Vaval. Analytically continued Fock space multireference coupled-cluster theory: Application to the shape resonance. *Chem. Phys.*, 329:283–289, 2006.

[48] A. Ghosh, N. Vaval, and S. Pal. Equation-of-motion coupled-cluster method for the study of shape resonances. *J. Chem. Phys.*, 136:234110, 2012.

[49] C.W. McCurdy, T.N. Rescigno, E.R. Davidson, and J.G. Lauderdale. Applicability of self-consistent field techniques based on the complex coordinate method to metastable electronic states. *J. Chem. Phys.*, 73:3268–3273, 1980.

[50] B.R. Junker. Recent computational developments in the use of complex scaling in resonance phenomena. *Adv. At. and Mol. Phys*, 18:207–263, 1982.

[51] K.B. Bravaya, D. Zuev, E. Epifanovsky, and A.I. Krylov. Complex-scaled equation-of-motion coupled-cluster method with single and double substitutions for autoionizing excited states: Theory, implementation, and examples. *J. Chem. Phys.*, 138:124106, 2013.

[52] J.F. Stanton and R.J. Bartlett. The equation of motion coupled-cluster method. A systematic biorthogonal approach to molecular excitation energies, transition probabilities, and excited state properties. *J. Chem. Phys.*, 98:7029–7039, 1993.

[53] A.I. Krylov. Equation-of-motion coupled-cluster methods for open-shell and electronically excited species: The hitchhiker's guide to Fock space. *Annu. Rev. Phys. Chem.*, 59:433–462, 2008.

[54] N. Moiseyev, P.R. Certain, and F. Weinhold. Resonance properties of complex-rotated hamiltonians. *Mol. Phys.*, 36:1613–1630, 1978.

[55] C.W. McCurdy. *ACS Symposium series*, volume 263, pages 17–34. American Chemical Society, 1984.

[56] T. Sommerfeld and F. Tarantelli. Subspace iteration techniques for the caluclation of resonances using complex-symmetric Hamiltonians. *J. Chem. Phys.*, 112:2106, 2000.

[57] N. Moiseyev, P.R. Certain, and F. Weinhold. Complex-coordinate studies of helium autoionizing resonances. *Int. J. Quant. Chem.*, 14:727–736, 1978.

[58] N. Moiseyev, S. Friedland, and P.R. Certain. Cusps, trajectories, and the complex virial theorem. *J. Chem. Phys.*, 74:4739–4740, 1981.

[59] D.T. Chuljian and J. Simons. Coordinate rotation studies of H^-, He^-, Be^-, Mg^- resonances: Basis set and configuration list dependence. *Int. J. Quant. Chem.*, XXIII:1723–1738, 1983.

[60] T.N. Rescigno, C.W. McCurdy, and A.E. Orel. Extensions of the complex-coordinate method to the study of resonances in many-electron systems. *Phys. Rev. A*, 17:1931–1938, 1978.

[61] J. Geertsen, M. Rittby, and R.J. Bartlett. The equation-of-motion coupled-cluster method: Excitation energies of Be and CO. *Chem. Phys. Lett.*, 164:57–62, 1989.

[62] D.C. Comeau and R.J. Bartlett. The equation-of-motion coupled-cluster method. Applications to open- and closed-shell reference states. *Chem. Phys. Lett.*, 207:414–423, 1993.

[63] S.V. Levchenko and A.I. Krylov. Equation-of-motion spin-flip coupled-cluster model with single and double substitutions: Theory and application to cyclobutadiene. *J. Chem. Phys.*, 120(1):175–185, 2004.

[64] R.J. Bartlett and M. Musial. Coupled-cluster theory in quantum mechanics. *Rev. Mod. Phys.*, 79:291–352, 2007.

[65] E.R. Davidson. The iterative calculation of a few of the lowest eigenvalues and corresponding eigenvectors of large real-symmetric matrices. *J. Comput. Phys.*, 17:87–94, 1975.

[66] S. Rettrup. An iterative method for calculating several of the extreme eigensolutions of large real non-symmetric matrices. *J. Comput. Phys.*, 45:100–107, 1982.

[67] K. Hirao and H. Nakatsuji. A generalization of the Davidson's method to large nonsymmetric eigenvalue problems. *J. Comput. Phys.*, 45:246–254, 1982.

[68] L.V. Slipchenko and A.I. Krylov. Spin-conserving and spin-flipping equation-of-motion coupled-cluster method with triple excitations. *J. Chem. Phys.*, 123:084107–084120, 2005.

[69] E. Epifanovsky, M. Wormit, T. Kuś, A. Landau, D. Zuev, K. Khistyaev, I. Kaliman, P. Manohar, A. Dreuw, and A.I. Krylov. New implementation of high-level correlated methods using a general block-tensor library for high-performance electronic structure calculations. http://iopenshell.usc.edu/downloads/tensor/, 2011.

[70] E. Epifanovsky, M. Wormit, T. Kuś, A. Landau, D. Zuev, K. Khistyaev, P. Manohar, I. Kaliman, A. Dreuw, and A.I. Krylov. New implementation of high-level correlated methods using a general block-tensor library for high-performance electronic structure calculations. *J. Comput. Chem.*, 34:2293–2309, 2013.

[71] Y.K. Ho. Complex-coordinate calculations for doubly excited states of two-electron atoms. *Phys. Rev. A*, 23:2137–2149, 1981.

[72] Y.K. Ho, A.K. Bhatia, and A. Temkin. Precision calculation of the lowest ^{1}s resonance in e-h scattering. *Phys. Rev. A*, 15:1423–1429, 1977.

[73] J. N. Bardsley and B.R. Junker. Complex coordinate space calculations for resonant states. *J. Phys. B*, 5:L178, 1972.

[74] A.K. Bhatia, A. Temkin, and H. Eiserike. Rigorous precision p -wave positron-hydrogen scattering calculation. *Phys. Rev. A*, 9:219–222, 1974.

[75] K. Kaufmann, W. Baumeister, and Jungen M. Universal gaussian basis sets for an optimum representation of rydberg and continuum wavefunctions. *J. Phys. B*, 22:2223–2240, 1989.

[76] I. Cacelli, R. Moccia, and A. Rizzo. Gaussian-type-orbital basis sets for the calculation of continuum properties in molecules: The differential photoionization cross section of molecular nitrogen. *Phys. Rev. A*, 57:1895–1905, 1998.

[77] A. Faure, J. D. Gorfinkiel, L. A. Morgan, and J. Tennyson. Gtobas: fitting continuum functions with gaussian-type orbitals. *Comp. Phys. Comm.*, 144:224–241, 2002.

[78] H. Barkay and N. Moiseyev. Complex density probability in non-hermitian quantum mechanics: Interpretation and a formula for resonant tunneling probability amplitude. *Phys. Rev. A*, 64:044702, 2001.

[79] A. Buchleitnert, B. Grémaud, and D. Delande. Wavefunctions of atomic resonances. *J. Phys. B*, 27:2663–2679, 1994.

[80] A. Venkatnathan, M.K. Mishra, and H.J. Aa. Jensen. An investigation of basis set effects in the characterization of electron $\pm$ atom scattering resonances using the dilated electron propagator method. *Theor. Chim. Acta*, 104:445–454, 2000.

[81] R. Wehlitz, D. Lukic, and B. Bluett. Resonance parameters of autoionizing be *2pnl* states. *Phys. Rev. A*, 68:052708, 2003.

Chapter 5: Complex absorbing potentials within EOM-CC family of methods: Theory, implementation, and benchmarks

5.1 Introduction

Metastable electronic states are important in diverse areas of science and technology ranging from high-energy applications (plasmas, attosecond and X-ray spectroscopies) to electron-molecule collisions (interstellar chemistry, radiolysis, DNA damage by slow electrons). These states (called resonances) can be accessed when molecules are excited above their ionization threshold, via electron attachment to closed-shell species, or by core ionization.

A concise and pedagogical introduction to the topic as well as references to earlier reviews can be found in Ref. 1. From the quantum mechanical point of view, resonance states belong to the continuum part of the spectrum and, therefore, their wave functions are not L^2-integrable. Yet, their wave functions bear certain resemblance to the bound states within the interaction region (i.e., close to the nuclei). Using boundary conditions

for the outgoing wave (Siegert or Gamow formalism, see Ref. 1), one arrives at the following form of the resonance wave function:

$$\Psi(x,t) = e^{-iEt}\phi_R(x) = e^{-\Gamma t/2}e^{-iE_R t}\phi_R(x) \tag{5.1}$$

where the phase-isolated part $\phi_R(x)$ resembles a bound-state wave function in the interaction region and E_R and Γ (real and imaginary parts of the complex energy $E = E_R - i\Gamma/2$) determine resonance position and width. The latter is inversely proportional to the resonance lifetime. Thus, the resonances appear as solutions of the Schrödinger equation with complex energy[1–4]. One can arrive at the same concept of complex energy via a completely different formalism (Feshbach approach) based on a separation of the Hamiltonian into coupled bound and continuum parts; in this approach, the resonance is described as a bound state coupled with the continuum, and the complex energy emerges from solving a non-Hermitian eigenproblem with an effective Hamiltonian[5].

One can avoid the inconveniences of working with continuum functions or fiddling with boundary conditions by reformulating the problem using complex variables[2–4]. The most rigorous approach is the complex-scaling formalism[2,6] in which all coordinates are scaled by a complex number $e^{-i\theta}$; however, practical applications of this method are limited by its extreme sensitivity to the one-electron basis set[7–11] as well as conceptual difficulties regarding the separation of nuclear and electronic motions of the scaled Hamiltonian[12–15].

These problems are avoided in an alternative approach in which the original (non-scaled) Hamiltonian is augmented by a complex potential $-i\eta\hat{W}$ devised to absorb the diverging tail of the resonance wave function[16–18]. In the complete basis set limit, these complex absorbing potential (CAP) methods yield exact resonance positions and widths

in the limit of zero CAP strength η[19]. Also, CAP methods are related to exterior complex scaling methods[20,21].

The use of CAPs in practical calculations is complicated by possible reflections leading to false resonances, sensitivity of the results to the form of the CAP W, and a strong basis set dependence[19,22]. Furthermore, one has to determine an optimal value for η, which is usually achieved by calculating trajectories $E(\eta)$ and requiring $|\eta\, dE/d\eta| = \min$.

In more familiar terms, reflections can be described as perturbations of the resonance wave functions and, consequently, energies caused by a finite-strength CAP. Finite basis sets give rise to additional reflections. In our previous paper[23], we introduced a simple density-matrix based correction to the energy that removes the perturbation due to the CAP. The correction was derived based on energy decomposition analysis and response theory. By analyzing the response equations, we also proposed an alternative criterion for finding an optimal value for η. Physically, our approach is grounded in the behavior of the resonance wave function and, ultimately, the one-particle density matrix. It was shown[23] that when the CAP is sufficiently strong, both real and imaginary parts of the density become near-stationary indicating that the resonance is stabilized. Then the perturbation to the resonance position by the CAP can be eliminated by subtracting the term $\eta\, Tr[\gamma W]$ from the energy. The optimal η is found by considering the de-perturbed resonance energies; moreover, we argued that η_{opt} is not the same for real and imaginary parts[23]. Preliminary benchmarks illustrated that this approach results in a computationally more robust scheme in which the dependence on the onset of the CAP is significantly reduced compared to the straightforward application of a CAP along with the original energy-based criterion for finding the optimal η, as was

done in most CAP applications[24–26].

One of the difficulties of understanding the capabilities and limitations of different approaches is that a method that has shown excellent performance for a small model problem may fail when applied to a realistic system. In the context of electronic structure, the results of calculations of resonances will also be affected by the quality of standard approximations such as the incompleteness of one- and many-electron basis sets[27]. Thus, it is important to test different methods for meta-stable states within robust and accurate *ab initio* approaches. For bound states, the coupled-cluster (CC) and equation-of-motion (EOM) hierarchies of methods[28–32] provide a reliable and predictive set of theoretical model chemistries[33]. These methods can be systematically improved to approach the exact solution, are size-extensive (or size-intensive for excitation energies), describe dynamical and non-dynamical correlation in one computational step, and do not involve system-dependent parameterization. The CC hierarchy of methods works best for wave functions dominated by a single Slater determinant, however, the EOM-CC approach extends this single-reference formalism to tackle various open-shell and multi-configurational cases[30,34].

In EOM-CC the target-state wave function is described by an excitation operator $\hat{R}$ acting on the reference-state CC wave function:

$$|\Psi\rangle = \hat{R}e^{\hat{T}}|0\rangle \tag{5.2}$$

with $|0\rangle$ as the reference Slater determinant (usually satisfying the HF equations) and $\hat{T}$ as the coupled-cluster operator. Different choices of $\hat{R}$ provide access to different target states, e.g., in EOM-EE-CC $\hat{R}$ is electron and spin-conserving thus enabling the

description of various excited states. Open-shell electron-attached states (such as temporary anions) can be described by EOM-EA-CC in which the reference state is again a well-behaved closed shell state and the operator $\hat{R}$ changes the number of electrons. Likewise, ionized states can be described by EOM-IP-CC with the operator $\hat{R}$ removing an electron. Thus, EOM-CC is a natural choice for extending the excited-state methodology to resonances via complex scaling and CAP approaches.

Recently, we presented an implementation of complex-scaled EOM-CCSD methods and illustrated their performance by considering several atomic systems (He, H^-, Be). Here we present an implementation of CAPs within the EOM-CCSD family of methods. Our main focus is on the EOM-EA-CC variant; however, our implementation also includes EOM-EE-CC. While limited implementations of CAPs within EOM-CC have been reported before (e.g., Refs. 24, 25), this work presents the first formally complete and production-level implementation of the method.

The main focus of the paper is on investigating the numeric performance of the method and the sensitivity of the results towards the CAP parameters and the choice of basis set. Our goal is to develop a black-box type approach that could be calibrated and then applied to the calculation of resonances without any prior knowledge of the system, as advocated by John Pople[33]. In particular, we want to avoid the system-dependent optimization of basis sets and the CAP's shape and onset. Thus, rather than aiming at results converged with respect to all computational parameters individually for each system, we wish to establish a uniform protocol that can be applied to any system and can be characterized by error bars estimated from prior calibration studies, as routinely performed in electronic structure calculations[27].

We note that the validation of the accuracy of computed resonance lifetimes in molecular systems is difficult[35]. A complete theoretical description should involve coupled electronic and nuclear dynamics; this is beyond the scope of the present paper, where we only compute the lifetime of the resonance state at a fixed molecular geometry. This is appropriate for resonances whose lifetimes are shorter than nuclear motions, or when nuclear motions do not strongly affect the computed Γ values (Condon-like approximation). Thus, our focus is on the comparison with other theoretical studies and the robustness of the results with respect to the one-electron basis set as well as small variations of the CAP parameters.

In this context, we add that the sensitivity of the results towards the one-electron basis set is of a fundamentally different origin in CAP calculations as compared to complex scaling. In the latter case, the basis should be sufficiently flexible to describe the resonance wave function at different values of the scaling angle, whereas in the former case, one simply needs to supply a basis set of sufficient spatial extent to represent a given CAP and a stabilized resonance wave function. This implies that the diffuseness of the basis must be coordinated with the CAP onset, e.g., in a compact basis, the CAP onset should be smaller, otherwise, the calculation will be blind to the CAP. Thus, although the basis-set dependence is a nuisance, its simpler nature in CAP calculations suggests that a solution can be found.

Originally CAP methods were introduced to study shape resonances. Since the decay of Feshbach resonances is a two-electron process (and the CAP is a one-electron operator), one may expect difficulties in describing Feshbach resonances within the CAP formalism. Moiseyev *et al.*[36–38] showed that additional steps need to be taken for the

construction of reflection-free CAPs in order to reliably calculate Feshbach-type resonances. The present paper focuses solely on understanding CAPs in the context of molecular shape resonances.

The article is structured as follows: Sections 5.2 and 5.3 present the formalism of CAP-augmented EOM-CC calculations and our implementation. In Section 5.4, we put forward a protocol to determine resonance positions and lifetimes and investigate its robustness towards the choice of the one-electron basis set and the CAP's onset. In Section 5.5, we subsequently apply our new scheme to a variety of molecular resonance states and compare the results to those obtained from experiment as well as using other theoretical approaches. Section 5.6 provides concluding remarks.

5.2 Theory

The basic idea of the CAP method[16–19] is the addition of an artificial complex potential to the original Hamiltonian:

$$H(\eta) = H - i\eta W \tag{5.3}$$

where W aims to absorbs an outgoing electron and η controls its strength. As in complex scaling[2–4,11,39], the addition of the CAP results in a non-Hermitian complex symmetric operator $H(\eta)$[16] converting resonances into square-integrable (L^2) wave functions. In our calculations we choose as CAP a quadratic potential with an unaffected region of cuboid (i.e., box) shape:

$$W = W_x + W_y + W_z \tag{5.4}$$

$$W_\alpha = 0 \quad \text{if} \quad |r_\alpha| < r_\alpha^0 \tag{5.5}$$

$$= (r_\alpha - r_\alpha^0)^2 \quad \text{if} \quad |r_\alpha| > r_\alpha^0$$

with r_α denoting the three Cartesian coordinates ($\alpha = x, y, z$). Thus, the CAP is controlled by 4 parameters: 3 parameters for the onset in each direction (r_x^0, r_y^0, r_z^0) and the strength η. In principle, the CAP strength is unbound ($\eta \in [0, \infty)$), but should be chosen such that the effect is large enough to absorb the wave function over a certain range, but not too large to prevent excessive perturbation of the wave function and the resonance energy[19].

In the complete one-electron basis set, the exact position of the resonance in the complex plane can be obtained as $\lim_{\eta \to 0} E(\eta)$[16]. That is, an infinitesimally weak CAP, which is represented exactly (and, therefore, goes to infinity at large r), is sufficient to stabilize the resonance without perturbing it. Working with finite Gaussian basis sets requires one to perform series of calculations for different η in order to find an optimal value of the strength parameter η_{opt} along the η-trajectory and the corresponding value of the resonance energy $E(\eta_{opt})$. A commonly used criterion for determining the optimal value of the strength parameter η is finding the minimum of the logarithmic velocity[16,19]:

$$v(\eta) = |\eta \frac{\partial E(\eta)}{\partial \eta}| \tag{5.6}$$

Unfortunately, the position of the resonance computed using this criterion is very sensitive to the CAP onset[17,23,26] and thus does not provide a black-box approach. In our recent paper[23], the first-order deperturbative correction to the raw resonance energies was introduced as:

$$U^R(\eta) = E^R(\eta) - \eta \mathrm{Tr}[\gamma^I(\eta) W] \tag{5.7}$$

$$U^I(\eta) = E^I(\eta) + \eta \mathrm{Tr}[\gamma^R(\eta) W] \tag{5.8}$$

with $\gamma(\eta)$ as the one-particle density matrix.

By looking separately at the real and imaginary parts of the deperturbed energy as a function of η, we showed that the energy becomes near stationary at certain values of optimal strength (η^R_{opt} and η^I_{opt}) giving the position and lifetime of the resonance. Our results showed that this recipe leads to values for the resonance position and lifetime which are less sensitive to the CAP onset and thus more robust than the raw values[23].

In our method the CAP is introduced at the HF level of theory, where we obtain a set of complex molecular orbitals (MOs) as the solution for a given strength η. As the next step we solve the CCSD equations for the ground state[28,29,40–42] using $H(\eta)$:

$$(\Phi_\mu|e^{-T}H(\eta)e^{T}|\Phi_0) = (\Phi_\mu|\bar{H}(\eta)|\Phi_0) = 0 \tag{5.9}$$

with Φ_μ denoting the excited determinants. The resulting amplitudes t^η are also complex.

To compute electronically excited and electron-attached resonance states we use EOM-EE-CCSD and EOM-EA-CCSD[30,43–47] methods that provide accurate and predictive descriptions for such target states. The wave function of the resonance state is found by solving a non-Hermitian eigenvalue problem for the right eigenvectors:

$$(\Phi_\mu|(\bar{H}(\eta) - E^\eta_{cc})R^\eta|\Phi_0) = R^\eta_\mu\Omega^\eta \tag{5.10}$$

which yields a set of complex amplitudes R^η, and complex excitation energies Ω^η. The latter are the raw, η-dependent resonance energies (which are equal to the difference between the total energy of the excited/attached EOM-CCSD state and the reference CCSD energy for a given η).

We note that for moderate CAP strengths and CAP onsets comparable with the spatial extent of the electron density of the reference state, the perturbation to the ground-state CCSD energy is small (10^{-5} a.u.) in contrast to complex-scaled calculations[11]. To compute the first-order correction to the raw resonance energies, the one-electron density matrix needs to be calculated. We employ an unrelaxed one-electron EOM-CCSD density matrix containing no amplitude or orbital-response terms[48]:

$$\gamma_{pq}(\eta) = \frac{1}{2}\,(0|L^{\eta}e^{-T^{\eta}}\{p^{+}q + q^{+}p\}\,e^{T^{\eta}}R^{\eta}|0) \tag{5.11}$$

where L^{η} and R^{η} are the left and right EOM-CCSD eigenvectors, respectively.

Because of the non-Hermitian nature of $\bar{H}$ left eigenvectors have to be computed and biorthogonalized against the right eigenvectors in order to compute the density matrix:

$$(\Phi_0|L^{\eta}(\bar{H}(\eta) - E^{\eta}_{cc})|\Phi_{\mu}) = \Omega^{\eta}L^{\eta}_{\mu}\ , \tag{5.12}$$

$$(L_i|R_j) = \delta_{ij}\ , \tag{5.13}$$

where i and j denote different electronic states. Once the density matrix is computed, the energy of the resonance state is corrected according to Eqs. (5.7) and (5.8).

The equations for CAP-CCSD and CAP-EOM-EE/EA-CCSD are identical to the original CCSD and EOM-EE/EA-CCSD equations except that all the input quantities such as the Fock matrix, the two-electron integrals, the MO matrix C, the T and R/L amplitudes are now complex and η-dependent. There is no need to add the CAP explicitly to the CCSD or EOM-CCSD equations since it is already included at the HF level.

In our paper on complex-scaled EOM-CC[11], we considered several variants of implementation, including the one in which the HF and CCSD equations for the reference state were solved for the unscaled Hamiltonian and the scaling was introduced

only at the EOM-CC level. This required significant reformulation of the EOM-CC equations. By analogy, one may also consider an implementation of CAP-EOM-CC in which the CAP is introduced only at the EOM-CC level; this will be the subject of future work.

Due to the CAP, the Hamiltonian becomes non-Hermitian and complex symmetric, which necessitates using a different metric, the so-called complex symmetric scalar product (c-product)[16,39,49,50], such that the variational principle is maintained:

$$(\psi_i|\psi_j) = \int \psi_i \psi_j dr \tag{5.14}$$

The difference to the regular scalar product is that the bra-vector is not complex conjugated. Mathematically, the c-product is a pseudoscalar product which does not induce a valid metric norm[39,49]. However one can still define the c-norm $(f|f)$ which is, contrary to the regular norm, complex in general and might become zero for a non-zero function f ("self-orthogonality"):

$$(f|f) = < f_{re}|f_{re} > - < f_{im}|f_{im} > +2i < f_{re}|f_{im} > = |a|e^{i\phi} \in \mathbb{C} \tag{5.15}$$

where $< | >$ is a regular scalar product which is equivalent to the c-product for real functions. Thus, the normalization of all vectors (for example left and right EOM-CC eigenvectors) is done by multiplying by a complex number[39]:

$$\hat{f} = |a|^{-\frac{1}{2}} e^{-i\phi/2} f \tag{5.16}$$

resulting in $\hat{f}$ being a normalized vector. As mentioned above, use of the c-norm may lead to "self-orthonormality" ($(f|f) = 0$ for $f \neq \vec{0}$), but this has not been observed in

practice. Orthogonality is defined for the c-product in the same manner as for scalar product as $(f|g) = 0$ (c-orthogonality).

5.3 Implementation

The suite of CAP-EOM-CC methods has been implemented in the Q-Chem electronic structure package[51,52] and will be available to users in the upcoming 4.2 release. For all complex CCSD and EOM-EE/EA-CCSD equations the libtensor library[53] for high-performance tensor operations has been used.

The calculations begin by solving the CAP-augmented restricted Hartree-Fock equations (CAP-RHF). CAP-RHF has been implemented as an extension to regular RHF using the object-oriented SCF library SCFman in Q-Chem that employs the Armadillo linear algebra library[54] for matrix computations. We add that an adaptation of our implementation for CAP-UHF will be straightforward. The CAP is introduced as an additional term in the regular Fock matrix:

$$F^{\eta}_{\mu\nu} = F^{0}_{\mu\nu} - i\eta W_{\mu\nu} \tag{5.17}$$

The molecular orbitals must satisfy the following orthonormalization condition in the c-product metric:

$$(C^{\eta})^{T} S C^{\eta} = I \tag{5.18}$$

where S is the overlap matrix in the atomic orbital (AO) basis and $(C^{\eta})^{T}$ is transposed but not conjugated. Since the augmented Fock matrix F^{η} is non-Hermitian, the orbitals obtained using standard linear algebra routines for the diagonalization of general matrices are not normalized. In order to satisfy orthogonality condition (Eq. 5.18), the MOs

are orthogonalized by using a modified Gram-Schmidt procedure with projections calculated using the c-product.

The Fock matrix $F^{\eta}_{\mu\nu}$ and the two-electron integrals $(\mu\nu|\lambda\sigma)$ are transformed into the MO basis by applying the complex orbital transformation matrix, $C^{\eta}_{\mu p}$; thus, these quantities become complex in the MO basis. The calculations proceed by solving the CCSD amplitude equations using a DIIS procedure[55] adapted for complex algebra with c-product. Once the complex t-amplitudes are converged, we find the excited-state energies and right eigenvectors by using Davidson's procedure[56] generalized for non-Hermitian complex matrices. Note that the original $\bar{H}$ matrix is also non-Hermitian but real, thus, one only needs to modify the procedure to make it work with complex quantities and the c-product. We observe that for large values of η the convergence of Davidson's procedure is sometimes problematic, likely due to more pronounced non-Hermiticity. However, we were always able to converge a reasonable number of roots (2-10) by tweaking the parameters of Davidson's procedure such as subspace size, residual inclusion threshold, etc. Since the one-electron density matrix is needed for the calculation of the first-order correction to the energies, we also solve for the left eigenvectors using Davidson's procedure, as well as for left and right eigenvectors together to ensure their c-biorthogonality [Eq. (5.13)].

The CAP is evaluated in the AO basis through numerical quadrature using a Becke-type grid[57] of (99, 590) points (99 radial points and 590 angular points per radial point). Currently, we have implemented a shifted quadratic potential $(r - r_0)^2$ for a rectangular cuboid [Eqs. (5.4) and (5.5)], but our implementation allows for an easy extension of the shape of the unaffected region as well as the type of potential, e.g., higher order monomials $(r - r_0)^4$, $(r - r_0)^6$, etc. Our implementation also includes the optional addition of a real potential to the CAP, as was advocated in Ref. 38.

Relative to the conventional CCSD and EOM-CCSD methods, the addition of the CAP does not change the scaling of the computational cost [$O(N^6)$ for CCSD and EOM-EE-CCSD, $O(N^5)$ for EOM-EA-CCSD] or the memory requirements [$O(N^4)$]. However, because we need to work with complex numbers, the computational cost increases roughly by a factor of 4 and the storage requirements increase by a factor of 2. Furthermore, computation of the first-order energy correction requires the left eigenvectors, which increases the computation time relative to EOM-CCSD energy calculations. Another possible issue arises when the resonance state is lying high in energy, so that the Davidson procedure will need to find all lower roots and it might require a lot of iterations to converge. To solve this issue, we have implemented iterative solvers for interior eigenstates for conventional EOM-CCSD methods. Implementation of the interior eigenvalue solvers for CAP-EOM methods is a subject of future work. Finally, the necessity to compute η-trajectories requires to run calculations for different values of η, but these calculations can be performed independently and can therefore be run in parallel.

5.4 Benchmark calculations

The necessity to find optimal values for the strength and the onset of the CAP as well as a pronounced basis set dependence of the results have prevented routine applications of CAP-based methods so far. Hence, investigating the numeric performance of CAP-EOM-CCSD, in particular with respect to the two aforementioned issues, is crucial for it to become a useful tool for studying resonances.

As for the one-electron basis set, it has been established that the straightforward application of standard basis sets yields poor results. Additional diffuse functions need

to be incorporated for two reasons: (i) to obtain a sufficiently good basis-set representation of the CAP and (ii) to describe the outgoing electron correctly[16,19,58]. Owing to these requirements, CAP-based computations were often carried out using non-standard basis sets[25,26,58–63]. While such approaches are able to provide results that agree with experiment for some resonance states, a treatment based on standard basis sets not involving any optimization procedure would be superior as it is of black-box type, has predictive power, and is also computationally less demanding. Since the shape of the resonance wave function is similar to a bound-state wave function in the interaction region, it should be possible to lessen the basis-set dependence to the degree observed in regular EOM-CCSD calculations.

Concerning the choice of the CAP onset, one has to realize that the artificial nature of the CAP implies that it is impossible to deduce from basic physical laws a universally applicable procedure for finding optimal parameters for the CAP strength, onset, and shape. While this is unsatisfying from a formal point of view, a pragmatic approach is to mitigate the dependence of the physically meaningful results on the artificial parameters as much as possible. Along these lines, we introduced a first-order correction[23] that was shown to desensitize resonance positions and widths to the choice of onset parameters by removing the perturbation due to the CAP. However, as this dependence cannot be removed completely, one has to develop a protocol for the unique and system-independent choice of the CAP onset to make CAP-EOM-CCSD applicable in a routine manner.

5.4.1 Computational Details

In the following we examine the π^* shape resonances of CO^- and $C_2H_4^-$ using different basis sets and CAP onsets. Both states arise from adding an electron to the lowest

unoccupied valence MO (LUMO) of the respective neutral molecule. Bond lengths and angles were chosen as R(CO) = 2.1316 a.u. for carbon monoxide and R(CC) = 2.5303 a.u., R(CH) = 2.0522 a.u., and $\angle$(CCH) = 121.2° for ethylene. All electrons were active in the correlation treatment. The CAP strength η was varied with a step size between 0.0001 a.u. and 0.001 a.u. Optimal values for η were determined according to the criterion from Eq. (5.6) as well as using the procedure outlined in Ref. 23. The respective results are referred to as zeroth-order and first-order in all tables and in the discussion below.

The basis sets used in our calculations were derived from the aug-cc-pV*X*Z (*X* = D, T, Q, 5) series[64] through augmentation by additional even-tempered basis functions. In all cases, the exponents for the first additional basis functions were obtained as one half of the exponent of the most diffuse basis function with the same angular momentum in the parent aug-cc-pV*X*Z basis set. The exponents for the remaining additional basis functions were calculated as one half of the exponent of the preceding function.

We explored two different series of basis sets, namely one where we augmented the basis sets for all atoms except for hydrogen (denoted as (A) below) and one where we placed only one set of diffuse functions with averaged exponents in the center of the molecule (denoted as (C) below). Since the second approach is computationally less demanding, it is especially preferable when targeting larger systems. To ensure that this strategy does not give rise to artifacts, we computed EOM-EE-CCSD excitation energies for a number of bound excited states of CO and C_2H_4 using the aug-cc-pVTZ+3s3p3d(C) and aug-cc-pVTZ+3s3p3d(A) bases. The results are reported in Table 5.4.1 together with the corresponding values for $\langle R^2 \rangle$, which are helpful in distinguishing valence states from Rydberg states. As apparent from Table 5.4.1 excitation energies based on the two basis sets differ by not more than 0.04 eV for the very diffuse

4 $^1A_1$ state of CO and by just 0.001 eV for all other states considered. This shows that placing the additional diffuse functions in the center does not lead to inferior results for the bound excited states and thus suggests the application of this scheme to resonances. We note that a similar scheme has been employed before in the context of stabilization techniques[65,66].

Table 5.1: EOM-EE-CCSD excitation energies and expectation values $\langle R^2 \rangle$ for several excited states of CO and C_2H_4 computed using the aug-cc-pVTZ basis set with additional diffuse basis functions placed at the all heavy atoms (A) or at the center of the molecule (C).

		aug-cc-pVTZ + 3s3p3d(A)		aug-cc-pVTZ + 3s3p3d(C)
Molecule	State	$\langle R^2 \rangle$/a.u.[a]	E/eV	E/eV
CO	$2\,^1A_1$	77.8	10.961	10.961
	$4\,^1A_1$	153.7	12.559	12.597
	$1\,^1B_2$	41.4	8.625	8.626
C_2H_4	$2\,^1A_g$	152.0	8.445	8.446
	$1\,^1B_{1g}$	116.7	9.791	9.791
	$1\,^1B_{1u}$	118.7	7.392	7.392

[a]The corresponding values for the ground states are 40.0 a.u. for CO and 83.3 a.u. for C_2H_4.

As for the choice of the CAP onset, we employed the square roots of the expectation values $\langle \alpha^2 \rangle$ ($\alpha = x,y,z$) for the ground states calculated at the CCSD level of theory as a starting point and considered the impact of small variations. The values used are $r_x^0 = r_y^0 = 2.76$ a.u. and $r_z^0 = 4.97$ a.u. for CO and $r_x^0 = 7.10$ a.u., $r_y^0 = 4.65$ a.u., and $r_z^0 = 3.40$ a.u. for C_2H_4. The orientation of the molecules was chosen as follows: For CO the z-axis formed the molecular axis, whereas the C_2H_4 molecule was placed in the xy-plane with the CC bond oriented along the x-axis.

Table 5.2: Dependence of resonance positions E_R and widths Γ of the $^2\Pi$ resonance of CO^- and the $^2B_{2g}$ resonance of $C_2H_4^-$ on the onset of the CAP. Values for η_{opt}, $(\eta \cdot dE/d\eta)_{\eta=\eta_{opt}}$, and $\|W\|$ are also reported. All values computed at the CAP-EOM-EA-CCSD/aug-cc-pVTZ+3s3p3d(C) level of theory.

Relative CAP onset[a]	Zeroth-order values				First-order values				
$\Delta r_x^0/\Delta r_y^0/\Delta r_z^0$/a.u.	E_R/eV	Γ/eV	η_{opt}/a.u.	$\eta\frac{dE}{d\eta}$/a.u.	E_R/eV	Γ/eV	η'_{opt}/a.u.	η''_{opt}/a.u.	$\|W\|$/a.u.
CO^-, $^2\Pi$ resonance									
0.0/0.0/0.0	2.088	0.650	0.0028	0.0017	1.981	0.585	0.0054	0.0048	241.9
0.5/0.5/0.0	2.061	0.612	0.0036	0.0021	1.956	0.573	0.0066	0.0060	214.0
-0.5/-0.5/0.0	2.113	0.691	0.0022	0.0011	1.999	0.591	0.0044	0.0040	274.2
0.0/0.0/0.5	2.087	0.644	0.0030	0.0017	1.981	0.582	0.0056	0.0050	235.4
0.0/0.0/-0.5	2.091	0.654	0.0028	0.0015	1.980	0.591	0.0052	0.0046	249.6
$C_2H_4^-$, $^2B_{2g}$ resonance									
0.0/0.0/0.0	2.091	0.430	0.0046	0.0023	2.032	0.328	0.0060	0.0085	272.0
0.5/0.0/0.0	2.089	0.434	0.0045	0.0023	2.032	0.330	0.0054	0.0089	266.7
-0.5/0.0/0.0	2.093	0.427	0.0046	0.0019	2.031	0.328	0.0054	0.0083	278.3
0.0/0.5/0.0	2.095	0.429	0.0050	0.0022	2.033	0.330	0.0057	0.0087	260.5
0.0/-0.5/0.0	2.093	0.431	0.0046	0.0019	2.032	0.326	0.0054	0.0083	285.4
0.0/0.0/0.5	2.088	0.388	0.0071	0.0020	2.023	0.301	0.0070	0.0109	255.3
0.0/0.0/-0.5	2.106	0.478	0.0037	0.0025	2.039	0.353	0.0042	0.0068	291.2

[a] A value of 0.0 refers to $r_\alpha^0 = \sqrt{\langle \alpha^2 \rangle}$, $\alpha = x, y, z$.

Table 5.3: Resonance positions E_R and widths Γ as well as values for η_{opt} and $\|W\|$ for the $^2\Pi$ resonance state of CO^- computed by CAP-EOMEA-CCSD using the aug-cc-pVTZ basis set with different additional augmentation. The variations reported for E_R and Γ refer to the change of these quantities upon varying the most important CAP onset parameter by 0.5 a.u. (see Section 5.4.2).

Basis Set	Raw Values			First-Order Corrected Values				
	E_R/eV	Γ/eV	η_{opt}/a.u.	E_R/eV	Γ/eV	η'_{opt}/a.u.	η''_{opt}/a.u.	$\|W\|$/a.u.
CO^-, $^2\Pi$ Resonance State								
aug-cc-pVTZ	2.517 ± 0.013	0.482 ± 0.120	0.0180	—[a]	0.252 ± 0.020	—[a]	0.0660	12.1
+ 3s(C)	2.517 ± 0.013	0.469 ± 0.120	0.0190	—[a]	0.215 ± 0.021	—[a]	0.0585	49.3
+ 6s(C)	2.518 ± 0.014	0.468 ± 0.012	0.0190	—[a]	—[a]	—[a]	—[a]	412.0
+ 3s3p(C)	2.025 ± 0.015	0.549 ± 0.024	0.0024	1.825 ± 0.004	0.357 ± 0.009	0.0082	0.0048	229.5
+ 6s6p(C)	2.023 ± 0.017	0.551 ± 0.023	0.0024	1.830 ± 0.004	0.364 ± 0.008	0.0082	0.0048	1078.3
+ 3s3p3d(C)	2.088 ± 0.026	0.650 ± 0.040	0.0028	1.981 ± 0.022	0.585 ± 0.012	0.0054	0.0048	241.9
+ 6s6p6d(C)	2.112 ± 0.027	0.665 ± 0.055	0.0034	2.015 ± 0.025	0.555 ± 0.057	0.0048	0.0340	1441.8
+ 3s3p3d3f(C)	2.081 ± 0.028	0.654 ± 0.043	0.0030	1.969 ± 0.022	0.588 ± 0.015	0.0056	0.0050	243.7
+ 3s3p(A)	2.102 ± 0.024	0.604 ± 0.050	0.0034	1.961 ± 0.016	0.446 ± 0.0026	0.0098	0.0066	505.9
+ 3s3p3d(A)	2.060 ± 0.022	0.885 ± 0.022	0.0016	1.969 ± 0.025	0.474 ± 0.032	0.0026	0.0305	541.0

[a] No stationary point could be located in the range $0 < \eta < 0.2$.

Table 5.4: Resonance positions E_R and widths Γ as well as values for η_{opt} and $\|W\|$ for the $^2B_{2g}$ resonance state of $C_2H_4^-$ computed by CAP-EOMEA-CCSD using the aug-cc-pVTZ basis set with different additional augmentation. The variations reported for E_R and Γ refer to the change of these quantities upon varying the most important CAP onset parameter by 0.5 a.u. (see Section 5.4.2).

Basis Set	Raw Values			First-Order Corrected Values				
	E_R/eV	Γ/eV	η_{opt}/a.u.	E_R/eV	Γ/eV	η'_{opt}/a.u.	η''_{opt}/a.u.	$\|W\|$/a.u.
$C_2H_4^-$, $^2B_{2g}$ Resonance State								
aug-cc-pVTZ	2.433[b]	0.479[b]	0.0380	2.411[b]	0.140[b]	0.0880	0.1610	11.8
+ 3s(C)	2.433[b]	0.479[b]	0.0383	2.411[b]	—[a]	0.0878	—[a]	51.9
+ 3s3p(C)	2.422 ± 0.024	0.495 ± 0.012	0.0370	2.410 ± 0.007	0.208 ± 0.030	0.1200	0.1700	253.5
+ 6s6p(C)	2.419[b]	0.494[b]	0.0360	2.409[b]	0.222[b]	0.1250	0.1690	1429.0
+ 3s3p3d(C)	2.091 ± 0.015	0.430 ± 0.046	0.0046	2.032 ± 0.009	0.328 ± 0.027	0.0060	0.0085	272.0
+ 6s6p6d(C)	1.976[b]	0.563[b]	0.0013	2.043[b]	0.334[b]	0.0076	0.0100	2014.7
+ 3s3p3d3f(C)	2.088[b]	0.441[b]	0.0046	2.028[b]	0.334[b]	0.0051	0.0085	274.0
+ 3s3p(A)	2.108 ± 0.018	0.420 ± 0.045	0.0049	2.017 ± 0.007	0.305 ± 0.030	0.0110	0.0085	502.8
+ 3s3p3d(A)	2.302 ± 0.043	0.536 ± 0.096	0.0245	2.180 ± 0.008	0.373 ± 0.050	0.0370	0.0290	539.2

5.4.2 The Impact of the CAP Onset

Table 5.2 compiles resonance positions E_R and lifetimes Γ for the $^2\Pi$ resonance of CO^- and the $^2B_{2g}$ resonance of $C_2H_4^-$ obtained using the aug-cc-pVTZ+3s3p3d(C) basis and different values for the CAP onset. We started with the aforementioned values for r_α^0 based on the spatial extent of the ground-state wave function and then varied r_x^0, r_y^0, and r_z^0 independently. In addition to E_R and Γ, we report optimal CAP strengths as well as values for the norm of the CAP in the AO representation. As expected, the representation of the CAP becomes more complete for smaller values of r_α^0. In addition, the results for $||W||$ show that the onset parameters are not all of the same importance: Consistent with the π^* character of the resonance states, r_z^0 makes the largest impact for $C_2H_4^-$ and $r_x^0 = r_y^0$ for CO^-. This trend is also reflected in all values for η_{opt}, E_R, and Γ: Varying the pivotal onset parameter by ± 0.5 a.u. shifts zeroth-order values for E_R by up to 0.028 eV and zeroth-order values for Γ by up to 0.048 eV, while the impact of the remaining onset parameters is roughly one order of magnitude smaller. We will thus focus on the onset parameter with the most pronounced influence in the remaining discussion.

Table 5.2 shows that both zeroth-order and first-order resonance positions and widths become smaller when increasing r_α^0, but we emphasize that these fluctuations are mitigated, especially for the width when considering first-order results: Here, E_R and Γ are both shifted by at most 0.025 eV upon variation of r_α^0. Also, it is apparent from Table 5.2 that smaller values for the CAP onset lead to smaller η_{opt} and that the first-order correction always entails larger values for η_{opt}. However, the relevance of the latter trends is debatable as the CAP strength η is not a physically meaningful quantity. One can argue along the same lines regarding the quantity $\eta \cdot dE/d\eta$ that needs to be minimized to find

the optimal value for η when using the conventional criterion from Eq. (5.6). As can be seen from Table 5.2, trends in $\eta \cdot dE/d\eta$ are weakly pronounced and not uniform.

5.4.3 The Role of Diffuse Basis Functions

To analyze the convergence of resonance positions and widths with respect to the addition of diffuse basis functions, we studied the π^* resonances of CO^- and $C_2H_4^-$ using different augmentations. All results are summarized in Tables 5.3 and 5.4. The crucial role of the angular momentum of the additional basis functions becomes clear at the first glance: In the case of CO^-, a jump of almost 0.5 eV is observed for the zeroth-order resonance position when going from aug-cc-pVTZ+3s(C) to aug-cc-pVTZ+3s3p(C), while an additional augmentation by three sets of d-functions leads to a change of 0.06 eV. Three sets of f-functions on top of aug-cc-pVTZ+3s3p3d(C) shift E_R by just 0.007 eV. For the resonance width, d-functions play a more important role: Going from the 3s(C) to the 3s3p(C) augmentation changes Γ by 0.08 eV and the next step to 3s3p3d(C) changes Γ by 0.10 eV, but the value for 3s3p3d3f(C) differs from that for the preceding augmentation by just 0.004 eV.

For $C_2H_4^-$, the changes are in general of similar magnitude as for CO^-, but the big jump is observed when adding d-functions for both E_R and Γ. We add that similar trends are found for the first-order E_R and Γ of both resonance states. Also, we note that the use of basis sets with an augmentation including just s-functions (for CO^-) or just s and p-functions (for $C_2H_4^-$) entails much larger η_{opt} values and sizable differences between zeroth-order and first-order values. Finally, the importance of the angular momentum of the diffuse basis functions is also reflected in the $E(\eta)$ trajectories for $C_2H_4^-$ displayed in Figure 5.1. Their shape is altered considerably when d-functions are added, but is very insensitive towards the addition of p-functions or f-functions. These findings about

the role of angular momentum can be easily related to the spatial symmetry of the resonance states and thus justify to choose an augmentation scheme based on symmetry considerations prior to the actual computations. In addition, we note that the values of $||W||$ show that adding basis functions with angular momentum higher than $\ell = 2$ does not significantly improve the basis-set representation of the CAP.

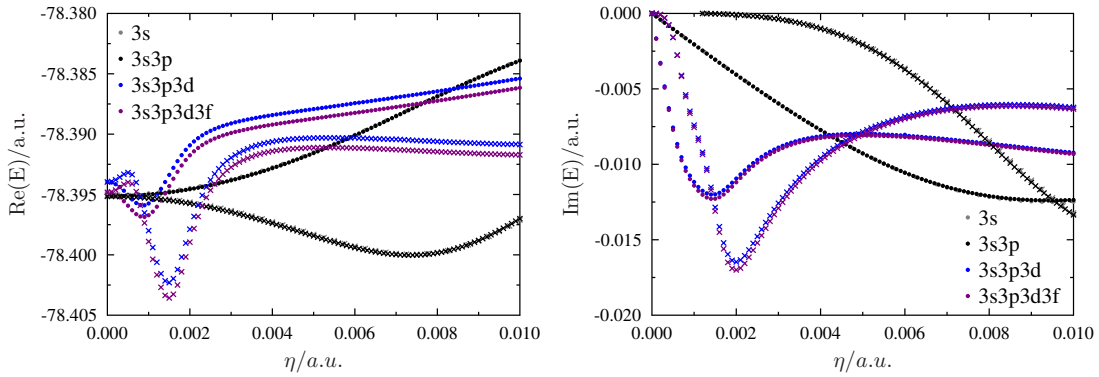

Figure 5.1: Real (right) and imaginary (left) parts of E and U as a function of the CAP strength parameter η for the $^2\Pi_g$ resonance of C_2H_4. All values computed by CAP-EOM-EA-CCSD/aug-cc-pVTZ with different additional diffuse functions. • refers to zeroth-order values, × to first-order values.

We also investigated the effect of adding more than three additional diffuse s, p, and d-functions. The corresponding results in Tables 5.3 and 5.4 show that, while values for $||W||$ become considerably larger indicating a more complete basis-set representation of W, the impact on resonance positions and widths does not exceed 0.035 eV except for one case: For $C_2H_4^-$, the zeroth-order E_R and Γ calculated using the augmentation schemes 3s3p3d(C) and 6s6p6d(C) differ by more than 0.1 eV. However, this discrepancy disappears when the first-order correction is applied. These results suggest that an accurate basis-set representation of the CAP near the interaction region is crucial for obtaining correct resonance positions and widths, whereas regions further away do not need to be covered by the basis set. Furthermore, since an increased dependence of E_R

and Γ on the CAP onset is found in some cases, we conclude that it is neither necessary nor advisable to employ more than three additional sets of diffuse basis functions with the required angular momentum.

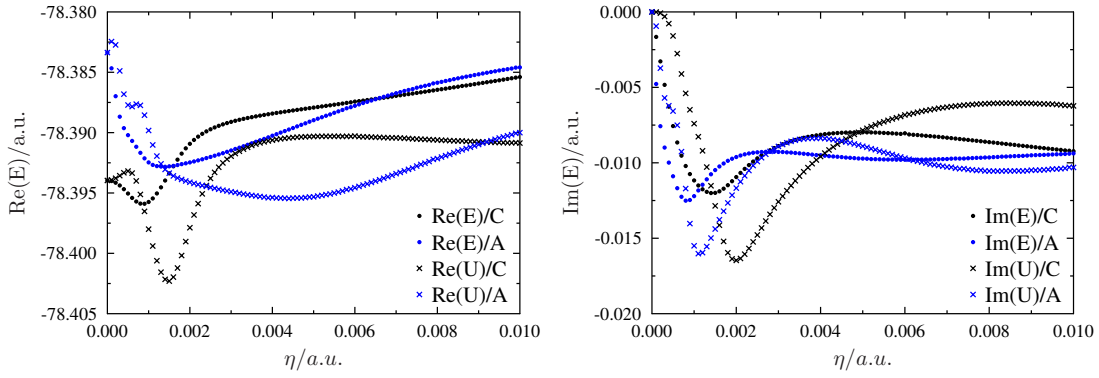

Figure 5.2: Real (right) and imaginary (left) parts of E and U as a function of the CAP strength parameter η for the $^2\Pi_g$ resonance of C_2H_4. All values computed by CAP-EOM-EA-CCSD/aug-cc-pVTZ+3s3p3d(C) and aug-cc-pVTZ+3s3p3d(A), respectively. • refers to zeroth-order values, × to first-order values.

Tables 5.3 and 5.4 also report the results from a number of calculations with the aug-cc-pVTZ+3s3p(A) and aug-cc-pVTZ+3s3p3d(A) bases. Contrary to what we observed for bound states (cf. Table 5.4.1), the differences between values for E_R and Γ obtained with the two augmentation schemes "C" and "A" are not negligible. Zeroth-order values differ by up to 0.23 eV and first-order values still by up to 0.15 eV. In one case, namely $C_2H_4^-$/aug-cc-pVTZ+3s3p, discrepancies of 0.4 eV are found, but this is probably related to the poor performance of the 3s3p augmentation scheme for $C_2H_4^-$ discussed earlier. However, we consider results obtained with the scheme "C" superior for several reasons: From the trajectories shown in Figure 5.2, one can see that the first-order quantities U^R and U^I enter the region of near-stationarity for smaller η, i.e., the resonance wave function shows faster convergence with respect to η, which is reflected in smaller η_{opt} values obtained in calculations using the augmentation scheme "C". Also,

an increased dependence on the CAP onset is found in some cases when using scheme "A".

5.4.4 The Role of the Valence Basis Set

Besides the impact of additional diffuse functions, variations in the valence basis set also influence the results for E_R and Γ. This is illustrated by Tables 5.5 and 5.6, which report values for resonance positions and widths of the $^2\Pi$ resonance of CO^- and the $^2B_{2g}$ resonance of $C_2H_4^-$ computed using the aug-cc-pVXZ (X = D, T, Q, 5) bases, each one augmented according to the 3s3p3d(C) scheme. Concerning the resonance position, one can see that for both zeroth-order and first-order values the basis-set dependence is more pronounced than for excitation energies corresponding to bound states of the neutral molecules. The position of the resonance state in CO^- still changes by 0.06 eV when going from aug-cc-pVQZ to aug-cc-pV5Z, whereas the largest shift observed for a bound state is less than 0.03 eV. We also note that the positions of the resonance states become smaller with increasing basis-set size, while the opposite is true for the excitation energies of the bound Rydberg states.

Concerning the resonance width, trends are less clear. For CO^-, both zeroth-order and first-order values show a non-monotonous behavior with respect to the basis-set size and no convergence is observed. The magnitude of the variations in Γ is however comparable to those in E_R. For $C_2H_4^-$ in contrast, the dependence of Γ on the basis-set size is much less pronounced and convergence seems to be reached. We also see that the dependence of both E_R and Γ on the CAP onset is somewhat mitigated when increasing the size of the valence basis set: For the aug-cc-pVDZ basis set, a decrease of r_x^0 and r_y^0 by 0.5 a.u. increases E_R and Γ of the $^2\Pi$ resonance of CO^- by 0.032 eV and 0.073 eV, respectively, whereas the same decrease leads to changes of just 0.025 eV and 0.026 eV

when using the aug-cc-pVQZ basis. This should be contrasted with the contrary impact of additional diffuse functions discussed before. Tables 5.5 and 5.6 also show that the values for η_{opt} decrease for larger basis sets, which is in line with that η_{opt} should be zero in the complete basis set limit[16].

Table 5.5: Resonance positions E_R and widths Γ as well as values for η_{opt} for the $^2\Pi$ resonance state of CO^- computed by CAP-EOMEA-CCSD using different valence basis sets. For comparison purposes, EOMEE-CCSD excitation energies for several bound states of CO are reported as well.

	aug-cc-pVDZ +3s3p3d(C)	aug-cc-pVTZ +3s3p3d(C)	aug-cc-pVQZ +3s3p3d(C)	aug-cc-pV5Z + 3s3p3d(C)
	$^2\Pi$ Resonance State of CO^-			
E_R (raw)/eV	2.303	2.088	1.987	1.926
Γ (raw)/eV	0.727	0.650	0.696	0.804
η_{opt}/a.u.	0.0046	0.0028	0.0020	0.0015
E_R (corr.)/eV	2.182	1.981	1.851	1.762
Γ (corr.)/eV	0.667	0.585	0.673	0.604
η'_{opt}/a.u.	0.0175	0.0054	0.0062	0.0034
η''_{opt}/a.u.	0.0100	0.0048	0.0046	0.0028
	Bound States of CO			
E ($2\ ^1A_1$)/eV	10.777	10.961	11.021	11.046
E ($4\ ^1A_1$)/eV	12.446	12.597	12.642	12.663
E ($1\ ^1B_2$)/eV	8.703	8.626	8.612	8.608

To gain further insight into the dependence of E_R and Γ on the size of the valence basis set we performed an energy decomposition analysis for the $^2\Pi$ resonance of CO^- and the $^2B_{2g}$ resonance of $C_2H_4^-$ based on the following partition of the electronic Hamiltonian:

$$H = \underbrace{E_{\text{HF}} + \sum_{pq} F_{pq}\{p^\dagger q\}}_{\text{one-electron part}} + \underbrace{\sum_{pqrs} \langle pq||rs\rangle \{p^\dagger q^\dagger sr\}}_{\text{two-electron part}} \tag{5.19}$$

Table 5.6: Resonance positions E_R and widths Γ as well as values for η_{opt} for the $^2B_{2g}$ resonance state of $C_2H_4^-$ computed by CAP-EOMEA-CCSD using different valence basis sets. For comparison purposes, EOMEE-CCSD excitation energies for several bound states of C_2H_4 are reported as well.

	aug-cc-pVDZ +3s3p3d(C)	aug-cc-pVTZ +3s3p3d(C)	aug-cc-pVQZ +3s3p3d(C)	aug-cc-pV5Z + 3s3p3d(C)
	$^2B_{2g}$ Resonance State of $C_2H_4^-$			
E_R (raw)/eV	2.191	2.091	1.988	—
Γ (raw)/eV	0.436	0.430	0.447	—
η_{opt}/a.u.	0.0032	0.0046	0.0025	—
E_R (corr.)/eV	2.230	2.032	1.903	—
Γ (corr.)/eV	0.302	0.328	0.373	—
η'_{opt}/a.u.	0.0210	0.0060	0.0054	—
η''_{opt}/a.u.	0.0248	0.0085	0.0043	—
	Bound States of C_2H_4			
E ($2\,^1A_g$)/eV	8.315	8.446	8.493	—
E ($1\,^1B_{1g}$)/eV	9.681	9.791	9.830	—
E ($1\,^1B_{1u}$)/eV	7.279	7.392	7.436	—

where the CAP is considered as a part of F_{pq} and $\langle pq||rs\rangle$ stands for the two-electron integrals in MO basis. The expectation value of the one-electron part is then interpreted as one-electron energy, whereas the expectation value of the remainder represents the contribution from the EOM-EA-CCSD two-particle density matrix. The results are compiled in Table 5.7. For the real part of the energy, this illustrates that the one-electron part converges significantly faster to the complete basis-set limit than the two-electron part, which suggests that the overall slow convergence of the total energy is mainly driven by an incomplete treatment of electron correlation. In contrast, for the imaginary part of the energy, the one-electron and two-electron parts seem to diverge in opposite directions with increasing basis-set size. This holds true for both molecules, but whereas the

Table 5.7: Energy decomposition analysis for the real and imaginary parts of the energies[a] of the $^2\Pi$ resonance of CO^- and the $^2B_{2g}$ resonance of $C_2H_4^-$ computed by CAP-EOM-EA-CCSD using different valence basis sets. All values in atomic units.

	aug-cc-pVDZ +3s3p3d(C)	aug-cc-pVTZ +3s3p3d(C)	aug-cc-pVQZ +3s3p3d(C)	aug-cc-pV5Z + 3s3p3d(C)
	$^2\Pi$ resonance of CO^-			
Total energy (real)	-112.9835	-113.0979	-113.1573	-113.1805
One-elec. part (real)[b]	-112.5652	-112.5920	-112.6078	-112.6167
Two-elec. part (real)	-0.4183	-0.5059	-0.5495	-0.5638
Total energy (imag.)	-0.0136	-0.0121	-0.0129	-0.0148
One-elec. part (imag.)	-0.0479	-0.0485	-0.0559	-0.0725
Two-elec. part (imag.)	0.0343	0.0364	0.0430	0.0577
	$^2B_{2g}$ resonance of $C_2H_4^-$			
Total energy (real)	-78.2836	-78.3881	-78.4333	—
One-elec. part (real)[b]	-77.8614	-77.8781	-77.8935	—
Two-elec. part (real)	-0.4223	-0.5100	-0.5399	—
Total energy (imag.)	-0.0080	-0.0080	-0.0082	—
One-elec. part (imag.)	-0.0289	-0.0318	-0.0389	—
Two-elec. part (imag.)	0.0209	0.0238	0.0307	—

[a]Evaluated at the respective η_{opt}. [b]Including nuclear repulsion energy.

trends roughly cancel out for $C_2H_4^-$, this is not the case for CO^- leading to a seemingly different behavior for the overall resonance width of the two systems.

One might be tempted to relate the basis set dependence of Γ to an insufficient description of the interaction of the resonance state with the continuum, but we point out that the addition of further diffuse functions has only little impact on E_R and Γ (cf. Section 5.4.3), which suggests the opposite. In total, we feel that the behavior of Γ requires further investigation in order to develop a scheme for the extrapolation to the complete basis set limit, but such an extension is beyond the scope of the present article.

We point out, however, that the variations in Γ observed for CO^- do not exceed 0.15 eV so that reliable computations are still possible based on our current approach.

5.5 Applications

In this section, we will report resonance positions and widths for a number of shape resonances of small to medium-sized molecules and compare the results from our CAP-EOM-EA-CCSD scheme to those obtained using other theoretical approaches or through experiment. Systems included in this study are N_2^-, CO^-, $C_2H_2^-$, $C_2H_4^-$, CH_2O^-, CO_2^-, and $C_4H_6^-$. All these resonance states except for the last one are derived by electron attachment to the π^* lowest unoccupied molecular orbital of the corresponding neutral molecules. $C_4H_6^-$ (1,3-butadiene) is a special case as its π system extends over more than a single double bond, which results in two low-lying resonance states.

We add that only the real part of the resonance wave function has a well defined single-attachment character, while the imaginary part has a considerably different form. Most often, it exhibits multireference character and is dominated by several single attachments to very diffuse orbitals. Also, its dependence on the CAP strength is more pronounced than that of the real part. A detailed investigation of this phenomenon is beyond the scope of this article.

In all calculations, we employed the scheme developed in Section 5.4, i.e., we chose the CAP onset based on the spatial extent of the ground-state wave function and used the aug-cc-pV*X*Z+3s3p3d(C) bases. Computational details are compiled in Table 5.8.

Table 5.8: Computational details of CAP-EOM-EA-CCSD calculations on N_2^-, CO^-, $C_2H_2^-$, $C_2H_4^-$, CH_2O^-, CO_2^-, and $C_4H_6^-$.

Molecule (State)	Leading configuration in the real part of the wave function	Bond lengths (bohr) and angles	Orientation	CAP onset (bohr) r_x^0	r_y^0	r_z^0
N_2^- $(1\,^2\Pi_g)$	$(1\sigma_g)^2(1\sigma_u)^2(2\sigma_g)^2(2\sigma_u)^2$ $(3\sigma_g)^2(1\pi_u)^4(1\pi_g)^1$	R(NN) = 2.0740	z-axis = molecular axis	2.76	2.76	4.88
CO^- $(1\,^2\Pi)$	$(1\sigma)^2(2\sigma)^2(3\sigma)^2(4\sigma)^2$ $(5\sigma)^2(1\pi)^4(2\pi)^1$	R(CO) = 2.1316	z-axis = molecular axis	2.76	2.76	4.97
$C_2H_2^-$ $(1\,^2\Pi_g)$	$(1\sigma_g)^2(1\sigma_u)^2(2\sigma_g)^2(2\sigma_u)^2$ $(3\sigma_g)^2(1\pi_u)^4(1\pi_g)^1$	R(CC) = 2.2733 R(CH) = 2.0088	z-axis = molecular axis	3.20	3.20	6.35
$C_2H_4^-$ $(1\,^2B_{2g})$	$(1a_g)^2(1b_{1u})^2(2a_g)^2(2b_{1u})^2$ $(1b_{2u})^2(3a_g)^2(1b_{3g})^2(1b_{3u})^2(1b_{2g})^1$	R(CC) = 2.5303 R(CH) = 2.0522 $\angle$(CCH) = 121.2°	z-axis $\perp$ molecular plane x-axis = CC bond	7.10	4.65	3.40
CH_2O^- $(1\,^2B_1)$	$(1a_1)^2(2a_1)^2(3a_1)^2(4a_1)^2$ $(1b_2)^2(5a_1)^2(1b_1)^2(2b_2)^2(2b_1)^1$	R(CO) = 2.2771 R(CH) = 2.0995 $\angle$(HCO) = 121.9°	z-axis = CO bond y-axis $\perp$ molecular plane	3.85	2.95	6.10
CO_2^- $(1\,^2\Pi_u)$	$(1\sigma_g)^2(1\sigma_u)^2(2\sigma_g)^2(2\sigma_u)^2(3\sigma_g)^2$ $1(\pi_u)^4(3\sigma_u)^2(4\sigma_g)^2(1\pi_g)^4(2\pi_u)^1$	R(CO) = 2.1978	z-axis = molecular axis	3.33	3.33	9.57
$C_4H_6^-$ $(1\,^2A_u)$ $(1\,^2B_g)$	$(\text{core})^2(6b_u)^2(7a_g)^2(1a_u)^2(1b_g)^2(2a_u)^1$ [a] $(\text{core})^2(6b_u)^2(7a_g)^2(1a_u)^2(1b_g)^2(2b_g)^1$ [a]	see footnote[b]		16.20	7.25	4.65

[a] $(\text{core})^2 = (1b_u)^2(1a_g)^2(2b_u)^2(2a_g)^2(3a_g)^2(3b_u)^2(4a_g)^2(4b_u)^2(5b_u)^2(5a_g)^2(6a_g)^2$ [b]Cartesian coordinates of symmetry-unique nuclei are in bohr: C(1.15735915, 0.76277974, 0.0), C(3.48113356, -0.22898634, 0.0), H(0.92483778, 2.80751355, 0.0), H(3.78431564, -2.26062161, 0.0), H(5.15268958, 0.95838430, 0.0)

5.5.1 $^2\Pi_g$ Resonance in N_2^-

The scattering of slow electrons by the N_2 molecule has been studied experimentally several times[67–74] so that the $^2\Pi_g$ resonance of N_2^- is rather well characterized. Consequently, this resonance has served as a testing ground for numerous theoretical approaches including stabilization techniques[65,66,75,76], methods based on complex scaling[10,77,78], CAP-based schemes[16,25,26,58–62] as well as further approaches[79–81]. Among other aspects, the impact of electron correlation on the resonance position and width[58] as well as their basis-set dependence[25,58,60] have been investigated in detail for this system. In addition, the resonance wave function has been studied over a wide range of different bond lengths and adiabatic excitation energies have been determined[10,76,82,83]. The potential interplay of the $^2\Pi_g$ ground state of N_2^- with other resonance states has been also investigated[10,84].

CAP-EOM-EA-CCSD results obtained for the resonance position and width are compiled in Table 5.9 together with several values available from the literature. The optimal CAP strengths found in our calculations are 0.0072 (0.0037) a.u. for the zeroth-order result and 0.0119 (0.0025) a.u. and 0.0148 (0.0071) a.u. for the real and imaginary part of the first-order result obtained with the aug-cc-pVTZ+3s3p3d(C) (aug-cc-pVQZ+3s3p3d(C)) basis set. We refrained from including experimental results in Table 5.9 except for the fixed-nuclei estimate by Berman *et al.* (E_R = 2.32 eV, Γ = 0.41 eV)[85], which has been often considered as the reference value in previous theoretical studies. We add that this value was not obtained directly from the experiment, but through a fit to the experimental data using Feshbach's projection operator formalism.

Table 5.9 illustrates that a confusing plethora of values for the resonance position and width of the $^2\Pi_g$ state of N_2^- have been reported. One can see that our results obtained from CAP-EOM-EA-CCSD overestimate E_R relative to the value from Ref.

85, while Γ is underestimated. For our highest-level calculation (first-order CAP-EOM-EA-CCSD/aug-cc-pVQZ+3s3p3d(C)) the deviation is about 0.15 eV for E_R and 0.13 eV for Γ. For E_R such a deviation is generally considered acceptable for EOM-EA-CCSD when dealing with bound states. An assessment of the deviation in Γ is more difficult as a comparison to bound states cannot be made. The differences between our highest-level value and our remaining results show however that the basis-set size and the correction for the CAP potential both make a sizable impact on E_R and Γ, but whereas these effects work in the same direction for the resonance position, the change in Γ is more involved. As for the first-order correction, the results obtained within the static-exchange approximation[16] exhibit trends similar to those observed in the present study.

Table 5.9 also shows that most approaches gave rise to too high values for the resonance position, whereas the reference value for the resonance width from Ref. 85 was often surprisingly well reproduced. The impact of electron correlation is illustrated by the comparison of high-level correlated methods to lower levels of theory. The position of the resonance state is consistently calculated to be above 3 eV with HF, DFT, and CIS based methods, regardless of whether stabilization techniques, complex scaling, or CAPs are employed, while the use of correlated methods leads to a significantly better agreement with the reference value. The only notable exception is the complex-scaled MRCI result (1.38 eV) from Ref. 10, which is almost 1 eV below the reference value. Interestingly, CAP-augmented MRCI calculations[59] with a rather similar basis set yielded a quite different resonance position (2.97 eV).

Compared to its effect on the resonance position, the role of electron correlation for the width Γ is less clear. For example, the complex-scaled HF and CAP-HF calculations

from Refs. 26, 77 agree with the reference value within 0.03 eV and 0.015 eV, respectively, while some correlated calculations led to deviations of more than 0.2 eV[59]. In fact, it was stated explicitly[58] that several values reported in the literature might have benefitted from error cancellation. We note that most authors reported values for Γ that were higher than the reference value with some low-level approaches overestimating the width by a factor of more than two, whereas our calculations underestimated Γ.

Regarding the basis-set dependence, a comparison between different schemes is hampered by the fact that a variety of different basis sets has been used in previous studies. Bearing in mind our findings from Sec. 5.4.4, it seems however justified to conclude for CAP-based methods that basis-set effects may account at least partly for the differences between values for Γ reported by different authors. In addition, the results from Ref. 76 suggest that, as compared to our CAP-augmented EOM-EA-CCSD scheme, the stabilization method combined with EOM-EA-CCSD leads to a somewhat faster convergence with respect to basis-set size. However, also the highest-level (aug-cc-pV5Z+3p) results obtained with the latter method (E_R = 2.49 eV, Γ = 0.496 eV) still show a sizable deviation from the reference values.

Table 5.9: Resonance positions E_R and widths Γ for the $^2\Pi_g$ resonance state of N_2^- obtained using different theoretical methods.

Method	E_R/eV	Γ/eV
Stieltjes imaging technique/special basis set[a]	2.23	0.40
Schwinger variational principle/ADC(3)/(11s8p3d)/[5s7p3d][b]	2.534	0.536
Complex scaling/HF-SCF/	3.19	0.44
Dunning's (9s5p)/[5s3p]+2d+(5p2d)/[3p2d]+4p6d[c]		
Complex scaling/MR-CI/Dunning's (9s5p)/[5s3p]+1d+10p[d]	1.38	0.414
Complex scaling/Σ^3 decouplings of the e^--propagator/[4s9p][e]	2.11	0.18
Stabilization/MR-CI/ Dunning's (9s5p)/[5s3p]+3p2d+4s1p1d(C)[f]	2.62	0.45
Stabilization/MR-CI/6-31+G*+3p[g]	2.34	0.51
Stabilization/MP-PT2/ANO(14s9p4d3f)/[4s3p2d1f]+2s2p7d4g(C)[h]	2.36	0.42
Stabilization/CIS/aug-cc-pVTZ+3p[i]	3.77	1.14
Stabilization/TDDFT(HFE_PBE)/aug-cc-pVTZ+3p[i]	3.078	0.54
Stabilization/EOMEA-CCSD/aug-cc-pVTZ+3p[i]	2.58	0.570
Stabilization/EOMEA-CCSD/aug-cc-pVQZ+3p[i]	2.49	0.502
Stabilization/EOMEA-CCSD/aug-cc-pV5Z+3p[i]	2.49	0.496
CAP/static exchange/[5s10p13d] (0th-order)[j]	3.888	1.363
CAP/static exchange/[5s10p13d] (1st-order)[j]	3.776	1.199
CAP-HF-SCF/(11s7p2d)/[5s4p2d][k]	3.28	0.395
CAP-DFT(LSD/XC)/(11s7p2d)/[5s4p2d][k]	3.39	0.506
CAP-MRCI/Dunning's (9s5p)/[5s3p]+(12p)/[9p]+2d[l]	2.97	0.65
TCAP-MRCI/Dunning's (11s6p)/[5s3p]+7p3d2f[m]	2.42	0.45
CAP-Σ(ADC(2))/TZP+9p2d2f[n]	2.58	0.55
CAP-Fock space-MRCC/TZ(7p2d)[o]	2.52	0.39
CAP-CIP/TZ(7p2d)[p]	2.28	0.482
CAP-EOMEA-CCSD/(11s8p3d)/[5s7p3d]+3p[q]	2.07	0.42
CAP-EOMEA-CCSD/aug-cc-pVTZ+3s3p3d(C) (0th-order)[r]	2.619	0.383
CAP-EOMEA-CCSD/aug-cc-pVTZ+3s3p3d(C) (1st-order)[r]	2.571	0.255
CAP-EOMEA-CCSD/aug-cc-pVQZ+3s3p3d(C) (0th-order)[r]	2.508	0.364
CAP-EOMEA-CCSD/aug-cc-pVQZ+3s3p3d(C) (1st-order)[r]	2.478	0.286
Estimate via Feshbach projection formalism based on experimental data[s]	2.32	0.41

[a] See Ref. 80. [b] See Ref. 81. [c] See Ref. 77. [d] See Ref. 10. [e] See Ref. 78. [f] See Ref. 65. [g] See Ref. 75. [h] See Ref. 66. [i] See Ref. 76. [j] See Ref. 16. [k] See Ref. 26. [l] See Ref. 59. [m] See Ref. 58. [n] See Ref. 60. [o] See Ref. 61. [p] See Ref. 62. [q] See Ref. 25. [r]This work. [s] See Ref. 85.

5.5.2 $^2\Pi$ Resonance in CO^-

While we have employed the $^2\Pi$ resonance of CO^- as a test system in Section 5.4, we will consider it in this section with a different focus, i.e., we will compare our results to those obtained using other methods. In contrast to N_2^-, which has been studied frequently, comparatively few results have been reported for the isoelectronic CO^-[23,25,66,78,86–89]. Table 5.10 compiles the values available from the literature together with some representative values from Section 5.4.

Table 5.10: Resonance positions E_R and widths Γ for the $^2\Pi$ resonance state of CO^- obtained using different methods.

Method	E_R/eV	Γ/eV
Boomerang model[a]	1.52	0.80
Close coupling method[b]	1.75	0.28
T-matrix/static exchange/(9s5p1d)/[4s3p1d][c]	3.4	1.65
Complex scaling/	1.71	0.08
Σ^2 decoupling of the electron propagator (real SCF)/4s5p[d]		
Complex scaling/Σ^3 decoupling of the electron propagator/4s5p[e]	1.65	0.14
Stabilization/MP-PT2/ANO(14s9p4d3f)/[4s3p2d1f]+2s4p7d5f(C)[f]	2.02	0.35
CAP-EOMEA-CCSD/4s5p(C)+4s5p1d(O)[g]	1.32	0.12
CAP-EOMEA-CCSD/maug-cc-pV(D+d)Z+3p[g]	1.42	0.44
CAP-EOMEA-CCSD/aug-cc-pVTZ+3s3p(A) (1st-order)[h]	1.954	0.433
CAP-EOMEA-CCSD/aug-cc-pVTZ+3s3p3d(C) (0th-order)[i]	2.088	0.650
CAP-EOMEA-CCSD/aug-cc-pVTZ+3s3p3d(C) (1st-order)[i]	1.981	0.585
CAP-EOMEA-CCSD/aug-cc-pV5Z+3s3p3d(C) (0th-order)[i]	1.926	0.804
CAP-EOMEA-CCSD/aug-cc-pV5Z+3s3p3d(C) (1st-order)[i]	1.762	0.604
Experiment[j]	1.50	0.40

[a] See Ref. 86. [b] See Ref. 87. [c] See Ref. 88. [d] See Ref. 89. [e] See Ref. 78. [f] See Ref. 66. [g] See Ref. 25. [h] See Ref. 23. [i] This work. [j] See Ref. 90.

Regarding the resonance position, Table 5.10 shows that most theoretical values are higher than the experimental value (1.50 eV)[74,90] as in the case of N_2^-. Also, similarly

to N_2^-, the resonance position is clearly overestimated in the static exchange approximation, in which electron correlation is neglected. Furthermore, CAP-EOM-EA-CCSD results obtained using different bases vary by up to 0.75 eV, which demonstrates the sizable impact of the basis set. We note, however, that our results obtained using the aug-cc-pV*X*Z+3s3p3d(C) bases approach the experimental value with growing basis-set size and that the first-order correction improves the resonance position with respect to experiment. Our highest-level result (1.762 eV, first order, aug-cc-pV5Z+3s3p3d(C) basis set) deviates from the experimental value by less than 0.3 eV.

The available values for the resonance width of CO^- differ by more than an order of magnitude as again illustrated by Table 5.10. The largest value reported (1.65 eV) was obtained in the static exchange approximation, while the narrowest width (0.08 eV) was computed from the Σ^2 decouplings of the electron propagator, a pattern that is again similar to N_2^-. The CAP-EOM-EA-CCSD results for the resonance width from the present work and Refs. 23, 25 vary by up to 0.68 eV, which illustrates once more the great influence of the basis set. As for the resonance position, the first-order correction improves the resonance width considerably with our highest-level result (0.604 eV, first-order, aug-cc-pV5Z+3s3p3d(C)) differing by 0.204 eV from the experimental value. However, we finally note that the experimental values for the resonance position and width of CO^- from Ref. 90 are not strictly comparable to the fixed-nuclei extrapolation for N_2^- from Ref. 85, which further complicates a rigorous assessment of the accuracy of theoretical approaches.

5.5.3 $^2\Pi_g$ Resonance in $C_2H_2^-$

$C_2H_2^-$ is a relatively well studied system and a number of theoretical[25,76,78,91–93] as well as experimental[94–99] values for the resonance position and width are available from the

literature. Those values as well as the results we obtained using our new CAP-EOM-EA-CCSD approach are compiled in Table 5.11. The optimal CAP strengths corresponding to our results are 0.0036 a.u. for the zeroth-order value and 0.0071 a.u. and 0.0058 a.u. for the real and imaginary part of the first-order value.

Table 5.11: Resonance positions E_R and widths Γ for the $^2\Pi_g$ resonance state of $C_2H_2^-$ obtained using different methods.

Method	E_R/eV	Γ/eV
Theory		
Multiple scattering Xα[a]	2.6	1.0
Feshbach projection/MR-CI/Dunning's (9s5p)/[5s3p]+1p1d+3p[b]	2.96	1.11
Complex scaling/	2.50	0.21
Σ^3 decouplings of the e^--propagator/5s9p1d, 3s3p(H)[c]		
Stabilization method/EOMEA-CCSD/aug-cc-pVTZ+3p[d]	2.77	1.50
Stabilization method/TDDFT(HFE_PBE)/aug-cc-pVTZ+3p[d]	2.4	0.6
CAP-EOMEA-CCSD/Dunning's (9s5p)/[5s3p]+4p1d, 2s1p(H)[e]	1.79	0.80
CAP-EOMEA-CCSD/aug-cc-pVTZ+3s3p3d(C) (0th-order)[f]	2.655	0.979
CAP-EOMEA-CCSD/aug-cc-pVTZ+3s3p3d(C) (1st-order)[f]	2.450	0.831
Experiment		
Trapped electron[g]	1.80/1.85	—
Vibrational excitation[h]	2.6	>1.0
Electron impact[i]	2.5	—
Dissociative attachment/electron transmission[j]	2.6	—
Electron transmission[k]	2.6	∼0.8

[a] See Ref. 91. [b] See Ref. 92. [c] See Ref. 78. [d] See Ref. 76. [e] See Ref. 25. [f] This work. [g] See Refs. 94 and 95. [h] See Ref. 97. [i] See Ref. 98. [j] See Ref. 99. [k] See Ref. 96.

Table 5.11 shows that our results for the resonance position are in qualitative agreement with those obtained from most experiments as well as from other theoretical approaches. Only when using the trapped electron method[94–96] considerably lower (∼0.7 eV) resonance positions were found. Our zeroth-order CAP-EOM-EA-CCSD result (2.655 eV) agrees within 0.05 eV with the experimental values from Refs.

96,97,99. We note that the first-order correction lowers the CAP-EOM-EA-CCSD result for E_R by about 0.2 eV bringing it closer to the experimental value from Ref. 98, but basis-set effects may have an impact of similar magnitude.

Theoretical values for the resonance width vary between 0.19 eV and 1.11 eV and only two rough estimates of 0.8 eV[96] and $>$1.0 eV[97] are available from experiment. Our calculations qualitatively confirm these two estimates with the zeroth-order result (0.979 eV) being closer to one value and the first-order result (0.831 eV) being closer to the other value. As mentioned for the resonance position, basis-set effects may have a sizable impact so that an ultimate decision between the two experimental values cannot be made.

5.5.4 $^2B_{2g}$ Resonance in $C_2H_4^-$

Similar to CO^-, the $^2B_{2g}$ resonance in $C_2H_4^-$ has been chosen as a benchmark system in Section 5.4 and here we will compare it with previously reported values. The $^2B_{2g}$ resonance in $C_2H_4^-$ has been studied quite extensively by both experimental[100–102] and theoretical methods[62,63,76,103–106]. Experimental measurements by electron scattering and electron impact techniques[100–102] located the position of the $^2B_{2g}$ resonance around 1.8 eV with a width of $\Gamma = 0.7$ eV. Theoretically this resonance has been studied by a wide variety of methods including complex scaling[103,105], CAP-based approaches[62,63], stabilization[76] as well as other techniques[104,106]. The reported theoretical values vary from 1.77 to 2.62 eV for the position of the resonance and from 0.11 to 1.32 eV for the width, i.e., by more than an order of the magnitude in the latter case. All values along with the results from our method are summarized in Table 5.12.

Similar to the trends observed for the previously discussed systems, the largest values for both position and lifetime are found by DFT in combination with the stabilization technique[76], whereas the shortest lifetimes are obtained when using electron propagator methods[106]. The resonance position obtained by CAP-EOM-EA-CCSD lies reasonably close (within 0.3 eV) to the experimental value (1.8 eV) for all basis sets used. Similar to results from EOM-CCSD calculations using stabilization techniques[76], the value of the resonance position is overestimated by CAP-EOM-EA-CCSD, but we observe a positive trend when enlarging the valence part of the basis set from triple zeta to quadruple zeta. Our best estimate for the position of the resonance (first-order CAP-EOM-EA-CCSD/aug-cc-pVQZ+3s3p3d(C)) is 1.903 eV, which differs from the experimental value by only 0.1 eV and is thus not worse than what is usually found in EOM-EA-CCSD calculations for bound states.

The resonance width calculated with CAP-EOM-EA-CCSD is underestimated in comparison to experiment by roughly a factor of two. However, similar to the position, enlargement of the valence basis set brings the theoretical value of the width closer to the experimental one. But in contrast to the position, the first-order correction worsens the value for the width as compared to experiment so that the best estimate from our calculations (0.373 eV, first-order CAP-EOM-EA-CCSD/aug-cc-pVQZ+3s3p3d(C)) still deviates by more than 0.3 eV. We add that we observed a similar underestimation of the resonance width in Section 5.5.1 for N_2^-.

Table 5.12: Resonance positions E_R and widths Γ for the $^2B_{2g}$ resonance state of $C_2H_4^-$ obtained using different methods.

Method	E_R/eV	Γ/eV
Theory		
Complex scaling/second order rotated propagator/5s7p[a]	1.94	0.110
Complex scaling/second order rotated propagator/5s8p[a]	2.49	0.234
Complex scaling/second order rotated propagator/5s9p[a]	1.88	0.442
Complex Kohn method[b]	1.83	0.460
Complex scaling/bi-variational SCF/5s7p [c]	1.93	0.2
Complex scaling/	1.86	0.18
Second order biorthogonal electron propagator/5s7p[d]		
Complex scaling/	1.89	0.18
Diagonal 2ph-TDA biorthogonal electron propagator/5s7p[d]		
CAP-CIP-$V_c^{(1,0)}(\eta^0)$/5s9p[e]	1.788	0.9675
CAP-CIP-$V_c^{(1,0)}(\eta^1)$/5s9p[e]	1.772	0.9520
CAP-CIP-$V_c^{(1,0)}(\eta^2)$/5s9p[e]	1.778	0.9076
CAP-FSMRCC-$V_c^{(1,0)}(\eta^1)$/aug-cc-pvDZ[f]	1.811	0.3780
CAP-FSMRCC-$V_c^{(1,0)}(\eta^2)$/aug-cc-pvDZ[f]	1.802	0.3662
Stabilization method/EOM-CCSD/aug-cc-pVTZ+3p[g]	2.06	0.64
Stabilization method/EOM-MP2/aug-cc-pVTZ+3p[g]	1.91	0.60
Stabilization method/ADC(2)/aug-cc-pVTZ+3p[g]	1.78	0.49
Stabilization method/KT(HFE_BLYP)/aug-cc-pVTZ+3p[g]	2.58	1.32
Stabilization method/KT(HFE_BPE)/aug-cc-pVTZ+3p[g]	2.62	1.08
Stabilization method/TDDFT(HFE_BPE)/aug-cc-pVTZ+3p[g]	2.49	0.31
CAP-EOMEA-CCSD/aug-cc-pVTZ+3s3p3d(C) (0th-order) [h]	2.091	0.430
CAP-EOMEA-CCSD/aug-cc-pVTZ+3s3p3d(C) (1st-order) [h]	2.032	0.328
CAP-EOMEA-CCSD/aug-cc-pVQZ+3s3p3d(C) (0th-order) [h]	1.988	0.447
CAP-EOMEA-CCSD/aug-cc-pVQZ+3s3p3d(C) (1st-order) [h]	1.903	0.373
Experiment		
Electron scattering[i]	1.78	—
Electron impact[j]	1.8	0.7
Elastic scattering[k]	1.8	0.7

[a] See Ref. 103. [b] Ref. 104. [c] See Ref. 105. [d] See Ref. 106. [e] See Ref. 62. [f] See Ref. 63. [g] See Ref. 76. [h] This work. [i] See Ref. 100, vertical electron affinity used. [j] See Ref. 101. [k] See Ref. 102.

5.5.5 $^2B_1$ Resonance in CH_2O^-

Formaldehyde is of particular interest for our study since it is the smallest molecule containing the highly-polar carbonyl group, which means that an accurate description of polarization and correlation effects is especially important. Zeroth-order and first-order estimates of the position and the lifetime of the $^2B_1$ resonance state of CH_2O^- along with previous experimental and theoretical data are compiled in Table 5.13. The optimal CAP strength for the zeroth-order CAP-EOM-EA-CCSD values is 0.02 a.u. and for the corresponding first-order values 0.024 a.u. and 0.021 a.u. for the real and imaginary part, respectively.

Experiments by electron transmission spectroscopy[107,108] and vibrational excitation[109] report values of 0.86-0.87 eV for the resonance position. For the resonance width, no experimental value is available from the literature, but only an estimate based on electron collision experiments near 1 eV[109], which shows the lifetime to be of the same order of magnitude as the period of the ν_2 vibrational mode (0.216 eV for neutral formaldehyde[110]). This vibrational excitation (ν_2) corresponds to the CO stretch mode, which is mainly excited after autodetachment of the electron from the $^2B_1$ resonance state[109]. We deduce that the width of the resonance should be of the order of 0.1 eV as it is the case for the π^* resonances of the molecules discussed before.

Previously reported theoretical values vary from 0.682 eV to 3.0 eV for the position and from 0.1 to 0.794 eV for the width of the resonance[24,111–116]. Similar to the molecules considered above, the static exchange approximation overestimates the position of the resonance by roughly a factor of three[111,112]. This can be explained by the high polarity of the carbonyl group and the reorganization effects when the molecule undergoes electron attachment, which results in strong correlation between the incident

electron and the electrons of the neutral formaldehyde and shows the need for an accurate treatment of electron correlation.

Table 5.13: Resonance positions E_R and widths Γ for the $^2B_1$ resonance state of CH_2O^- obtained using different methods.

Method	E_R/eV	Γ/eV
Theory		
Complex Kohn method[a]	1.0	0.5
Static exchange[a]	3.0	—
Complex scaling/electron propagator, zeroth order/4s6p1d(C)2s1p(H)[b]	1.0	0.1
Complex scaling/electron propagator, quasiparticle second order/4s6p1d(C)2s1p(H)[b]	0.99	0.1
Complex scaling/electron propagator, quasiparticle diagonal 2ph-TDA/4s6p1d(C)2s1p(H)[b]	0.98	0.11
Complex scaling/electron propagator, Diagonal 2ph-TDA/4s6p1d(C)2s1p(H)[b]	0.89	0.12
R-matrix method/augmented DZP [c]	1.32	0.546
R-matrix method/DZP[d]	1.46	0.794
Finite-element-discrete-model method[e]	0.682	0.429
CAP-SAC-CI /cc-pVDZ+[2s5p2d/2s2p] [f]	1.219	0.488
CAP-SAC-CI /cc-pVTZ+[2s5p2d/2s2p] [f]	1.119	0.462
CAP-SAC-CI /cc-pVQZ+[2s5p2d/2s2p] [f]	1.094	0.418
CAP-EOMEA-CCSD/aug-cc-pVTZ+3s3p3d(C) (0th-order)[g]	1.418	0.440
CAP-EOMEA-CCSD/aug-cc-pVTZ+3s3p3d(C) (1st-order)[g]	1.314	0.277
Experiment		
Electron transmission spectroscopy[h]	0.86	—
Vibrational excitation[i]	0.87	—

[a] See Ref. 111, 112. [b] See Ref. 113. [c] See Ref. 114. [d] See Ref. 115. [e] See Ref. 116. [f] See Ref. 24. [g] This work. [h] See Ref. 107, 108. [i] See Ref. 109.

We also note that the smallest width (0.1-0.12 eV) is reported for electron propagator methods[113], a pattern similar to N_2^-, CO^- and $C_2H_4^-$. Our method yields resonance positions of 1.418 eV and 1.314 eV in zeroth order and first order, respectively, which is

significantly higher than the experimental value, but close to the values obtained with the R-matrix method[114,115]. The widths obtained with CAP-EOM-EA-CCSD are 0.440 and 0.277 eV in zeroth order and first order, which agrees best with the results from SAC-CI calculations[24]. However, the lack of experimental data prevents a more rigorous assessment of the values for the width obtained with our method.

5.5.6 $^2\Pi_u$ Resonance in CO_2^-

The scattering of slow electrons by the CO_2 molecule is well characterized experimentally[117–123]. Besides higher-lying resonance states, the existence of a $^2\Pi_u$ metastable state in the range of 3.8-4 eV was established. Theoretically, this system has been studied most often with a special emphasis on the changes when going from the linear to a bent structure, where the $^2\Pi_u$ state splits into a $^2A_1$ and a $^2B_2$ component[124–127]. The role of a virtual state near 2 eV[128] and the interplay with other resonance states[127] have also been investigated. Somewhat surprisingly, the position and width of the $^2\Pi_u$ resonance of the linear molecule have not yet been studied using high-level quantum-chemical methods but only within the static exchange approximation[129–132].

Table 5.14 reports the results from the CAP-EOM-EA-CCSD calculations for the $^2\Pi_u$ resonance of linear CO_2^- along with theoretical and experimental values available from the literature. Optimal CAP strengths corresponding to our values are 0.0074 a.u. in zeroth order and 0.0295 a.u. (real part) and 0.0810 a.u. (imaginary part) in first order. One can see that CAP-EOM-EA-CCSD qualitatively reproduces the experimental values for the resonance position and also agrees within 0.2 eV with results from static exchange calculations. This is especially noteworthy as we observed in the preceding sections that the static-exchange approximation tends to overestimate the resonance position significantly. We also note that the impact of the first-order correction on the

Table 5.14: Resonance positions E_R and widths Γ for the $^2\Pi_u$ resonance state of CO_2^- obtained using different methods.

Method	E_R/eV	Γ/eV
Theory		
Scattering/static exchange+polarization/DZP basis set[a]	3.8	0.5
Schwinger variational method/static exchange/[5p4d/5p4d1f][b]	5.39	0.64
Schwinger variational method/	3.78	0.23
static exchange+polarization/[5s3p]+4s3p3d[c]		
Close coupling/	3.88	0.34
static exchange+polarization/DZP+add. diffuse functions[d]		
CAP-EOM-EA-CCSD/aug-cc-pVTZ+3s3p3d(C) (0th order)[e]	4.020	0.119
CAP-EOM-EA-CCSD/aug-cc-pVTZ+3s3p3d(C) (1st order)[e]	3.997	0.198
Experiment		
Electron scattering[f]	3.8	–
Electron transmission spectroscopy[g]	3.14[h]	0.20 ± 0.07
Electron impact[i]	3.8	–
Impact of slow electrons[j]	3.6	–
Electron transmission spectroscopy[k]	3.58	–
High resolution attachment spectrometry[l]	4.4	–

[a] See Ref. 129. [b] See Ref. 130. [c] See Ref. 131. [d] See Ref. 132. [e] This work. [f] See Ref. 117. [g] See Refs. 118, 119. [h] The energy of the lowest observed vibrational level is given. [i] See Ref. 120. [j] See Ref. 121. [k] See Ref. 122. [l] See Ref. 123.

resonance position is relatively small (0.02 eV) as compared to the systems discussed above. With respect to the resonance width, Table 5.14 shows that CAP-EOMEA-CCSD yields considerably smaller values than calculations in the static-exchange approximation, which can be related to the superior description of electron correlation in the former case. Also, the impact of the first-order correction on the width is sizable (0.08 eV). We finally point out that our first-order result for the resonance width (0.198 eV) agrees very well with the experimental value (0.20 eV) available from the literature[118].

5.5.7 ^2A_u and ^2B_g Resonances in $C_4H_6^-$

1,3-Butadiene is different from all species discussed before in that its π system extends over more than a single double bond. Two low-lying π^* resonances of ^2A_u and ^2B_g symmetry result from this electronic structure, both of which have been characterized experimentally[100,133]. However, while experimental values for the resonance position (0.62 eV and 2.82 eV) are available, no values for the width of either state have been reported in the literature. It was only concluded that the lower lying ^2A_u state should be longer lived as its spectrum exhibits vibrational structure. As for previous theoretical treatments of these resonances, only one study on the ^2A_u state employing conventional DFT/B3LYP, which found a surprisingly good agreement with experiment for the resonance position (0.76 eV), is available from the literature[134], but the resonance widths have apparently never been studied theoretically.

In Table 5.15, we report CAP-EOM-EA-CCSD results for the resonance positions and widths of both π^* resonances of 1,3-butadiene. For technical reasons, we employed the aug-cc-pVDZ+3s3p3d(C) basis instead of the aug-cc-pVTZ+3s3p3d(C) basis for this molecule, but in order to test again the validity of the "C" as compared to the "A" scheme, results obtained with the larger aug-cc-pVDZ+3s3p3d(A) basis are also included in Table 5.15. Optimal CAP strengths corresponding to the results for the ^2A_u state in Table 5.15 are 0.0074 a.u, 0.0115 a.u., and 0.0210 a.u. for the zeroth-order and first-order CAP-EOM-EA-CCSD calculations with the "C" basis-set and 0.0135 a.u., 0.0175 a.u., and 0.0310 a.u. for the respective calculations with the "A" basis set. For the ^2B_g state, optimal CAP strengths of 0.0098 a.u., 0.0270 a.u., and 0.0190 a.u. were obtained with the "C" basis set and of 0.0165 a.u., 0.0170 a.u., and 0.0350 a.u. with the "A" basis set.

Table 5.15: Resonance positions E_R and widths Γ for the ^2A_u and ^2B_g resonance states of $C_4H_6^-$ (1,3-butadiene anion) obtained using different methods.

Method	E_R/eV	Γ/eV
^2A_u state		
Theory		
DFT/B3-LYP/6-311+G(2df,p)[a]	0.76	–
CAP-EOM-EA-CCSD/aug-cc-pVDZ+3s3p3d(C) (0th order)[b]	1.336	0.110
CAP-EOM-EA-CCSD/aug-cc-pVDZ+3s3p3d(C) (1st order)[b]	1.327	0.059
CAP-EOM-EA-CCSD/aug-cc-pVDZ+3s3p3d(A) (0th order)[b]	1.348	0.145
CAP-EOM-EA-CCSD/aug-cc-pVDZ+3s3p3d(A) (1st order)[b]	1.332	0.103
Experiment[c]	0.62	–
^2B_g state		
Theory		
CAP-EOM-EA-CCSD/aug-cc-pVDZ+3s3p3d(C) (0th order)[b]	2.683	0.720
CAP-EOM-EA-CCSD/aug-cc-pVDZ+3s3p3d(C) (1st order)[b]	2.538	0.509
CAP-EOM-EA-CCSD/aug-cc-pVDZ+3s3p3d(A) (0th order)[b]	2.647	0.919
CAP-EOM-EA-CCSD/aug-cc-pVDZ+3s3p3d(A) (1st order)[b]	2.544	0.630
Experiment[c]	2.82	–

[a] See Ref. 134. [b] This work. [c] See Ref. 100.

Table 5.15 illustrates that aug-cc-pVDZ+3s3p3d(C) and aug-cc-pVDZ+3s3p3d(A) yield very similar results for the resonance position. CAP-EOM-EA-CCSD overestimates the position of the ^2A_u resonance by about 0.7 eV regardless of the basis set used and also independent of whether the first-order correction is applied. For the ^2B_g state an overall better agreement with experiment is found (0.2-0.3 eV), but the first-order correction makes a sizable impact and moves the CAP-EOM-EA-CCSD values away from the experimental value. Note that based on the findings from Section 5.4, one should expect a significant change of all results when increasing the valence basis set.

Concerning the resonance width, our results support the experiment's hypothesis that the ^2A_u state is considerably longer lived than the ^2B_g state. We also note that first-order

results for the resonance width are smaller by 0.05 eV for the ^2A_u state and by 0.2-0.3 eV for the ^2B_g state. Also, the change from the "C" to the "A" basis set makes an impact of similar magnitude but in opposite direction. A final judgment of the accuracy of the results, however, cannot be made due to the lack of other theoretical or experimental estimates for the resonance width.

5.6 Conclusions

A complete and robust implementation of CAPs within EOM-EE-CCSD and EOM-EA-CCSD methods has been presented together with a protocol for studying molecular shape resonances without system-dependent optimization of basis set and CAP parameters.

In our approach, we have chosen the onset of the CAP as the expectation value of the spatial extent of the ground-state wave function, which ensures that the ground state is minimally perturbed by the CAP ($\sim 10^{-5}$ a.u.). We showed that resonance positions and lifetimes obtained from energies, which are corrected for the CAP potential in first order[16,23], are less sensitive ($\sim$ 0.03 eV) towards variation of the CAP onset than uncorrected zeroth-order energies. To determine the optimal CAP strength, we used the criterion from Ref. 23 for the separate stabilization of the real and imaginary part of the first-order corrected energy instead of the most widely used criterion $|\eta\, dE/d\eta| = min$ based on the zeroth-order energy.

Based on benchmark studies for the π^* resonances of CO^- and $C_2H_4^-$, we illustrated that standard valence basis sets (for example, aug-cc-pVTZ) augmented by a set of diffuse functions in the center of the molecule are suitable for the study of resonance states with CAP-EOM-EA-CCSD. We showed that the use of only few diffuse functions of each angular momentum is sufficient for an accurate description of the diffuse part of

the resonance wave function. The further addition of diffuse functions has little impact on resonance positions and lifetimes. We also note that the inclusion of diffuse functions with angular momentum up to $\ell = 2$ (d-functions) is essential for π^* resonances, thus suggesting that a set [3s3p3d] of diffuse functions should be sufficient for most applications. The convergence of resonance positions and especially lifetimes with respect to the valence basis set is less clear, which indicates that electron correlation is of higher importance for resonances than for bound states. Although the theoretical understanding of the lifetime's dependence on the valence basis set remains an open problem, we emphasize that we did not observe variations of more than 0.15 eV in the lifetime. Regarding the resonance position, we showed that the performance of CAP-EOM-EA-CCSD is overall similar to that of EOM-EA-CCSD for bound electron-attached states. In total, our results for a variety of π^* shape resonances demonstrate that CAP-EOM-EA-CCSD is competitive relative to other approaches for the theoretical treatment of resonances and often able to reproduce experimental results for resonance positions and lifetimes. The importance of electron correlation is again illustrated comparing with the results from mean-field approaches, which often disagree qualitatively with experiment.

While the current paper shows the potential of CAP-EOM-CCSD approaches, it is also clear that the application to larger systems is hampered by the need to calculate η-trajectories, i.e., to recalculate the energy for different values of the CAP strength, which increases the computational cost considerably as compared to conventional EOM-CCSD calculations. To make our current implementation of CAP-EOM-CCSD faster and to increase its black-box character, a number of improvements will be the subject of future work. As the wave function changes smoothly with the CAP strength, one can expect that the use of the wave function parameters from the previous step as guess will accelerate the calculation of η-trajectories significantly provided that sufficiently small

step sizes are used. A further automatization will be possible by the implementation of analytic derivatives $dE/d\eta$ as this will enable the determination of optimal CAP strengths without that the user has to specify a step size and a range, where the search is performed. Put together, these developments will allow for the application of CAP-EOM-CCSD to resonance states of larger molecules as, for example, biochromophores, where standard EOM-CCSD is routinely used for the characterization of bound states.

5.7 Chapter 5 references

[1] S. Klaiman and I. Gilary. On resonance: a first glance into the behavior of unstable states. In C.A. Nicolaides, J.R. Sabin, and E.J. Brändas, editors, *Adv. Quantum Chem.*, volume 63, chapter 1, pages 1–31. Elsevier Inc., 2012.

[2] W. P. Reinhardt. Complex coordinates in the theory of atomic and molecular structure and dynamics. *Annu. Rev. Phys. Chem.*, 33:223–255, 1982.

[3] N. Moiseyev. Quantum theory of resonances: calculating energies, widths and cross-sections by complex scaling. *Phys. Rep.*, 302:212–293, 1998.

[4] N. Moiseyev. *Non-Hermitian quantum mechanics*. Cambridge University Press, 2011.

[5] H. Feshbach. A unified theory of nuclear reactions .2. *Ann. Phys. (N.Y.)*, 19:287–313, 1962.

[6] J. Aguilar and J. M. Combes. A class of analytic perturbations for one-body Schrödinger Hamiltonians. *Commun. Math. Phys.*, 22:269–279, 1971.

[7] T.N. Rescigno, C.W. McCurdy, and A.E. Orel. Extensions of the complex-coordinate method to the study of resonances in many-electron systems. *Phys. Rev. A*, 17:1931–1938, 1978.

[8] D.T. Chuljian and J. Simons. Coordinate rotation studies of H^-, He^-, Be^-, Mg^- resonances: Basis set and configuration list dependence. *Int. J. Quant. Chem.*, XXIII:1723–1738, 1983.

[9] P.R. Zdanska and N. Moiseyev. Hartree-Fock orbitals for complex-scaled configuration interaction calculation of highly excited Feshbach resonances. *J. Chem. Phys.*, 123:194105, 2005.

[10] M. Honigmann, R. J. Buenker, and H.-P. Liebermann. Complex self-consistent field and multireference single- and double-excitation configuration interaction calculations for the $^2\Pi_g$ resonance state of N_2^-. *J. Chem. Phys.*, 125(23):234304, 2006.

[11] K.B. Bravaya, D. Zuev, E. Epifanovsky, and A.I. Krylov. Complex-scaled equation-of-motion coupled-cluster method with single and double substitutions for autoionizing excited states: Theory, implementation, and examples. *J. Chem. Phys.*, 138:124106, 2013.

[12] C.W. McCurdy and T.N. Rescigno. Extension of the method of complex basis functions to molecular resonances. *Phys. Rev. Lett.*, 41:1364–1368, 1978.

[13] C.W. McCurdy. Complex-coordinate calculation of matrix elements of the resolvent of the Born-Oppenheimer Hamiltonian. *Phys. Rev. A*, 21:464–470, 1980.

[14] C. W. McCurdy and T. N. Rescigno. Complex-basis-function calculations of resolvent matrix elements: Molecular photoionization. *Phys. Rev. A*, 21:1499–1505, 1980.

[15] P. Balanarayan, Y. Sajeev Y., and N. Moiseyev. Ab initio complex molecular potential energy surfaces by back-rotation transformation method. *Chem. Phys. Lett.*, 524:84–89, 2012.

[16] U. V. Riss and H.-D. Meyer. Calculation of resonance energies and widths using the complex absorbing potential method. *J. Phys. B*, 26:4503–4536, 1993.

[17] R. Santra and L.S. Cederbaum. Non-hermitian electronic theory and applications to clusters. *Phys. Rep.*, 368:1–117, 2002.

[18] J.G. Muga, J.P. Palao, B. Navarro, and I.L. Egusquiza. Complex absorbing potentials. *Phys. Rep.*, 395:357–426, 2004.

[19] U.V. Riss and H.-D. Meyer. Reflection-free complex absorbing potentials. *J. Phys. B*, 28:1475–1493, 1995.

[20] N. Lipkin, N. Moiseyev, and E. Brändas. Resonances by the exterior-scaling method within the framework of the finite-basis-set approximation. *Phys. Rev. A*, 40:549–553, 1989.

[21] C.W. McCurdy, T.N. Rescigno, and D. Byrum. Making complex scaling work for long-range potentials. *Phys. Rev. A*, 56:1958–1969, 1997.

[22] U.V. Riss and H.-D. Meyer. The transformative complex absorbing potential method: a bridge between complex absorbing potentials and smooth exterior scaling. *J. Phys. B*, 31:2279–2304, 1998.

[23] T.-C. Jagau, K.B. Bravaya D. Zuev, E. Epifanovsky, and A.I. Krylov. A fresh look at resonances and complex absorbing potentials: Density matrix based approach. *J. Phys. Chem. Lett.*, 5:310–315, 2014.

[24] M. Ehara and T. Sommerfeld. CAP/SAC-CI method for calculating resonance states of metastable anions. *Chem. Phys. Lett.*, 537:107–112, 2012.

[25] A. Ghosh, N. Vaval, and S. Pal. Equation-of-motion coupled-cluster method for the study of shape resonances. *J. Chem. Phys.*, 136:234110, 2012.

[26] Y. Zhou and M. Ernzerhof. Calculating the lifetimes of metastable states with complex density functional theory. *J. Phys. Chem. Lett.*, 3:1916–1920, 2012.

[27] T. Helgaker, P. Jørgensen, and J. Olsen. *Molecular electronic structure theory*. Wiley & Sons, 2000.

[28] R.J. Bartlett and M. Musial. Coupled-cluster theory in quantum mechanics. *Rev. Mod. Phys.*, 79:291–352, 2007.

[29] R.J. Bartlett. The coupled-cluster revolution. *Mol. Phys.*, 108:2905–2920, 2010.

[30] A.I. Krylov. Equation-of-motion coupled-cluster methods for open-shell and electronically excited species: The hitchhiker's guide to Fock space. *Annu. Rev. Phys. Chem.*, 59:433–462, 2008.

[31] K. Sneskov and O. Christiansen. Excited state coupled cluster methods. *Wiley Interdisciplinary Reviews: Computational Molecular Science*, 2:566, 2011.

[32] R.J. Bartlett. Coupled-cluster theory and its equation-of-motion extensions. *Wiley Interdisciplinary Reviews: Computational Molecular Science*, 2(1):126–138, 2012.

[33] J.A. Pople. Theoretical models for chemistry. In D.W. Smith and W.B. McRae, editors, *Energy, Structure and Reactivity: Proceedings of the 1972 Boulder Summer Research Conference on Theoretical Chemistry*, pages 51–61. Wiley, New York, 1973.

[34] R.J. Bartlett. To multireference or not to multireference: That is the question? *Int. J. Mol. Sci.*, 3:579–603, 2002.

[35] T. Sommerfeld and H.-D. Meyer. Computing the energy-dependent width of temporary anions from L^2 ab initio methods. *J. Phys. B*, 35:1841–1863, 2002.

[36] Y. Sajeev, M. Sindelka, and N. Moiseyev. Reflection-free complex absorbing potential for electronic structure calculations: Feshbach type autoionization of helium. *Chem. Phys.*, 329:307–312, 2006.

[37] Y. Sajeev and N. Moiseyev. Reflection-free complex absorbing potential for electronic structure calculations: Feshbach-type autoionization resonances of molecules. *J. Chem. Phys.*, 127:034105, 2007.

[38] Y. Sajeev, V. Vysotskiy, L.S. Cederbaum, and N. Moiseyev. Continuum remover-complex absorbing potential: Efficient removal of the nonphysical stabilization points. *J. Chem. Phys.*, 131(21):211102, 2009.

[39] N. Moiseyev, P.R. Certain, and F. Weinhold. Resonance properties of complex-rotated hamiltonians. *Mol. Phys.*, 36:1613–1630, 1978.

[40] J. Cizek. On the correlation problem in atomic and molecular systems. Calculation of wavefunction components in Ursell-type expansion using quantum-field theoretical methods. *J. Chem. Phys.*, 45:4256–4266, 1966.

[41] J.A. Pople, R. Krishnan, H.B. Schlegel, and J.S. Binkley. Electron correlation theories and their application to the study of simple reaction potential surfaces. *Int. J. Quant. Chem.*, 14:545–560, 1978.

[42] G.D. Purvis and R.J. Bartlett. A full coupled-cluster singles and doubles model: The inclusion of disconnected triples. *J. Chem. Phys.*, 76:1910–1918, 1982.

[43] H. Sekino and R.J. Bartlett. A linear response, coupled-cluster theory for excitation energy. *Int. J. Quant. Chem. Symp.*, 26:255–265, 1984.

[44] J.F. Stanton and R.J. Bartlett. The equation of motion coupled-cluster method. A systematic biorthogonal approach to molecular excitation energies, transition probabilities, and excited state properties. *J. Chem. Phys.*, 98:7029–7039, 1993.

[45] M. Head-Gordon and T.J. Lee. Single reference coupled cluster and perturbation theories of electronic excitation energies. In R.J. Bartlett, editor, *Modern Ideas in Coupled Cluster Theory*. World Scientific, Singapore, 1997.

[46] J. Simons. *Encyclopedia of computational chemistry*, chapter Equation of motion (EOM) methods for computing electron affinities. J. Wiley & Son, New York, 1998.

[47] M. Nooijen and R.J. Bartlett. Equation of motion coupled cluster method for electron attachment. *J. Chem. Phys.*, 102:3629–3647, 1995.

[48] S.V. Levchenko, T. Wang, and A.I. Krylov. Analytic gradients for the spin-conserving and spin-flipping equation-of-motion coupled-cluster models with single and double substitutions. *J. Chem. Phys.*, 122:224106–224116, 2005.

[49] T. Sommerfeld and F. Tarantelli. Subspace iteration techniques for the caluclation of resonances using complex-symmetric Hamiltonians. *J. Chem. Phys.*, 112:2106, 2000.

[50] D. Zuev, K.B. Bravaya, T.D. Crawford, R. Lindh, and A.I. Krylov. Electronic structure of the two isomers of the anionic form of p-coumaric acid chromophore. *J. Chem. Phys.*, 134:034310, 2011.

[51] A.I. Krylov and P.M.W. Gill. Q-Chem: An engine for innovation. *WIREs Comput. Mol. Sci.*, 3:317–326, 2013.

[52] Y. Shao, L. Fusti-Molnar, Y. Jung, J. Kussmann, C. Ochsenfeld, S. Brown, A.T.B. Gilbert, L.V. Slipchenko, S.V. Levchenko, D.P. O'Neill, R.A. Distasio Jr, R.C. Lochan, T. Wang, G.J.O. Beran, N.A. Besley, J.M. Herbert, C.Y. Lin, T. Van Voorhis, S.H. Chien, A. Sodt, R.P. Steele, V.A. Rassolov, P. Maslen, P.P. Korambath, R.D. Adamson, B. Austin, J. Baker, E.F.C. Byrd, H. Daschel, R.J. Doerksen, A. Dreuw, B.D. Dunietz, A.D. Dutoi, T.R. Furlani, S.R. Gwaltney, A. Heyden, S. Hirata, C.-P. Hsu, G.S. Kedziora, R.Z. Khalliulin, P. Klunziger, A.M. Lee, W.Z. Liang, I. Lotan, N. Nair, B. Peters, E.I. Proynov, P.A. Pieniazek, Y.M. Rhee, J. Ritchie, E. Rosta, C.D. Sherrill, A.C. Simmonett, J.E. Subotnik, H.L. Woodcock III, W. Zhang, A.T. Bell, A.K. Chakraborty, D.M. Chipman, F.J. Keil, A. Warshel, W.J. Hehre, H.F. Schaefer III, J. Kong, A.I. Krylov, P.M.W. Gill, M. Head-Gordon. Advances in methods and algorithms in a modern quantum chemistry program package. *Phys. Chem. Chem. Phys.*, 8:3172–3191, 2006.

[53] E. Epifanovsky, M. Wormit, T. Kuś, A. Landau, D. Zuev, K. Khistyaev, P. Manohar, I. Kaliman, A. Dreuw, and A.I. Krylov. New implementation of high-level correlated methods using a general block-tensor library for high-performance electronic structure calculations. *J. Comput. Chem.*, 34:2293–2309, 2013.

[54] C. Sanderson. Armadillo: An open source C++ linear algebra library for fast prototyping and computationally intensive experiments, 2010. NICT.

[55] P. Pulay. *Chem. Phys. Lett.*, 73:393, 1980.

[56] E.R. Davidson. The iterative calculation of a few of the lowest eigenvalues and corresponding eigenvectors of large real-symmetric matrices. *J. Comput. Phys.*, 17:87–94, 1975.

[57] A. D. Becke. A multicenter numerical integration scheme for polyatomic molecules. *J. Chem. Phys.*, 88(4):2547, 1988.

[58] T. Sommerfeld, U. V. Riss, H.-D. Meyer, L. S. Cederbaum, B. Engels, and H. U. Suter. Temporary anions - calculation of energy and lifetime by absorbing potentials: the N_2^- $^2\Pi_g$ resonance. *J. Phys. B*, 31(18):4107, 1998.

[59] T. Sommerfeld and R. Santra. Efficient method to perform CAP/CI calculations for temporary anions. *Int. J. Quant. Chem.*, 82:218–226, 2001.

[60] S. Feuerbacher, T. Sommerfeld, R. Santra, and L. S. Cederbaum. Complex absorbing potentials in the framework of electron propagator theory. II. Application to temporary anions. *J. Chem. Phys.*, 118(14):6188–6199, 2003.

[61] Y. Sajeev, R. Santra, and S. Pal. Analytically continued Fock-space multireference coupled-cluster theory: Application to the $^2\Pi_g$ shape resonance in e-N_2 scattering. *J. Chem. Phys.*, 122:234320, 2005.

[62] Y. Sajeev, R. Santra, and S. Pal. Correlated complex independent particle potential for calculating electronic resonances. *J. Chem. Phys.*, 123(20):–, 2005.

[63] S. Pal, Y. Sajeev, and N. Vaval. Analytically continued Fock space multireference coupled-cluster theory: Application to the shape resonance. *Chem. Phys.*, 329:283–289, 2006.

[64] R.A. Kendall, Jr. T.H. Dunning, and R.J. Harrison. Electron affinities of the first-row atoms revisited. systematic basis sets and wavefunctions. *J. Chem. Phys.*, 96:6796–6806, 1992.

[65] B. M. Nestmann and S. D. Peyerimhoff. CI method for determining the location and width of resonances in electron-molecule collision processes. *J. Phys. B*, 18(21):4309, 1985.

[66] A. F. Izmaylov, S. O. Adamson, and A. Zaitsevskii. Multipartitioning many-body perturbation theory calculations on temporary anions: applications to N_2^- and CO^-. *J. Phys. B*, 37(11):2321, 2004.

[67] C. Ramsauer and R. Kollath. Die Winkelverteilung bei der Streuung langsamer Elektronen an Gasmolekülen. *Ann. Phys.*, 402:143–154, 1931.

[68] G. J. Schulz. Vibrational excitation of nitrogen by electron impact. *Phys. Rev.*, 125:229–232, 1962.

[69] G. J . Schulz. Vibrational excitation of N_2, CO, and H_2 by electron impact. *Phys. Rev.*, 135:A988, 1964.

[70] H. G. M. Heideman, C. E. Kuyatt, and G. E. Chamberlain. Resonances in the elastic and inelastic electron scattering from N_2. *J. Chem. Phys.*, 44:355–358, 1966.

[71] D. E. Golden. Low-energy resonances in e^--N_2 total scattering cross sections: The temporary formation of N_2^-. *Phys. Rev. Lett.*, 17:847–848, 1966.

[72] H. Ehrhardt and K. Willmann. Die Winkelabhängigkeit der Resonanzstreuung niederenergetischer Elektronen an N_2. *Z. Phys.*, 204:462–473, 1967.

[73] R. E. Kennerly. Absolute total electron scattering cross sections for N_2 between 0.5 and 50 eV. *Phys. Rev. A*, 21:1876–1883, 1980.

[74] G. J. Schulz. Resonances in electron impact on diatomic molecules. *Rev. Mod. Phys.*, 45:423, 1973.

[75] J. S.-Y. Chao, M. F. Falcetta, and K. D. Jordan. Application of the stabilization method to the N_2^- ($^2\Pi_g$) and Mg^- (^{2}P) temporary anion states. *J. Chem. Phys.*, 93(2):1125–1135, 1990.

[76] M. F. Falcetta, L. A. Di Falco, D. S. Ackerman, J. C. Barlow, and K. D. Jordan. Assessment of various electronic structure methods for characterizing temporary anion states: Application to the ground state anions of N_2, C_2H_2, C_2H_4, and C_6H_6. *J. Phys. Chem. A*, page DOI: 10.1021/jp5003287, 2014.

[77] T. N. Rescigno, A. E. Orel, and C. W. McCurdy. Application of complex coordinate SCF techniques to a molecular shape resonance: The $^2\Pi_g$ state of N_2^-. *J. Chem. Phys.*, 73(12):6347–6348, 1980.

[78] S. Mahalakshmi, A. Venkatnathan, and M. K. Mishra. Application of higher order decouplings of the dilated electron propagator to $^2\Pi$ CO^-, $^2\Pi_g$ N_2^-, and $^2\Pi_g$ $C_2H_2^-$ shape resonances. *J. Chem. Phys.*, 115(10):4549–4557, 2001.

[79] L. Dubé and A. Herzenberg. Absolute cross sections from the boomerang model for resonant electron-molecule scattering. *Phys. Rev. A*, 20:194–213, 1979.

[80] A. U. Hazi, T. N. Rescigno, and M. Kurilla. Cross sections for resonant vibrational excitation of N_2 by electron impact. *Phys. Rev. A*, 23:1089–11099, 1981.

[81] H.-D. Meyer. Optical potentials for electron-molecule scattering: A comparative study on the N_2 $^2\Pi_g$ resonance. *Phys. Rev. A*, 40(10):5605–5613, 1989.

[82] J. G. Lauderdale, C. W. McCurdy, and A. U. Hazi. Conversion of bound states to resonances with changing internuclear distance in molecular anions. *J. Chem. Phys.*, 79:2200–2205, 1983.

[83] A. Ghosh, A. Karne, S. Pal, and N. Vaval. CAP/EOM-CCSD method for the study of potential curves of resonant states. *Phys. Chem. Chem. Phys.*, 15:17915–17921, 2013.

[84] M. Honigmann, R. J. Buenker, and H.-P. Liebermann. Complex multireference configuration interaction calculations employing a coupled diabatic representation for the $^2\Pi_g$ resonance states of N_2^-. *J. Chem. Phys.*, 131:–, 2009.

[85] M. Berman, H. Estrada, L. S. Cederbaum, and W. Domcke. Nuclear dynamics in resonant electron-molecule scattering beyond the local approximation: The 2.3-eV shape resonance in N_2. *Phys. Rev. A*, 28:1363–1381, 1983.

[86] M. Zubek and C. Szmytkowski. Calculation of resonant vibrational excitation of CO by scattering of electrons. *J. Phys. B*, 10(1):L27–L29, 1977.

[87] N. Chandra. Low-energy electron scattering from CO. II. Ab initio study using the frame-transformation theory. *Phys. Rev. A*, 16(1):80–108, 1977.

[88] D. A. Levin, A. W. Fliflet, and V. McKoy. Low-energy e^--CO scattering in the static-exchange approximation. *Phys. Rev. A*, 21(4):1202–1209, 1980.

[89] R. A. Donnelly. Second-order calculation on the Doublet Pi CO shape resonance. *Int. J. Quant. Chem.*, 19:363–367, 1986.

[90] H. Erhardt, L. Langhans, F. Linder, and H. S. Taylor. Resonance scattering of slow electrons from H_2 and CO angular distributions. *Phys. Rev.*, 173:222–230, 1968.

[91] J. A. Tossell. Multiple-scattering X alpha calculation of spectral energies involving the π and π^* orbitals of C_2H_2. *J. Phys. B*, 18(3):387, 1985.

[92] V. Krumbach, B. M. Nestmann, and S. D. Peyerimhoff. The $^2\Pi_g$ shape resonance of the electron-acetylene scattering system: An ab initio treatment. *J. Phys. B*, 22(24):4001, 1989.

[93] A. Venkatnathan and M. K. Mishra. The $^2\Pi_g$ shape resonance in electron-acetylene scattering: an investigation using the dilated electron propagator method. *Chem. Phys. Lett.*, 296:223 – 232, 1998.

[94] D.F. Dance and I. C. Walker. Threshold electron impact excitation of acetylene. *Chem. Phys. Lett.*, 18(4):601 – 603, 1973.

[95] E. H. van Veen and F. L. Plantenga. Low-energy electron-impact excitation spectra of acetylene. *Chem. Phys. Lett.*, 38(3):493 – 497, 1976.

[96] K. D. Jordan and P. D. Burrow. Studies of the temporary anion states of unsaturated hydrocarbons by electron transmission spectroscopy. *Acc. Chem. Res.*, 11(9):341–348, 1978.

[97] K.-H. Kochem, W. Sohn, K. Jung, H. Ehrhardt, and E. S. Chang. Direct and resonant vibrational excitation of C_2H_2 by electron impact from 0 to 3.6 eV. *J. Phys. B*, 18(6):1253, 1985.

[98] L. Andric and R. I. Hall. Resonance phenomena observed in electron scattering from acetylene. *J. Phys. B*, 21(2):355, 1988.

[99] R. Dressler and M. Allan. A dissociative electron attachment, electron transmission, and electron energy-loss study of the temporary negative ion of acetylene. *J. Chem. Phys.*, 87(8):4510–4518, 1987.

[100] P. D. Burrow and K. D. Jordan. On the electron affinities of ethylene and 1,3-butadiene. *Chem. Phys. Lett.*, 36:595, 1975.

[101] I. C. Walker, A. Stamatovic, and S. F. Wong. Vibrational excitation of ethylene by electron impact: 1-11 eV. *J. Chem. Phys.*, 69:5532, 1978.

[102] R. Panajotovic, M. Kitajima, H. Tanaka, M. Jelisavcic, J. Lower, L. Campbell, M. J. Brunger, and S. J. Buckman. Electron collisions with ethylene. *J. Phys. B*, 36:1615, 2003.

[103] R. A. Donelly. Complex coordinate calculation on an ethylene shape resonance. *J. Chem. Phys.*, 84:6200, 1986.

[104] B. I. Schneider, T. N. Rescigno, B. H. Lengsfield III, and C. W. McCurdy. Accurate *ab initio* treatment of low-energy electron collisions with ethylene. *Phys. Rev. Lett.*, 66:2728, 1991.

[105] M. N. Medikeri and M. K. Mishra. Lowest unoccupied molecular orbital as the resonant orbital. An investigation using the bi-variational self-consistent field method. *Chem. Phys. Lett.*, 246:26–32, 1995.

[106] M. N. Medikeri and M. K. Mishra. Characterization of molecular shape resonances using different decouplings of the dilated electron propagator with application to ^{2}P CO_2 and $^2B_{2g}$ C_2H_4 shape resonances. *J. Chem. Phys.*, 103:676, 1995.

[107] P. D. Burrow and J. A. Michejda. Electron transmission study of the formaldehyde electron affinity. *Chem. Phys. Lett.*, 42:223–226, 1976.

[108] E. H. Van Veen, W. L. Van Dijk, and H. H. Brongersma. Low-energy electron-impact excitation spectra of formaldehyde, acetaldehyde and acetone. *Chem. Phys.*, 16:337–345, 1976.

[109] C. Benoit and R. Abouaf. Low-energy electron collisions with formaldehyde: interference phenomena in the differential vibrational excitation cross section. *Chem. Phys. Lett.*, 123:134–138, 1986.

[110] D. C. Moule and A. D. Walsh. Ultraviolet spectra and excited states of formaldehyde. *Chem. Rev.*, 75:67–84, 1975.

[111] T. N. Rescigno, C. W. McCurdy, and B. I. Schneider. Accurate ab initio treatment of low-energy electron collisions with polyatomic molecules: Resonant electron-formaldehyde scattering. *Phys. Rev. Lett.*, 63:248, 1989.

[112] B. I. Schneider, T. N. Rescigno, and C. W. McCurdy. Resonant vibrational excitation of h_2co by low-energy electron impact. *Phys. Rev. A*, 42:3132, 1990.

[113] S. Mahalakshmi and M. K. Mishra. The $^2B_1$ shape resonance in electron-formaldehyde scattering: An investigation using the dilated electron propagator method. *Chem. Phys. Lett.*, 296:43–50, 1998.

[114] S. Kaur and K.L. Baluja. Electron-impact study of formaldehyde using the R-matrix method. *J. Phys. B*, 38:3917–3933, 2005.

[115] M. Vinodkumar, H. Bhutadia, B. Antony, and N. Mason. Electron-impact rotationally elastic total cross sections for H_2CO and HCOOH over a wide range of incident energy (0.01-2000 eV). *Phys. Rev. A*, 84, 2011.

[116] G. A. Gallup. Application of the finite-element-discrete-model method for calculating resonance properties. *Phys. Rev. A*, 84:012701, 2011.

[117] C. R. Claydon, G. A. Segal, and H. S. Taylor. Theoretical interpretation of the electron scattering spectrum of CO_2. *J. Chem. Phys.*, 52:3387–3398, 1970.

[118] L. Sanche and G. J. Schulz. Electron transmission spectroscopy: Resonances in triatomic molecules and hydrocarbons. *J. Chem. Phys.*, 58:479, 1973.

[119] P. D. Burrow and L. Sanche. Elastic scattering of low-energy electrons at 180° in CO_2. *Phys. Rev. Lett.*, 28:333, 1972.

[120] M. J. W. Boness and G. J. Schulz. Vibrational excitation in CO_2 via the 3.8-eV resonance. *Phys. Rev. A*, 9:1969, 1974.

[121] M. Allan. Selectivity in the excitation of fermi-coupled vibrations in CO_2 by impact of slow electrons. *Phys. Rev. Lett.*, 87:033201, 2001.

[122] K. Aflatooni, B. Hitt, G. A. Gallup, and P. D. Burrow. Temporary anion states of selected amino acids. *J. Chem. Phys.*, 115:6489, 2001.

[123] S. Denifl, V. Vizcaino, T. D. Märk, E. Illenberger, and P. Scheier. High resolution electron attachment to CO_2 clusters. *Phys. Chem. Chem. Phys.*, 12:5219–5224, 2010.

[124] Y. Yoshioka, H. F. Schaefer, and K. D. Jordan. Theoretical investigation of the electron affinity of CO_2. *J. Chem. Phys.*, 75:1040, 1981.

[125] T. N. Rescigno, D. A. Byrum, W. A. Isaacs, and C.W. McCurdy. Theoretical studies of low-energy electron-CO_2 scattering: Total, elastic, and differential cross sections. *Phys. Rev. A*, 60:2186, 1999.

[126] T. N. Rescigno, W. A. Isaacs, A. E. Orel, H.-D. Meyer, and C. W. McCurdy. Theoretical study of resonant vibrational excitation of CO_2 by electron impact. *Phys. Rev. A*, 65:032716, 2002.

[127] A. Moradmand, D. S. Slaughter, D. J. Haxton, T. N. Rescigno, C. W. McCurdy, T. Weber, S. Matsika, A. L. Landers, A. Belkacem, and M. Fogle. Dissociative electron attachment to carbon dioxide via the $^2\Pi_u$ shape resonance. *Phys. Rev. A*, 88:032703, 2013.

[128] L. A. Morgan. Virtual states and resonances in electron scattering by CO_2. *Phys. Rev. Lett.*, 80:1873, 1998.

[129] M. A. Morrison, N. F. Lane, and L. A. Collins. Low-energy electron-molecule scattering: Application of coupled-channel theory to e-CO_2 collisions. *Phys. Rev. A*, 15:2186, 1977.

[130] R. R. Lucchese and V. McKoy. Study of electron scattering by CO_2 at the static-exchange level. *Phys. Rev. A*, 25:1963, 1982.

[131] C.-H. Lee, C. Winstead, and V. McKoy. Collisions of low-energy electrons with CO_2. *J. Chem. Phys.*, 111:5056, 1999.

[132] F. A. Gianturco and T. Stoecklin. The elastic scattering of electrons from CO_2 molecules: I. close coupling calcuations of integral and differential cross sections. *J. Phys. B*, 29:3933–3954, 1996.

[133] K. D. Jordan and P. D. Burrow. Temporary anion states of polyatomic hydrocarbons. *Chem. Rev.*, 87:557–588, 1987.

[134] D. Mariano, A. Vera, and A. B. Pierini. Species with negative electron affinity and standard DFT methods. *Phys. Chem. Chem. Phys.*, 6:2899–2903, 2004.

Chapter 6: Cholesky representation of electron-repulsion integrals within coupled-cluster and equation-of-motion methods

6.1 Introduction

Theoretical model chemistries[1] based on wave function methods provide the most reliable approach to electron correlation. Among different *ab initio*-based techniques[2], coupled-cluster (CC) theory holds a pre-eminent position[3]. The single-reference CC hierarchy of approximations allows one to compute highly accurate molecular structures, reaction energies, and other properties for ground-state species[2]. The equation-of-motion (EOM), or linear response, approach[4–6] extends the CC formalism to a variety of multi-configurational wave functions encountered in electronically excited states and various open-shell species. Unfortunately, similarly to other wave function based methods, the computational cost and hardware requirements (disk and memory) of CC and EOM-CC scale quite steeply with the number of electrons and the size of the one-electron basis set, i.e., the number of occupied (O) and unoccupied, or virtual (V),

orbitals. For example, the scaling of a CCSD (coupled-cluster with single and double substitutions) calculation is O^2V^4, and for CCSDT (CCSD plus explicit triple excitations) it is O^3V^5. The disk usage in CC and EOM-CC calculations depends on the implementation specifics and can reach $O(V^4)$; integral-direct algorithms could be employed to reduce storage requirements.

The high cost of electronic structure calculations originates in the two-electron part of the molecular Hamiltonian that describes electron-electron repulsion. The representation of the electron-repulsion integrals (ERIs) in an atomic orbital (AO) basis gives rise to a four-index tensor:

$$(\mu\nu|\lambda\sigma) = \int \chi_\mu(\vec{r}_1)\chi_\nu(\vec{r}_1)\frac{1}{|\vec{r}_1 - \vec{r}_2|}\chi_\lambda(\vec{r}_2)\chi_\sigma(\vec{r}_2)d\vec{r}_1 d\vec{r}_2$$

The size of this object scales as N^4 where N is the number of basis functions $\chi_i(\vec{r})$. For accurate results the size of the AO basis needs to be sufficiently large, for example a popular cc-pVTZ basis defines 30 contracted Gaussian functions per second-row atom.

All electronic structure methods include contractions of ERIs with various tensors, such as reduced density matrices, wave functions amplitudes, etc. Thus, the large size of ERIs propagates through the electron structure calculations from self-consistent field up to correlated methods.

Fortunately, the structure of the ERI matrix is sparse, which can be exploited in efficient computer implementations. It was recognized a long time ago that representing the "densities" by a linear expansion over the products of particular one-electron functions, such as $\chi_\mu(\vec{r}_1)\chi_\nu(\vec{r}_1)$, includes linear dependencies and could be rewritten in a more compact form using a new set of basis functions.

There are two alternative approaches to achieve this goal, the density fitting, or resolution-of-the-identity (RI)[7–13], approximation and the Cholesky decomposition (CD)[14–20]. In both approaches, the decomposed ERI matrix is represented as:

$$(\mu\nu|\lambda\sigma) \approx \sum_{P=1}^{M} B_{\mu\nu}^{P} B_{\lambda\sigma}^{P}, \tag{6.1}$$

where M is the rank of the decomposition, which depends on the target accuracy. The algorithm for determining B is different in RI and CD approaches: RI uses a predetermined auxiliary basis set that corresponds to the primary one-electron basis, whereas Cholesky vectors are obtained by performing the Cholesky decomposition of the actual ERI matrix. CD is thus a more general approach that can work with any primary basis and is free from externally optimized auxiliary basis sets. The Cholesky approach can be viewed as system-specific density fitting[17–19].

Decomposition shown in Eq. (6.1) produces a more compact representation of ERIs compared with the full ERI matrix, thus enabling memory and disk savings. In addition, it allows one to achieve improved parallel performance of calculations involving ERI through reduced disk input-output (I/O) penalties and better CPU utilization. For example, the AO-MO integral transformation has a computational cost of $O(N^5)$ when using the canonical procedure, now only involves the transformation of the RI/Cholesky vectors and therefore requires only $O(N^3M)$ steps. The transformed B-matrices can be used to assemble $\langle pq||rs\rangle$ integrals as needed in integral-direct implementations. However, to realize the maximum potential of the method, programmable equations that involve contractions of ERIs with the amplitudes and density matrices need to be rewritten.

The RI/Cholesky representation by itself does not lead to a scaling reduction in CCSD and EOM equations unless special care is taken about exchange-like terms. A number of strategies have been pursued to this end[19,21,22], including using Cholesky

decomposed wave function amplitudes[23,24] and local correlation schemes (see, for example, Ref. 25, 26 and references therein). However, even without these more advanced algorithms, computational savings due to a straightforward implementation of RI/Cholesky representations are very useful, especially in view of improved parallel scaling.

We present our implementation of RI/Cholesky within the CCSD and EOM-CCSD suite of methods in the Q-Chem electronic structure package[27,28]. The implementation eliminates the storage of the most expensive four-index integrals and intermediates. As described below, in the EOM-CCSD implementation we choose to keep two smallest four-index intermediates, OOOO and OOOV.

While CCSD implementations have been reported before[29], the EOM-CCSD methods have not been reimplemented using RI/CD. Below we briefly describe the algorithms used to produce Cholesky and RI vectors (Sections 6.2.1 and 6.2.2) and explain its implementation within CCSD and EOM-CCSD (Section 6.3). The following EOM methods have been implemented: EE/SF, IP, and EA. We discuss the performance of the new implementation in Section 6.4.

6.2 Algorithms

6.2.1 Cholesky algorithm

The idea of Cholesky decomposition (CD) of ERI[14,15,17,30] was proposed over 30 years ago by Beebe and Linderberg[14]. The ERI matrix in the AO basis, which is a positive-semidefinite[14] matrix, can be represented in the Cholesky-decomposed form as given by Eq. (6.1). The rank of the decomposition, M, is typically 3–10 times the number of basis functions N[17]. It depends on the decomposition threshold δ and is considerably smaller

than the full rank of the matrix, $N(N+1)/2$[14, 17, 31]. CD removes linear dependencies in product densities[17] $(\mu\nu|$, allowing one to approximate the original matrix to arbitrary accuracy.

Decomposition threshold δ defined by the user is the only parameter that controls the accuracy and the rank of the decomposition. The algorithm[15, 17, 30] proceeds as follows:

(1) Compute all diagonal elements of ERI: $D^0_{\lambda\sigma,\lambda\sigma} = (\lambda\sigma|\lambda\sigma)$.

(2) Choose the largest diagonal element $(\lambda\sigma_0|\lambda\sigma_0)$. $(\lambda\sigma)_0$ here is a fixed index corresponding to the largest diagonal element.

(3) Compute densities $(\mu\nu|\lambda\sigma_0)$.

(4) Compute first Cholesky vector $B^1_{\mu\nu} = (\mu\nu|\lambda\sigma_0)/\sqrt{(\lambda\sigma_0|\lambda\sigma_0)}$.

From this point the algorithm proceeds in an iterative manner, checking the accuracy and generating a new Cholesky vector to refine the previous-step approximation at every iteration. k is an iteration count that starts from 2 and increments after every iteration.

(5) Update the residual of the diagonal by subtracting the Cholesky vector obtained in the previous iteration $D^{(k-1)}_{\lambda\sigma,\lambda\sigma} = D^{(k-2)}_{\lambda\sigma,\lambda\sigma} - B^{(k-1)}_{\lambda\sigma} B^{(k-1)}_{\lambda\sigma}$.

(6) Choose the largest element of the diagonal residual $D^{k-1}_{\lambda\sigma_{k-1},\lambda\sigma_{k-1}}$. If $D^{k-1}_{\lambda\sigma_{k-1},\lambda\sigma_{k-1}} < \delta$, then terminate and return the Cholesky vectors, $\{B^i_{\mu\nu}\}^{k-1}_{i=1}$.

(7) Compute densities $(\mu\nu|\lambda\sigma_{k-1})$ and the corresponding residual, $D^{(k-1)}_{\mu\nu,\lambda\sigma_{k-1}} = (\mu\nu|\lambda\sigma_{k-1}) - \sum_{i=1}^{k-1} B^i_{\mu\nu} B^i_{\lambda\sigma_{k-1}}$.

(8) Compute new Cholesky vector $B^k_{\mu\nu} = D^{k-1}_{\mu\nu,\lambda\sigma_{k-1}}/\sqrt{D^{k-1}_{\lambda\sigma_{k-1},\lambda\sigma_{k-1}}}$. Repeat from step (5).

Since the ERI matrix is positive-semidefinite[8, 14, 32], it follows that:

$$|D^{k-1}_{\mu\nu,\lambda\sigma}| \leq \sqrt{D^{k-1}_{\mu\nu,\mu\nu} D^{k-1}_{\lambda\sigma,\lambda\sigma}}$$

Thus, the accuracy of the decomposition is given by the largest element of diagonal residual matrix $D_{\lambda\sigma,\lambda\sigma}$ at every iteration (step 6), which ensures that the error in any ERI matrix element does not exceed δ.

Note that the algorithm does not require the calculation and storage of the full ERI matrix [$O(N^4)$], which would be prohibitive for large systems. At the initialization of the algorithm only the calculation of the diagonal elements is necessary [step 1, $O(N^2)$], which are updated at each iteration by subtracting newly produced Cholesky vectors to form a residual diagonal matrix (step 5). The calculation of the densities $(\mu\nu|\lambda\sigma_{k-1})$ [step 7, $O(N^2)$] are performed at each step with subsequent calculation of the residual and the corresponding Cholesky vector (step 8). At each iteration only the calculation of new $O(N^2)$ elements of the ERI matrix is required and the number of Cholesky vectors grows by one resulting in the $O(MN^2)$ memory storage of all Cholesky vectors for the final decomposition. Thus, only a small fraction of about 1–5% of the full ERI matrix needs to be calculated in the decomposition procedure[17].

The most expensive step is the calculation of the residual matrix[17] (step 7), which requires $(M-1)$ subtractions of previously obtained Cholesky vectors at each iteration [$O((M-1)N^2)$ operations at each iteration], giving rise to the full complexity of the algorithm of $O(M^2N^2)$. For correlated calculations, the Cholesky vectors obtained in the AO basis are usually transformed to the molecular orbital (MO) basis.

This algorithm is implemented using our tensor algebra library[33] such that Cholesky vectors are stored as a list of two-dimensional block tensors, i.e., a list of block matrices. The library is based on virtual memory management such that block tensors are stored in RAM if sufficient memory is available or saved on disk and reloaded as necessary. Note that the generation of a new Cholesky vector [steps 5–8] does not require vectors from previous iterations ($k-1$ at step k) to be in RAM; for calculation of the residual

matrix (step 5) they can be uploaded from disk sequentially, or even block-by-block. After all Cholesky vectors $B_{\mu\nu}$ are generated, the list of block matrices is merged to form a three-dimensional block tensor $B^M_{\mu\nu}$ containing all the Cholesky vectors.

6.2.2 Resolution-of-the-identity algorithm

Similar to the Cholesky decomposition, the RI approach[8–13] allows one to expand product densities $(\mu\nu|$ in an auxiliary basis set:

$$(\mu\nu|\lambda\sigma) \approx \sum_{PQ} C^P_{\mu\nu}(P|Q)C^Q_{\lambda\sigma} \equiv \sum_{PQ}(\mu\nu|P)(P|Q)^{-1}(Q|\lambda\sigma)$$

Indices P and Q denote auxiliary basis functions and $(P|Q)$ defines a Coulomb metric matrix[13,17,20]:

$$(P|Q) = \int \frac{P(\vec{r}_1)Q(\vec{r}_2)}{|\vec{r}_1 - \vec{r}_2|} d\vec{r}_1 d\vec{r}_2$$

The auxiliary basis expansion coefficients ($C^L_{\mu\nu}$) are found by minimizing the difference between the actual and fitted product densities[13,17,18], leading to the following set of linear equations:

$$\sum_L (K|L)C^L_{\mu\nu} = (K|\mu\nu)$$

By defining new auxiliary basis coefficients

$$B^K_{\mu\nu} = \sum_L C^L_{\mu\nu}(L|K)^{1/2} \equiv \sum_L (K|\mu\nu)(K|L)^{-1/2}$$

we can rewrite approximate ERIs in a form identical to the Cholesky representation[13] as given by Eq. (6.1).

The accuracy and performance of RI depend on the quality of the chosen auxiliary basis set. Ideally an auxiliary basis set should be balanced between accuracy and compactness. Errors should be at least an order of magnitude smaller than the error due to one-electron basis set incompleteness. Rank M should be no more that 2–4 times larger than the number of AO basis functions N[7,17,34–39]. To achieve these goals, auxiliary basis sets are usually optimized for each atom, AO basis set and level of theory (e.g., Hartree–Fock, MP2)[7,17,34–39]. In this work we employ auxiliary basis sets developed for MP2.

6.3 RI/CD CCSD and EOM-CCSD methods: Theory

6.3.1 Coupled-cluster equations with single and double substitutions

The exact solution of the Schrödinger equation can be written as the exponential of a cluster operator $\hat{T}$ operating on a reference function[40]:

$$\Psi_{exact} = \Psi_{CC} = e^{\hat{T}}\Phi_0$$

where Φ_0 is a single Slater determinant. In CCSD, the expansion of $\hat{T}$ is truncated at a two-electron excitation level:

$$\hat{T} \approx \hat{T}_1 + \hat{T}_2$$

For $\hat{T}_1$ and $\hat{T}_2$, the expansions are[a]:

$$\hat{T}_1 = \sum_{ia} t_i^a a^\dagger i \qquad \hat{T}_2 = \frac{1}{4} \sum_{ijab} t_{ij}^{ab} a^\dagger i b^\dagger j$$

Thus,

$$\Psi_{CCSD} = e^{\hat{T}_1 + \hat{T}_2} \Phi_0$$

The equations to determine CCSD correlation energy E_{CCSD} and cluster amplitudes t_i^a, t_{ij}^{ab} are derived algebraically by a projection approach such that the Schrödinger equation is satisfied in the subspace spanned by the reference, singly, and doubly excited determinants:

$$\begin{aligned}
E_{CCSD} &= \langle \Phi_0 | \hat{H} | \Psi_{CCSD} \rangle = \langle \Phi_0 | \hat{H} | (1 + \hat{T}_1 + \frac{1}{2}\hat{T}_1^2 + \hat{T}_2) \Phi_0 \rangle && (6.2) \\
0 &= \langle \Phi_i^a | \hat{H} - E_{CCSD} | \Psi_{CCSD} \rangle \\
&= \langle \Phi_i^a | \hat{H} - E_{CCSD} | (1 + \hat{T}_1 + \frac{1}{2}\hat{T}_1^2 + \hat{T}_2 + \hat{T}_1\hat{T}_2 + \frac{1}{3!}\hat{T}_1^3) \Phi_0 \rangle && (6.3) \\
0 &= \langle \Phi_{ij}^{ab} | \hat{H} - E_{CCSD} | \Psi_{CCSD} \rangle \\
&= \langle \Phi_{ij}^{ab} | \hat{H} - E_{CCSD} | \\
&\quad (1 + \hat{T}_1 + \frac{1}{2}\hat{T}_1^2 + \hat{T}_2 + \hat{T}_1\hat{T}_2 + \frac{1}{3!}\hat{T}_1^3 + \frac{1}{2}\hat{T}_2^2 + \frac{1}{2}\hat{T}_1^2\hat{T}_2 + \frac{1}{4!}\hat{T}_1^4) \Phi_0 \rangle && (6.4)
\end{aligned}$$

Evaluating Eq. (6.2) in terms of amplitudes t_i^a and t_{ij}^{ab} yields the following expression:

$$E_{CCSD} = \langle \Phi_0 | \hat{H} | \Phi_0 \rangle + \sum_{ia} f_{ia} t_i^a + \frac{1}{2} \sum_{ijab} \langle ij||ab \rangle t_i^a t_j^b + \frac{1}{4} \sum_{ijab} \langle ij||ab \rangle t_{ij}^{ab} \qquad (6.5)$$

[a]Throughout the paper, we adhere to the convention that *ijkl* denote occupied orbitals, *abcd* denote virtual orbitals, and *pqrs* denote orbitals that can be either occupied or virtual.

where

$$
\begin{aligned}
f_{ia} &= \langle \Phi_i^a | \hat{H} | \Phi_0 \rangle = h_{ia} + \sum_j \langle ij||aj\rangle \\
\langle ij||ab\rangle &= \langle ij|ab\rangle - \langle ij|ba\rangle = (ia|jb) - (ib|ja) \\
(ia|jb) &= \int \phi_i(1)\phi_j(2)\frac{1}{r_{12}}\phi_a(1)\phi_b(2)d1d2
\end{aligned}
$$

Once Eq. (6.5) is substituted into Eqns. (6.3) and (6.4), t_i^a and t_{ij}^{ab} amplitudes can be solved iteratively by:

$$
\begin{aligned}
t_i^a \Delta_i^a = f_{ia} - \sum_l F_{li}^{(3)} t_l^a + \sum_d F_{ad}^{(1)} t_i^d + \sum_{kc} F_{kc}^{(2)} t_{ik}^{ac} - \sum_{kc} \langle ic||ka\rangle t_k^c \\
- \frac{1}{2}\sum_{klc} \langle kl||ic\rangle t_{kl}^{ac} + \frac{1}{2}\sum_{kcd} \langle ka||cd\rangle t_{ki}^{cd}
\end{aligned}
$$

and

$$
\begin{aligned}
t_{ij}^{ab}\Delta_{ij}^{ab} =& \langle ij||ab\rangle + \mathcal{P}_{ab}^{-}\left\{ \sum_c t_{ij}^{ac} F_{bc}^{(2)} - \sum_k I_{ijkb}^{(2a)} t_k^a + \mathcal{P}_{ij}^{-} \sum_{kc} I_{kbic}^{(1a)} t_{jk}^{ac} \right\} \\
&+ \mathcal{P}_{ij}^{-}\left\{ \sum_c \langle jc||ba\rangle t_i^c - \sum_k t_{ik}^{ab} F_{jk}^{(2)} \right\} + \frac{1}{2}\sum_{cd} \langle ab||cd\rangle \tilde{t}_{ij}^{cd} + \frac{1}{2}\sum_{kl} t_{kl}^{ab} I_{ijkl}^{(4)}
\end{aligned}
$$

where $\Delta_i^a = f_{ii} - f_{aa}$ and $\Delta_{ij}^{ab} = \Delta_i^a + \Delta_j^b$. The expressions for the intermediates are given in Table 6.1.

Memory requirements for the T amplitude update procedure in the closed-shell case are[b]:

$$
\frac{9}{8}O^4 + 3O^3V + 6O^2V^2 + \frac{3}{2}OV^3 + \frac{3}{8}V^4 \tag{6.6}
$$

[b]In the closed-shell case, two spin cases of integrals and amplitudes are stored: $\langle \alpha\alpha||\alpha\alpha\rangle$ and $\langle \alpha\beta||\alpha\beta\rangle$; in the open-shell case there is additionally a third spin case: $\langle \beta\beta||\beta\beta\rangle$. With applicable permutational symmetry taken into consideration and an assumption of no point group symmetry in the molecule, the disk requirement for ERI objects in the closed-shell case are: $\langle ij||kl\rangle : \frac{3}{8}O^4$, $\langle ij||ka\rangle : \frac{3}{2}O^3V$, $\langle ij||ab\rangle : \frac{3}{4}O^2V^2$, $\langle ia||jb\rangle : O^2V^2$, $\langle ia||bc\rangle : \frac{3}{2}OV^3$, $\langle ab||cd\rangle : \frac{3}{8}V^4$.

Table 6.1: Intermediates for CCSD calculations and estimates to store and compute them (closed-shell case).

Equation	Memory	Flops
$F_{bc}^{(1)} = f_{bc} + \sum_{kd}\langle kb\|\|dc\rangle t_k^d - \frac{1}{2}\sum_{kld}\langle kl\|\|cd\rangle t_{kl}^{bd}$		
$F_{ij}^{(2)} = f_{ij} + \sum_a f_{ja} t_i^a + \sum_{ka}\langle jk\|\|ia\rangle t_k^a$		
$+\sum_{kab}\langle jk\|\|ab\rangle t_i^a t_k^b + \frac{1}{2}\sum_{kab}\langle jk\|\|ab\rangle t_{ik}^{ab}$		
$F_{ia}^{(2)} = f_{ia} + \sum_{jb}\langle ij\|\|ab\rangle t_j^b$		
$F_{bc}^{(2)} = F_{bc}^{(1)} - \sum_k f_{kc} t_k^b - \sum_{kld}\langle kl\|\|cd\rangle t_k^b t_l^d$		
$F_{ki}^{(3)} = f_{ki} + \sum_c F_{kc}^{(2)} t_i^c + \frac{1}{2}\sum_{jab}\langle kj\|\|ab\rangle t_{ij}^{ab} + \sum_{lc}\langle kl\|\|ic\rangle t_l^c$		
$\tilde{t}_{ij}^{ab} = t_{ij}^{ab} + \mathcal{P}_{ab}^{-} t_i^a t_j^b$	$\frac{3}{4}O^2V^2$	
$I_{iajb}^{(1a)} = \langle ia\|\|jb\rangle - \sum_c\langle ia\|\|bc\rangle t_j^c - \sum_k\langle ik\|\|jb\rangle t_k^a$	$2O^2V^2$	$3O^3V^3$
$-\frac{1}{2}\sum_{kc}\langle ik\|\|cb\rangle\left(t_{jk}^{ca} + 2t_j^c t_k^a\right)$		
$I_{ijkb}^{(2a)} = \langle ij\|\|kb\rangle - \frac{1}{2}\sum_l I_{ijkl}^{(4)} t_l^b + \frac{1}{2}\sum_{cd}\langle kb\|\|cd\rangle\tilde{t}_{ij}^{cd} + \mathcal{P}_{ij}^{-}\sum_c\langle kb\|\|ic\rangle t_j^c$	$\frac{3}{2}O^3V$	$\frac{5}{4}O^3V^3$
$I_{ijkl}^{(4)} = \langle ij\|\|kl\rangle + \frac{1}{2}\sum_{ab}\langle kl\|\|ab\rangle\tilde{t}_{ij}^{ab} + \mathcal{P}_{ij}^{-}\sum_a\langle kl\|\|ia\rangle t_j^a$	$\frac{3}{4}O^4$	$\frac{5}{8}O^4V^2$
$\sum_{kc} I_{kbic}^{(1a)} t_{jk}^{ac}$		$3O^3V^3$
$\sum_{cd}\langle ab\|\|cd\rangle\tilde{t}_{ij}^{cd}$		$\frac{5}{8}O^2V^4$
$\sum_{kl} t_{kl}^{ab} I_{ijkl}^{(4)}$		$\frac{5}{8}O^4V^2$

This estimate includes all the blocks of ERIs, necessary four-index intermediates, and two sets of T_2 amplitudes. Excluded are additional copies of T amplitudes required by the DIIS[c] procedure and lower-dimensional quantities. The $O(N^6)$ part of the total computational cost of updating T amplitudes is $\frac{7}{4}O^4V^2 + \frac{29}{4}O^3V^3 + \frac{5}{8}O^2V^4$.

Because RI and Cholesky representations of ERI use identical expressions, we begin with the following expression for anti-symmetrized integrals:

$$\langle\mu\lambda||\nu\sigma\rangle \approx \sum_P B_{\mu\nu}^P B_{\lambda\sigma}^P - \sum_P B_{\mu\sigma}^P B_{\lambda\nu}^P = \mathcal{P}_{\nu\sigma}^{-}\sum_P B_{\mu\nu}^P B_{\lambda\sigma}^P \tag{6.7}$$

[c]Usually, several T_2 vectors are stored for the DIIS algorithm.

Upon substituting Eq. (6.7) into Eq. (6.5), (6.3), (6.4) and corresponding intermidiates (Table 6.1) the equations for RI/CD CCSD can be obtained. The details on derivation of equations as well as new intermediates formed for RI/CD CCSD can be found in Ref. 41.

To illustrate the difference in storage requirements, consider a calculation of closed-shell naphthalene using the cc-pVTZ/rimp2-cc-pVTZ basis set. There are 68 electrons, 412 basis functions ($O = 34$, $V = 378$), 1050 auxiliary basis functions ($M = 1050$).

Whereas conventional CCSD calculation requires 10917 Mwords (85 GB), CD/RI-CCSD requires 846 Mwords (6.6 GB). Thus, for this calculation the data set is almost 13 times smaller in the case of RI-CCSD.

The number of floating point operations scales as $O(N^6)$ for both CCSD and CD/RI-CCSD. The most significant contraction in CCSD, $\sum_{cd}\langle ab||cd\rangle\tilde{t}_{ij}^{cd}$, and its CD/RI-CCSD counterpart, take the same number of flops. In the latter case the intermediate $\mathcal{P}_{ab}^{-}\sum_P M_{da}^P M_{cb}^P$ is formed on the fly thus reducing overall memory requirements. The CD/RI-CCSD equations involve fewer O^3V^3-type contractions, leading to a smaller prefactor ($4O^3V^3$ vs. $\frac{29}{4}O^3V^3$ in conventional CCSD). While this improvement is offset by the increased number and cost of $O(N^5)$ steps, in practical applications CD/RI-CCSD are superior in terms of floating point operations, memory and I/O, as illustrated by benchmark calculations in Section 6.4.

6.3.2 EOM-EE/SF-CCSD and CD/RI EOM-EE/SF-CCSD

In the EOM-CCSD framework, the target excited-state wave functions are written as[42,43]:

$$|\Psi_R\rangle = Re^{\hat{T}}|\Phi_0\rangle \tag{6.8}$$

$$\langle\Psi_L| = \langle\Phi_0|e^{-\hat{T}}L^{\dagger} \tag{6.9}$$

The operators R and L are linear excitation operators:

$$R = R_0 + R_1 + R_2 + \cdots \tag{6.10}$$

$$R_n = \frac{1}{n!^2}\sum r_{ijk\cdots}^{abc\cdots} a^{\dagger}ib^{\dagger}jc^{\dagger}k\cdots \tag{6.11}$$

In EOM-EE operators R_n are spin-conserving ($M_s = 0$ operators), whereas in EOM-SF they involve changing the spin of an electron ($M_s = -1$). The spin-orbital form of the EOM-CCSD equations is the same in EOM-EE and EOM-SF[43,44].

By introducing a similarity-transformed Hamiltonian $\bar{H}$:

$$\bar{H} \equiv e^{-\hat{T}}He^{\hat{T}} \tag{6.12}$$

the energy and CCSD amplitude equations become:

$$E_{CC} = \langle\Phi_0|\bar{H}|\Phi_0\rangle \tag{6.13}$$

$$0 = \langle\Phi_i^a|\bar{H} - E_{CC}|\Phi_0\rangle \tag{6.14}$$

$$0 = \langle\Phi_{ij}^{ab}|\bar{H} - E_{CC}|\Phi_0\rangle \tag{6.15}$$

$$\cdots$$

where E_{CC} is the coupled-cluster energy for the reference state. Usually both T and R are truncated at the same level, which is the single (S) and double (D) excitations in this work. Thus, in the basis of the reference (O), S, and D we have:

$$\begin{pmatrix} 0 & \bar{H}_{OS} & \bar{H}_{OD} \\ 0 & \bar{H}_{SS} - E_{CC} & \bar{H}_{SD} \\ 0 & \bar{H}_{DS} & \bar{H}_{DD} - E_{CC} \end{pmatrix} \begin{pmatrix} R_0 \\ R_1 \\ R_2 \end{pmatrix} = \omega \begin{pmatrix} R_0 \\ R_1 \\ R_2 \end{pmatrix} \tag{6.16}$$

where on the left-hand side E_{CC} only appears for the diagonal elements in the diagonal blocks and $\omega = E - E_{CC}$. Because the right eigenvectors do not form an orthonormal set, $R_0 = r_0\hat{1}$ can be present in the target excited states:

$$r_0 = \frac{1}{\omega}(\bar{H}_{OS}R_1 + \bar{H}_{OD}R_2) = \frac{1}{\omega}\left\{\sum_{ia} F^{(2)}_{ia} r^a_i + \frac{1}{4}\sum_{ijab}\langle ij||ab\rangle r^{ab}_{ij}\right\} \tag{6.17}$$

Eq. (6.16) is solved by using the generalized Davidson iterative diagonalization procedure[43], which involves the calculation of the following σ-vectors:

$$\begin{aligned} \sigma^a_i &= ([\bar{H}_{SS} - E_{CC}]R_1)^a_i + (\bar{H}_{SD}R_2)^a_i \\ &= \sum_b F^{(2)}_{ab} r^b_i - \sum_j F^{(2)}_{ij} r^a_j - \sum_{jb} I^{(1)}_{ibja} r^b_j + \sum_{jb} F^{(2)}_{jb} r^{ab}_{ij} - \frac{1}{2}\sum_{jkb} I^{(6)}_{jkib} r^{ab}_{jk} - \frac{1}{2}\sum_{jbc} I^{(7)}_{jabc} r^{bc}_{ij} \end{aligned} \tag{6.18}$$

Table 6.2: I and T intermediates for EOM-CCSD and estimated cost to store and compute them (closed-shell case).

Equation	Memory	Flops
$I^{(1)}_{ickb} = \langle ic\|\|kb\rangle - \sum_d \langle kb\|\|cd\rangle t^d_i - \sum_{ld}\langle kl\|\|cd\rangle t^{bd}_{il}$	$2O^2V^2$	$3O^3V^3$
$+\sum_l \left[\sum_d \langle kl\|\|cd\rangle t^d_i - \langle kl\|\|ic\rangle\right] t^b_l$		
$I^{(2)}_{ijkb} = \langle ij\|\|kb\rangle - \sum_l I^{(4)}_{ijkl} t^b_l + \frac{1}{2}\sum_{cd}\langle kb\|\|cd\rangle \tilde{t}^{cd}_{ij}$		
$+\sum_d \left[\sum_{lc}\langle kl\|\|cd\rangle t^c_l\right] t^{bd}_{ij} - \sum_c t^{bc}_{ij} f_{kc}$		
$-\mathcal{P}^-_{ij}\left\{\sum_c \left[\langle kb\|\|jc\rangle - \sum_{ld}\langle kl\|\|cd\rangle t^{bd}_{jl}\right] t^c_i + \sum_{lc}\langle kl\|\|jc\rangle t^{bc}_{il}\right\}$	$\frac{3}{2}O^3V$	$\frac{21}{4}O^3V^3$
$I^{(3)}_{jcab} = \langle jc\|\|ab\rangle - \sum_d I^{(5)}_{abcd} t^d_j + \frac{1}{2}\sum_{kl}\langle kl\|\|jc\rangle t^{ab}_{kl}$		
$-\sum_l \left(\sum_{kd}\langle lk\|\|cd\rangle t^d_k\right) t^{ab}_{jl} - \sum_l t^{ab}_{jl} f_{lc}$		
$+\mathcal{P}^-_{ab}[\sum_k \left(\langle ka\|\|jc\rangle - \frac{1}{2}\sum_l \langle kl\|\|jc\rangle t^a_l - \sum_{ld}\langle kl\|\|cd\rangle t^{ad}_{jl}\right) t^b_k$		
$-\sum_{ld}\langle lb\|\|cd\rangle t^{ad}_{jl}]$	$\frac{3}{2}OV^3$	$\frac{33}{4}O^3V^3$
$I^{(4)}_{ijkl} = \langle ij\|\|kl\rangle + \frac{1}{2}\sum_{ab}\langle kl\|\|ab\rangle \tilde{t}^{ab}_{ij} + \mathcal{P}^-_{ij}\sum_a \langle kl\|\|ia\rangle t^a_j$	$\frac{3}{4}O^4$	$\frac{5}{8}O^4V^2$
$I^{(5)}_{abcd} = \langle ab\|\|cd\rangle + \frac{1}{2}\sum_{kl}\langle kl\|\|cd\rangle \tilde{t}^{ab}_{kl} - \mathcal{P}^-_{ab}\sum_k \langle kb\|\|cd\rangle t^a_k$	$\frac{3}{4}V^4$	$\frac{5}{8}O^2V^4$
$I^{(6)}_{klic} = \langle kl\|\|ic\rangle - \sum_d t^d_i \langle kl\|\|cd\rangle$	$\frac{3}{2}O^3V$	
$I^{(7)}_{kacd} = \langle ka\|\|cd\rangle - \sum_l t^a_l \langle kl\|\|cd\rangle$	$\frac{3}{2}OV^3$	
$T^{(1)}_{ij} = \sum_{kc} r^c_k I^{(6)}_{jkic}$		
$T^{(2)}_{ab} = \sum_{kc} r^c_k I^{(7)}_{kabc}$		
$T^{(3)}_{ij} = \frac{1}{2}\sum_{kab}\langle jk\|\|ab\rangle r^{ab}_{ik}$		
$T^{(4)}_{ab} = \frac{1}{2}\sum_{ijc}\langle ij\|\|bc\rangle r^{ac}_{ij}$		

$$
\begin{aligned}
\sigma^{ab}_{ij} &= (\bar{H}_{DS}R_1)^{ab}_{ij} - ([\bar{H}_{DD} - E_{CC}]R_2)^{ab}_{ij} \\
&= -\mathcal{P}^-_{ab}\sum_k I^{(2)}_{ijkb} r^a_k - \mathcal{P}^-_{ij}\sum_c I^{(3)}_{jcab} r^c_i + \mathcal{P}^-_{ij}\sum_l T^{(1)}_{il} t^{ab}_{jl} + \mathcal{P}^-_{ab}\sum_d T^{(2)}_{ad} t^{bd}_{ij} + \mathcal{P}^-_{ij}\sum_k r^{ab}_{jk} F^{(2)}_{ik} \\
&\quad + \mathcal{P}^-_{ab}\sum_c r^{ac}_{ij} F^{(2)}_{bc} + \mathcal{P}^-_{ij}\mathcal{P}^-_{ab}\sum_{kc} I^{(1)}_{ickb} r^{ac}_{jk} + \frac{1}{2}\sum_{kl} r^{ab}_{kl} I^{(4)}_{ijkl} + \frac{1}{2}\sum_{cd} r^{cd}_{ij} I^{(5)}_{abcd} \\
&\quad + \mathcal{P}^-_{ij}\sum_l T^{(3)}_{il} t^{ab}_{jl} + \mathcal{P}^-_{ab}\sum_d T^{(4)}_{ad} t^{bd}_{ij}
\end{aligned}
\tag{6.19}
$$

The I, F, and T intermediates used in Eq. (6.18) and (6.19) are collected in Tables 6.1 and 6.2. Total storage requirements for computing a σ-vector, including a set of T, R, σ amplitudes and all the integrals and intermediates, are:

$$\frac{9}{8}O^4 + \frac{9}{2}O^3V + 6O^2V^2 + \frac{9}{2}OV^3 + \frac{9}{8}V^4 \tag{6.20}$$

Note that multiple sets of R and σ amplitudes are required in the Davidson procedure for finding the excitation energies. Following the same procedure as in the derivation of the CD/RI-CCSD equations one arrives at the equations with RI/CD integrals, details can be found in Ref. 41.

For the computation of a σ-vector in the Davidson iterative procedure, the storage requirement for CD/RI-EOM-EE implementation becomes:

$$\frac{5}{2}O^2M + 5OVM + \frac{5}{2}V^2M + \frac{3}{2}O^4 + \frac{3}{2}O^3V + \frac{21}{4}O^2V^2 \tag{6.21}$$

For the naphthalene example the RI version of EOM-EE reduces the amount of required memory by a factor of 24 relative to the canonical implementation, that is, the conventional EOM-EE needs 30795 Mwords (241 GB), whereas CD/RI-EOM-EE uses 1275 Mwords (10 GB). The number of floating point operations in the σ-vector update procedure for both conventional and RI/CD implementations scales as $O(N^6)$. The cost of EOM-EE is $\frac{5}{8}O^2V^4 + \frac{3}{4}O^3V^3 + \frac{5}{8}O^4V^2$, whereas RI/CD-EOM-EE takes $\frac{5}{8}O^2V^4 + 9O^3V^3 + \frac{5}{4}O^4V^2$ operations. There is a larger number of O^3V^3 contractions in the latter case, leading to a bigger prefactor. This is the result of the on-the-fly reassembly of some fourth-order intermediates that are stored in memory in the case of conventional EOM-EE.

6.3.3 EOM-IP-CCSD and CD/RI EOM-IP-CCSD

In EOM-IP-CCSD (EOM-CCSD for ionization potentials), the operator R is not particle-conserving:

$$R_n(N-1) = \frac{1}{n!^2} \sum r^{bc\cdots}_{ijk\cdots} ib^+ jc^+ k \cdots \tag{6.22}$$

In EOM-IP-CCSD, R is truncated at the two-hole-one-particle excitation level. The equations for σ-vectors are as follows:

$$\begin{aligned}
\sigma_i &= -\sum_j F^{(2)}_{ij} r_j + \sum_{jb} F^{(2)}_{jb} r^b_{ij} + \frac{1}{2} \sum_{jkb} I^{(6)}_{kjib} r^b_{jk} \\
\sigma^a_{ij} &= -\sum_k r_k I^{(2)}_{ijka} + \mathcal{P}^-_{ij} \sum_k r^a_{jk} F^{(2)}_{ik} + \sum_b r^b_{ij} F^{(2)}_{ab} - \\
&\quad \mathcal{P}^-_{ij} \sum_{kb} I^{(1)}_{jbka} r^b_{ik} + \frac{1}{2} \sum_{kl} I^{(4)}_{ijkl} r^a_{kl} + \sum_b t^{ab}_{ij} T^{(4)}_b \\
T^{(4)}_b &= \frac{1}{2} \sum_{klb} \langle kl||ab\rangle r^b_{kl}
\end{aligned}$$

where F and I intermediates are collected in Tables 6.1 and 6.2. Memory requirements for the σ update procedure are:

$$\frac{3}{4}O^4 + 3O^3V + \frac{11}{4}O^2V^2 \tag{6.23}$$

This estimate excludes any three-dimensional quantities, e.g. EOM-IP amplitudes.

The CD/RI equations are derived following the same procedure as in the EOM-EE case. For the naphthalene example, memory savings achieved by using RI are limited to about 20%, that is, conventional EOM-IP requires 477 Mwords (3.7 GB), whereas CD/RI-EOM-IP, needs 382 Mwords (3.0 GB). The difference in memory requirements is not as large as in the case of EOM-EE because EOM-IP does not use the OVVV and VVVV blocks of the ERIs.

The number of floating point operations in the σ-vector update procedure for both implementations is $O(N^5)$. The CD/RI scheme requires six $O(N^5)$-type contractions, the dominant contraction being O^2V^2M. The canonical EOM-IP requires two $O(N^5)$-type contractions, the dominant contraction being O^3V^2. Therefore, the σ-vector update procedure in CD/RI-EOM-IP is expected to be about three times slower than in canonical EOM-IP; however, some of this cost increase is offset by more favorable parallel scaling. Moreover, for fair comparison, the calculation of the intermediates should also be considered.

6.3.4 EOM-EA-CCSD and CD/RI EOM-EA-CCSD

In EOM-EA (EOM for electron attachment), the operator R is:

$$R_n(N+1) = \frac{1}{n!^2} \sum r^{abc\cdots}_{jk\cdots} a^+ b^+ j c^+ k \cdots \tag{6.24}$$

In EOM-EA-CCSD, R is truncated at the one-hole-two-particles level and the equations for the σ-vectors are:

$$\begin{aligned}
\sigma^a &= \sum_c F^{(2)}_{ac} r^c + \sum_{kc} F^{(2)}_{kc} r^{ac}_k + \frac{1}{2} \sum_{kcd} I^{(7)}_{kacd} r^{cd}_k \\
\sigma^{ab}_i &= \mathcal{P}^-_{ab} \sum_c F^{(2)}_{ac} r^{cb}_i - \sum_k F^{(2)}_{ki} r^{ab}_k - \sum_c I^{(3)}_{icab} r^c + \\
&\quad \frac{1}{2} \sum_{cd} I^{(5)}_{abcd} r^{cd}_i + \mathcal{P}^-_{ab} \sum_{kc} I^{(1)}_{kbic} r^{ac}_k - \sum_k T^{(3)}_k t^{ab}_{ik} \\
T^{(3)}_k &= \frac{1}{2} \sum_{kcd} r^{cd}_k \langle ki||cd\rangle
\end{aligned}$$

where $F^{(2)}$ and I intermediates are given in Tables 6.1 and 6.2. The disk requirements for the EOM-EA σ update procedure are estimated at:

$$\frac{7}{2}O^2V^2 + 3OV^3 + \frac{3}{4}V^4 \tag{6.25}$$

Following the same procedire as for EOM-EE and EOM-IP of substituting of RI/CD decomposed integrals one arrives at RI/CD EOM-EA, details can be found in Ref. 41.

The storage requirement for CD/RI-EOM-EA σ-vector update is:

$$\frac{3}{2}O^2M + 2OVM + \frac{3}{2}V^2M + \frac{3}{4}O^2V^2 \tag{6.26}$$

To again illustrate memory savings using the naphthalene example, conventional EOM-EA uses 20408 Mwords (159 GB), whereas CD/RI-EOM-EA needs only 360 Mwords (2.8 GB). Because the most expensive in terms of storage intermediates have been eliminated in the CD/RI implementation, the procedure requires about 57 times less memory.

Similar to EOM-IP-CCSD, the number of floating point operations for both implementations scales as $O(N^5)$. The dominant $O(N^5)$-type contraction, out of two in canonical EOM-EA, is the OV^4-type, whereas in CD/RI, which has ten $O(N^5)$-type contractions, the dominant one is V^4M-type.

6.4 Benchmarks

The errors introduced by the RI and CD approximations have been extensively benchmarked for quantities like total energies, molecular structures, dipole moments, and excitation energies[7,15,18,20,35,37–39,45–49]; for a recent review see Ref. 19. Total energies

have been analyzed for density functional theory[18–20,35,45], Hartree-Fock[15,18–20,45,46] and MP2 methods[7,15,18–20,37,45,46]. Typical errors in absolute energies are in a millihartree (mE_h) range [or 0.01 kcal/(mol-electron)] for common auxiliary basis sets[20,35,37] and for CD with a threshold of 10^{-4}[18,19,45].

The accuracy in energy differences, such as activation energies[16], is better by a factor of 2–3 in comparison to total energies due to error cancellation. The errors in dipole moments computed with RI[37,38] and CD[19] are below 0.01 D and are usually an order of magnitude smaller that the errors due to the incompleteness of basis sets. The RI/CD bond lengths are within 0.01 pm from the respective full calculations[20,38,48]. Aquilante *et al.*[19] have also reported vertical excitation energies (computed with CASSCF and CASPT2) that show average errors less than 0.01 eV and 0.001 eV for thresholds of 10^{-3} and 10^{-4}, respectively. The effect of the RI approximation on excitation energies within an approximate second-order coupled-cluster model, CC2, has been thoroughly investigated by Köhn and Hättig who reported errors of 0.01 eV or less[48].

In the present paper, we focus mostly on the effect of using RI/CD representations on energy differences between different electronic states, such as electronic excitation energies and ionization/electron attachment energies. We also consider energy differences along potential energy surfaces.

We compare the timings for RI/CD versus canonical implementations and investigate the parallel performance of the code[d]. All calculations were performed on designated benchmark nodes. The hardware configuration is Xeon X5675 (2 processors, 6 cores each, 3.0 GHz, 12 Mb cache), 126 GB RAM, RAID 0 4×600 GB=2.2 TB. This configuration was referred to as Xeon-USC in our previous benchmark study[33].

[d]During the final revision stage, a small algorithmic improvement has been implemented that resulted in ∼5% speed-up in CD/RI CC/EOM calculations. Thus, the reported timings are roughly 5% slower than the current code.

We use the following test cases:

1. Phenolate form of the anionic chromophore of the photoactive yellow protein (PYPb)[50,51]. We perform CCSD calculations as well as EOM-EE/IP/EA-CCSD. We consider the energy difference between the cis- and trans-isomers and electronic energy differences between various states (electronically excited, electron-attached, and ionized states). The calculations were performed with three basis sets — 6-31+G(d,p) (test1), aug-cc-pVDZ (test2), and cc-pVTZ (test3).

2. Cluster of two methylated uracils and a water molecule (test4)[33]. Energy differences between different electronic states are considered.

3. Tetramer of 4 nucleobases, AATT, from Ref. 52 (test5).

4. Oligoporphyrin dimer used in previous benchmarks[33] (test6).

5. Cluster of methylated uracil, mU, and water from Ref. 53. We focus on the potential energy profiles along the proton-transfer reaction coordinate.

The following thresholds were used in CCSD and EOM-CCSD calculations[e]: T-amplitudes convergence of $|T_n - T_{n-1}| \leq 10^{-4}$, energy convergence $|E_n - E_{n-1}| \leq 10^{-6}$, Davidson's procedure convergence $|R_n| \leq 10^{-5}$ (here R_n is the Davidson residual), threshold for subspace expansion in Davidson's procedure $|R_n| > 10^{-5}$. Table 6.3 lists parameters for different benchmark examples. All electrons were active in test1; test2 was executed with and without frozen core; core electrons were frozen in test3–6. In some cases, we also employed Frozen Natural Orbitals (FNO) approximation[54]. All Cartesian geometries and relevant energies are given in supplementary materials for Ref.

[e]Q-Chem's keywords controlling the CC and EOM convergence: CC_T_CONV = 4, CC_E_CONV = 6, EOM_DAVIDSON_CONV = 5, EOM_DAVIDSON_THRESH = 5.

41. All calculations were performed using regular (i.e., employing non-decomposed ERI) Hartree–Fock procedure. Correlation energies in Table 6.3 are for canonical calculations (using full ERI) except for test5.

Tables 6.4 and 6.5 presents the comparison of the canonical CCSD calculation and RI/CD approximations. We note that the errors in total CCSD energies for RI and CD/10^{-3} approximations are comparable (and are in a millihartree range). However, the rank of CD/10^{-3} is often less than that of RI giving rise to a more significant speed-up (the situation is reversed in for test3 which uses the cc-pVTZ basis). We also note that CD/10^{-4} leads to the rank comparable to the size of the auxiliary basis in RI (1065 versus 1099), but yields two orders of magnitude more accurate total energies (error 8.27×10^{-6} versus 8.10×10^{-4} hartree).

Overall, RI/CD CCSD calculations are 10–60% faster than the canonical implementation. We observe a more significant speed-up for larger calculations, e.g., compare test4, test3, and test2 versus test1, likely because the I/O penalties are more pronounced for larger jobs. For the same molecule, we observe more significant speed-up in larger bases (compare test3 versus test2 and test1), because larger bases have more linear dependencies. Using test4 as an example, we observe that combination of CD with FNO approximation leads to a very impressive speed-up, i.e., CD/10^{-3}/FNO calculation takes only 15% of the time of the full CCSD calculation.

Table 6.3: Test systems used for benchmarks, converged CCSD correlation energies (hartree), and number of CC iterations.

Name	Molecule	Formula	Symm	N_{el}	Basis[a]	# b.f.	E_{corr}	N_{iter}
Test1	PYPb[b,c]	$C_9O_3H_7$	C_s	86	6-31+G(d,p)	263	-1.838 498	14
Test2	PYPb[b,c]	$C_9O_3H_7$	C_s	86	aug-cc-pVDZ	363	-1.955 977	14
Test2-fc	PYPb[b,d]	$C_9O_3H_7$	C_s	86	aug-cc-pVDZ	363	-1.875 348	14
Test3	PYPb[b,d]	$C_9O_3H_7$	C_s	86	cc-pVTZ	489	-2.147 251	14
Test4	$(mU)_2 \cdot H_2O$[c]	$C_{12}O_5N_4H_{18}$	C_1	158	6-31+G(d,p)	489	-3.334 026	12
Test5	AATT[d]	$C_{20}O_4N_{14}H_{22}$	C_1	386	6-311+G(d,p)	968	-5.975 572[e]	12
Test6	Porphyrin[d]	$C_{46}N_{12}H_{26}$	D_{2h}	272	cc-pVDZ	942	-7.995 344	11

[a] Ref. 55, 56 for 6-31+G(d,p), Ref. 56, 57 for 6-311+G(d,p), Ref. 58 for cc-pVDZ, cc-pVTZ and aug-cc-pVDZ. [b] PYPb: anti-syn conformation. [c] Core electrons active. [d] Core electrons frozen. [e] Calculation using conventional CCSD with RI integrals (rimp2-cc-pVDZ[37] auxiliary basis set).

Table 6.4: CCSD errors and wall times (sec) using 12 cores for test1-test3

Name	Method	Rank	CCSD error	CCSD wall	Ratio[a]	CD wall time[b]
Test1	Full			1894		
	RI/rimp2-aug-cc-pVDZ	1099	8.10×10^{-4}	1771	0.94	
	CD/10^{-1}	135	1.49×10^{-1}	1500	0.79	85
	CD/10^{-2}	505	1.71×10^{-3}	1591	0.84	530
	CD/10^{-3}	715	2.74×10^{-4}	1642	0.87	978
	CD/10^{-4}	1065	8.27×10^{-6}	1773	0.94	2035
Test2	Full			9490		
	RI/rimp2-aug-cc-pVDZ	1099	7.8×10^{-4}	5175	0.55	
	CD/10^{-3}	804	2.1×10^{-3}	4750	0.50	2345
Test2-fc	Full			2870		
	RI/rimp2-aug-cc-pVDZ	1099	1.1×10^{-3}	2847	0.99	
	CD/10^{-3}	804	4.2×10^{-4}	2626	0.91	2348
Test3	Full			21257		
	RI/rimp2-cc-pVTZ	1256	1.4×10^{-3}	9209	0.43	
	CD/10^{-3}	1629	1.9×10^{-4}	10367	0.49	15491

[a] Ratio=Time(RI/CD)/Time(full) for CCSD iterations. [b] Wall time for Cholesky decomposition (CD) procedure.
Memory settings: test1 — 20 GB, test2 — 50 GB, test3 — 80 GB

Table 6.5: CCSD errors and wall times (sec) using 12 cores for test4-test6.

Name	Method	Rank	CCSD error	CCSD wall	Ratio[a]	CD wall time[b]
Test4	Full			110379		
	RI/rimp2-aug-cc-pVDZ	2067	1.6×10^{-3}	85425	0.77	
	CD/10^{-3}	1335	6.4×10^{-4}	88198	0.80	10301
	CD/10^{-3}/FNO[c]	1335		25464	0.15	10392
Test5	Full/rimp2-cc-pVTZ/FNO[d,e,f]			726.4 h		
	RI/rimp2-cc-pVTZ/FNO[d]	3738		699.2 h	0.96	
	CD/10^{-2}/FNO[d]	1688		443.6 h	0.61	15.4 h
Test6	Full		4.7×10^{-3}	211.0 h		
	RI/rimp2-cc-pVDZ	3612	4.7×10^{-3}	194.9 h	0.92	
	RI/rimp2-cc-pVDZ/FNO[g]	3612		63.3 h	0.30	

[a] Ratio=Time(RI/CD)/Time(full) for CCSD iterations. [b] Wall time for Cholesky decomposition (CD) procedure. [c] Using FNO (see Ref. 54), 99.50% occupation threshold and frozen core (350 active orbitals). CCSD converges in 11 iterations. [d] Using FNO, 99.50% occupation threshold and frozen core (649 active orbitals). CCSD converges in 12 iterations. [e] From Ref. 33. [f] Canonical CCSD calculations using RI integrals. [g] Using FNO, 99.50% occupation threshold and frozen core (754 active orbitals). CCSD converges in 16 iterations.
Memory settings: test4 — 48 GB, test5 — 100 GB, test6 — 100 GB.

Finally, let us consider two large examples, i.e., a nucleobase tetramer (AATT)[33,52] (test5, C_1 symmetry, 966 basis functions, 38 core orbitals frozen) and the oligoporphyrin dimer (test6, D_{2h} symmetry, 942 basis functions, 58 core orbitals frozen)[33] and compare them to the canonical calculations[33]. In test5 we also employ FNO approximation (279 out of 830 virtuals frozen, total 649 active orbitals). First, we note significant reduction in disk requirements for both examples (e.g., 382 GB versus 2.8 TB for AATT). For test6, the first RI/CD CCSD iteration is more than twice faster than in the canonical implementation (6.33 hours for RI-CCSD versus 13.2 hours for the canonical CCSD[33]). However, we observe a slowdown of the subsequent iterations due to the increasing number of T-amplitudes that need to be handled by the DIIS procedure. The average time per iteration for oligoporphyrin is 12 hours (194.9 hours total time, 16 iterations), although the first iteration is two times faster (6.33 hrs). We also computed oligoporphyrin in combination with FNO (130 out of 749 virtual orbitals frozen, 754 active orbitals) with time for first iteration 2.35 hours and the average time per iteration 3.95 hours. For AATT we observe a similar speed-up of RI-CCSD iterations, the first RI-CCSD iteration takes 39 hours (to be compared to 60 hours in the canonical implementation[33]). AATT computed with CD/10^{-2} yields a rank of 1688 and the first CCSD iteration takes 28.25 hours, to be compared with 60 hours in the canonical implementation and 39 hours with RI/rimp2-cc-pVTZ.

A more detailed breakdown of timings for CCSD calculations is given in supplementary materials for Ref. 41 (Table S1). As expected, the evaluation of intermediate $I^{(2i)}_{ijab}$ takes a significant fraction of time, especially in larger bases (it scales as O^2V^4). Evaluation of equation for t_2 amlitudes, which contains one O^3V^3 (third term) and one O^4V^2 (the last term) contractions, is also significant and becomes dominant in an electron-rich case, test6.

The time used for the decomposition and integral transformation steps is also shown in Tables 6.4 and 6.5. Since the present implementation of the decomposition algorithm does not use point group symmetry, the timings for test1–test3 are relatively large. We note that for test4 (C_1), the time of decomposition with a threshold of 10^{-3} is about 12% of the total time for CCSD iterations.

We investigate parallel performance using test4 (Table 6.6). The parallel scaling is improved, e.g., the canonical implementation shows a factor of 6 speed-up on 12 cores, whereas the RI/CD code is accelerated by a factor of 9. Thus, the speed-up relative to the canonical CCSD code becomes more pronounced on 12 cores, e.g., on a single CPU, RI/CD calculation is about 20% faster, whereas on 12 cores, it is almost a factor of two faster than the canonical code. This improvement in the parallel performance is due to the significant reduction of the amount of data to be handled in the CCSD calculations.

Table 6.6: Wall time per CCSD iteration (sec) using 80 GB RAM.

Job	1 core	4 cores	8 cores	12 cores
Full	46405	14278 ($\times$3.25)	9506 ($\times$4.88)	7973 ($\times$5.82)
RI/rimp2-aug-cc-pVDZ	39347	10283 ($\times$3.83)	5539 ($\times$7.10)	4342 ($\times$9.06)
CD/10^{-3}	37330	9889 ($\times$3.78)	4973 ($\times$7.51)	4185 ($\times$8.92)

Table 6.7 shows EOM energies and timings for test1 and test2; the results for test2-fc and test3 are presented in Table 6.8. We note that RI and CD/10^{-3} give comparable errors in excitation, attachment, and ionization energies, i.e., less than 0.01-0.001 eV. These errors are consistent with those reported for the CASSCF and CASPT2 methods[19]. The errors in the energies are systematically reduced with the Cholesky threshold decrease from 10^{-2} to 10^{-4} for all methods. We observe that a threshold of 10^{-2} yields errors of $\sim$0.03 eV, which is acceptable in many situations and is less than error bars of EOM-CCSD.

For test1, the timings for RI/CD EOM methods are slower than of the canonical implementation due to the increased number of contractions, as explained in Section 6.3. However, in a larger basis (aug-cc-pVDZ versus 6-31+G*), the gap shrinks for EOM-IP (total RI/CD EOM time is almost the same as of the canonical calculation), and RI/CD EOM-EE shows 60-70% speed-up. Further increase of the basis (to cc-pVTZ) leads to an additional speed-up, i.e., RI/CD EOM-EE calculations for test3 take 25% of the full EOM-EE time. This is because the increased number of time-determining contractions in RI/CD EOM-EE (7 for RI/CD EOM-EE versus 3 N^6 operations in canonical EOM) is offset by the significantly reduced disk and memory usage by RI/CD EOM that reduces I/O penalties and improves parallel scaling. For example, for test5 (AATT) EOM-EE-CCSD calculations (with frozen core and FNO) the estimated disk usage is 7.2 TB, whereas for the corresponding RI/rimp2-cc-pVTZ calculation it is only 590 GB. For test3, we observe that canonical EOM shows rather poor parallel scaling (CPU 102655 s, wall 93432 s, ratio=1.09), whereas for RI EOM we see more than a 10 fold CPU/wall ratio (CPU 228202 s, wall 21553 s, ratio=10.58), leading to an overall 5-fold speedup of Davidson iterations. Thus, RI/CD implementation of EOM not only extends the applicability of the method to larger systems that may not be accessible by canonical EOM-CCSD due to disk/memory bottlenecks, but also improves timings of the calculations by removing the overheads due to large size of the data.

The calculation time of the intermediates for EOM calculations is significantly reduced for all RI/CD methods, as illustrated by test2 timings revealing that the intermediates calculations (dominated by the VVVV block of the transformed integrals) take almost as much time as Davidson iterations. Thus, the overall CD/RI EOM-EE timings (Davidson iterations plus intermediates) are considerably faster (3-5 times) than those of the canonical code when only of few EOM roots are computed for large systems.

The detailed timings for RI EOM-EE-CCSD calculations are given in supplementary information for Ref. 41 (Table S2). We observe that σ_2-vector update procedure takes most of total EOM time (96% for test 3). Within it, the calculation of I^{1i}_{ijab}, is dominant (70% of the total EOM time for test3), as expected based on O^2V^4 operations required to evaluate this term.

Calculations of ionization energies for test4 (Table 6.9) show the errors of the same order of the magnitude, 0.001 eV and 0.0001 eV for RI and CD/10^{-3}, respectively, as in the PYPb examples (test1 and test2). Calculations of EOM-IP σ-vectors with RI/CD are slightly slower than in the canonical calculations, however the time required for calculation of intermediates is significantly smaller for RI/CD, resulting in more than 2-fold overall speedup. The speed-up for RI/CD EOM-IP is less than for RI/CD EOM-EE due to smaller size of the data used by EOM-IP, which does not involve VVVV and OVVV intermediates; thus, the canonical code shows much better parallel performance than EOM-EE (for full EOM-IP, CPU 587 s, wall 63 s, ratio=9.45; for RI EOM-IP, CPU 2067 s, wall 214 s, ratio=9.70).

Using FNO (threshold 99.5%, 118 virtual orbitals frozen out of 410 total) significantly improves the total EOM timings making it more than 6 times faster than the full canonical calculation. The errors introduced by the FNO approximation are larger than those due to CD ($\sim$0.01 eV), but they are still acceptable for most applications. Thus, RI/CD in conjunction with FNO leads to significant reduction of both memory and computational cost requirements, with only minor losses in accuracy.

Table 6.7: EOM-CCSD energies for the 2 lowest states in each irrep and errors in energy differences (eV), and wall times for EOM (sec) using 12 cores.

Method	EOM time				EOM	1A'	2A'	1A"	2A"
	Int[a]	Iter[b]	Total[c]	Ratio[d]	calls[e]				
Test1									
EOM-EE-CCSD	342	3344	3686		46	3.158 eV	4.233 eV	3.860 eV	4.171 eV
RI[f]	65	6641	6706	1.8 (2.0)	46	1.0×10^{-4}	1.0×10^{-4}	1.2×10^{-3}	1.2×10^{-3}
CD/10^{-2}	56	6093	6149	1.7 (1.8)	46	2.8×10^{-2}	3.5×10^{-2}	2.5×10^{-2}	2.0×10^{-2}
CD/10^{-3}	59	6276	6335	1.7 (1.9)	46	4.2×10^{-3}	6.7×10^{-3}	6.5×10^{-3}	3.9×10^{-3}
CD/10^{-4}	64	6588	6652	1.8 (2.0)	46	2.0×10^{-4}	6.0×10^{-4}	1.0×10^{-3}	9.0×10^{-4}
EOM-EA-CCSD	351	486	837		31	3.931 eV	4.329 eV	3.700 eV	5.268 eV
RI[f]	65	984	1049	1.3 (2.0)	31	1.0×10^{-4}	$< 10^{-4}$	1.3×10^{-3}	1.0×10^{-4}
CD/10^{-2}	56	710	766	0.9 (1.5)	31	1.9×10^{-2}	9.8×10^{-3}	1.5×10^{-2}	2.5×10^{-2}
CD/10^{-3}	59	788	847	1.0 (1.6)	31	7.5×10^{-3}	5.6×10^{-3}	2.5×10^{-3}	6.6×10^{-3}
CD/10^{-4}	65	975	1040	1.2 (2.0)	31	4.0×10^{-4}	1.4×10^{-3}	3.0×10^{-4}	1.1×10^{-3}
EOM-IP-CCSD	93	46	139		26	4.328 eV	6.758 eV	2.735 eV	5.353 eV
RI[f]	65	132	197	1.4 (2.9)	26	6.0×10^{-4}	8.0×10^{-4}	1.3×10^{-3}	1.1×10^{-3}
CD/10^{-2}	57	108	165	1.2 (2.4)	26	1.3×10^{-2}	6.9×10^{-3}	2.3×10^{-3}	2.8×10^{-3}
CD/10^{-3}	60	117	177	1.3 (2.5)	26	2.0×10^{-4}	1.0×10^{-4}	2.0×10^{-4}	7.0×10^{-4}
CD/10^{-4}	65	132	197	1.4 (2.9)	26	$< 10^{-4}$	$< 10^{-4}$	1.0×10^{-4}	$< 10^{-4}$
Test2									
EOM-EE-CCSD	20021	39991	60012		49	3.167 eV	4.148 eV	3.349 eV	5.666 eV
RI[f]	139	18522	18661	0.3 (0.5)	49	1.0×10^{-4}	1.0×10^{-4}	1.0×10^{-3}	1.1×10^{-3}
CD/10^{-3}	125	18572	18697	0.3 (0.5)	49	5.0×10^{-4}	1.2×10^{-3}	2.0×10^{-4}	$< 10^{-4}$
EOM-IP-CCSD	245	70	315		26	4.467 eV	6.772 eV	2.904 eV	5.462 eV
RI[f]	165	211	376	1.2 (3.0)	26	9.0×10^{-4}	8.0×10^{-4}	1.3×10^{-3}	8.0×10^{-4}
CD/10^{-3}	159	196	355	1.1 (2.8)	26	9.0×10^{-4}	7.0×10^{-4}	9.0×10^{-4}	8.0×10^{-4}

[a] Time for calculations of the EOM-CCSD intermediates for the Davidson procedure. [b] Time for EOM iterations. [c] Total EOM time (intermediates + Davidson iterations). [d] Ratio= Time(RI/CD)/Time(full). The first value is the ratio of total EOM times; the ratio for Davidson iterations is given in parentheses. [e] σ-vector update calls. [f] rimp2-aug-cc-pVDZ auxiliary basis.

Table 6.8: EOM-CCSD energies for the 2 lowest states in each irrep and errors in energy differences (eV), and wall times (sec) using 12 cores.

Method	EOM time				EOM	1A'	2A'	1A"	2A"
	Int[a]	Iter[b]	Total[c]	Ratio[d]	calls[e]				
Test2-fc									
EOM-EE-CCSD	4565	6917	11482		48	3.166 eV	4.148 eV	3.344 eV	5.662 eV
RI[f]	68	9619	9687	0.8 (1.4)	48	1.0×10^{-4}	1.0×10^{-4}	1.1×10^{-3}	1.1×10^{-3}
CD/10^{-3}	62	8987	9049	1.3 (2.3)	48	5.0×10^{-4}	1.2×10^{-3}	2.0×10^{-4}	$< 10^{-4}$
Test3									
EOM-EE-CCSD	47946	93432	141378		36	3.307 eV	4.333 eV	5.513 eV	5.690 eV
RI[g]	170	21552	21722	0.2 (0.2)	36	3.0×10^{-4}	1.0×10^{-4}	4.0×10^{-4}	3.0×10^{-4}
CD/10^{-3}	194	26839	27033	0.2 (0.3)	36	8.0×10^{-4}	9.0×10^{-4}	2.6×10^{-3}	2.4×10^{-3}
EOM-IP-CCSD	426	62	488		26	4.450 eV	6.795 eV	2.872 eV	5.447 eV
RI[g]	166	214	380	0.8 (3.5)	26	1.3×10^{-3}	1.3×10^{-3}	1.0×10^{-3}	8.0×10^{-4}
CD/10^{-3}	189	245	434	0.9 (4.0)	26	1.0×10^{-4}	1.0×10^{-4}	2.0×10^{-4}	3.0×10^{-4}

[a] Time for calculations of the EOM-CCSD intermediates for the Davidson procedure. [b] Time for EOM iterations. [c] Total EOM time (intermediates + Davidson iterations). [d] Ratio= Time(RI/CD)/Time(full). The first value is the ratio of total EOM times; the ratio for Davidson iterations is given in parentheses. [e] σ-vector update calls. [f] rimp2-aug-cc-pVDZ auxiliary basis. [g] rimp2-cc-pVTZ auxiliary basis.

Table 6.9: EOM-IP-CCSD energies (absolute errors for RI/CD) and EOM wall times (sec) for test4 (two lowest EOM roots).

Method	EOM time				EOM	State 1	State 2
	Int[a]	Iter[b]	Total[c]	Ratio[d]	calls[e]		
EOM-IP-CCSD	5088	503	5591		10	8.421 eV	8.858 eV
RI[f]	1866	576	2442	0.4	10	1.0×10^{-3}	1.0×10^{-3}
CD/10^{-3}	2083	514	2597	0.5	10	5.0×10^{-4}	2.0×10^{-4}
CD/10^{-3}/FNO[g]	541	270	811	0.2	10	1.6×10^{-2}	1.5×10^{-2}

[a] Time for calculations of the EOM-CCSD intermediates for the Davidson procedure. [b] Time for EOM iterations. [c] Total EOM time (intermediates + Davidson iterations). [d] Ratio of total times: Time(RI/CD)/Time(Full). [e] Number of calls of σ-update procedure. [f] rimp2-aug-cc-pVDZ auxiliary basis. [g] Frozen core and FNO (threshold 99.50%) was used.

To quantify the errors in energy differences along potential energy surfaces, we consider two examples. We begin by considering the energy differences between two PYP isomers[51] shown in Table 6.10. The energy difference between two PYPb isomers (anti-syn and anti-anti) is 4.15 kcal/mol at the CCSD/6-31+G(d,p) level of theory. The errors introduced by RI and CD are: 2.40×10^{-3} (rimp2-aug-cc-pVDZ), 6.42×10^{-2} (CD/10^{-2}), 2.12×10^{-2} (CD/10^{-3}), and 9.00×10^{-4} (CD/10^{-4}) kcal/mol; the errors are considerably smaller than the errors in the total CCSD correlation energy due to error cancellation. Note that even for the crudest CD threshold (10^{-2}) the error in the energy differences is quite satisfactory ($\sim$0.1 kcal/mol). The error cancellation effect is more pronounced for RI where the error in energy differences is more than 2 orders of magnitude less than the error in the total energy, whereas for CD the difference is more modest (about 1 order of magnitude). Thus, in terms of the energy differences, RI is more accurate than CD/10^{-3}, but is still slightly less accurate than CD/10^{-4}.

As a more challenging case, we consider scans along proton-transfer coordinate in ionized mU-H_2O cluster from Ref. 53. Fig. 6.1 shows CCSD and EOM-IP-CCSD energies along the proton-transfer reaction coordinate computed in the 6-311+G(d,p)

Table 6.10: Energy differences between PYPb isomers ($E_{anit-anti} - E_{anti-syn}$, kcal/mol) and the corresponding errors against full CCSD.

Method	Energy difference	Error, kcal/mol	Error, hartree
Full	4.1531		
RI/rimp2-aug-cc-pVDZ	4.1507	2.40×10^{-3}	3.82×10^{-6}
CD/10^{-2}	4.0889	6.42×10^{-2}	1.02×10^{-4}
CD/10^{-3}	4.1319	2.12×10^{-2}	3.37×10^{-5}
CD/10^{-4}	4.1540	9.00×10^{-4}	1.43×10^{-6}

basis set. We note that RI features the smallest errors, both in terms of absolute values (around 10^{-4}–10^{-5} eV) and in terms of non-parallelity errors (NPEs) (4×10^{-5} and 5×10^{-5} eV for CCSD and EOM-IP-CCSD energies, respectively). This is because the auxiliary basis in RI is atom-centered and does not depend on geometry[59]. CD shows larger errors along the scan; however, the respective NPEs are small and do not exceed 0.001 eV for CD/10^{-3} and 0.0003 eV for CD/10^{-4}. We note that the range of changes in total energy along this scan is about 2 eV. Smooth behavior of the CD scans is consistent with small variations of the rank along this scan, e.g., for CD/10^{-3} and CD/10^{-4} the rank is 834$\pm$2 and 1188$\pm$3, respectively.

6.5 Conclusions

We present a new implementation of RI and Cholesky decompositions within the CCSD/EOM-CCSD suite of methods in the Q-Chem electronic structure package[27,28]. This implementation eliminates the storage of the most expensive four-index electron repulsion integrals and intermediates, such as VVVV, OVVV and OVOV blocks of ERI, leading to a significant reduction in storage requirements and I/O overheads. The number of floating-point operations is reduced for CCSD; however, it is increased by approximately a factor of 3 in EOM calculations (σ-vectors update) because the transformed

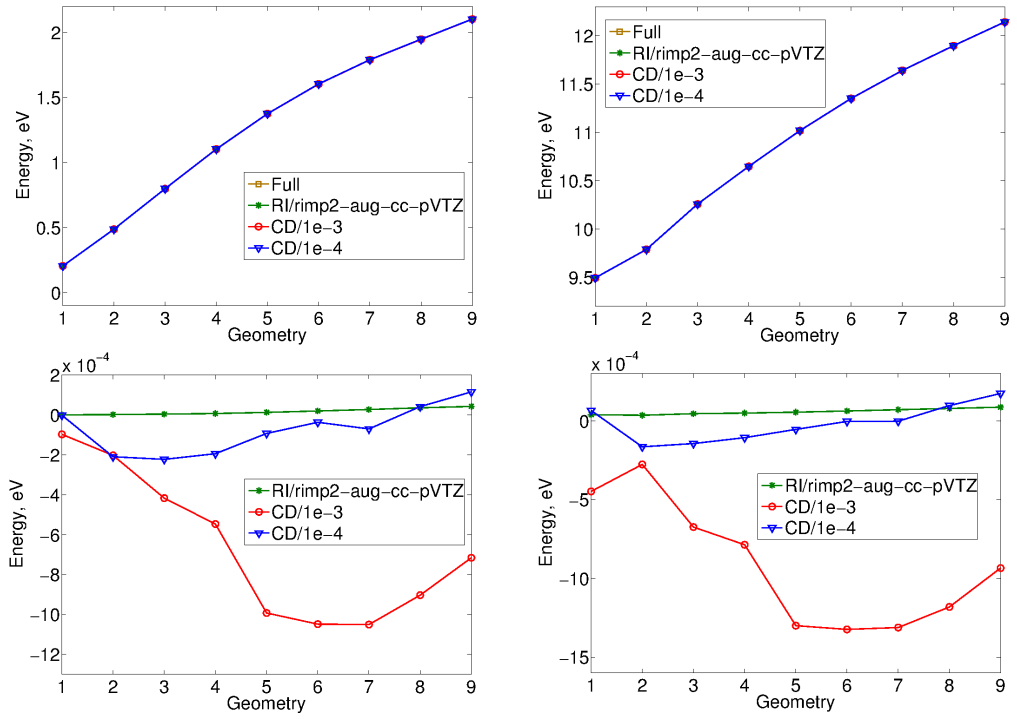

Figure 6.1: Top: CCSD (left) and EOM-IP-CCSD (right) energies along the proton-transfer coordinate in mU-H_2O. Bottom: Errors of RI/rimp2-aug-cc-pVTZ and CD approximations.

integrals and related intermediates, which are computed only once in canonical EOM, need to be reassembled at each Davidson iteration in the RI/CD implementation. However, this undesirable increase in computations is offset by significantly reduced I/O overheads. In a shared-memory parallel setting the reduction of I/O also leads to better CPU utilization and improved parallel scalability. When the calculation of the intermediates is included, the ratio between RI/CD and canonical EOM-EE timings is about 0.3–0.5 for moderate-size basis sets. The gains are more significant in large bases, e.g., a RI-EOM-EE-CCSD/cc-pVTZ calculation takes only 15% of the time required for the full calculation. Additional computational savings can be achieved by combining RI/CD and FNO approaches[54].

The accuracy of RI/CD implementations is benchmarked with an emphasis on energy differences, such as excitation energies. In agreement with previous benchmarks based on the CASSCF, CASPT2, and CC2 methods[19,48], we observe that the errors in energy differences are smaller than the errors in total energies due to error cancellation. Typical errors in the CCSD correlation energy are less than a millihartree for the RI approximation with RI-MP2 auxiliary bases, however, the respective EOM errors are less than 0.001 eV. The accuracy of CD can be controlled by a single threshold. For a threshold of 10^{-4}, which results in a rank similar to RI, the errors in total energies are two orders of magnitude less than for RI; however, the errors in energy differences are roughly the same. This threshold is therefore recommended when high accuracy is required. We note that errors in excitation energies are quite small when using thresholds of 10^{-2} and 10^{-3} (less than 0.04 and 0.008 eV, respectively); therefore these thresholds can be used in most calculations.

This paper presents our first step towards developing reduced-scaling CC/EOM-CC codes. While the present implementation does not reduce scaling of the calculations, it affords significant computational savings thus extending the applicability of these methods to larger systems. In order to achieve further gains, additional steps should be taken. Among promising strategies[19] are a tensor hyper-contraction approach[21,22], local correlation schemes and pair natural orbitals[25,26,60,61], as well as reduced-rank representations of the CC/EOM amplitudes[23,24,62,63].

6.6 Chapter 6 references

[1] J.A. Pople. Theoretical models for chemistry. In D.W. Smith and W.B. McRae, editors, *Energy, Structure and Reactivity: Proceedings of the 1972 Boulder Summer Research Conference on Theoretical Chemistry*, pages 51–61. Wiley, New York, 1973.

[2] T. Helgaker, P. Jørgensen, and J. Olsen. *Molecular electronic structure theory*. Wiley & Sons, 2000.

[3] R.J. Bartlett. The coupled-cluster revolution. *Mol. Phys.*, 108:2905–2920, 2010.

[4] A.I. Krylov. Equation-of-motion coupled-cluster methods for open-shell and electronically excited species: The hitchhiker's guide to Fock space. *Annu. Rev. Phys. Chem.*, 59:433–462, 2008.

[5] K. Sneskov and O. Christiansen. Excited state coupled cluster methods. *Wiley Interdisciplinary Reviews: Computational Molecular Science*, 2:566, 2011.

[6] R.J. Bartlett. Coupled-cluster theory and its equation-of-motion extensions. *Wiley Interdisciplinary Reviews: Computational Molecular Science*, 2(1):126–138, 2012.

[7] F. Weigend, M. Häser, H. Patzelt, and R. Ahlrichs. RI-MP2: optimized auxiliary basis sets and demonstration of efficiency. *Chem. Phys. Lett.*, 294:143–152, 1998.

[8] J.L. Whitten. Coulombic potential energy integrals and approximations. *J. Chem. Phys.*, 58:4496, 1973.

[9] M.W. Feyereisen, G. Fitzgerald, and A. Komornicki. *Chem. Phys. Lett.*, 208:359, 1993.

[10] O. Vahtras, J. Almlöf, and M.W. Feyereisen. *Chem. Phys. Lett.*, 213:514, 1993.

[11] A. Komornicki and G. Fitzgerald. *J. Chem. Phys.*, 98:1398, 1993.

[12] D.E. Bernhold and R.J. Harrison. *Chem. Phys. Lett.*, 250:477, 1996.

[13] Y. Jung, A. Sodt, P. M. W. Gill, and M. Head-Gordon. Auxiliary basis expansions for large-scale electronic structure calculations. *Proc. Nat. Acad. Sci.*, 102:6692–6697, 2005.

[14] N.H.F. Beebe and J. Linderberg. Simplifications in the generation and transformation of two-electron integrals in molecular calculations. *Int. J. Quant. Chem.*, 12:683–705, 1977.

[15] H. Koch, A.S. de Merás, and T.B. Pedersen. Reduced scaling in electronic structure calculations using Cholesky decompositions. *J. Chem. Phys.*, 118:9481, 2003.

[16] F. Aquilante, R. Lindh, and T. B. Pedersen. Unbiased auxiliary basis sets for accurate two-electron integral approximations. *J. Chem. Phys.*, 127:114107, 2007.

[17] F. Aquilante, T. B. Pedersen, and R. Lindh. Density fitting with auxiliary basis sets from Cholesky decompositions. *Theor. Chem. Acc.*, 124:1–10, 2009.

[18] F. Aquilante, L. Gagliardi, T. B. Pedersen, and R. Lindh. Atomic Cholesky decompositions: A route to unbiased auxiliary basis sets for density fitting approximation with tunable accuracy and efficiency. *J. Chem. Phys.*, 130:154107, 2009.

[19] F. Aquilante, L. Boman, J. Boström, H. Koch, R. Lindh, A.S. de Merás, and T.B. Pedersen. Cholesky decomposition techniques in electronic structure theory. In R. Zaleśny, M.G. Papadopoulos, P.G. Mezey, and J. Leszczynski, editors, *Linear-Scaling Techniques in Computational Chemistry and Physics*, Challenges and advances in computational chemistry and physics, pages 301–343. Springer, 2011.

[20] F. Weigend, M. Kattannek, and R. Ahlrichs. Approximated electron repulsion integrals: Cholesky decomposition versus resolution of the identity methods. *J. Chem. Phys.*, 130:164106, 2009.

[21] R.M. Parrish, E.G. Hohenstein, T.J. Martínez, and C.D. Sherrill. Tensor hypercontraction. II. Least-squares renormalization. *J. Chem. Phys.*, 137(22):224106, 2012.

[22] E.G. Hohenstein, R.M. Parrish, C.D. Sherrill, and T.J. Martínez. Communication: Tensor hypercontraction. III. Least-squares tensor hypercontraction for the determination of correlated wavefunctions. *J. Chem. Phys.*, 137(22):221101, 2012.

[23] F. Aquilante, T.K. Todorova, L. Gagliardi, T.B. Pedersen, and B.O. Roos. Systematic truncation of the virtual space in multiconfigurational perturbation theory. *J. Chem. Phys.*, 131:034113, 2009.

[24] F. Aquilante and T.B. Pedersen. Quartic scaling evaluation of canonical scaled opposite spin second-order MøllerPlesset correlation energy using Cholesky decompositions. *Chem. Phys. Lett.*, 449:354–357, 2007.

[25] C. Riplinger and F. Neese. An efficient and near linear scaling pair natural orbital based local coupled cluster method. *J. Chem. Phys.*, 138:034106, 2013.

[26] D. Kats, T. Korona, and M. Schütz. Local CC2 electronic excitation energies for large molecules with density fitting. *J. Chem. Phys.*, 125:104106–104121, 2006.

[27] Y. Shao, L. Fusti-Molnar, Y. Jung, J. Kussmann, C. Ochsenfeld, S. Brown, A.T.B. Gilbert, L.V. Slipchenko, S.V. Levchenko, D.P. O'Neill, R.A. Distasio Jr, R.C. Lochan, T. Wang, G.J.O. Beran, N.A. Besley, J.M. Herbert, C.Y. Lin, T. Van Voorhis, S.H. Chien, A. Sodt, R.P. Steele, V.A. Rassolov, P. Maslen, P.P. Korambath, R.D. Adamson, B. Austin, J. Baker, E.F.C. Byrd, H. Daschel, R.J. Doerksen, A. Dreuw, B.D. Dunietz, A.D. Dutoi, T.R. Furlani, S.R. Gwaltney, A. Heyden, S. Hirata, C.-P. Hsu, G.S. Kedziora, R.Z. Khalliulin, P. Klunziger, A.M. Lee, W.Z. Liang, I. Lotan, N. Nair, B. Peters, E.I. Proynov, P.A. Pieniazek, Y.M. Rhee, J. Ritchie, E. Rosta, C.D. Sherrill, A.C. Simmonett, J.E. Subotnik, H.L. Woodcock III, W. Zhang, A.T. Bell, A.K. Chakraborty, D.M. Chipman, F.J. Keil, A. Warshel, W.J. Hehre, H.F. Schaefer III, J. Kong, A.I. Krylov, P.M.W. Gill, M. Head-Gordon. Advances in methods and algorithms in a modern quantum chemistry program package. *Phys. Chem. Chem. Phys.*, 8:3172–3191, 2006.

[28] A.I. Krylov and P.M.W. Gill. Q-Chem: An engine for innovation. *WIREs Comput. Mol. Sci.*, 3:317–326, 2013.

[29] A.P. Rendell and T.J. Lee. Coupled-cluster theory employing approximate integrals - an approach to avoid the input/output and storage bottlenecks. *J. Chem. Phys.*, 101:400–408, 1994.

[30] F. Aquilante, L. de Vico, N. Ferré, G. Ghigo, P-Å Malmqvist, P. Neogrády, T. B. Pedersen, M. Pitonăk, M. Reiher, B. Roos, L. Serrano-Andrés, M. Urban, V. Veryazov, and R. Lindh. Molcas 7: The next generation. *J. Comput. Chem.*, 31:224–247, 2010.

[31] S. Wilson. Universal basis sets and Cholesky decomposition of the two-electron integral matrix. *Comp. Phys. Comm.*, 58:71–81, 1990.

[32] G.H. Golub and C.F. Van Loan. *Matrix computations*. Johns Hopkins University Press, 1996.

[33] E. Epifanovsky, M. Wormit, T. Kuś, A. Landau, D. Zuev, K. Khistyaev, P. Manohar, I. Kaliman, A. Dreuw, and A.I. Krylov. New implementation of high-level correlated methods using a general block-tensor library for high-performance electronic structure calculations. *J. Comput. Chem.*, 34:2293–2309, 2013.

[34] K. Eichkorn, O. Treutler, H.Öhm, M. Häser, and R. Ahlrichs. Auxiliary basis sets to approximate Coulomb potentials. *Chem. Phys. Lett.*, 242:652–660, 1995.

[35] K. Eichkorn, F. Weigend, O. Treutler, and R. Ahlrichs. Auxiliary basis sets for main row atoms and transition metals and their use to approximate Coulomb potentials. *Theor. Chem. Acc.*, 97:119–124, 1997.

[36] F. Weigend. Hartree-Fock exchange fitting basis sets for H to Rn. *J. Comput. Chem.*, 29:167–175, 2008.

[37] F. Weigend, A. Köhn, and C. Hättig. Efficient use of the correlation consistent basis sets in resolution of the identity MP2 calculations. *J. Chem. Phys.*, 116:3175, 2002.

[38] F. Weigend. Accurate coulomb-fitting basis sets for H to Rn. *Phys. Chem. Chem. Phys.*, 8:1057–1065, 2006.

[39] A. Hellweg, C. Hättig, S. Höfener, and W. Klopper. Optimized accurate auxiliary basis sets for RI-MP2 and RI-CC2 calculations for the atoms Rb to Rn. *Theor. Chem. Acc.*, 117:587–597, 2007.

[40] G.D. Purvis and R.J. Bartlett. A full coupled-cluster singles and doubles model: The inclusion of disconnected triples. *J. Chem. Phys.*, 76:1910–1918, 1982.

[41] E. Epifanovsky, D. Zuev, X. Feng, K. Khistyaev, Y. Shao, and A.I. Krylov. General implementation of resolition-of-identity and Cholesky representations of electron-repulsion integrals within coupled-cluster and equation-of-motion methods: Theory and benchmarks. *J. Chem. Phys.*, 139:134105, 2013.

[42] J.F. Stanton and R.J. Bartlett. The equation of motion coupled-cluster method. A systematic biorthogonal approach to molecular excitation energies, transition probabilities, and excited state properties. *J. Chem. Phys.*, 98:7029–7039, 1993.

[43] S.V. Levchenko and A.I. Krylov. Equation-of-motion spin-flip coupled-cluster model with single and double substitutions: Theory and application to cyclobutadiene. *J. Chem. Phys.*, 120(1):175–185, 2004.

[44] A.I. Krylov. The spin-flip equation-of-motion coupled-cluster electronic structure method for a description of excited states, bond-breaking, diradicals, and triradicals. *Acc. Chem. Res.*, 39:83–91, 2006.

[45] J. Boström, F. Aquilante, T. B. Pedersen, and R. Lindh. *Ab Initio* density fitting: Accuracy assessment of auxiliary basis sets from Cholesky decompositions. *J. Chem. Theory Comput.*, 5:1545–1553, 2009.

[46] V. P. Vysotskiy and L. S. Cederbaum. On the Cholesky decomposition for electron propagator methods: General aspects and application on C_{60}. *J. Chem. Phys.*, 132:044110, 2010.

[47] C. Hättig and F. Weigend. CC2 excitation energy calculations on large molecules using the resolution of the identity approximation. *J. Chem. Phys.*, 113(13):5154–5161, 2000.

[48] A. Köhn and C. Hättig. Analytic gradients for excited states in the coupled-cluster model CC2 employing the resolution-of-the-identity approximation. *J. Chem. Phys.*, 119(10):5021–5036, 2003.

[49] C. Hättig and A. Köhn. Transition moments and excited-state first-order properties in the coupled-cluster model CC2 using the resolution-of-the-identity approximation. *J. Chem. Phys.*, 117(15):6939–6951, 2002.

[50] T. Rocha-Rinza, O. Christiansen, J. Rajput, A. Gopalan, D.B. Rahbek, L.H. Andersen, A.V. Bochenkova, A.A.Granovsky, K.B. Bravaya, A.V. Nemukhin, K.L. Christiansen, and M.B. Nielsen. Gas phase absorption studies of photoactive yellow protein chromophore derivatives. *J. Phys. Chem. A*, 113:9442–9449, 2009.

[51] D. Zuev, K.B. Bravaya, T.D. Crawford, R. Lindh, and A.I. Krylov. Electronic structure of the two isomers of the anionic form of p-coumaric acid chromophore. *J. Chem. Phys.*, 134:034310, 2011.

[52] K.B. Bravaya, E. Epifanovsky, and Anna I. Krylov. Four bases score a run: Ab initio calculations quantify a cooperative effect of h-bonding and pi-stacking on ionization energy of adenine in the AATT tetramer. *J. Phys. Chem. Lett.*, 3:2726–2732, 2012.

[53] K. Khistyaev, A. Golan, K.B. Bravaya, N. Orms, A.I. Krylov, and M. Ahmed. Proton transfer in nucleobases is mediated by water. *J. Phys. Chem. A*, 117:6789–6797, 2013.

[54] A. Landau, K. Khistyaev, S. Dolgikh, and A.I. Krylov. Frozen natural orbitals for ionized states within equation-of-motion coupled-cluster formalism. *J. Chem. Phys.*, 132:014109, 2010.

[55] W.J. Hehre, R. Ditchfield, and J.A. Pople. Self-consistent molecular orbital methods. XII. Further extensions of gaussian-type basis sets for use in molecular orbital studies of organic molecules. *J. Chem. Phys.*, 56:2257, 1972.

[56] T. Clark, J. Chandrasekhar, and P.V.R. Schleyer. Efficient diffuse function-augmented basis sets for anion calculations. III. The 3-21+g basis set for first-row elements, li-f. *J. Comput. Chem.*, 4:294–301, 1983.

[57] R. Krishnan, J.S. Binkley, R. Seeger, and J.A. Pople. Self-consistent molecular orbital methods. XX. A basis set for correlated wave functions. *J. Chem. Phys.*, 72:650, 1980.

[58] T.H. Dunning. Gaussian basis sets for use in correlated molecular calculations. I. The atoms boron through neon and hydrogen. *J. Chem. Phys.*, 90:1007–1023, 1989.

[59] F. Weigend and M. Häser. RI-MP2: first derivatives and global consistency. *Theor. Chim. Acta*, 97:331–340, 1997.

[60] J. Yang, Y. Kurashige, F.R. Manby, and G.K.L. Chan. Tensor factorizations of local second-order Moller-Plesset theory. *J. Chem. Phys.*, 134:044123, 2011.

[61] J.E. Subotnik and M. Head-Gordon. A local correlation model that yields intrinsically smooth potential energy surfaces. *J. Chem. Phys.*, 123:064108, 2005.

[62] U. Benedikt, A.A. Auer, M. Espig, and W. Hackbusch. Tensor decomposition in post-Hartree-Fock methods. *J. Chem. Phys.*, 134:054118, 2011.

[63] F. Bell, D. Lambrecht, and M. Head-Gordon. Higher order singular value decomposition (HOSVD) in quantum chemistry. *Mol. Phys.*, 108:2759–2773, 2010.

Chapter 7: Root-specific eigenvalue solvers in the EOM family of methods: Implementation and benchmarks

7.1 Introduction

The task of finding several eigenpairs of large matrices is ubiquitous in science and engineering. It appears in structural dynamics, electrical networks, magnetohydrodynamics, control theory and many more[1]. In quantum chemistry it arises in the context of finding excited-state solutions in configuration interaction (CI)[2,3] and equation-of-motion (EOM) methods[3–7].

Even though the computational power has been growing very rapidly for the last two decades, the standard algorithms that find the entire eigenvalue spectrum (like the QR algorithm[8–10]) cannot handle very large matrices (e.g., $N > 10^5$). In EOM-EE calculation of a moderate-size system (around 300 Gaussian basis functions) the dimension of the full matrix exceeds 10^9. Obviously, it would be unwise to construct, store, and attempt to diagonalize the full matrix of such a size using standard numerical methods of finding the entire set of matrix's eigenpairs.

Many numerical methods aiming to compute only a few eigenvalues of a large matrix have been developed. These methods usually do not require the construction of the entire matrix, but rather involve a projection of the original matrix onto a search subspace. One of the most popular algorithms of this class are the Arnoldi's[1,11] and Lancsoz[1,12] algorithms; for a detailed description of the algorithms for solving large eigenvalue problems we refer the reader to a specialized book[1].

In the quantum chemistry community, Davidson's method[13] has been predominantly used for solving both Hermitian and non-Hermitian eigen-problems. Davidson's method can be viewed as a generalization of Lancsoz algorithm that uses the diagonal of the matrix as a preconditioner (Jacobi preconditioner) for new vectors that are added to the subspace[1]. The original matrix is projected to the search subspace of an increasing dimension and diagonalized, yelding approximate eigenpairs of the original matrix. Most of the matrices in quantum-chemical calculations are extremely sparse (only about 1-5% elements are non-zero) and strongly diagonally dominant, that is why Davidson's method is so successful and efective. The detailed description of Davidson's algorithm is given in section 7.3.1.

The original Davidson method was designed to find a few lowest eigenpairs of a matrix. However, in many applications one might be interested in finding a few highly lying states. For example, in core-ionization processes[14–16] the electron is ejected from a low lying orbital with energy as high as several hundred electron-volts. Another example is Feshbach resonances where the excited state is a highly lying state above the ionization threshold. If using the conventional Davidson method, one would need to request a tremendous number (very often, more than 100) of roots to find the one desired root. In most cases it is not feasible to compute so many roots, since in practice the convergence of Davidson's method for more than 10 roots is poor.

Motivated by this class of problems, we present new modifications of Davidson's algorithm that target states specified by the user. The first algorithm we present finds the roots around an energy shift specified by the user. This algorithm will be useful if there is experimental or other data on an approximate energy value of a desired transition. Another variant of the algorithm that we present is one targeting the solution dominated by a specific transition, e.g., from/to user defined orbitals (e.g., from HOMO-3). This solver will be useful for cases where we are interested in the root dominated by a particular transition (e.g. ionization from 1s orbital of carbon[14,16]).

We also present an implementation of a completely new solver introduced by Eugene Vecharynski *et al* - Generalized Preconditioned Locally Minimal Residual Method (GPLMR)[17]. This method involves construction of an orthogonal subspace based on the Krylov-space residuals, where the original matrix is projected and the eigenproblem solved for the projected matrix. Similar to modified Davidson's method it allows to find the roots around a specified energy shift. The size of the search subspace can be controlled by the user, thus allowing to limit the amount of memory and the number of matrix-vector multiplications (σ-vectors updates) at each iteration. The benchmarks of GPLMR and Davidson's method are presented in section 7.4 for finding both lowest eigenvalues and eigevalues around a specific energy.

7.2 Equation-of-motion (EOM) family of methods

Equation-of-motion (EOM) family of methods[3–7] is a powerful tool for the description of electronically excited, ionized, and attached states in molecular systems. It provides a balanced treatment of the ground and selected target states, accurate recovery of correlation energy, and is size-intensive. The wave function of the target state is written as:

$$\Psi_{EOM} = \hat{R} exp(\hat{T}) |\Phi_0> \tag{7.1}$$

where $\hat{R}$ is a general excitation operator. Depending on the type of the physical process (excitation, ionization, electron attachment) the operator has different forms:

$$R^{\hat{E}E} = r_0 + \sum_{ia} r_i^a a^\dagger i + \frac{1}{4} \sum_{ijab} r_{ij}^{ab} a^\dagger b^\dagger ji + ... \tag{7.2}$$

$$R^{\hat{I}P} = \sum_{i} r_i i + \frac{1}{2} \sum_{ija} r_{ij}^{a} a^\dagger ji + ... \tag{7.3}$$

$$R^{\hat{E}A} = \sum_{a} r^a a^\dagger + \frac{1}{2} \sum_{iab} r_{i}^{ab} a^\dagger b^\dagger i + ... \tag{7.4}$$

In singles and doubles approximation, the series are truncated after including corresponding double amplitude term. Similar to configuration interaction (CI) the problem of finding the wave function is a problem of diagonalizing of the similarity transformed Hamiltonian:

$$\bar{H} = e^{-T} H e^{T} \tag{7.5}$$

where $\bar{H}$ is a real, non-Hermitian, and diagonally dominant matrix. By solving the non-Hermitian eigenvalue problem for the right and left eigenvectors we obtain the energies and wave function coefficients of the target states:

$$(\bar{H} - E_{CC} I) R = R\Omega \tag{7.6}$$

$$L(\bar{H} - E_{CC} I) = \Omega L \tag{7.7}$$

$$< L|R >= I \tag{7.8}$$

Where Ω is a diagonal matrix containing eigenenergies, and matrices R and L contain the right and left eigenvectors (wave function coefficients) as columns.

7.3 Algorithms

7.3.1 Davidson's method

The development of the original Davidson algorithm was driven by large-scale CI calculations[13] in which matrices are real and symmetric. The basic idea of Davidson's method is to project the original matrix onto an orthogonal search subspace and solve the eigenvalue problem for the projected matrix which allows one to obtain approximate eigenpairs of the original matrix. At each step, the search subspace is expanded by using preconditioned unconverged residuals as new vectors which, after performing an orthogonalization, are added to the search subspace. The details of the algorithm for finding n smallest roots of diagonally dominant matrix A are given below:

Original Davidson's method

(1) Generate guess vectors based on the diagonal D of matrix A - sort the diagonal elements in the ascending order and generate the corresponding unit vectors. Orthogonalize those guess vectors and form the initial search subspace, $V = \{v_1, v_2, .., v_n\}$.

(2) Compute σ-vectors corresponding to the new vectors added to search subspace, $\sigma_i = Av_i$.

(3) Compute the subspace matrix: $A_V = V^T\sigma$.

(4) Solve the eigenvalue problem for subspace matrix: $A_V X = X\Lambda$. Sort the eigenvalues in the ascending order ($\lambda_1 \leq \lambda_2 \leq ... \leq \lambda_k$), choose n smallest. Discard the rest of eigenpairs.

(5) Compute the residuals of the eigenpairs corresponding to matrix A: $r_i = \sigma X_i - \lambda_i V X_i$, where λ_i are eigenvalues from step (4) and X_i are the corresponding eigenvectors.

(6) if $||r_i|| < \varepsilon$ for all residuals (ε is the convergence threshold) - terminate and return eigenvalues $\{\lambda_1, \lambda_2, ..., \lambda_n\}$ and corresponding eigenvectors $\{VX_1, VX_2, ..., VX_n\} = \{R_1, R_2, ..., R_n\}$.

(7) If the subspace size reached the maximum specified value, use current approximations of eigenvectors as a new guess, orthogonalize them and go to step (2).

(8) Apply preconditioner to unconverged residuals: $s_i = (D - \lambda_i)^{-1} r_i$, where D is the diagonal of matrix A. Discard all $||s_i|| < \delta$, where δ is the threshold for adding new vectors to the subspace.

(9) Orthogonalize the preconditioned residuals against all other vectors in the search subspace, normalize and add them to the search subspace. Go to step (2).

The most expensive step of the algorithm is the projection of the original matrix to the search subspace vectors (matrix-vector multiplication, step 2), so-called σ-vector calculations. The number of matrix-vector evaluations at each step is equal to the number of new vectors added to the subspace. For EOM-EE, each matrix-vector multiplication scales as $O(N^6)$, for EOM-EA and EOM-IP as $O(N^5)$. In terms of memory, the most expensive ($O(N^4)$ for EOM-EE and $O(N^3)$ for EOM-IP/EA) is to store the subspace vectors v_i and the associated σ-vectors $\sigma_i = A v_i$. Thus, the maximum number of stored vectors at each iteration is twice the size of the subspace.

The original Davidson method for symmetric matrices has been generalized for nonsymmetric matrices[18]. For the non-symmetric case, the right and left search subspace vectors are constructed separately and the resulting left and right eigenvectors are bi-orthogonalized. If only the eigenvalues and the right eigenvectors are needed, the

method will be equivalent to the symmetric Davidson, with only exception that the subspace matrix (step 3 and 4) is non-symmetric. Recently, Davidson's method has been successfully combined with Jacobi's approach for eigenvalue approximation leading to the Jacobi-Davidson method[1,19]. It can be viewed as an instance of Newton's method with subspace acceleration for eigenvalue problems.

The original method proposed by Davidson[13] is designed to find a few (1-10) lowest eigenpairs of the original matrix. However, in many applications one might need to compute a few eigenpairs that lie high in the spectrum (so-called interior eigenvalues). We present a modification to the original Davidson algorithm that enables computation of the few eigenpairs closest to shift η specified by the user. The changes to the algorithm are minor and only required in steps (1) and (4):

Davidson's method with shift (only steps that are different from the original algorithm are presented)

(1) Generate guess vectors based on the absolute value of diagonal D shifted by η, sort the values in the ascending order ($|D_1-\eta| \leq |D_2-\eta| \leq ... \leq |D_n-\eta|$) and generate the corresponding unit vectors. Orthogonalize these guess vectors and form the initial search subspace, $V = \{v_1, v_2, .., v_n\}$.

(4) Solve the eigenvalue problem for subspace matrix: $A_V X = X\Lambda$. Sort the absolute values of eigenvalues shifted by η in the ascending order ($|\lambda_1-\eta| \leq |\lambda_2-\eta| \leq ... \leq |\lambda_k-\eta|$), choose n lowest. Discard the rest of eigenpairs.

This algorithm targets the eigenvalues that lie close to shift η (e.g., transitions close to η =300 eV) specified by the user. This feature will be useful if an experimental or theoretical estimate of the energy is available that can be chosen as energy shift η.

We also present another modification to Davidson's algorithm that allows one to find a single root dominated by a particular transition chosen by the user (e.g., an IP transition

from HOMO - 3). Mathematically, it means that the eigenvector will be dominated by a single component corresponding to a physical transition specified by the user. The algorithm will be looking only for a single root (number of roots n = 1) corresponding to the eigenvector of this character. The changes to the algorithm are also minor:

Davidson's method with user-defined guess (only steps that are different from the original algorithm are presented)

(1) Generate the guess vector as a unit vector corresponding to the transition specified by the user. Form the initial search subspace, $V = \{v_1\}$.

(4) Solve the eigenvalue problem for the subspace matrix: $A_V X = X\Lambda$. Sort eigenpairs in the descending order of the overlap of the current eigenvector approximation with the user guess vector: $< v_1|VX_1 > \geq < v_1|VX_2 > ... \geq < v_1|VX_k >$ and choose the largest one. Since the approximate eigenvector is constructed as a linear combination of the vectors in the search subspace (which are orthonormal), the value of the overlap is given by the first row of matrix X: $< v_1|VX_i > = < v_1|\sum_j v_j X_{ji} > = \sum_j < v_1|v_j > x_{ji} = x_{1i}$.

7.3.2 Generalized Preconditioned Locally Minimal Residual (GPLMR) method

Generalized Preconditioned Locally Minimal Residual (GPLMR) method is a new eigensolver for computation of a subset of eigenpairs of a non-Hermitian matrices that are closest to the chosen shift η[17] like the modified Davidson method. This solver is also a matrix-free solver that uses preconditioning and shows the convergence behavior similar to the state-of-the art solvers. At every iteration the orthonormal search subspace is constructed based on the approximations from previous iterations as well as from preconditioned Krylov-space residuals. The eigenvalue approximation at each step is calculated based on the harmonic Ritz eigenvalue of the projected matrix, with

the eigenvector by the linear combination of search subspace vectors such that the minimal possible norm of the residual is achieved. The details of the algorithm for finding n roots of non-Hermitian matrix A closest to shift η are given below:

Generalized Preconditioned Locally Minimal Residual (GPLMR) method

(1) Generate guess vectors based on the absolute value of diagonal D shifted by η, sort the values in the ascending order ($|D_1-\eta| \leq |D_2-\eta| \leq ... \leq |D_n-\eta|$) and generate the corresponding unit vectors $V = \{v_1, v_2, .., v_n\}$ as guess vectors.

(2) Form the search subspace by orthogonalizing the set of vectors $\{V, W, S^{(1)}, ..., S^{(m)}, P\}$, where:

- V is a block of current approximations to the eigenvectors $V = \{v_1, v_2, .., v_n\}$
- W is a block of unconverged residuals $w_i = T(Av_i - \rho_i v_i)$, $W = \{w_1, w_2, .., w_k\}$. T is a preconditioner and $\rho_i = v_i^* A v_i$
- $S^{(j)}$ is a block of Krylov-space residuals corresponding to the unconverged roots computed recursevely from $S^{(j-1)}$ ($S^{(0)}$=W): $s_i^j = T(As_i^{(j-1)} - \rho_i s_i^{(j-1)})$, $S^{(j)} = \{S_1^{(j)}, S_2^{(j)}, ..., S_k^{(j)}\}$
- P is a block of vectors from the span of the two previous approximations of the unconverged roots (not computed at the first iteration): $P = \{p_1, p_2, .., p_k\}$

Orthogonalize the set of vectors $\{V, W, S^{(1)}, ..., S^{(m)}, P\}$ (ignoring vectors with norm less than threshold δ) and form search subspace Z=orth$\{V, W, S^{(1)}, ..., S^{(m)}, P\}$.

(3) Solve the generalized eigenvalue problem of the shifted matrix, A-ηI, projected to the search subspace, find n smallest (in absolute value) eigenvalues of the projected matrix (θ_j):

$$Z^*(A-\eta I)^*(A-\eta I)Zx_j = \theta_j Z^*(A-\eta I)Zx_j \tag{7.9}$$

Compute approximate eigenvalues based on the harmonic Ritz eigenvalues of the projected matrix: $\lambda_i = \theta_i + \eta$

(4) Compute the eigenvectors associated with the eigenvalues computed at step (3) as:

$$Z^*(A-\lambda_i I)^*(A-\lambda_i I)ZX_i = \beta_i X_i \tag{7.10}$$

Construct the approximation to the eigenvectors as: $V^{j+1} = ZX$, where $X = \{X_1, X_2, .., X_n\}$. Construct the vector in the span of the new and the previous eigenvector approximation: $P = V^{j+1} - \sum_i V^j X_V$, where X_V is the first n rows of matrix X, and V^j is the approximation to eigenvectors from the previous iteration. Discard the previous eigenvector approximation, V^j. Set $V = V^{j+1}$

(5) Compute the residuals of the obtained eigenpairs:

$$r_i = AV_i - \lambda_i V_i, i = 1, 2, ..., n \tag{7.11}$$

if $||r_i|| < \varepsilon$ for all residuals (ε is the convergence threshold), than return the set of eigenvalues, $\lambda_1, \lambda_2, ..., \lambda_n$, and their corresponding eigenvectors, $v_1, v_2, ..., v_n$. Else destroy current search subspace Z and go to the step (2).

Note that the algorithm can use different preconditioners depending on the structure of the matrix. In the present implementation, Davidson's preconditioner ($(D-\lambda_i)^{-1}$, where λ_i is the current approximation to the eigenvalue) is used, since it provides robust convergence for matrices in quantum-chemical calculations. One feature of the GPLMR algorithm is that the maximum size of the search subspace is fixed (at most n*(m+3) vectors if no vectors are ignored after the orhtogonalization) and can be controlled by the user by choosing the number of Krylov space residuals m. Thus, the amount of memory

for the GPLMR algorithm depends on the parameter m and is at most 2*n*(m+3) to store the subspace vectors (Z) and the corresponding σ vectors (σ=AZ). In Davidson's algorithm, the size of the subspace is growing at each iteration until reaching the maximum (user specified) subspace size when the space is collapsed (step (7) in Davidson's algorithm).

Similar to Davidson's method, the most expensive steps in the GPLMR algorithm are matrix-vector multiplications that also depend on the size of the subspace. At each iteration the algorithm performs m+1 matrix-vector multiplications to construct $w_i, s_i^{(1)}, s_i^{(2)}, ..., s_i^{(m)}$ residual vectors of the unconverged roots and at most m+3 matrix-vector multiplications to project the matrix on the orthogonal search subspace corresponding to the unconverged roots. Thus, the total maximum number of matrix-vector multiplications per iteration is limited by n*(2m+4) if no vectors are ignored during the orthogonalization and when none of the roots have converged. In general, GPLMR requires more matrix-vector multiplications per iteration, as compared to Davidson, but the memory and computational costs can be controlled by the user by choosing the number of Krylov-space residuals, m. We also found that the convergence properties of the algorithm can be enhanced by increasing the number of Krylov-space residuals when only few unconverged roots are left. Since residual vectors $w_i, s_i^{(1)}, s_i^{(2)}, ..., s_i^{(m)}$ and vector p_i are generated only for the unconverged roots, the size of the subspace, n(unconverged)*(m+3)+nconverged, can be insufficient, thus the parameter m could be augmented (for example by integer fraction of (#converged)/(#unconverged) if #converged $>$ #unconverged).

7.4 Benchmarks

All benchmarks were done using the Q-Chem electronic structure package[20], version 4.2. All algorithms presented in section 7.3 are implemented for the EOM-EE/EA/IP methods. The details on how to use and control parameters of the eigenvalue solvers within the EOM family of methods in Q-Chem can be found in the user manual[20].

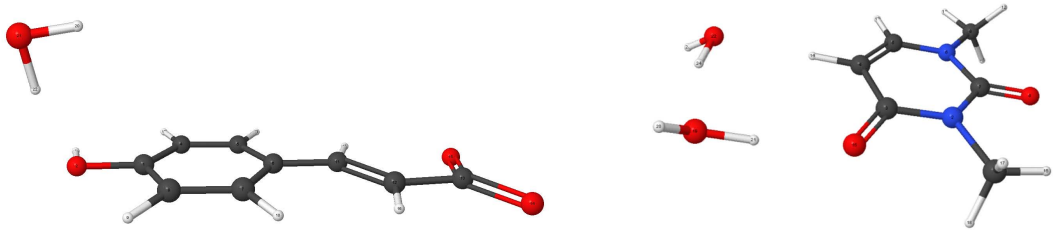

Figure 7.1: Benchmark systems: a hydrated photoactive yellow protein chromophore PYPa-W$_p$ (left) and dihydrated 1,3-dimethyluracil (mU)$_2$-(H$_2$O)$_2$ (right)

For benchmark purposes, we choose two biologically relevant systems of C_1 symmetry (Fig 7.1) - a hydrated photoactive yellow protein chromophore (PYPa-W$_p$ from Ref. 21) and dihydrated 1,3-dimethyluracil ((mU)$_2$-(H$_2$O)$_2$ from Ref. 22). For PYPa-W$_p$, we used the 6-31+G(d,p) basis set (total 292 b.f.), whereas for (mU)$_2$-(H$_2$O)$_2$, we employed the 6-311+G(d,p) basis set (336 b.f.). We studied the convergence properties of the GPLMR and Davidson solvers with the EOM-IP method for calculation of ionization potentials; this EOM method has the smallest cost of matrix-vector multiplications, as compared to EOM-EA and EOM-EE.

Table 7.1: The comparison of the conventional Davidson and GPLMR($\eta = 0$) solvers in convergence of different number of lowest roots

PYPa-W$_p$/6-31+G(d,p)

Davidson's method

nroots[a]	niters[b]	Max. # of stored vectors[c]	# matvec[d]
1	19	38	19
3	13	60	30
5	10	74	37
10	21	82	41

GPLMR

nroots[a]	niters[b]	m	Max. # of stored vectors[c]	# matvec[d]
1	8	3	12	72
3	5	3	36	127
5	4	5	80	216
10	5	5	158	510

(mU)$_2$-(H$_2$O)$_2$/6-311+G(d,p)

Davidson's method

nroots[a]	niters[b]	Max. # of stored vectors[c]	# matvec[d]
1	7	14	7
3	9	48	24
5	9	76	38
10	16	120	99
12	14	120	118

GPLMR

nroots[a]	niters[b]	m	Max. # of stored vectors[c]	# matvec[d]
1	2	5	16	26
3	5	5	48	163
5	5	5	80	236
10	14	3	120	783
12	5	3	136	503

[a] The number of requested roots. [b] The number of iterations to converge all roots. [c] only the subspace vectors and the corresponding σ-vectors are taken into account. [d] The total number of matrix-vector multiplications (σ-vector updates).

Table 7.2: The comparison of the Davidson and GPLMR solvers in convergence of different number roots around a specified energy shift

PYPa-W$_p$/6-31+G(d,p)

Davidson's method ($\eta = 11$ a.u.)

nroots[a]	niters[b]	Max. # of stored vectors[c]	# matvec[d]
1	DNC[e]	–	–
2	DNC[e]	–	–
3	DNC[e]	–	–

GPLMR ($\eta = 11$ a.u.)

nroots[a]	niters[b]	m	Max. # of stored vectors[c]	# matvec[d]
1	3	3	12	27
2	3	3	24	57
3	DNC[e]	3	–	–

(mU)$_2$-(H$_2$O)$_2$/6-311+G(d,p)

Davidson's method[f] ($\eta = 0.5$ a.u.)

nroots[a]	niters[b]	Max. # of stored vectors[c]	# matvec[d]
1	32	66	33
2	27	106	53
3	35	78	39

GPLMR[f] ($\eta = 0.5$ a.u.)

nroots[a]	niters[b]	m	Max. # of stored vectors[c]	# matvec[d]
1	3	3	12	27
2	4	3	24	68
3	18	3	36	387

[a] The number of requested roots. [b] The number of iterations to converge all roots. [c] only the subspace vectors and the corresponding σ-vectors are taken into account. [d] The total number of matrix-vector multiplications (σ-vector updates). [e] Did not converge all roots in 60 iterations. [f] In this case GPLMR and Davidson converged different roots.

Table 7.3: Convergence of the GPLMR solver for the different numbers of Krylov-space residuals

PYPa-W$_p$/6-31+G(d,p)
GPLMR

nroots[a]	niters[b]	m	Max. # of stored vectors[c]	# matvec[d]
3	26	1	24	358
3	7	2	30	141
3	5	3	36	127
3	5	5	48	167

(mU)$_2$-(H$_2$O)$_2$/6-311+G(d,p)
GPLMR

nroots[a]	niters[b]	m	Max. # of stored vectors[c]	# matvec[d]
3	DNC[e]	1	–	–
3	22	2	30	355
3	9	3	36	201
3	5	5	48	163

[a] The number of requested roots. [b] The number of iterations to converge all roots. [c] only the subspace vectors and the corresponding σ-vectors are taken into account. [d] The total number of matrix-vector multiplications (σ-vector updates). [e] Did not converge all roots in 60 iterations.

Table 7.4: Convergence properties of Davidson's solver with user-defined guess PYPa-W$_p$/6-31+G(d,p)

Davidson's method ($\eta = 11$ a.u.)

nroots[a]	orb. coeff.[b]	niters[c]	Max. # of stored vectors[d]	# matvec[e]
4	0.908	7	14	7
13	0.892	7	14	7
30	0.885	59	118	59

(mU)$_2$-(H$_2$O)$_2$/6-311+G(d,p)

Davidson's method[c] ($\eta = 0.5$ a.u.)

nroots[a]	orb. coeff.[b]	niters[c]	Max. # of stored vectors[d]	# matvec[e]
4	0.896	DNC[f]	–	–
10	0.901	6	12	6
28	0.920	36	72	36

[a] The number of requested roots. [b] The r_1 coefficient of user defined orbital in the final solution [c] The number of iterations to converge all roots. [d] only the subspace vectors and the corresponding σ-vectors are taken into account. [e] The total number of matrix-vector multiplications (σ-vector updates). [f] Did not converge all roots in 60 iterations.

The following convergence parameters have been used in benchmarks: $||r||^2 < 10^{-5}$ as the convergence criterion for both Davidson's and the GPLMR solvers, $||r||^2 < \frac{1}{2}10^{-5}$ as the criterion to ignore insignificant vectors for Davidson and $||r||^2 < 10^{-14}$ for GPLMR. The maximum number of iterations for both methods has been set at 60; the maximum size of the subspace size was set 60 for Davidson. The Krylov-space residuals and vectors p_i were constructed only for the unconverged roots, for the converged roots, only the current approximation of the eigenvector was used to expand the subspace in GPLMR. If the number of the converged roots was higher than the number of the unconverged ones in GPLMR, the parameter m for the unconverged roots have been amplified by the factor $\lfloor \frac{\#converged}{\#unconverged} \rfloor$, but such that the augmented m does not exceed 10. In the following benchmarks, we evaluate the convergence properties of the solvers (the number of iterations to converge) as well as its computational (the number of matrix vector operations) and memory (the number of stored vectors) costs.

First, Table 7.1 compares the performance of the conventional Davidson and GPLMR solvers (no shift) in finding different number of the lowest roots. The GPLMR solver was executed with parameters m=1,2,3, and 5 and the results with the smallest number of matrix-vector multiplications for each quantity of the requested roots are compiled in Table 7.1. One can see that in all cases the GPLMR solver converges the requested number of roots faster than Davidson, usually in up to 3 times less iterations. However, since each iteration of the GPLMR solver is significantly more expensive than Davidson's, the overall number of matrix-vector multiplications is in some cases more than 10 times larger for GPLMR. We also note that in the case of PYPa-W_p m = 3 is working slightly better for converging 1 and 3 roots, and m = 5 is better for converging of 5 and 10 roots, whereas for $(mU)_2$-$(H_2O)_2$ the situation is opposite.

Next, we compare the convergence of the interior eigenvalues by the solvers in the cases of large and moderate energy shifts (Table 7.2). For PYPa-W_p, we choose large energy shift of 11 a.u. (299.32 eV). The GPLMR solver very easily converges 1 and 2 roots (288.66 and 289.13 eV) around the specified energy shift, but fails to converge a block of 3 roots in 60 iterations. At the same time, Davidson is unable to converge even a single root for a chosen energy shift within 60 iterations. For $(mU)_2$-$(H_2O)_2$, we choose a moderate shift of 0.5 a.u. (13.61 eV). In this case GPLMR converges 1 and 2 roots quite fast, but takes more than 10 iterations to converge 3 roots. The Davidson algorithm converges 1,2, and 3 roots for the specified shift in nearly 30 iterations. Interestingly, GPLMR and Davidson converged to different solutions: GPLMR converged 3 roots to 12.14, 11.62, 11.24 eV, whereas Davidson converged to 13.60, 13.67 and 14.11 eV that is clearly much closer to chosen energy shift (13.61 eV).

As was mentioned before, the size of the subspace in the GPLMR algorithm can be controlled by the user by changing the number of Krylov-space residuals generated for the unconverged roots. In Table 7.3, we compare how this parameter affects the convergence and the total number of matrix-vector multiplications for 3 lowest roots. We see that, obviously, by increasing the number of the Krylov-space residuals, the number of iterations decreases. For PYPa-W_p the parameter m=1 gives a very poor convergence (26 iterations). Increasing the parameter to m=2 accelerates the convergence by more than 3 times (7 iterations). A further increase of parameter m to 3 and 5 decreases the number of iterations to only 5. However, one needs to note that by increasing the subspace size, we also increase memory and computational costs per iteration (the two last columns in Table 7.3). In terms of matrix-vector multiplications, the most efficient is m=3 for PYPa-W_p system, since it converges the solution as fast as m=5 (5 iterations),

but each iteration is cheaper. We also see a somewhat similar behavior for $(mU)_2$-$(H_2O)_2$ system - m = 1 is clearly a poor choice that is unable to converge the solution in 60 iterations. The increase of the subspace size significantly decreases the number of iterations needed for convergence, the most efficient, in terms of matrix-vector multiplications, for this system is one with m=5. In Figure 7.2 we plot the norm of the residuals of the 1st and 3rd root at each iteration for different parameter m of the GPLMR and for Davidson for the two systems. We see that, in general, GPLMR gives much smoother convergence than Davidson, for example, even for a quite small subspace size (m=2) the requested roots for PYPa-W_p are converging faster and more monotonically than with Davidson. As was noted before, increasing the size of the subspace significantly improves the convergence, but at the price of the increased computational cost of each iteration.

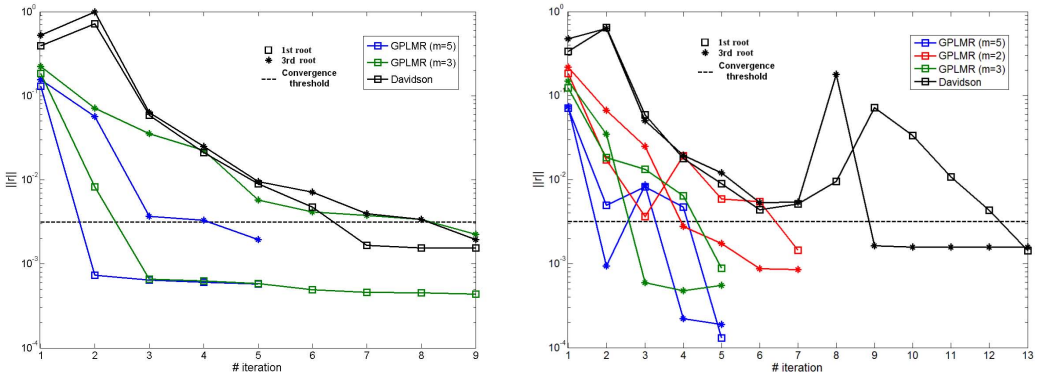

Figure 7.2: Norm of the residual for the 1st and 3rd root for the GPLMR and Davidson solvers at each iteration. Left: PYPa-W_p/6-31+G(d,p), right: $(mU)_2$-$(H_2O)_2$/6-311+G(d,p).

Lastly, in Table 7.4 we show how the Davidson procedure with the user-defined guess converges the roots of a specified transition character. We see that in most cases modified Davidson's method successfully converges the solution to the root dominated by the transition from the orbital chosen by the user. In all cases, the contribution of the

chosen orbital to the EOM wave function (r_1 coefficient) is higher than 0.88. We also note that the problematic convergence (e.g. transition from 30th orbital in PYPa-W_p) corresponds to the case when another orbital has considerable contributions to the wave function (larger than 0.1).

7.5 Conclusions

Two new modifications of the canonical Davidson method are presented - the first one enables finding the multiple roots around a specified energy shift (Davidson with shift); another one allows one to solve for a single root dominated by the user-specified transition (Davidson with user-defined guess). This new functionality will allow calculating the roots lying high in energy that would be inaccessible by the standard method that is designed to find only few lowest in energy transitions. For example, if an experimental or theoretical estimation of the energy of transition is available one can use Davidson with energy shift to calculate the transitions around the chosen energy. As another example, if one is interested in finding the root dominated by a particular transition (e.g., core ionization of the 1s carbon orbital), the Davidson with the user-defined guess can be used. We also present an implementation of an entirely new solver for non-Hermitian interior eigenvalue problems - Generalized Preconditioned Locally Minimal Residual Method (GPLMR)[17], which also has capabilities of finding the roots closest to the chosen energy shift. The subspace size of the GPLMR solver can be controlled by the user by choosing the number of Krylov-space residuals generated for each unconverged root. Bigger subspace sizes will provide better convergence (fewer number of iterations), but requires more memory and matrix-vector multiplications per iteration. All aforecited methods are implemented for the EOM families of methods (EA,EE, and IP) in the Q-Chem[20] electronic structure package.

New solvers are tested for EOM-IP for two biological systems and, in most cases, successfully find the roots targeted by the user. We observe that, in general, GPLMR with zero shift converges much faster in terms of total number of iteration than conventional Davidson. However, the cost of each iteration of GPLMR is significantly higher than that of Davidson's method, thus the overall number of time determining operations (matrix-vector multiplications) is significantly higher for GPLMR. However for the cases of finding interior eigenvalues around the chosen energy shift, GPLMR shows better and more robust convergence than modified Davidson's method with shift which sometimes fails to find the requested solution. Thus, the use of GPLMR can be advised for the problematic cases when Davidson's method with shift is unable to converge.

7.6 Chapter 7 references

[1] Y. Saad. *Numerical methods for large eigenvalue problems*. SIAM, 2 edition, 2001.

[2] A. Szabo and N.S. Ostlund. *Modern Quantum Chemistry: Introduction to Advanced Electronic Structure Theory*. McGraw-Hill, New York, 1989.

[3] T. Helgaker, P. Jørgensen, and J. Olsen. *Molecular electronic structure theory*. Wiley & Sons, 2000.

[4] H. Sekino and R.J. Bartlett. A linear response, coupled-cluster theory for excitation energy. *Int. J. Quant. Chem. Symp.*, 26:255–265, 1984.

[5] J.F. Stanton and R.J. Bartlett. The equation of motion coupled-cluster method. A systematic biorthogonal approach to molecular excitation energies, transition probabilities, and excited state properties. *J. Chem. Phys.*, 98:7029–7039, 1993.

[6] M. Head-Gordon and T.J. Lee. Single reference coupled cluster and perturbation theories of electronic excitation energies. In R.J. Bartlett, editor, *Modern Ideas in Coupled Cluster Theory*. World Scientific, Singapore, 1997.

[7] A.I. Krylov. Equation-of-motion coupled-cluster methods for open-shell and electronically excited species: The hitchhiker's guide to Fock space. *Annu. Rev. Phys. Chem.*, 59:433–462, 2008.

[8] J. G. F. Francis. The qr transformation a unitary analogue to the lr transformation - part 1. *The Computer Journal*, 4:265–271, 1961.

[9] J. G. F. Francis. The qr transformation - part 2. *The Computer Journal*, 4:332–345, 1962.

[10] G.H. Golub and C.F. Van Loan. *Matrix computations*. Johns Hopkins University Press, 1996.

[11] W. E. Arnoldi. The principle of minimized iterations in the solution of the matrix eigenvalue problem. *Quart. Appl. Math.*, 9:17–29, 1951.

[12] C. Lanczos. An iteration method for the solution of the eigenvalue problem of linear differential and integral operators. *J. Res. Nat. Bur. Stand.*, 45:255, 1950.

[13] E.R. Davidson. The iterative calculation of a few of the lowest eigenvalues and corresponding eigenvectors of large real-symmetric matrices. *J. Comput. Phys.*, 17:87–94, 1975.

[14] R. Franchy and D. Menzel. Adsorbate core ionization as primary process in electron-and photon-stimulated desorption from metal surfaces. *Phys. Rev. Lett.*, 43:865–867, 1979.

[15] J. F. Morar, F. J. Himpsel, G. Hollinger, J. L. Jordan, G. Hughes, and F. R. McFeely. C 1s excitation studies of diamond (111). i. surface core levels. *Phys. Rev. B*, 33:1340, 1986.

[16] P.-F. Loos and X. Assfeld. Core-ionized and core-excited states of macromolecules. *Int. J. Quant. Chem.*, 107:2243–2252, 2007.

[17] E. Vecharynski, F. Xue, and C. Yang. Generalized preconditioned locally minimal residual (GPLMR) method. private communication, 2013.

[18] K. Hirao and H. Nakatsuji. A generalization of the Davidson's method to large nonsymmetric eigenvalue problems. *J. Comput. Phys.*, 45:246–254, 1982.

[19] G. L. G. Sleijpen and H. A. Van der Vorst. A Jacobi-Davidson iteration method for linear eigenvalue problems. *SIAM review*, 42:267–293, 2000.

[20] Y. Shao, L. Fusti-Molnar, Y. Jung, J. Kussmann, C. Ochsenfeld, S. Brown, A.T.B. Gilbert, L.V. Slipchenko, S.V. Levchenko, D.P. O'Neill, R.A. Distasio Jr, R.C. Lochan, T. Wang, G.J.O. Beran, N.A. Besley, J.M. Herbert, C.Y. Lin, T. Van Voorhis, S.H. Chien, A. Sodt, R.P. Steele, V.A. Rassolov, P. Maslen, P.P. Korambath, R.D. Adamson, B. Austin, J. Baker, E.F.C. Byrd, H. Daschel, R.J. Doerksen, A. Dreuw, B.D. Dunietz, A.D. Dutoi, T.R. Furlani, S.R. Gwaltney, A. Heyden, S. Hirata, C.-P. Hsu, G.S. Kedziora, R.Z. Khalliulin, P. Klunziger, A.M. Lee, W.Z. Liang, I. Lotan, N. Nair, B. Peters, E.I. Proynov, P.A. Pieniazek, Y.M. Rhee, J. Ritchie, E. Rosta, C.D. Sherrill, A.C. Simmonett, J.E. Subotnik, H.L. Woodcock III, W. Zhang, A.T. Bell, A.K. Chakraborty, D.M. Chipman, F.J. Keil, A. Warshel, W.J. Hehre, H.F. Schaefer III, J. Kong, A.I. Krylov, P.M.W. Gill, M. Head-Gordon. Advances in methods and algorithms in a modern quantum chemistry program package. *Phys. Chem. Chem. Phys.*, 8:3172–3191, 2006.

[21] D. Zuev, K. Bravaya, M. Makarova, and A.I. Krylov. Effect of microhydration on the electronic structure of the chromophores of the photoactive yellow and green fluorescent proteins. *J. Chem. Phys.*, 135:194304, 2011.

[22] K. Khistyaev, A. Golan, K.B. Bravaya, N. Orms, A.I. Krylov, and M. Ahmed. Proton transfer in nucleobases is mediated by water. *J. Phys. Chem. A*, 117:6789–6797, 2013.

Chapter 8: Future work

The research presented in this thesis opens numerous ways for further method development and chemical applications. The combination of complex absorbing potentials with EOM family of methods presented in Chapter 5 is a powerful *ab initio* tool for the theoretical description of autoionizing resonances. In Chapter 5 application of CAP-EOM-EA to shape resonances in mid-size molecules is described. Besides EOM-EA, resonances resulting from electron excitation would be also interesting to study using CAP-EOM-EE implemented in Q-Chem. The possible candidates for this study could be closed-shell molecular anions such as model chromophores of photoactive yellow and green fluorescent proteins that are described in Chapters 2 and 3. Another interesting systems to study with CAP-augmented EOM methods are resonance states in dianions. For this goal EOM-DEA method[1] needs to be implemented and combined with CAP. In this new CAP-EOM-DEA method one will start with a closed-shell reference state and by attaching two electrons arrive at doubly attached dianion resonance. The possible candidates for this study could be resonances in C_2^{2-}, CN_2^{2-}, CO_3^{2-}[2,3].

Regarding the technical aspects of the implementation of CAP-EOM methods there are also few possible ways for improvement. In current implementation each point for different CAP strength η_i is calculated independently using guess for HF, CCSD, and EOM of an unmodified Hamiltonian. Alternatively, we can use information obtained for previous CAP strength η_{i-1} (molecular orbitals, T amplitudes, left and right EOM

vectors) as guesses for HF, CCSD, and EOM calculation with new strength parameter η_i. I anticipate that it would significantly accelerate the calculation of η-trajectories, since we usually vary strength parameter by small increment $\Delta\eta$ that results in small changes in the solutions. This improvement will provide better and more robust convergence of the solution at all levels of theory. It will also provide a more user-friendly way of setting up calculations in which only step, starting and ending points of η-trajectory need to be specified in a single input. Ideally the CAP-EOM methods should be made "truly" *ab initio* by reducing the number of parameters (such as "box" size and CAP strength) needed from the user. The box size can be automatically set up by performing CCSD calculation of ground state properties for zero strength and choosing length of the box as $\sqrt{< X^2 >}$, $\sqrt{< Y^2 >}$m and $\sqrt{< Z^2 >}$. The step ($\Delta\eta$) in calculation of η-trajectories can be chosen using some numerical schemes (for example Newton's optimization method) for finding the extremum of corrected real and imaginary parts of energies.

It would be also beneficial to extend the functionality of complex Davidson's procedure for finding highly lying state specified by the shift or user guess as described for the real case in Chapter 7. Since many resonance states (e.g., Feshbach resonance in helium) are lying high in energy this feature will allow one to find the solution for this particular states, without calculating many roots lying below the resonance state or performing full diagonalization.

Cholesky decomposition of two electron integrals presented in Chapter 6 opens the way to calculate much larger systems while controlling the accuracy of the approximation. Since the data size is significantly reduced, it enables not only memory savings, but also allows one to achieve much more efficient parallelization due to reduced I/O overheads. This can be exploited on supercomputers or graphical processing units (GPU)[4,5] where the time to transfer large amount of data very often surpasses actual calculation

time. However, one need to mention that even though Cholesky decomposition reduces the storage of integrals and its intermediates significantly, the formal memory scaling is still $O(N^4)$ (but with much reduced prefactor) due to necessity to store t_2 amplitudes in CCSD calculations and r_2 in EOM. The equations cannot be simplified to remove all $O(N^6)$ types of contractions, thus there is no reduction in computational scaling. In order to address these problems, reduced-rank approximation representation of t_2 and r_2 amplitudes can be applied. By reducing the rank of the wave function parameters one can not only reduce memory scaling (by removing all $O(N^4)$ terms left), but also possibly reduce computational scaling by simplifying the contractions to the operations with lower order tensors. The reduction in computational scaling of CCSD and EOM ($O(N^6)$) would broaden the area of applicability of this methods to significantly larger systems. Among one of the most promising techniques is a tensor hypercontraction (THC) approach[6,7] in which tensor is decomposed using physical spatial grid. For CCSD it has been already shown that using both two-electron integrals and t amplitudes in THC decomposed format and by rewriting the equations one can reduce the computational scaling to $O(N^4)$[7]. However, the choice of the decomposition grid and ability to control the numerical errors for decomposed tensors remain open questions for THC method.

Another way of speeding up calculations and reducing memory of post Hartree-Fock calculations is to use the fact that for large systems all the tensors become extremely sparse. The Cholesky decomposed two-electron integrals inherit sparsity of the original ERI tensor in which the number of significant non-zero elements grows as $O(N^2)$. In Figure 8.1 the number of elements below the chosen threshold in each Cholesky vector $L_{\mu\nu}$ is presented for cluster of 15 water molecules in 6-31+G(d,p) basis set. We can see that even for a conservative threshold of 10^{-9} there is only half of significantly large

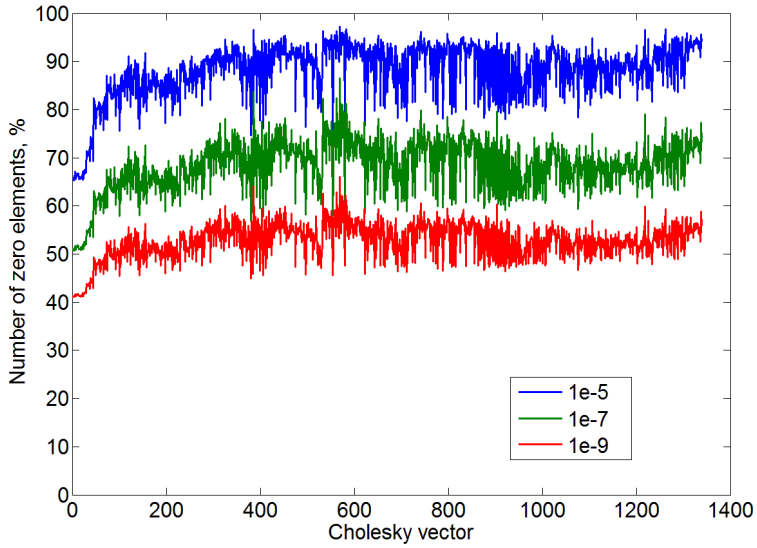

Figure 8.1: The number of zero elements (smaller in absolute value than 10^{-9}, 10^{-7} and 10^{-5} thresholds) in each Cholesky vector for the cluster of 15 water molecules in the 6-31+G(d,p) basis set. The ERI is decomposed in AO basis with Cholesky threshold 10^{-3}.

elements, whereas for 10^{-5} more than 80% are negligible. By adopting efficient integral screening procedures such as Shwartz[8,9] and QQR[10] integral estimates, one can avoid calculation and storage of blocks with nearly zero elements. These schemes have been successfully applied for calculation of AO-MP2 energy[11] of systems with more than 10000 Gaussian basis functions. Similar ideas can be also applied to exploiting sparsity of wave function coefficients (such as t_2 and r_2 amplitudes).

It is also worth mentioning that CAP-EOM methods can be enhanced by using Cholesky decomposition as well as other low-rank techniques. The reduction in memory for CAP calculations will be more crucial because of larger basis sets needed for calculations and since complex algebra requires twice the data to store comparing to conventional methods. Thus, implementation of CD-CAP-EOM methods will be essential for studying the resonance in large molecules (for example in biochromophores).

8.1 Chapter 8 references

[1] M. Nooijen and R.J. Bartlett. Similarity transformed equation-of-motion coupled-cluster theory: Details, examples, and comparisons. *J. Chem. Phys.*, 107:6812–6830, 1997.

[2] T. Sommerfeld, F. Tarantelli, H.-D. Meyer, and L. S. Cederbaum. Ab initio calculation of energies and lifetimes of metastable dianions:the c_2^{2-}resonance. *J. Chem. Phys.*, 112(15):6635–6642, 2000.

[3] T. Sommerfeld. Lifetimes of metastable dianions: Cn_2^{2-}, c_4^{2-}, and co_3^{2-}. *J. Phys. Chem. A*, 104:8806–8813, 2000.

[4] L. Vogt, R. Olivares-Amaya, S. Kermes, Y. Shao, C. Amador-Bedolla, and A. Aspuru-Guzik. Accelerating resolution-of-the-identity second-order moller-plesset quantum chemistry calculations with graphical processing units. *J. Phys. Chem. A*, 112:2049–2057, 2008.

[5] R. Olivares-Amaya, M. A. Watson, R. G. Edgar, L. Vogt, Y. Shao, and A. Aspuru-Guzik. Accelerating correlated quantum chemistry calculations using graphical processing units and a mixed precision matrix multiplication library. *J. Chem. Theory Comput.*, 6:135–144, 2010.

[6] R.M. Parrish, E.G. Hohenstein, T.J. Martínez, and C.D. Sherrill. Tensor hypercontraction. II. Least-squares renormalization. *J. Chem. Phys.*, 137(22):224106, 2012.

[7] E.G. Hohenstein, R.M. Parrish, C.D. Sherrill, and T.J. Martínez. Communication: Tensor hypercontraction. III. Least-squares tensor hypercontraction for the determination of correlated wavefunctions. *J. Chem. Phys.*, 137(22):221101, 2012.

[8] J.L. Whitten. Coulombic potential energy integrals and approximations. *J. Chem. Phys.*, 58:4496, 1973.

[9] M. Häser and R. Ahlrichs. Improvements on the direct SCF method. *J. Comput. Chem.*, 10, 1988.

[10] S. A. Maurer, D. S. Lambrecht, D. Flaig, and C. Ochsenfeld. Distance-dependent schwarz-based integral estimates for two-electron integrals: Reliable tightness vs. rigorous upper bounds. *J. Chem. Phys.*, 136, 2012.

[11] S. A. Maurer, D. S. Lambrecht, J. Kussmann, and C. Ochsenfeld. Efficient distance-including integral screening in linear-scaling moller-plesset perturbation theory. *J. Chem. Phys.*, 138, 2013.

Bibliography

K. Aflatooni, B. Hitt, G. A. Gallup, and P. D. Burrow. *J. Chem. Phys.*, 115:6489, 2001.

J. Aguilar and J. M. Combes. *Commun. Math. Phys.*, 22:269–279, 1971.

M. Allan. *Phys. Rev. Lett.*, 87:033201, 2001.

L.H. Andersen, H. Bluhme, S. Boyé, T.J.D. Jørgensen, H. Krogh, I.B. Nielsen, S.B. Nielsen, and A. Svendsen. *Phys. Chem. Chem. Phys.*, 6:2617–2627, 2004.

L.H. Andersen, A. Lappierre, S.B. Nielsen, I.B. Nielsen, S.U. Pedersen, U.V. Pedersen, and S. Tomita. *Eur. Phys. J. D*, 20:597–600, 2002.

K. Andersson, P.-Å. Malmqvist, B.O. Roos, A.J. Sadlej, and K. Wolinski. *J. Phys. Chem.*, 94:5483–5488, 1990.

L. Andric and R. I. Hall. *J. Phys. B*, 21(2):355, 1988. URL `http://stacks.iop.org/0953-4075/21/i=2/a=019`.

F. Aquilante, L. Boman, J. Boström, H. Koch, R. Lindh, A.S. de Merás, and T.B. Pedersen. F. Aquilante, L. Boman, J. Boström, H. Koch, R. Lindh, A.S. de Merás, and T.B. Pedersen. In R. Zaleśny, M.G. Papadopoulos, P.G. Mezey, and J. Leszczynski, editors, *Linear-Scaling Techniques in Computational Chemistry and Physics*, Challenges and advances in computational chemistry and physics, pages 301–343. Springer, 2011.

F. Aquilante, L. de Vico, N. Ferré, G. Ghigo, P-Å Malmqvist, P. Neogrády, T. B. Pedersen, M. Pitonňak, M. Reiher, B. Roos, L. Serrano-Andrés, M. Urban, V. Veryazov, and R. Lindh. *J. Comput. Chem.*, 31:224–247, 2010.

F. Aquilante, L. Gagliardi, T. B. Pedersen, and R. Lindh. *J. Chem. Phys.*, 130:154107, 2009.

F. Aquilante, R. Lindh, and T. B. Pedersen. *J. Chem. Phys.*, 127:114107, 2007.

F. Aquilante, P.Å. Malmqvist, T. B. Pedersen, A. Ghosh, and B.O. Roos. *J. Theor. Comput. Chem.*, 4:694–702, 2008.

F. Aquilante, T. B. Pedersen, and R. Lindh. *J. Chem. Phys.*, 126:194106, 2007.

F. Aquilante, T. B. Pedersen, and R. Lindh. *Theor. Chem. Acc.*, 124:1–10, 2009.

F. Aquilante, T. B. Pedersen, R. Lindh, B. O. Roos, A. S. de Merás, and H. Koch. *J. Chem. Phys.*, 129:024113, 2008.

F. Aquilante and T.B. Pedersen. *Chem. Phys. Lett.*, 449:354–357, 2007.

F. Aquilante, T.K. Todorova, L. Gagliardi, T.B. Pedersen, and B.O. Roos. *J. Chem. Phys.*, 131:034113, 2009.

W. E. Arnoldi. *Quart. Appl. Math.*, 9:17–29, 1951.

M. Baca, G.E.O. Borgstahl, M. Boissinot, P.M. Burke, D.R. Williams, K.A. Slater, and E.D. Getzoff. *Biochemistry*, 33:14369–14377, 1994.

P. Balanarayan, Y. Sajeev Y., and N. Moiseyev. *Chem. Phys. Lett.*, 524:84–89, 2012.

E. Balslev and J. M. Combes. *Commun. Math. Phys.*, 22:280–294, 1971.

J. N. Bardsley and B.R. Junker. *J. Phys. B*, 5:L178, 1972.

H. Barkay and N. Moiseyev. *Phys. Rev. A*, 64:044702, 2001.

R.J. Bartlett. *Int. J. Mol. Sci.*, 3:579–603, 2002.

R.J. Bartlett. *Mol. Phys.*, 108:2905–2920, 2010.

R.J. Bartlett. *Wiley Interdisciplinary Reviews: Computational Molecular Science*, 2 (1):126–138, 2012.

R.J. Bartlett and M. Musial. *Rev. Mod. Phys.*, 79:291–352, 2007.

A. D. Becke. *J. Chem. Phys.*, 88(4):2547, 1988. ISSN 00219606. URL `http://link.aip.org/link/JCPSA6/v88/i4/p2547/s1\&Agg=doi`.

N.H.F. Beebe and J. Linderberg. *Int. J. Quant. Chem.*, 12:683–705, 1977.

F. Bell, D. Lambrecht, and M. Head-Gordon. *Mol. Phys.*, 108:2759–2773, 2010.

U. Benedikt, A.A. Auer, M. Espig, and W. Hackbusch. *J. Chem. Phys.*, 134:054118, 2011.

C. Benoit and R. Abouaf. *Chem. Phys. Lett.*, 123:134–138, 1986.

M. Berman, H. Estrada, L. S. Cederbaum, and W. Domcke. *Phys. Rev. A*, 28:1363–1381, 1983.

D.E. Bernhold and R.J. Harrison. *Chem. Phys. Lett.*, 250:477, 1996.

A.K. Bhatia, A. Temkin, and H. Eiserike. *Phys. Rev. A*, 9:219–222, 1974.

M. J. W. Boness and G. J. Schulz. *Phys. Rev. A*, 9:1969, 1974.

J. Boström, F. Aquilante, T. B. Pedersen, and R. Lindh. *J. Chem. Theory Comput.*, 5: 1545–1553, 2009.

J. Boström, M. G. Delcey, F. Aquilante, L. Serrano-Andrés, T. B. Pedersen, and R. Lindh. *J. Theor. Comput. Chem.*, 6:747–754, 2010.

B. Boudaïffa, P. Cloutier, D. Hunting, M. A. Huels, and L. Sanche. *Science*, 287: 1658–1660, 2000.

K. Bravaya, B.L. Grigorenko, A.V. Nemukhin, and A.I. Krylov. *Acc. Chem. Res.*, 45: 265–275, 2012.

K. Bravaya, M.G. Khrenova, B.L. Grigorenko, A.V. Nemukhin, and A.I. Krylov. *J. Phys. Chem. B*, 8:8296–8303, 2011.

K.B. Bravaya, E. Epifanovsky, and Anna I. Krylov. *J. Phys. Chem. Lett.*, 3:2726–2732, 2012.

K.B. Bravaya, D. Zuev, E. Epifanovsky, and A.I. Krylov. *J. Chem. Phys.*, 138:124106, 2013.

C. Bressler and M. Chergui. *Chem. Rev.*, 104:1781–1812, 2004.

A. Buchleitnert, B. Grémaud, and D. Delande. *J. Phys. B*, 27:2663–2679, 1994.

P. D. Burrow and K. D. Jordan. *Chem. Phys. Lett.*, 36:595, 1975.

P. D. Burrow and J. A. Michejda. *Chem. Phys. Lett.*, 42:223–226, 1976.

P. D. Burrow and L. Sanche. *Phys. Rev. Lett.*, 28:333, 1972.

I. Cacelli, R. Moccia, and A. Rizzo. *Phys. Rev. A*, 57:1895–1905, 1998.

J.-D. Chai and M. Head-Gordon. *Phys. Chem. Chem. Phys.*, 10:6615–6620, 2008.

J.-D. Chai and M. Head-Gordon. *J. Chem. Phys.*, 128:084106, 2008.

M. Chalfie, Y. Tu, G. Euskirchen, W.W. Ward, and D.C. Prasher. *Science*, 263:802–805, 1994.

N. Chandra. *Phys. Rev. A*, 16(1):80–108, 1977.

P. Changenet-Barret, P. Plaza, and M.M. Martin. *Chem. Phys. Lett.*, 336:439–444, 2001.

P. Changenet-Barret, P. Plaza, M.M. Matrin, H.Chosrowjan, S. Taniguchi, N. Mataga, Y. Imamoto, and M. Kataoka. *J. Phys. Chem. C*, 113:11605–11613, 2009.

J. S.-Y. Chao, M. F. Falcetta, and K. D. Jordan. *J. Chem. Phys.*, 93(2):1125–1135, 1990.

K. Chingin, R.M. Balabin, V. Frankevich, K. Barylyuk, R. Nieckarz, P. Sagulenko, and R. Zenobi. *Int. J. Mass Spectrom.*, 306:241–245, 2011.

D.T. Chuljian and J. Simons. *Int. J. Quant. Chem.*, XXIII:1723–1738, 1983.

J. Cizek. *J. Chem. Phys.*, 45:4256–4266, 1966.

T. Clark, J. Chandrasekhar, and P.V.R. Schleyer. *J. Comput. Chem.*, 4:294–301, 1983.

C. R. Claydon, G. A. Segal, and H. S. Taylor. *J. Chem. Phys.*, 52:3387–3398, 1970.

D.C. Comeau and R.J. Bartlett. *Chem. Phys. Lett.*, 207:414–423, 1993.

P.B. Corkum and F. Krausz. *Nat. Phys.*, 3:381–387, 2007.

T.D. Crawford, C.D. Sherrill, E.F. Valeev, J.T. Fermann, R.A. King, M.L. Leininger, S.T. Brown, C.L. Janssen, E.T. Seidl, J.P. Kenny, and W.D. Allen. *J. Comput. Chem.*, 28:1610–1616, 2007.

D.F. Dance and I. C. Walker. *Chem. Phys. Lett.*, 18(4):601 – 603, 1973. URL `http://www.sciencedirect.com/science/article/pii/0009261473804774`.

E.R. Davidson. *J. Comput. Phys.*, 17:87–94, 1975.

R. N. Day and M. W. Davidson. *Chem. Soc. Rev.*, 38:2887–2921, 2009.

M. de Groot, E.V. Gromov, H. Köppel, and W.J. Buma. *J. Phys. Chem. B*, 112:4427–4434, 2008.

S. Denifl, V. Vizcaino, T. D. Märk, E. Illenberger, and P. Scheier. *Phys. Chem. Chem. Phys.*, 12:5219–5224, 2010.

W. Domcke. *Phys. Reports*, 208:97–188, 1991.

R. A. Donelly. *J. Chem. Phys.*, 84:6200, 1986.

J. Dong, F. Abulwerdi, A. Baldridge, J. Kowalik, K.M. Solntsev, and L.M. Tolbert. *J. Am. Chem. Soc.*, 130:14096–14098, 2008.

R. A. Donnelly. *Int. J. Quant. Chem.*, 19:363–367, 1986.

M. Douglas and N.M. Kroll. *Ann. Phys. (NY)*, 82:89–155, 1974.

R. Dressler and M. Allan. *J. Chem. Phys.*, 87(8):4510–4518, 1987. URL `http://scitation.aip.org/content/aip/journal/jcp/87/8/10.1063/1.452864`.

L. Dubé and A. Herzenberg. *Phys. Rev. A*, 20:194–213, 1979.

T.H. Dunning. *J. Chem. Phys.*, 90:1007–1023, 1989.

M. Ehara and T. Sommerfeld. *Chem. Phys. Lett.*, 537:107–112, 2012.

H. Ehrhardt and K. Willmann. *Z. Phys.*, 204:462–473, 1967.

K. Eichkorn, O. Treutler, H.Öhm, M. Häser, and R. Ahlrichs. *Chem. Phys. Lett.*, 242: 652–660, 1995.

K. Eichkorn, F. Weigend, O. Treutler, and R. Ahlrichs. *Theor. Chem. Acc.*, 97:119–124, 1997.

E. Eichten. *Phys. Rev. D*, 22:1819, 1980.

E. Epifanovsky, K. Kowalski, P.-D. Fan, M. Valiev, S. Matsika, and A.I. Krylov. *J. Phys. Chem. A*, 112:9983–9992, 2008.

E. Epifanovsky, I. Polyakov, B.L. Grigorenko, A.V. Nemukhin, and A.I. Krylov. *J. Chem. Theory Comput.*, 5:1895–1906, 2009.

E. Epifanovsky, I. Polyakov, B.L. Grigorenko, A.V. Nemukhin, and A.I. Krylov. *J. Chem. Phys.*, 132:115104, 2010.

E. Epifanovsky, M. Wormit, T. Kuś, A. Landau, D. Zuev, K. Khistyaev, I. Kaliman, P. Manohar, A. Dreuw, and A.I. Krylov. E. Epifanovsky, M. Wormit, T. Kuś, A. Landau, D. Zuev, K. Khistyaev, I. Kaliman, P. Manohar, A. Dreuw, and A.I. Krylov. http://iopenshell.usc.edu/downloads/tensor/, 2011.

E. Epifanovsky, M. Wormit, T. Kuś, A. Landau, D. Zuev, K. Khistyaev, P. Manohar, I. Kaliman, A. Dreuw, and A.I. Krylov. *J. Comput. Chem.*, 34:2293–2309, 2013.

E. Epifanovsky, D. Zuev, X. Feng, K. Khistyaev, Y. Shao, and A.I. Krylov. *J. Chem. Phys.*, 139:134105, 2013.

H. Erhardt, L. Langhans, F. Linder, and H. S. Taylor. *Phys. Rev.*, 173:222–230, 1968.

A. Espagne, P. Changenet-Barret, J.-B. Baudina, P. Plaza, and M.M. Martin. *J. Photochem. Photobiol. A*, 185:245–252, 2007.

A. Espagne, P. Changenet-Barret, P. Plaza, and M.M. Martin. *J. Phys. Chem. A*, 110: 3393–3404, 2006.

M. F. Falcetta, L. A. Di Falco, D. S. Ackerman, J. C. Barlow, and K. D. Jordan. *J. Phys. Chem. A*, page DOI: 10.1021/jp5003287, 2014. URL `http://pubs.acs.org/doi/abs/10.1021/jp5003287`.

A. Faure, J. D. Gorfinkiel, L. A. Morgan, and J. Tennyson. *Comp. Phys. Comm.*, 144: 224–241, 2002.

H. Feshbach. *Ann. Phys. (N.Y.)*, 19:287–313, 1962.

S. Feuerbacher, T. Sommerfeld, R. Santra, and L. S. Cederbaum. *J. Chem. Phys.*, 118 (14):6188–6199, 2003.

M.W. Feyereisen, G. Fitzgerald, and A. Komornicki. *Chem. Phys. Lett.*, 208:359, 1993.

J. Finley, P.-Å. Malmqvist, B.O. Roos, and L. Serrano-Andrés. *Chem. Phys. Lett.*, 288:299–306, 1998.

M.W. Forbes and R.A. Jockusch. *J. Am. Chem. Soc.*, 131:17038–17039, 2009.

R. Franchy and D. Menzel. *Phys. Rev. Lett.*, 43:865–867, 1979.

J. G. F. Francis. *The Computer Journal*, 4:265–271, 1961.

J. G. F. Francis. *The Computer Journal*, 4:332–345, 1962.

M.J. Frisch, J.A. Pople, and J.S. Binkley. *J. Chem. Phys.*, 80:3265–3269, 1984.

G. A. Gallup. *Phys. Rev. A*, 84:012701, 2011.

G. Gamow. *Z. Phys.*, 51:204, 1928.

G. Garcia-Calderon. *Phys. Low-Dimens. Semicond. Struct.*, 6:1993, 267.

J. Geertsen, M. Rittby, and R.J. Bartlett. *Chem. Phys. Lett.*, 164:57–62, 1989.

U.K. Genick, S.M. Soltis, P. Kuhn, I.L. Canestrelli, and E.D. Getzoff. *Nature*, 392: 206–209, 1998.

G. Ghigo, B.O. Roos, and P.-Å. Malmqvist. *Chem. Phys. Lett.*, 396:142, 2004.

A. Ghosh, A. Karne, S. Pal, and N. Vaval. *Phys. Chem. Chem. Phys.*, 15:17915–17921, 2013.

A. Ghosh, N. Vaval, and S. Pal. *J. Chem. Phys.*, 136:234110, 2012.

D. Ghosh, O. Isayev, L.V. Slipchenko, and A.I. Krylov. *J. Phys. Chem. A*, 115:6028–6038, 2011.

F. A. Gianturco and T. Stoecklin. *J. Phys. B*, 29:3933–3954, 1996.

E.D. Glendening, J.K. Badenhoop, A.E. Reed, J.E. Carpenter, J.A. Bohmann, C.M. Morales, and F. Weinhold. E.D. Glendening, J.K. Badenhoop, A.E. Reed, J.E. Carpenter, J.A. Bohmann, C.M. Morales, and F. Weinhold. Theoretical Chemistry Institute, University of Wisconsin, Madison, WI, 2001.

D. E. Golden. *Phys. Rev. Lett.*, 17:847–848, 1966.

G.H. Golub and C.F. Van Loan. *Matrix computations*. Johns Hopkins University Press, 1996.

A.A. Golubeva and A.I. Krylov. *Phys. Chem. Chem. Phys.*, 11:1303–1311, 2009.

A.A. Golubeva, P.A. Pieniazek, and A.I. Krylov. *J. Chem. Phys.*, 130(12):124113, 2009. URL `http://link.aip.org/link/?JCP/130/124113/1`.

E.M. Gonzalez, L. Guidonib, and C. Molteni. *Phys. Chem. Chem. Phys.*, 11:4556–4563, 2009.

E. Gromov, I. Burghardt, J. Hynes, H. Köppel, and L. Cederbaum. *Photochem. and Photobiol.*, 190:241–257, 2007.

E. V. Gromov, I. Burghardt, H. Köppel, and L. S. Cederbaum. *J. Phys. Chem. A*, 109: 4623–4631, 2005.

E. V. Gromov, I. Burghardt, H. Köppel, and L. S. Cederbaum. *J. Am. Chem. Soc.*, 129:6798–6806, 2007.

F. Grossmann. *Chem. Phys. Lett.*, 262:470–476, 1996.

P.C. Hariharan and J.A. Pople. *Theor. Chim. Acta*, 28:213, 1973.

M. Häser and R. Ahlrichs. *J. Comput. Chem.*, 10, 1988.

C. Hättig and A. Köhn. *J. Chem. Phys.*, 117(15):6939–6951, 2002.

C. Hättig and F. Weigend. *J. Chem. Phys.*, 113(13):5154–5161, 2000.

A. U. Hazi, T. N. Rescigno, and M. Kurilla. *Phys. Rev. A*, 23:1089–11099, 1981.

A.U. Hazi and H.S. Taylor. *Phys. Rev. A*, 1:1109, 1970.

Z. He, C. H. Martin, R. Birge, and K.F. Freed. *J. Phys. Chem. A*, 104:2939–2952, 2000.

M. Head-Gordon and T.J. Lee. M. Head-Gordon and T.J. Lee. In R.J. Bartlett, editor, *Modern Ideas in Coupled Cluster Theory*. World Scientific, Singapore, 1997.

W.J. Hehre, R. Ditchfield, and J.A. Pople. *J. Chem. Phys.*, 56:2257, 1972.

M. Heiblum, M.V. Fischetti, W.P. Dumke, D.J. Frank, I.M. Anderson, C.M. Knoedler, and L. Osterling. *Phys. Rev. Lett.*, 58:816, 1987.

H. G. M. Heideman, C. E. Kuyatt, and G. E. Chamberlain. *J. Chem. Phys.*, 44:355–358, 1966.

R. Heim, D.C. Prasher, and R.Y. Tsien. *Proc. Nat. Acad. Sci.*, 91:12501, 1994.

T. Helgaker, P. Jørgensen, and J. Olsen. *Molecular electronic structure theory*. Wiley & Sons, 2000.

E.J. Heller. *Acc. Chem. Res.*, 14:368–375, 1981.

K.J. Hellingwerf, J. Hendriks, and Thomas Gensch. *J. Phys. Chem.*, 107:1082–1094, 2003.

A. Hellweg, C. Hättig, S. Höfener, and W. Klopper. *Theor. Chem. Acc.*, 117:587–597, 2007.

K. Hirao and H. Nakatsuji. *J. Comput. Phys.*, 45:246–254, 1982.

Y.K. Ho. *Phys. Rev. A*, 23:2137–2149, 1981.

Y.K. Ho, A.K. Bhatia, and A. Temkin. *Phys. Rev. A*, 15:1423–1429, 1977.

W. D. Hoff, P. Düx, K. Hård, B. Devreese, I. M. Nugteren-Roodzant, W. Crielaard, R. Boelens, R. Kaptein, J. van Beeuman, and K. J. Hellingwerf. *Biochemistry*, 33: 13959–13962, 1994.

M. Hoffmann, M. Wanko, P.Strodel, P.H. König, T. Frauenhrim, K.Schulten, W. Thiel, E. Tajkorshid, and M. Elstner. *J. Am. Chem. Soc.*, 128:10808–10818, 2006.

E.G. Hohenstein, R.M. Parrish, C.D. Sherrill, and T.J. Martínez. *J. Chem. Phys.*, 137 (22):221101, 2012.

M. Honigmann, R. J. Buenker, and H.-P. Liebermann. *J. Chem. Phys.*, 125(23): 234304, 2006.

M. Honigmann, R. J. Buenker, and H.-P. Liebermann. *J. Chem. Phys.*, 131:–, 2009.

S. J. Martinez III and J. C. Alfano annd D. H. Levy. *J. Molec. Spect.*, 152:80–88, 1992.

A. F. Izmaylov, S. O. Adamson, and A. Zaitsevskii. *J. Phys. B*, 37(11):2321, 2004.

T.-C. Jagau, K.B. Bravaya D. Zuev, E. Epifanovsky, and A.I. Krylov. *J. Phys. Chem. Lett.*, 5:310–315, 2014.

G. Jolicard and E. J. Austin. *Chem. Phys. Lett.*, 121:106–110, 1985.

K. D. Jordan and P. D. Burrow. *Acc. Chem. Res.*, 11(9):341–348, 1978. URL `http://pubs.acs.org/doi/abs/10.1021/ar50129a004`.

K. D. Jordan and P. D. Burrow. *Chem. Rev.*, 87:557–588, 1987.

K.D. Jordan and F. Wang. *Annu. Rev. Phys. Chem.*, 54:367–396, 2003.

G. Jung, J. Wiehler, and A.Zumbusch. *Biophys. J.*, 88:1932–1947, 2005.

Y. Jung, A. Sodt, P. M. W. Gill, and M. Head-Gordon. *Proc. Nat. Acad. Sci.*, 102: 6692–6697, 2005.

B.R. Junker. *Adv. At. and Mol. Phys*, 18:207–263, 1982.

M. Kamiya and S. Hirata. *J. Chem. Phys.*, 125:074111–074125, 2006.

D.O. Kashinski, D. Talbi, and A.P. Hickman. *Chem. Phys. Lett.*, 529:10–15, 2012.

D. Kats, T. Korona, and M. Schütz. *J. Chem. Phys.*, 125:104106–104121, 2006.

K. Kaufmann, W. Baumeister, and Jungen M. *J. Phys. B*, 22:2223–2240, 1989.

S. Kaur and K.L. Baluja. *J. Phys. B*, 38:3917–3933, 2005.

R.A. Kendall, Jr. T.H. Dunning, and R.J. Harrison. *J. Chem. Phys.*, 96:6796–6806, 1992.

R. E. Kennerly. *Phys. Rev. A*, 21:1876–1883, 1980.

K. Khistyaev, A. Golan, K.B. Bravaya, N. Orms, A.I. Krylov, and M. Ahmed. *J. Phys. Chem. A*, 117:6789–6797, 2013.

S. Klaiman and I. Gilary. S. Klaiman and I. Gilary. In C.A. Nicolaides, J.R. Sabin, and E.J. Brändas, editors, *Adv. Quantum Chem.*, volume 63, chapter 1, pages 1–31. Elsevier Inc., 2012.

M. Kneen, J. Farinas, Y. Li, and A.S. Verkman. *Biophys. J.*, 74:1591–1599, 1998.

H. Koch, O. Christiansen, P. Jørgensen, A.M.S. de Meras, and T. Helgaker. *J. Chem. Phys.*, 106:1808–1818, 1997.

H. Koch, A.S. de Merás, and T.B. Pedersen. *J. Chem. Phys.*, 118:9481, 2003.

K.-H. Kochem, W. Sohn, K. Jung, H. Ehrhardt, and E. S. Chang. *J. Phys. B*, 18 (6):1253, 1985. URL `http://stacks.iop.org/0022-3700/18/i=6/a=025`.

A. Köhn and C. Hättig. *J. Chem. Phys.*, 119(10):5021–5036, 2003.

A. Komornicki and G. Fitzgerald. *J. Chem. Phys.*, 98:1398, 1993.

R. Kort, H. Vonk, X. Xu, W.D. Hoff, W. Crielaard, and K. J. Hellingwerf. *FEBS Lett.*, 382:73 – 78, 1996.

R. Kosloff and D. Kosloff. *J. Comput. Phys.*, 63(2):363–376, 1986.

R. Krishnan, J.S. Binkley, R. Seeger, and J.A. Pople. *J. Chem. Phys.*, 72:650, 1980.

V. Krumbach, B. M. Nestmann, and S. D. Peyerimhoff. *J. Phys. B*, 22(24):4001, 1989. URL `http://stacks.iop.org/0953-4075/22/i=24/a=008`.

A.I. Krylov. *Acc. Chem. Res.*, 39:83–91, 2006.

A.I. Krylov. *Annu. Rev. Phys. Chem.*, 59:433–462, 2008.

A.I. Krylov and P.M.W. Gill. *WIREs Comput. Mol. Sci.*, 3:317–326, 2013.

L. Lammich, J. Rajput, and L.H. Andersen. *Phys. Rev. E*, 78:051916, 2008.

C. Lanczos. *J. Res. Nat. Bur. Stand.*, 45:255, 1950.

A. Landau, K. Khistyaev, S. Dolgikh, and A.I. Krylov. *J. Chem. Phys.*, 132:014109, 2010.

P.W. Langhoff. P.W. Langhoff. In V. McKoy T. Rescigno and B. Schneider, editors, *Electron Molecule and Photon Molecule Collisions*, pages 183–224. Plenum, New

York, 1979.

D.S. Larsen, M. Vengris, I.H.M. van Stokkum, M.A. van der Horst, R.A. Cordfunke, K.J. Hellingwerf, and R. van Grondelle. *Chem. Phys. Lett.*, 369:563–569, 2003.

D.S. Larsen, M. Vengris, I.H.M. van Stokkum, M.A. van der Horst, F.L. de Weerd, K.J. Hellingwerf, and R. van Grondelle. *Biophys. J.*, 86:2538–2550, 2004.

H. Larsen, K. Hald, J. Olsen, and P. Jørgensen. *J. Chem. Phys.*, 115:3015–3020, 2001.

J. G. Lauderdale, C. W. McCurdy, and A. U. Hazi. *J. Chem. Phys.*, 79:2200–2205, 1983.

V.I. Lebedev. *Zh. Vychisl. Mat. Mat. Fiz.*, 15:48–54, 1975.

C.-H. Lee, C. Winstead, and V. McKoy. *J. Chem. Phys.*, 111:5056, 1999.

I-R. Lee, W. Lee, and A H. Zewail. *Proc. Nat. Acad. Sci.*, 103:258–262, 2006.

S.V. Levchenko and A.I. Krylov. *J. Chem. Phys.*, 120(1):175–185, 2004.

S.V. Levchenko, T. Wang, and A.I. Krylov. *J. Chem. Phys.*, 122:224106–224116, 2005.

D. A. Levin, A. W. Fliflet, and V. McKoy. *Phys. Rev. A*, 21(4):1202–1209, 1980.

N. Lipkin, N. Moiseyev, and E. Brändas. *Phys. Rev. A*, 40:549–553, 1989.

Y.-J. Liu, L. De Vico, and R. Lindh. *J. Photochem. Photobiol. A*, 194:261–267, 2008.

P.-F. Loos and X. Assfeld. *Int. J. Quant. Chem.*, 107:2243–2252, 2007.

R. R. Lucchese and V. McKoy. *Phys. Rev. A*, 25:1963, 1982.

Y. Ma, M. Rohlfing, and C. Molteni. *J. Chem. Theory Comput.*, 6:257–265, 2010.

S. Mahalakshmi and M. K. Mishra. *Chem. Phys. Lett.*, 296:43–50, 1998.

S. Mahalakshmi, A. Venkatnathan, and M. K. Mishra. *J. Chem. Phys.*, 115 (10):4549–4557, 2001. URL `http://scitation.aip.org/content/aip/journal/jcp/115/10/10.1063/1.1394754`.

P.-Å. Malmqvist and B.O. Roos. *Chem. Phys. Lett.*, 155:189–194, 1989.

V.A. Mandelshtam, T.R. Ravuri, and H.S. Taylor. *J. Chem. Phys.*, 101:8792–8799,

1994.

V.A. Mandelshtam and H.S. Taylor. *J. Chem. Phys.*, 102:7390–7399, 1995.

D. Mariano, A. Vera, and A. B. Pierini. *Phys. Chem. Chem. Phys.*, 6:2899–2903, 2004.

S. A. Maurer, D. S. Lambrecht, D. Flaig, and C. Ochsenfeld. *J. Chem. Phys.*, 136, 2012.

S. A. Maurer, D. S. Lambrecht, J. Kussmann, and C. Ochsenfeld. *J. Chem. Phys.*, 138, 2013.

C. W. McCurdy and T. N. Rescigno. *Phys. Rev. A*, 21:1499–1505, 1980.

C.W. McCurdy. *Phys. Rev. A*, 21:464–470, 1980.

C.W. McCurdy. *ACS Symposium series*, volume 263, pages 17–34. American Chemical Society, 1984.

C.W. McCurdy and T.N. Rescigno. *Phys. Rev. Lett.*, 41:1364–1368, 1978.

C.W. McCurdy, T.N. Rescigno, and D. Byrum. *Phys. Rev. A*, 56:1958–1969, 1997.

C.W. McCurdy, T.N. Rescigno, E.R. Davidson, and J.G. Lauderdale. *J. Chem. Phys.*, 73:3268–3273, 1980.

M. N. Medikeri and M. K. Mishra. *J. Chem. Phys.*, 103:676, 1995.

M. N. Medikeri and M. K. Mishra. *Chem. Phys. Lett.*, 246:26–32, 1995.

H.-D. Meyer. *Phys. Rev. A*, 40(10):5605–5613, 1989.

T.E. Meyer. *Biochem. and Biophys. J.*, 806:175–183, 1985.

T.E. Meyer, E. Yakali, M.A. Cusanovich, and G. Tollint. *Biochem. J.*, 26:418–423, 1987.

K. Mihara, O. Hisatomi, Y. Imamoto, M. Kataoka, and F. Tokunaga. *Biochem. J.*, 121:876–880, 1997.

N. Moiseyev. *Phys. Rep.*, 302:212–293, 1998.

N. Moiseyev. *Non-Hermitian quantum mechanics*. Cambridge University Press, 2011.

N. Moiseyev, P.R. Certain, and F. Weinhold. *Int. J. Quant. Chem.*, 14:727–736, 1978.

N. Moiseyev, P.R. Certain, and F. Weinhold. *Mol. Phys.*, 36:1613–1630, 1978.

N. Moiseyev and C. Corcoran. *Phys. Rev. A*, 20:814–817, 1979.

N. Moiseyev, S. Friedland, and P.R. Certain. *J. Chem. Phys.*, 74:4739–4740, 1981.

N. Moiseyev and J.O. Hirschfelder. *J. Chem. Phys.*, 88:1063, 1988.

A. Moradmand, D. S. Slaughter, D. J. Haxton, T. N. Rescigno, C. W. McCurdy, T. Weber, S. Matsika, A. L. Landers, A. Belkacem, and M. Fogle. *Phys. Rev. A*, 88: 032703, 2013.

J. F. Morar, F. J. Himpsel, G. Hollinger, J. L. Jordan, G. Hughes, and F. R. McFeely. *Phys. Rev. B*, 33:1340, 1986.

L. A. Morgan. *Phys. Rev. Lett.*, 80:1873, 1998.

M. A. Morrison, N. F. Lane, and L. A. Collins. *Phys. Rev. A*, 15:2186, 1977.

R. Moukhametzianov, J.P. Klare, R. Efremov, C. Baeken, A. Göppner, J. Labahn, M. Engelhard, G. Büldt, and V.I. Gordeliy. *Nature*, 440:115–119, 2006.

D. C. Moule and A. D. Walsh. *Chem. Rev.*, 75:67–84, 1975.

J.G. Muga, J.P. Palao, B. Navarro, and I.L. Egusquiza. *Phys. Rep.*, 395:357–426, 2004.

W.C. Murray, N.C. Handy, and G.J. Laming. *Mol. Phys.*, 78:997–1014, 1993.

H. Nakano. *J. Chem. Phys.*, 99:7983–7992, 1993.

B. M. Nestmann and S. D. Peyerimhoff. *J. Phys. B*, 18(21):4309, 1985.

D. Neuhauser. *J. Chem. Phys.*, 95:4927–4932, 1991.

I.B. Nielsen, S. Boye-Peronne, M.O.A. El Ghazaly, M.B. Kristensen, S.B. Nielsen, and L.H. Andersen. *Biophys. J.*, 89:2597–2604, 2005.

S.B. Nielsen, A. Lapierre, J.U. Andersen, U.V. Pedersen, S. Tomita, and L.H. Andersen. *Phys. Rev. Lett.*, 87:228102, 2001.

M. Nooijen and R.J. Bartlett. *J. Chem. Phys.*, 102:3629–3647, 1995.

M. Nooijen and R.J. Bartlett. *J. Chem. Phys.*, 107:6812–6830, 1997.

R. Olivares-Amaya, M. A. Watson, R. G. Edgar, L. Vogt, Y. Shao, and A. Aspuru-Guzik. *J. Chem. Theory Comput.*, 6:135–144, 2010.

S. Olsen and S.C. Smith. *J. Am. Chem. Soc.*, 130:8677–8689, 2008.

A.A. Pakhomov and V.I. Martynov. *Chem. Biol.*, 15:755–764, 2008.

S. Pal, M. Rittby, R.J. Bartlett, D. Sinha, and D. Mukherjee. *Chem. Phys. Lett.*, 137: 273–278, 1987.

S. Pal, Y. Sajeev, and N. Vaval. *Chem. Phys.*, 329:283–289, 2006.

R. Panajotovic, M. Kitajima, H. Tanaka, M. Jelisavcic, J. Lower, L. Campbell, M. J. Brunger, and S. J. Buckman. *J. Phys. B*, 36:1615, 2003.

R.M. Parrish, E.G. Hohenstein, T.J. Martínez, and C.D. Sherrill. *J. Chem. Phys.*, 137 (22):224106, 2012.

A. Philip, K. Eisenman, G. Papadantonakis, and W. Hoff. *Biochemistry*, 47:13800–13810, 2008.

P.A. Pieniazek, S.A. Arnstein, S.E. Bradforth, A.I. Krylov, and C.D. Sherrill. *J. Chem. Phys.*, 127:164110, 2007.

P.A. Pieniazek, S.E. Bradforth, and A.I. Krylov. *J. Chem. Phys.*, 129:074104, 2008.

I. Polyakov, E. Epifanovsky, B.L. Grigorenko, A.I. Krylov, and A.V. Nemukhin. *J. Chem. Theory Comput.*, 5:1907–1914, 2009.

J.A. Pople. J.A. Pople. In D.W. Smith and W.B. McRae, editors, *Energy, Structure and Reactivity: Proceedings of the 1972 Boulder Summer Research Conference on Theoretical Chemistry*, pages 51–61. Wiley, New York, 1973.

J.A. Pople, R. Krishnan, H.B. Schlegel, and J.S. Binkley. *Int. J. Quant. Chem.*, 14: 545–560, 1978.

P. Pulay. *Chem. Phys. Lett.*, 73:393, 1980.

G.D. Purvis and R.J. Bartlett. *J. Chem. Phys.*, 76:1910–1918, 1982.

D. Rahbek. D. Rahbek. private communication, 2011.

J. Rajput, D.B. Rahbek, G. Aravind, and L.H. Andersen. *Biophys. J.*, 98:488–492, 2010.

C. Ramsauer and R. Kollath. *Ann. Phys.*, 402:143–154, 1931.

W. P. Reinhardt. *Annu. Rev. Phys. Chem.*, 33:223–255, 1982.

A.P. Rendell and T.J. Lee. *J. Chem. Phys.*, 101:400–408, 1994.

T. N. Rescigno, D. A. Byrum, W. A. Isaacs, and C.W. McCurdy. *Phys. Rev. A*, 60: 2186, 1999.

T. N. Rescigno, W. A. Isaacs, A. E. Orel, H.-D. Meyer, and C. W. McCurdy. *Phys. Rev. A*, 65:032716, 2002.

T. N. Rescigno, C. W. McCurdy, and B. I. Schneider. *Phys. Rev. Lett.*, 63:248, 1989.

T. N. Rescigno, A. E. Orel, and C. W. McCurdy. *J. Chem. Phys.*, 73(12):6347–6348, 1980.

T.N. Rescigno, C.W. McCurdy, and A.E. Orel. *Phys. Rev. A*, 17:1931–1938, 1978.

S. Rettrup. *J. Comput. Phys.*, 45:100–107, 1982.

Y.M. Rhee and M. Head-Gordon. *J. Phys. Chem. A*, 111:5314–5326, 2007.

C. Riplinger and F. Neese. *J. Chem. Phys.*, 138:034106, 2013.

U. V. Riss and H.-D. Meyer. *J. Phys. B*, 26:4503–4536, 1993.

U.V. Riss and H.-D. Meyer. *J. Phys. B*, 28:1475–1493, 1995.

U.V. Riss and H.-D. Meyer. *J. Phys. B*, 31:2279–2304, 1998.

T. Rocha-Rinza, O. Christiansen, J. Rajput, A. Gopalan, D.B. Rahbek, L.H. Andersen, A.V. Bochenkova, A.A.Granovsky, K.B. Bravaya, A.V. Nemukhin, K.L. Christiansen, and M.B. Nielsen. *J. Phys. Chem. A*, 113:9442–9449, 2009.

T. Rocha-Rinza, K. Sneskov, O. Christiansen, U. Ryde, and J.I. Kongsted. *Phys. Chem. Chem. Phys.*, 13:1585–1589, 2011.

B.O. Roos, R. Lindh, P.Å. Malmqvist, V. Veryazov, and P.O. Widmark. *J. Phys. Chem.*, 108:2851–2858, 2004.

B.O. Roos, P.R. Taylor, and P.E.M. Siegbahn. *Chem. Phys.*, 48:157–173, 1980.

N. Rosen and P.M. Morse. *Phys. Rev.*, 42:210, 1932.

Y. Saad. *Numerical methods for large eigenvalue problems*. SIAM, 2 edition, 2001.

Y. Sajeev and N. Moiseyev. *J. Chem. Phys.*, 127:034105, 2007.

Y. Sajeev, R. Santra, and S. Pal. *J. Chem. Phys.*, 122:234320, 2005.

Y. Sajeev, R. Santra, and S. Pal. *J. Chem. Phys.*, 123(20):–, 2005.

Y. Sajeev, M. Sindelka, and N. Moiseyev. *Chem. Phys.*, 329:307–312, 2006.

Y. Sajeev, V. Vysotskiy, L.S. Cederbaum, and N. Moiseyev. *J. Chem. Phys.*, 131(21): 211102, 2009.

K. Samanta and D.L. Yeager. *J. Phys. Chem. B*, 112:16214–16219, 2008.

L. Sanche and G. J. Schulz. *J. Chem. Phys.*, 58:479, 1973.

C. Sanderson. C. Sanderson, 2010. NICT.

R. Santra. *J. Phys. B.*, 42:023001, 2009.

R. Santra and L.S. Cederbaum. *Phys. Rep.*, 368:1–117, 2002.

B. I. Schneider, T. N. Rescigno, B. H. Lengsfield III, and C. W. McCurdy. *Phys. Rev. Lett.*, 66:2728, 1991.

B. I. Schneider, T. N. Rescigno, and C. W. McCurdy. *Phys. Rev. A*, 42:3132, 1990.

M. Schreiber, M.R. Silva-Junior, S.P.A. Sauer, and W. Thiel. *J. Chem. Phys.*, 128: 134110, 2008.

G. J . Schulz. *Phys. Rev.*, 135:A988, 1964.

G. J. Schulz. *Phys. Rev.*, 125:229–232, 1962.

G. J. Schulz. *Rev. Mod. Phys.*, 45:423, 1973.

H. Sekino and R.J. Bartlett. *Int. J. Quant. Chem. Symp.*, 26:255–265, 1984.

A. Sergi, M. Grüning, M.Ferrario, and F. Buda. *J. Phys. Chem. B*, 105:4386, 2001.

L. Serrano-Andrés, M. Merchán, and R. Lindh. *J. Chem. Phys.*, 122:104107, 2005.

I. Shimamura. I. Shimamura. In *Advances in Quantum Chemistry*, volume 63, pages 165–245. Elsevier Inc., 2012.

O. Shimomura, F. Johnson, and Y. Saiga. *J. Cell. Comp. Physiol.*, 59:223–239, 1962.

A. J. F. Siegert. *Phys. Rev.*, 56:750, 1939.

B. Simon. *Commun. Math. Phys.*, 27:1–9, 1972.

J. Simons. *Encyclopedia of computational chemistry*, chapter Equation of motion

(EOM) methods for computing electron affinities. J. Wiley & Son, New York, 1998.

J. Simons. *Acc. Chem. Res.*, 39:772–779, 2006.

J. Simons. *J. Phys. Chem. A*, 112:6401–6511, 2008.

D. Sinha, D. Mukhopadhyay, and D. Mukherjee. *Chem. Phys. Lett.*, 129:369–374, 1986.

A. Sinicropi, T. Anduniow, N. Ferre, R. Basosi, and M. Olivucci. *J. Am. Chem. Soc.*, 127:11534–11535, 2005.

G. L. G. Sleijpen and H. A. Van der Vorst. *SIAM review*, 42:267–293, 2000.

L.V. Slipchenko and A.I. Krylov. *J. Chem. Phys.*, 123:084107–084120, 2005.

K. Sneskov and O. Christiansen. *Wiley Interdisciplinary Reviews: Computational Molecular Science*, 2:566, 2011.

J. Sniegowski, M. Phail, and R. Wachter. *Biochem. Biophys. Res. Commun*, 332: 657–663, 2005.

M. Sobczyk and J. Simons. *J. Phys. Chem. B*, 110:7519, 2006.

K.M. Solntsev, D. Ghosh, A. Amador, M. Josowicz, and A.I. Krylov. *J. Phys. Chem. Lett.*, 2:2593–2597, 2011.

K.M. Solntsev, O. Poizat, J. Dong, J. Rehault, Y. Lou, C. Burda, and L.M. Tolbert. *J. Phys. Chem. B*, 112:2700–2711, 2008.

T. Sommerfeld. *J. Phys. Chem. A*, 104:8806–8813, 2000. URL `http://pubs.acs.org/doi/abs/10.1021/jp0017590`.

T. Sommerfeld and H.-D. Meyer. *J. Phys. B*, 35:1841–1863, 2002.

T. Sommerfeld, U. V. Riss, H.-D. Meyer, L. S. Cederbaum, B. Engels, and H. U. Suter. *J. Phys. B*, 31(18):4107, 1998.

T. Sommerfeld and R. Santra. *Int. J. Quant. Chem.*, 82:218–226, 2001.

T. Sommerfeld and F. Tarantelli. *J. Chem. Phys.*, 112:2106, 2000.

T. Sommerfeld, F. Tarantelli, H.-D. Meyer, and L. S. Cederbaum. *J. Chem. Phys.*, 112(15):6635–6642, 2000. URL `http://scitation.aip.org/content/aip/journal/jcp/112/15/10.1063/1.481236`.

W.W. Sprenger, W.D. Hoff, J.P. Armitage, and K.J. Hellingwer. *J. of Bacteriology*,

175:3096–3104, 1993.

J.F. Stanton and R.J. Bartlett. *J. Chem. Phys.*, 98:7029–7039, 1993.

J.F. Stanton and J. Gauss. *J. Chem. Phys.*, 101(10):8938–8944, 1994.

J.F. Stanton, J. Gauss, J.D. Watts, and R.J. Bartlett. *J. Chem. Phys.*, 94:4334–4345, 1990.

O.V. Stepanenko, V.V. Verkhusha, I.M. Kuznetsova, V.N. Uversky, and K.K. Turoverov. *Curr. Protein Pept. Sci.*, 9:338, 2008.

V. Strelkov. *Phys. Rev. Lett.*, 104:123901, 2010.

J.E. Subotnik and M. Head-Gordon. *J. Chem. Phys.*, 123:064108, 2005.

A. Szabo and N.S. Ostlund. *Modern Quantum Chemistry: Introduction to Advanced Electronic Structure Theory*. McGraw-Hill, New York, 1989.

R.D. Thomas. *Mass Spec. Rev.*, 27:485–530, 2008.

Z. Tian and S. R. Kass. 130:10842 – 10843, 2008.

L.M. Tolbert, A. Baldridge, J. Kowalik, and K.M. Solntsev. *Acc. Chem. Res.*, 45: 171–181, 2012.

J. A. Tossell. *J. Phys. B*, 18(3):387, 1985. URL `http://stacks.iop.org/0022-3700/18/i=3/a=014`.

R.Y. Tsien. *Annu. Rev. Biochem.*, 67:509–544, 1998.

J. Ullrich, A. Rudenko, and R. Moshammer. *Annu. Rev. Phys. Chem.*, 63, 2012. 635-660.

O. Vahtras, J. Almlöf, and M.W. Feyereisen. *Chem. Phys. Lett.*, 213:514, 1993.

M.A. van der Horst, J.C. Arents, R. Kort, and K.J. Hellingwerf. *Photochem. and Photobiol. Sci.*, 6:571–579, 2007.

E. H. van Veen and F. L. Plantenga. *Chem. Phys. Lett.*, 38(3):493 – 497, 1976. URL `http://www.sciencedirect.com/science/article/pii/0009261476800243`.

L. J. G. W. van Wilderen, M. A. van der Horst, I. H. M. van Stokkum, K. J. Hellingwerf, R. van Grondelle, and M. L. Groot. *Proc. Nat. Acad. Sci.*, 103(41):15050–15055, 2006.

E. Vecharynski, F. Xue, and C. Yang. E. Vecharynski, F. Xue, and C. Yang. private communication, 2013.

E. H. Van Veen, W. L. Van Dijk, and H. H. Brongersma. *Chem. Phys.*, 16:337–345, 1976.

M. Vengris, I.H.M. van Stokkum, X. He, A.F. Bell, P. Tonge, R. van Grondelle, and D.S. Larsen. *J. Phys. Chem. A*, 108:4587–4598, 2004.

A. Venkatnathan and M. K. Mishra. *Chem. Phys. Lett.*, 296:223 – 232, 1998.

A. Venkatnathan, M.K. Mishra, and H.J. Aa. Jensen. *Theor. Chim. Acta*, 104:445–454, 2000.

M. Vinodkumar, H. Bhutadia, B. Antony, and N. Mason. *Phys. Rev. A*, 84, 2011.

L. Vogt, R. Olivares-Amaya, S. Kermes, Y. Shao, C. Amador-Bedolla, and A. Aspuru-Guzik. *J. Phys. Chem. A*, 112:2049–2057, 2008.

V. P. Vysotskiy and L. S. Cederbaum. *J. Chem. Phys.*, 132:044110, 2010.

I. C. Walker, A. Stamatovic, and S. F. Wong. *J. Chem. Phys.*, 69:5532, 1978.

Y. Wang, J.Y.-J. Shyy, and S. Chien. *Ann. Rev. Biomed. Eng.*, 10:1–38, 2008.

R. Wehlitz, D. Lukic, and B. Bluett. *Phys. Rev. A*, 68:052708, 2003.

F. Weigend. *Phys. Chem. Chem. Phys.*, 8:1057–1065, 2006.

F. Weigend. *J. Comput. Chem.*, 29:167–175, 2008.

F. Weigend and M. Häser. *Theor. Chim. Acta*, 97:331–340, 1997.

F. Weigend, M. Häser, H. Patzelt, and R. Ahlrichs. *Chem. Phys. Lett.*, 294:143–152, 1998.

F. Weigend, M. Kattannek, and R. Ahlrichs. *J. Chem. Phys.*, 130:164106, 2009.

F. Weigend, A. Köhn, and C. Hättig. *J. Chem. Phys.*, 116:3175, 2002.

F. Weinhold and C. R. Landis. *Chem. Ed.: Res. & Pract. Eur.*, 2:91–104, 2001.

J.L. Whitten. *J. Chem. Phys.*, 58:4496, 1973.

P.O. Widmark, P.Å. Malmqvist, and B. Roos. *Theor. Chim. Acta*, 77:291, 1990.

S. Wilson. *Comp. Phys. Comm.*, 58:71–81, 1990.

Y. Shao, L. Fusti-Molnar, Y. Jung, J. Kussmann, C. Ochsenfeld, S. Brown, A.T.B. Gilbert, L.V. Slipchenko, S.V. Levchenko, D.P. O'Neill, R.A. Distasio Jr, R.C. Lochan, T. Wang, G.J.O. Beran, N.A. Besley, J.M. Herbert, C.Y. Lin, T. Van Voorhis, S.H. Chien, A. Sodt, R.P. Steele, V.A. Rassolov, P. Maslen, P.P. Korambath, R.D. Adamson, B. Austin, J. Baker, E.F.C. Byrd, H. Daschel, R.J. Doerksen, A. Dreuw, B.D. Dunietz, A.D. Dutoi, T.R. Furlani, S.R. Gwaltney, A. Heyden, S. Hirata, C.-P. Hsu, G.S. Kedziora, R.Z. Khalliulin, P. Klunziger, A.M. Lee, W.Z. Liang, I. Lotan, N. Nair, B. Peters, E.I. Proynov, P.A. Pieniazek, Y.M. Rhee, J. Ritchie, E. Rosta, C.D. Sherrill, A.C. Simmonett, J.E. Subotnik, H.L. Woodcock III, W. Zhang, A.T. Bell, A.K. Chakraborty, D.M. Chipman, F.J. Keil, A. Warshel, W.J. Hehre, H.F. Schaefer III, J. Kong, A.I. Krylov, P.M.W. Gill, M. Head-Gordon. *Phys. Chem. Chem. Phys.*, 8:3172–3191, 2006.

J. Yang, Y. Kurashige, F.R. Manby, and G.K.L. Chan. *J. Chem. Phys.*, 134:044123, 2011.

J.-S. Yang, G.-J. Huang, Yi-H. Liu, and S.-M. Peng. *Chem. Commun.*, pages 1344–1346, 2008.

D.L. Yeager and M.K. Mishra. *Int. J. Quant. Chem.*, 104:871–879, 2005.

Y. Yoshioka, H. F. Schaefer, and K. D. Jordan. *J. Chem. Phys.*, 75:1040, 1981.

P.R. Zdanska and N. Moiseyev. *J. Chem. Phys.*, 123:194105, 2005.

S. B. Zhang and D. L. Yeager. *Mol. Phys.*, 110:663–667, 2012.

Y. Zhou and M. Ernzerhof. *J. Phys. Chem. Lett.*, 3:1916–1920, 2012.

M. Zimmer. *Chem. Rev.*, 102:759–781, 2002.

M. Zubek and C. Szmytkowski. *J. Phys. B*, 10(1):L27–L29, 1977.

D. Zuev, K. Bravaya, M. Makarova, and A.I. Krylov. *J. Chem. Phys.*, 135:194304, 2011.

D. Zuev, K.B. Bravaya, T.D. Crawford, R. Lindh, and A.I. Krylov. *J. Chem. Phys.*, 134:034310, 2011.